FINAL REPORT
FOR THE
AVHRR/2 AND HIRS/2I
IMPROVEMENT STUDY
CONTRACT NAS5-29121

JULY, 1986

Prepared For

National Aeronautics and Space Administration
Goddard Space Flight Center
Greenbelt, Maryland 20771

L. D. Owens
AVHRR Project Engineer

R. J. Koczor
Manager, E-O Systems
Engineering Department

AEROSPACE/OPTICAL DIVISION ITT

Table of Contents

Table of Contents (Continued)

Table of Contents (Continued)

Table of Contents (Continued)

APPENDICES

List of Figures

List of Figures (Continued)

List of Figures (Continued)

List of Figures (Continued)

List of Tables

List of Tables (Continued)

1.0   INTRODUCTION

1.1   General

          This report covers the results of a study performed by ITT
Aerospace Optical Division Fort Wayne, Indiana under contract
NASS-29121 for NASA Goddard Space Flight Center.

          The scope of the study was to determine the feasibility,
impacts and design as well as cost associated with incorporation of
desired improvements to the AVHRR/2 and HIRS/2I instruments for the
NOAA-K, L and M satellites. A determination of the effects of these
changes on all aspects of the instrument assembly, tests at ITT and
RCA, flight operation and software was included.

1.2   Areas of Study

          The study Statement of Work included 11 areas of study.
These are listed in Table 1.1-1. The Statement of Work is included as
Appendix A to this report.

Table 1.1-1. Areas of Study

 1. Improve channels 1 and 2 Spectral Characteristics - AVHRR
 2. Stability Monitor for Channels 1 and 2 - AVHRR
 3. Add Channel 3A - AVHRR
 4. IR Calibration Target Study - AVHRR
 5. Scan Motor Change - AVHRR
 6. Channels 1, 2 and 3A Gain Change - AVHRR
 7. Test Equipment Changes - AVHRR
 8. Electronic Redesign - AVHRR
 9. Dynamic Range Increase, CH. 4 and 5 - AVHRR
10. RFI Suppression Investigation - AVHRR
11. Widen Channel 20 - HIRS

          The output of this study includes this final report plus a
design data package consisting of electrical schematics, mechanical
detail drawings, optical detail drawings, procurement specifications
and a preliminary interface drawing.

          Several of the study areas were conceptual in nature.
these areas are identified as such in this report. The results of
these conceptual studies do not include detailed design drawings as
they are intended merely to cover feasibility.

1.3   Report Format

          Each of the eleven areas of study is covered in this report
in a separate section. The section begins with the pertinent require-
ments from the Statement of Work. The areas of study and various trade
offs follow. The final part of each section gives the selected
approach and performance expected.

The scope of the study was such that many approaches were investigated in some areas before a selection was made. While this report will try to cover all of these approaches the main thrust of this report is to cover in detail the selected approaches and designs.

1.4   Description of the AVHRR/3

Figure 1.4-1 is an exploded view of the AVHRR/3 showing the various subsystems of the instrument. The design maintains the modular concept which has been our basic design approach from the first AVHRR instrument. This flexible approach allows modifications to an individual subsystem without affecting other subsystems. Due to this modular approach ITT was able to implement the changes asked for in the work statement without a major redesign of the instrument.

The exploded view of the AVHRR/3 shows an instrument with all of the major changes included. A collimated lamp source stability monitor is shown on this illustration as this would be the simplest option to implement in our design.

Figure 1.4-2 is an outline drawing of the AVHRR/3 instrument. The darkened areas on the drawing indicate the growth in the package size from an AVHRR/2 to an AVHRR/3. The major growth is in the + "Y" direction and a slight growth in the + "X" direction. All other changes are internal to the package.

The outline drawing does not show any growth for a stability monitor. This program has developed several concepts for a stability monitor and presented them in Section 3.0. The decision for the type of monitor to be developed or even the need for a monitor has not been made at this point, therefore no monitor is shown on the outline drawing.

Figure 1.4-1 AVHRR/3

+YAW

—ROLL   —PITCH

ELECTRONICS SUBSYSTEM

OPTICAL SUBSYSTEM

STABILITY MONITOR SUBSYSTEM

SCANNER SUBSYSTEM

BASEPLATE

RADIANT COOLER SUBSYSTEM

STABILITY MONITOR DIODES

AEROSPACE/OPTICAL DIVISION ITT

3
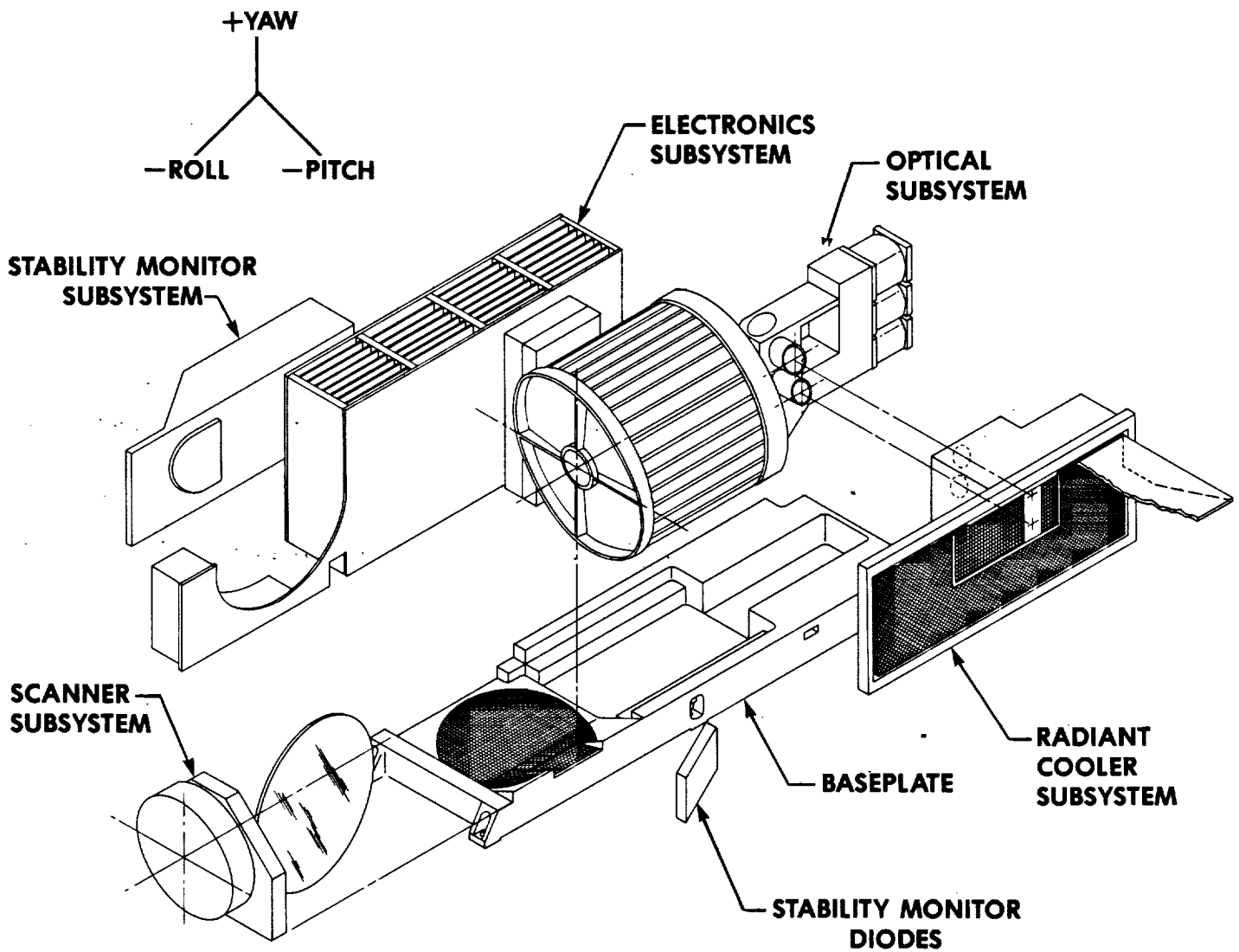
2.0   AVHRR CHANNELS 1 AND 2 IMPROVEMENTS

2.1   Requirements

Changes are desired in the spectral responses of channel 1 and channel 2 as well as an increase in signal-to-noise ratio in both channels.

There will be some modification to the channel 1 and 2 relay optic design as a result of the added channel 3A. The primary change is elimination of the very inefficient neutral density beamsplitter to separate channels 1 and 2. It will be replaced with a high efficiency dichroic beamsplitter.

Complete discussion of the optical design of these channels is found in Section 4.0 where channel 3A implementation is discussed.

2.1.1   Channel 1

Improve Channel 1 spectral symmetry and uniformity. Eliminate out-of-band response at approximately 0.92 micrometers (µm). It is desired that the present Channel 1 signal-to-noise requirement of 3:1 be changed to 9:1 at 0.5% Albedo. The desired Channel 1 characteristics are as follows:

The total instrument response characteristics of Channel 1 shall be symmetric about 0.63 µm ± 0.01 µm as follows:

● 50% of maximum response points:

0.58 ± 0.02 µm, and

0.68 ± 0.02 µm.

A separation between the 50% points of 0.1 µm shall not be exceeded.

● 5% response points: 0.04 µm or less from the 50% points.

● 80% response points: 0.02 µm or less from the 50% points.

● The response between the 80% response points on opposite sides of the center frequency shall always exceed 80%.

● The 50% response point tolerance of 0.02 µm may be extended to TBD if the above requirements cannot be met.

● The total out-of-band response shall be less than 2% of the total integrated response within the bandpass region when viewing a solar source which simulates the solar spectral energy distribution.

2.1.2   Channel 2

        Change Channel 2 spectral bandwidth. Spectral symmetry,
uniformity, and minimum spectral out-of-band response shall also be
considered in re-designing this channel. It is desired that the pre-
sent Channel 2 signal-to-noise requirements of 3:1 be changed to 9:1 at
0.5% Albedo.

        The total instrument response characteristics of Channel 2
shall be symmetric about 0.855 µm ± 0.005 µm as follows:

        ● 50% of maximum response points:

           0.840 ± 0.005 µm, and

           0.870 ± 0.005 µm.

A separation between the 50% points of 0.03 µm shall not be exceeded.

        ● 5% response points: 0.015 µm or less from the 50%
          points.

        ● 80% response points: 0.01 µm or less from the 50%
          points.

        ● The response between the 80% response points on opposite
          sides of the center frequency shall always exceed 80%.

        ● The 50% response point tolerance of 0.005 µm may be
          extended to TBD if the above requirements cannot be met.

        ● The total out-of-band response shall be less than 2% of
          the total integrated response within the bandpass region
          when viewing a solar source which simulates the solar
          spectral energy distribution.

        The Channel 1 and 2 changes are being requested because it
is the desire by NOAA to use these channels for radiometric measure-
ments for monitoring terrestrial vegetation, and enhance aerosol remote
sensing. Therefore, minimum polarization is required for these chan-
nels, as well as field-of-view symmetry.

2.2   Approaches Studied

2.2.1   Channel 1 Spectral Response

        The two changes requested include the elimination of a
spurious response and an improvement in spectral symmetry.

        Figure 2.2-1 is the channel 1 spectral response measured on
SN205. It shows the non-symmetric response on the shortwave side of
the bandpass as well as the secondary peak around 0.90 microns. This

Figure 2.2-1 TYPICAL AVHRR/2 CHANNEL 1 SPECTRAL RESPONSE

3-29-84
AVHRR/2, SN-205
SPECTRAL RESP.
CH. #1
EXPANDED

EXPANDED X 10

INTEGRATED OUT-OF-BAND RESPONSE

$$(EST.) \cong \frac{16.5}{1217} = .014$$

RELATIVE RESPONSE

1.0
0.9
0.8
0.7
0.6
0.5
0.4
0.3
0.2
0.1
0

0.50   0.60   0.70   0.80   0.90   1.0   1.1

WAVELENGTH (μm)

AEROSPACE/OPTICAL DIVISION ITT

7
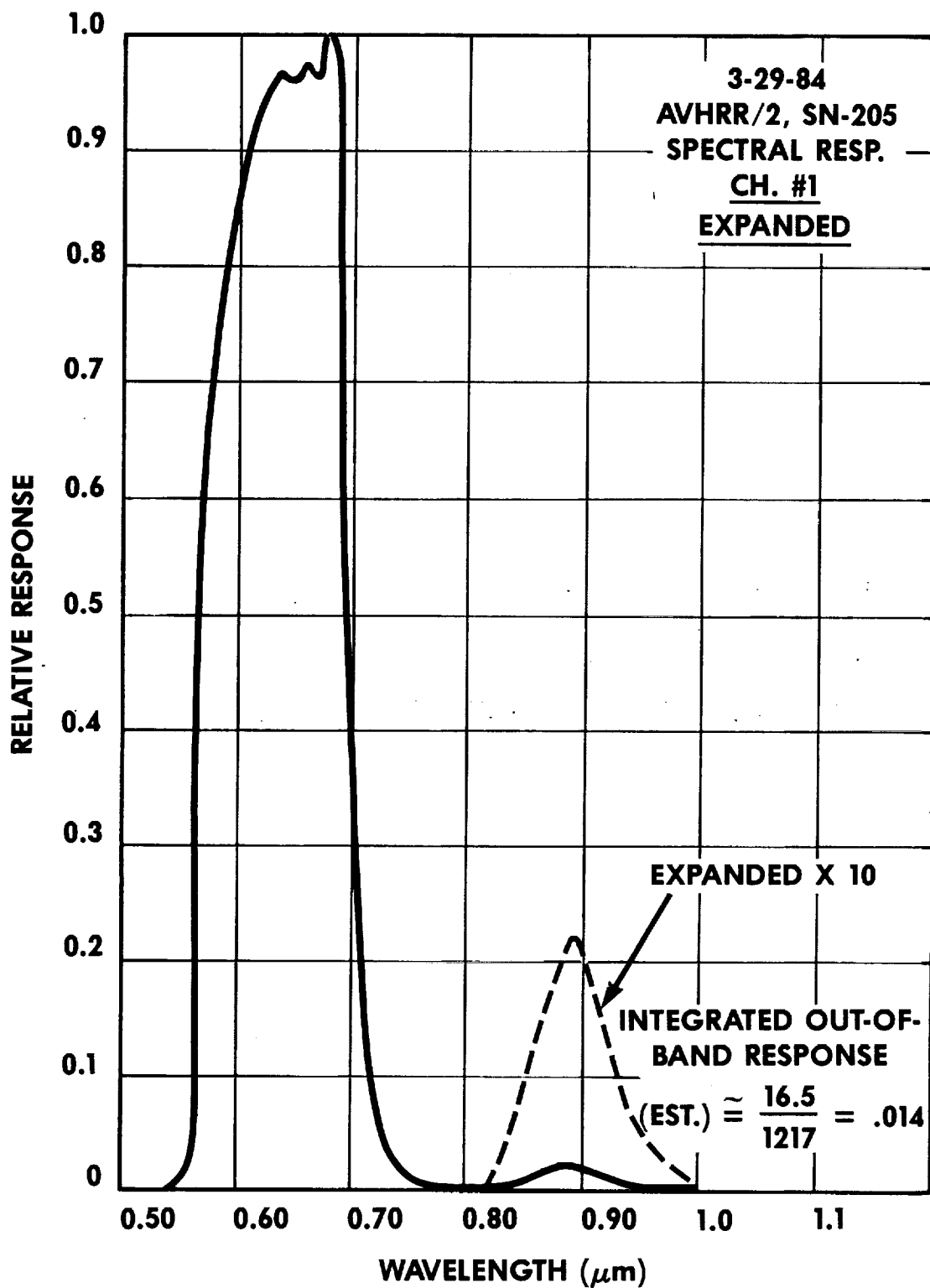
secondary response averaged around 2% in all flight models since AVHRR/1 Protoflight Model.

The poor shortwave cut-on slope is primarily defined by the silicon detector. The filter response is symmetrical. The system passband can be improved by adding an optical element to compensate for the rising detector response in the passband.

Several optical elements were investigated. The basic approach is to add a Schott glass shortwave pass filter which has a slope opposite of the detector (that is, it is decreasing toward longer wavelengths). Figure 2.2-2 gives a representation of the technique.

Several glasses in the KG-1 through KG-4 series were investigated along with variations in thickness. Thicker glasses absorb the .90 micron peak more completely; however, the passband symmetry degrades on the longwave side. Less absorption improves symmetry but gives less absorption of the secondary peak. Figure 2.2-3 gives the channel 1 response with the present AVHRR/2 silicon detector response and two glass filters, 1.5 mm of KG-1 and 3.0 mm of KG-4. The KG-1 attenuates the secondary peak to about 0.04%; however, it skews the passband toward short wavelengths. The KG-4 gives a more symmetrical passband but less attenuation of the secondary response.

Improved longwave attenuation can be obtained (without degrading passband symmetry) by changing to a "blue enhanced" response detector. This detector is identical in construction to the regular silicon except that it is anti-reflection coated for shorter wavelengths and is doped to have a slightly different junction depth than the regular silicon detector.

Use of this detector with no Schott filter glass would result in the system spectral response shown in Figure 2.2-4. Passband symmetry is very good but the secondary peak is still present.

The optimum combination appears to be use of a blue enhanced detector with 6.0 mm of KG-4 filter glass. This combination gives reasonable symmetry and excellent rejection of the longwave spurious peak.

Expected total system response for this combination is given in Figure 2.2-5. This is the proposed modification.

A question was raised by GSFC personnel as to the radiation hardness of the Schott KG-4 filter. Literature search revealed no specific data. Therefore samples of the KG-4 were given to GSFC Metsat Project Office for radiation testing. Results are unknown at the time this report was prepared.

Figure 2.2-2 TECHNIQUE FOR REDUCING SECONDARY RESPONSE IN CHANNEL 1

SILICON DETECTOR
(S.D.C. BLUE-ENHANCED)

SCHOTT FILTER
GLASS, TYPE KG4
(6.0 mm THICK)

SYSTEM RELATIVE
RESPONSE

AVHRR CH. 1
SPECTRAL BAND

RELATIVE RESPONSE

WAVELENGTH (NANOMETERS)
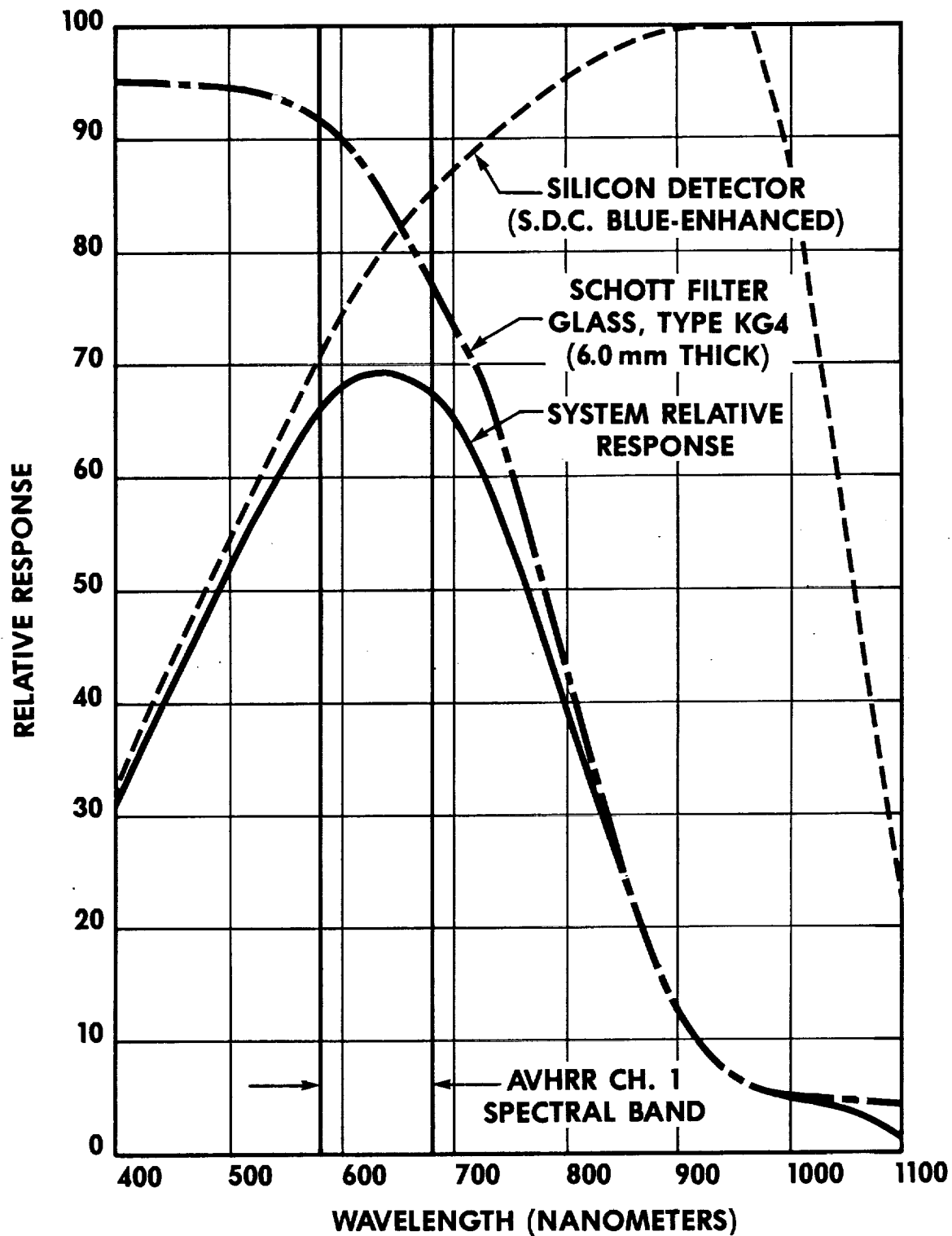
AEROSPACE/OPTICAL DIVISION ITT

Figure 2.2-3 CALCULATED RESPONSE FOR VARIOUS FILTER GLASSES

AEROSPACE/OPTICAL DIVISION **ITT**

10
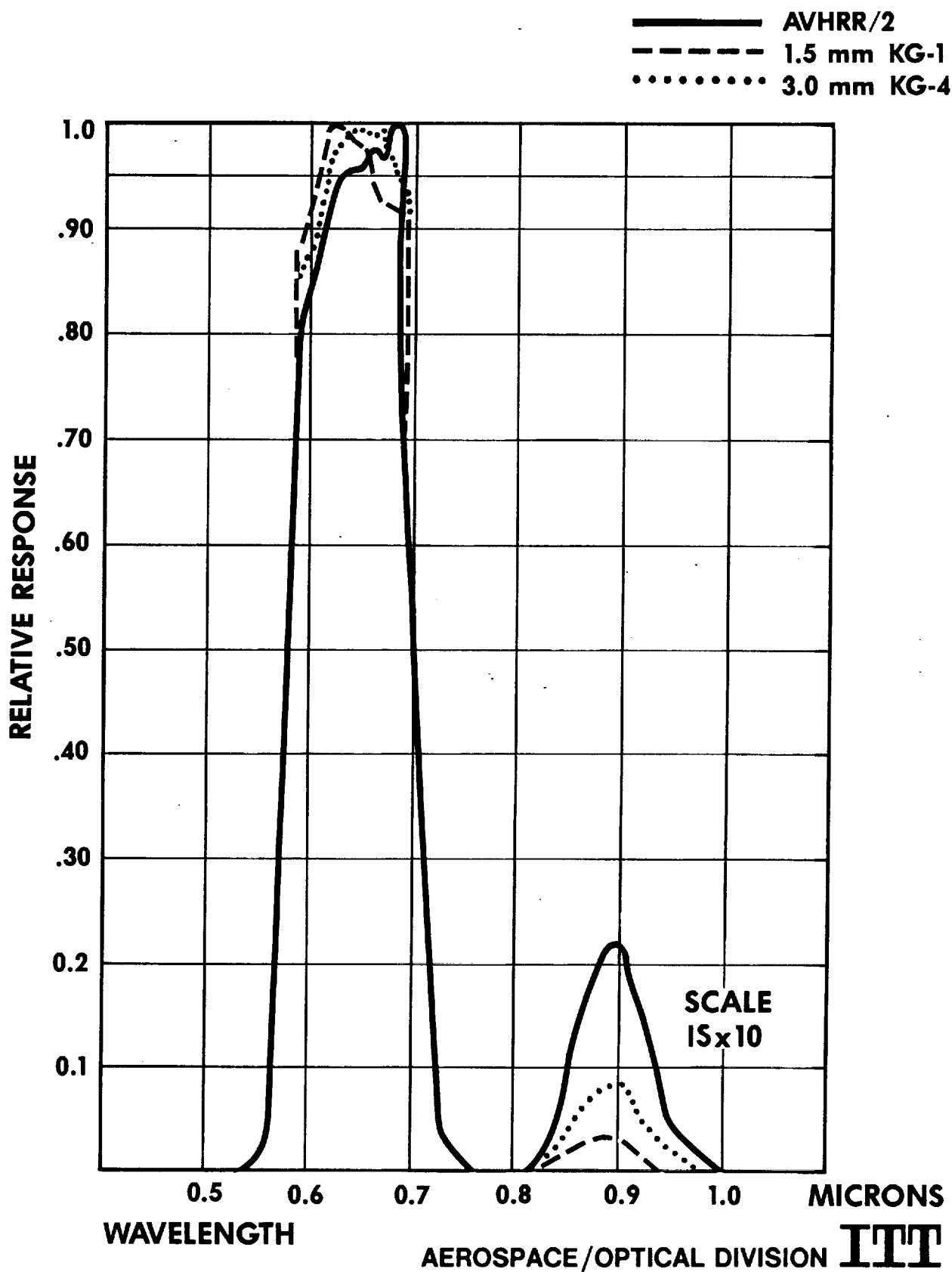
Figure 2.2-4 CHANNEL 1 SYSTEM RESPONSE WITH BLUE ENHANCED SILICON DETECTOR

SCALE IS x 10
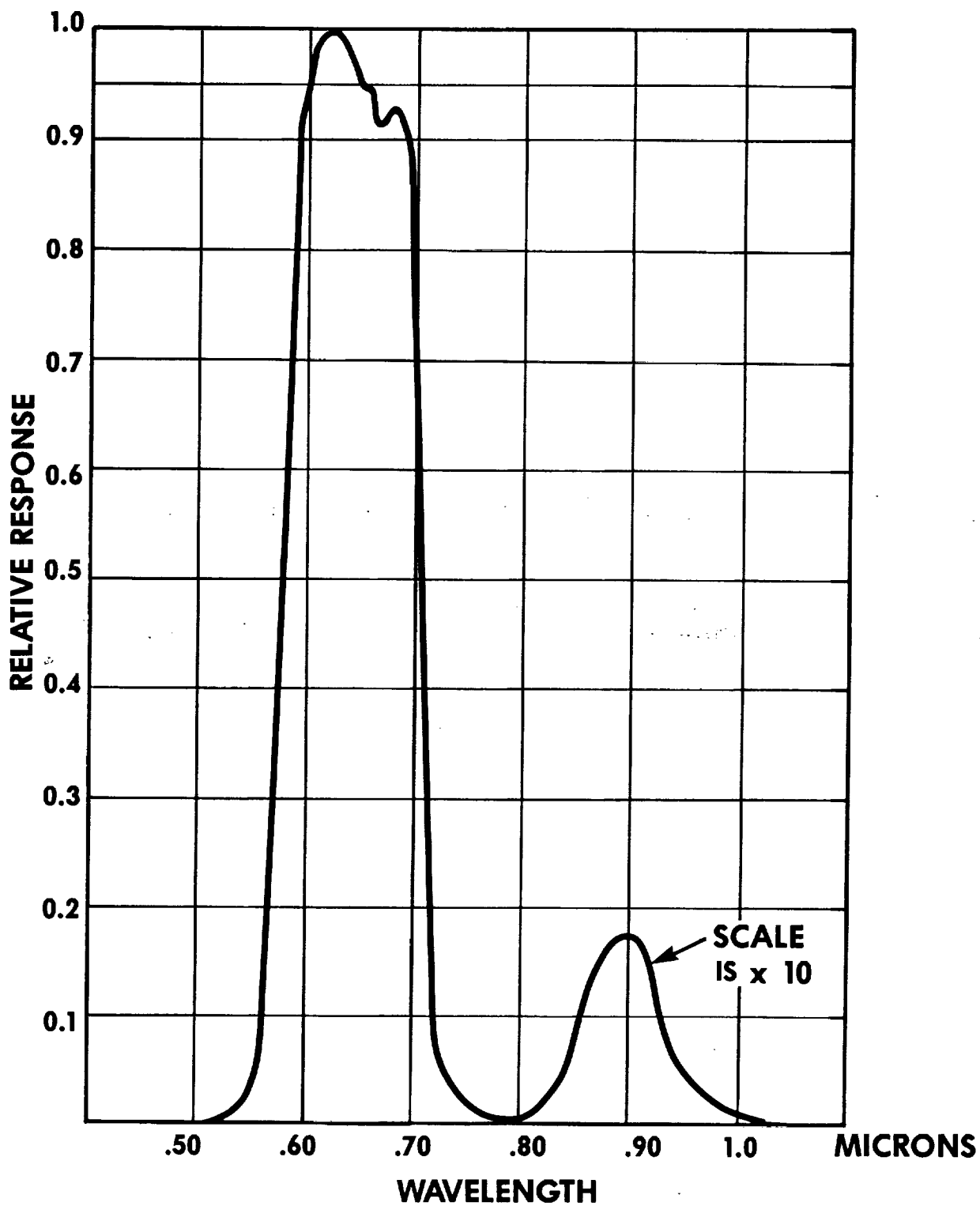
AEROSPACE/OPTICAL DIVISION ITT

Figure 2.2-5   CHANNEL 1 RESPONSE WITH KG-4 FILTER AND BLUE ENHANCED DETECTOR

SCALE
IS x 10

RELATIVE RESPONSE

WAVELENGTH

MICRONS
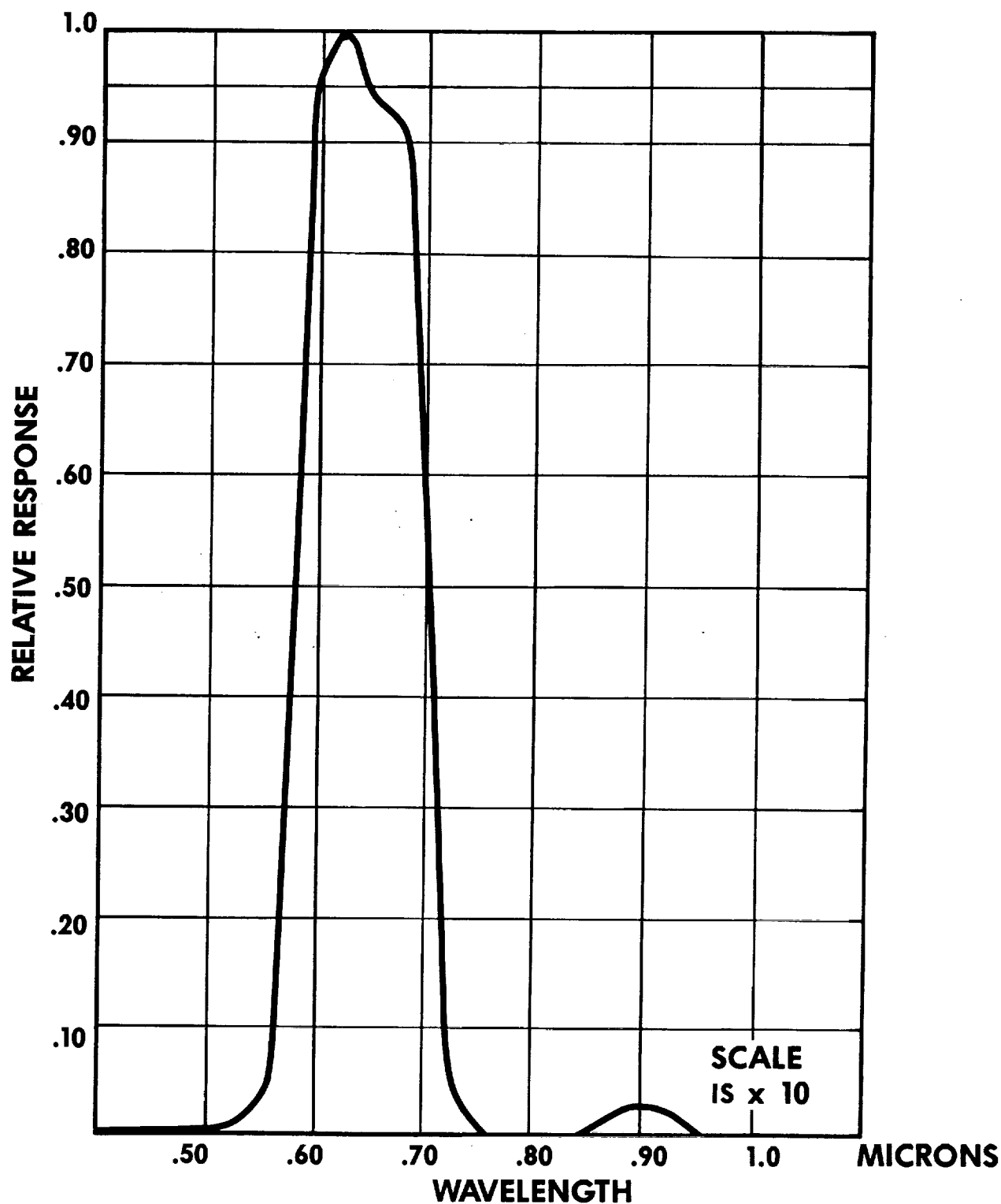
AEROSPACE/OPTICAL DIVISION **ITT**

Table 2.2-1. AVHRR/3, Optical Transmission, Nominal Average In-Band

Component	CH. 1	CH. 2	CH. 3A
SCAN MIRROR [1]	0.94	0.91	0.885
TEL. PRIMARY[1]	0.94	0.91	0.885
TEL. SECONDARY[1]	0.94	0.91	0.885
OBSCURATION	0.92	0.92	0.92
ITO DICHORIC #1[2]	0.93	0.91	0.76
ITO DICHORIC #2[2]	0.93	0.91	0.76
DICHROIC B/S, TRANS. 3A[2]	0.99	0.99	0.81
DICHROIC B/S, TRANS. #2[2]	0.99	0.91	N.A.
FOLD MIRROR, GOLD	N.A.	0.96	N.A.
FILTER, BANDPASS[3]	0.75	0.75	0.75
FOCUS LENS #1[4]	0.98	0.98	0.98
FOCUS LENS #2[4]	0.98	0.98	0.98
FOCUS LENS #3[4]	0.98	0.98	0.98
SPECTRAL BALANCE	0.85	N.A.	N.A.
TOTAL	0.389	0.350	0.237

NOTES:

(1) MIRROR REFLECTIVITIES FROM EVAPORATED METAL FILMS, INC: VALUES LISTED ARE 1% ABSOLUTE LESS THAN CALCULATED VALUE FOR ENHANCED ALUMINUM.

(2) LISTED VALUES FOR ITO DICHROICS AND DICHROIC BEAMSPLITTERS TO SEPARATE CHS. 1, 2 AND 3A ARE 1% ABSOLUTE GREATER THAN OUR SPECIFIED MINIMUM VALUES.

(3) LISTED TRANSMISSION VALUES FOR BANDPASS FILTERS ARE 3% ABSOLUTE GREATER THAN OUR SPECIFIED MINIMUM VALUES.

(4) FOCUS LENS TRANSMISSION VALUES ARE ESTIMATED NOMINAL VALUES BASED ON AVHRR/2 MEASURED DATA FOR CHS. 1 AND 2; CHANNEL 3A VALUE OBTAINED FROM II-VI CO.

2.2.2   Channel 2 Spectral Response

        The change to channel 2 is basically a narrowing of the
response. Implementation will be straight-forward, requiring only a
new spectral bandpass filter.

        A preliminary filter specification has been generated and
reviewed by potential vendors. No problems are anticipated in meeting
the desired parameters.

        A decision to change the spectral bandpass of channel 2 can
be delayed if there is a question as to the need or desire to change.
ITT could procure filters for both old and new channel 2 responses and
install the desired one during system optical assembly.

2.2.3   Channels 1 and 2 Sensitivity

        An increase in signal-to-noise ratio was requested for
these channels. The present specified minimum value is 3 to 1 for a
1/2% albedo scene at a noon nadir point. The proposed minimum value is
9 to 1 under the same conditions.

        Two changes will occur which will accommodate this
increased sensitivity. First, the relay optic transmission will be
increased due to the changes needed to incorporate channel 3A (see
Section 4.0). These changes increase the optical transmission from
about 6% to 39% in channel 1 and from about 8% to 35% in channel 2.
The elements in the optics and the values of transmission (or reflec-
tion) assigned to each is given in Table 2.2-1. This table also gives
values for channel 3A to be discussed later.

        Second, the silicon detectors will be operated in a reduced
noise mode by removing the bias voltage.

2.2.3.1   AVHRR/3 Channels 1 and 2 Detector Operation

        The silicon detector channels in the AVHRR use a 0.100-in x
0.100-in detector behind a field stop aperture combined with a 4MΩ
feedback resistor in a transconductance (current-to-voltage)
preamplifier. The detector has a specified maximum dark (leakage)
current of 17nA at 25°C and at the applied bias of -15V. Except for
the size of the field stop, this design is identical to that used in
the HCMR.

        Although this design may be sufficient (i.e., has adequate
design margin) to meet the increased signal-to-noise requirement of 9:1
in both channels, it is far from optimum. In fact, the existing design
can easily be improved, so that the sensitivity is, once again, limited
by the digitization level in both silicon detector channels.

        The 4MΩ feedback resistor has a Johnson noise current at
300K of 7.75 x 10^{-12}A over the 14.5 kHz bandwidth of the AVHRR. The
maximum detector dark current has a shot noise current of 8.88 x 10^{-12}A

over the same bandwidth. When combined with a small shot noise in the
signal current at the 0.5% Albedo level, the total rms noise current is
$1.19 \times 10^{-11}A$. With the improvements to the spectral response and
polarization design, the signal current is reduced by a factor of 4.87x
which reduces the signal shot noise to a negligible level. To further
reduce the noise level and thereby increase the signal-to-noise ratio,
we can a) use a larger feedback resistor, and/or b) reduce the detector
dark current.

The AEM HCMR had an electrical bandwidth of 53 kHz, so that
we know the feedback resistor can be increased to at least

$$R_f = 4 \times \frac{53}{14.5} = 15M\Omega$$

without affecting the frequency response. Fifteen megohms is, inciden-
tally, the feedback resistance used in the INSAT VHRR (IVHRR) silicon
channel. Further increases in R_f are possible, even to the point where
it limits the frequency response of the preamplifier and must be com-
pensated by treble boosting at the post amplifier. However, such a
complication in the circuitry design is neither desirable nor
necessary. At the very least, then, we can increase R_f to $15M\Omega$, which
reduces the Johnson noise current to $4.00 \times 10^{-12}A$ and the total noise
current, to $9.72 \times 10^{-12}A$.

With the increase in the feedback resistance, the dominant
noise becomes the shot noise in the detector dark current. The dark
current can be reduced by a) reducing the detector area and/or b)
reducing or eliminating the bias voltage (-15V). The 0.10-in square
detector is in back of a 0.0238-in square field stop. A significant
reduction in detector area (17.7:1) can therefore be realized if the
detector is used as the field stop. Use of the smaller detector in the
unbiased mode, or at a small back bias, would then reduce the shot
noise in the dark current to the point where the channel sensitivity is
limited by the Johnson noise in the $15M\Omega$ feedback resistor.

2.2.3.1.1   Reverse Bias

Theoretically, the highest sensitivity from a photodiode is
achieved   in the absence of bias. In practice, the optimum is often
a small reverse bias, generally between 0 and 1.0V. In view of these
facts, we would like to know why a large reverse bias (e.g., -15V)
would be applied to a silicon detector. There are several possibili-
ties:

1) To reduce the response time of the detector. The reduc-
tion in response time is of no importance in the present
application; the upper-frequency response can be as high
as 10^6 Hz in the unbiased mode.

2) To reduce the detector shunt capacity. An increase in the shunt capacity does not affect the signal level, it does increase the high-frequency amplitude of the voltage noise associated with the operational amplifier. However, the reduction in shunt capacity that results from reducing the detector area from 0.10-in square to 0.0238-in square is at least as great as the reduction that results from applying -15V to the larger detector.

3) To provide high linearity over a large dynamic range. Comparable linearity is achieved by the use of the transconductance amplifier, which provides a low resistance (short circuit) load to the silicon detector.

4) To stabilize the electronic calibration levels over temperature. The removal of the reverse bias (-15V) from the IVHRR silicon detectors caused the electronic calibration to be a function of temperature. However, the temperature range of the AVHRR is much smaller than that of the IVHRR. In addition, such a temperature dependence is probably dependent upon the method used to inject the calibration signal.

2.2.3.1.2 Photodiode Noise

All three channels involved in the spectral modifications to the AVHRR (0.63 μm, 0.855 μm, and 1.61 μm) will likely use a photodiode-operational amplifier combination to detect and amplify the incoming signal. Channels 1 and 2 use Si photodiodes. The amplifier converts the signal current to a useful voltage level by passing it through a large load resistance at the same time that it presents a low load resistance (short-circuit condition) to the photodiode.

For the low-level, relatively low-frequency signals of interest in the AVHRR, the noise associated with the biased or photoconductive mode of the photodiode is considerably greater than that of the same device operated in the unbiased or photovoltaic mode. This is principally the result of the shot noise associated with the reverse bias leakage current. In the absence of bias and radiation, the detector can produce only Johnson noise; any excess would violate thermodynamic principles. The photodiode noise current is then given by

$$i_d = (\frac{4kT\Delta f}{R_d})^{1/2}$$

where
- k = Boltzmann constant
- T = absolute temperature,
- Δf = noise bandwidth,

and
- R_d = diode shunt (dark, dynamic) resistance.

The shunt resistance can be determined from the equation that relates the diode current I to its junction voltage V.

$$I = I_o \, \underline{/} \exp(qV/\beta kT) - 1 \, \underline{\,/}$$

where I_o = reverse leakage current,
               q = electronic charge,
and β = a constant close to unity

Differentiating this equation, we obtain

$$\frac{1}{R_d} = \frac{dI}{dV} = \frac{I_o q}{\beta kT} \exp(qV/\beta kT)$$

The quantity kT/q is called the thermal voltage V_t; it is the potential by which an electron is accelerated when it absorbs the energy kT from a photon. At room temperature ($T = 300K$), $V_t = 0.026V$.

For $V = 0$ and $\beta = 1$, the above becomes

$$\frac{1}{R_d} = \frac{I_o q}{kT}$$

Substituting this expression into the first equation, we obtain

$$i_d = (4qI_o\Delta f)^{1/2},$$

which is the shot noise in a current $2I_0$. At zero bias ($V = 0$), $I = 0$ and the dark leakage current I_o is exactly cancelled by an equal and opposite diffusion current. Because the two currents are uncorrelated, both contribute full shot noise, and we obtain a noise current equal to the shot noise in a dark current $I_d = 2I_0$. This shows us that the zero bias noise from a photodiode can be interpreted as either the Johnson noise in the dark resistance R_d or the shot noise in the equivalent dark current I_d.

In an ideal photodiode, the dark current is reduced by a factor of 2 by reverse biasing the diode with a voltage $v < 0$ of sufficient magnitude that

$$\exp(qV/kT) \ll 1.$$

In real photodiodes, however, application of the reverse bias produces a leakage (dark) current that increases rapidly with V. On the other hand, some photodiodes show a small increase in quantum efficiency (current responsivity) when a reverse bias is applied. As a result, maximum sensitivity is obtained at zero or a very small reverse bias.

2.2.3.1.3   Silicon Characteristics

A survey of Si photodiodes manufactured by SDC, EG&G, and UDT shows that

$$R_d A_d \approx 1 \times 10^9 \text{ ohm mm}^2,$$

where A_d is the sensitive area of the photodiode. For the 0.0238-inch square field stop for channels 1 and 2, $R_d \approx 2.7 \times 10^9$ ohms. This is much greater than the 1.5×10^7 ohm feedback resistor R_f, so that the noise from the photodiode at zero bias is negligible compared with that from R_f. Hamamatsu manufactures silicon photodiodes with even higher shunt resistance at zero bias. For their low C_j (junction capacity) planar diffussion type (S1336, S1337 Series),

$$R_d A_d \approx 2 \times 10^9 \text{ ohm mm}^2 \text{ (min.)}, \ 10 \times 10^9 \text{ ohm mm}^2 \text{ (typ.)}.$$

2.2.3.1.4   Amplifier Noise

The amplifier noise in these channels is small compared with the noise from other sources. The amplifier noise is usually stated in terms of an input leakage current (I_i) and a noise input voltage per root bandwidth (e_n). A typical value of I_i at 25°C is 20pA − 0.02nA, which is much less than the photodiode dark current or the equivalent dark current from the 15 megohm load resistance (3.45 nA). The high frequency amplitude of the noise voltage e_n is increased by the input capacitance C_i, so that the corresponding input noise current becomes

$$i_e = R_f^{-1} e_n (\Delta f)^{1/2} \left[1 + \frac{(\Delta f)^2}{3} (2\pi R_f C_i)^2 \right]^{1/2}$$

where $e_n = 1 \times 10^{-8} \text{ VHz}^{-1/2}$ (typ.).

Δf = electrical bandwidth − 14.5×10^3 Hz,

and R_f = feedback resistance − 15×10^6 ohms.

This equation can be obtained under the following conditions:

    a) The amplifier input resistance ($\sim 10^{11}$ ohms is much greater than the feedback resistance R_f.

    b) The capacitance C_f across R_f is much less than the input capacitance C_i.

    c) The reciprocal of the amplifier gain-bandwidth product ($A/2\pi T$) is much less than $2\pi R_f C_f$.

For comparison with other noise sources, we will express i_e in terms of the equivalent dark current I_e, according to

$$i_e/(\Delta f)^{1/2} = (2q I_e)^{1/2}.$$

where q is the electronic charge.

In order to calculate I_e, we need to know the input capacitance C_1, which is mostly the photodiode capacitance C_d at zero bias. The capacitance per unit area is approximately constant for a given photodiode design. Typical values for Si are:

Mfg.	Series	C_d/A_d @ zero bias (pF/mm^2)
EG&G	PV	29
SDC	photovoltaic	100
	photoconductive	15
UDT	UDT-FIL SXD	5
Hamamatsu	S874, S875	100-130
	S1336, S1337	

The present AVHRR has a specified maximum C_d of 15 pF. If we are to retain this level when the unbiased detector is used as the field stop, we need a silicon photodiode with

$$\frac{C_d}{A_d} < \frac{15pF}{(0.0238 \times 25.4)} 2 = 41pF/mm^2$$

This requirement can be met by selecting the proper series (type of material). From the above list, we can use a silicon detector with $C_d < 15$ pF/mm^2, which corresponds to $C_d = 5.5pF$. Adding 0.5pF for other capacitances, we have $C_1 = 6pF$, which gives us $I_e = 0.03nA$. This is much less than the equivalent dark current current of the 15 megohm resistance, $I_f = 3.45nA$.

2.2.3.2   Channel 1 and 2 Sensitivity Calculation

The signal-to-noise ratio (S/N) in channels 1 and 2 of AVHRR/3 can readily be designed to be limited by the present digitization process. On AVHRR/3 we will no longer use reverse bias on the silicon photodiode detectors because the detectors will be smaller and therefore have lower capacitance. With no reverse bias on the detectors there is no dark leakage current so the detector noise is smaller than on AVHRR/2, hence S/N is larger. The detector dynamic impedance for this size detector at zero bias is on the order of 10^9 ohms (e.g. Silicon Detector Corp.) so the Johnson noise from the 15M ohm feedback resistor is the dominant noise source (with no light input on the detector). At 0.5% scene albedo there is a contribution to total noise from the signal current fluctuation (especially in Channel 1). Ignoring the "noise" from the digitization process we find that the calculated S/N ratio in Channel 1 is 345:1 and in Channel 2 it is 92:1 for 0.5% albedo when using a 15MΩ feedback resistor; an even larger feedback resistor could probably be used to improve the S/N ratio further but is obviously unnecessary.

The signal current (I_s) from the silicon photodiode can be calculated from the following equation:

$$I_s = \frac{1}{4} N \rho(\Delta\lambda) \theta^2 \tau D^2 R$$

where
N = average solar irradiance outside the earth's atmosphere in the spectral band of interest

ρ = average scene (earth) albedo in the spectral band (=0.005)

$\Delta\lambda$ = spectral bandpass (50% amplitude) of AVHRR/3

θ = width of IFOV = 1.31 m r.

τ = optical system transmission in the spectral band

D = diameter of optical aperture (20.3 cm)

R = average silicon photodiode responsivity in the spectral band.

The following table lists the nominal values for each of the parameters and the resulting signal current (for 0.5% albedo).

Parameter	Channel 1	Channel 2
N (watts cm^{-2} μm^{-1})	0.161	0.100
$\Delta\lambda$	0.10 μm	0.03 μm
τ	0.33	0.34
R (amp $Watt^{-1}$)	0.37	0.45
I_s (Amp)	1.74×10^{-9}	4.05×10^{-10}
i_s (Amp rms)	2.84×10^{-12}	1.37×10^{-12}

The signal current fluctuation (i_s) in the photodiode current was calculated from the following equation (for an electrical bandwidth of 14,500 Hz) and is also given in the table:

$$i_s = \sqrt{2\ q\ I_s\ \Delta f}$$

where
q = electrical charge on an electron (1.6×10^{-19} coulomb)

Δf = 3 dB electrical bandwidth.

The Johnson noise current (i_j) from a 15M ohm feedback resistor (in the preamplifier) is given by the equation

$$i_j = \left(\frac{4\ kT\ \Delta f}{R_f} \right)^{1/2}$$

where k = Boltzmann constant (1.38×10^{-23} Joule Kelvin^{-1})

T = temperature of resistor (295 Kelvin)

R_f = 15×10^6 ohms.

The result is 3.97×10^{-12} ampere rms. The only other significant noise is caused by the photodiode capacitance. As a worst case, assume a photodiode capacitance of 20 pf (eg. 55 pf per mm^2 with a detector width of 0.0238 inch = 0.605 mm); this gives $I_e = 0.35 \times 10^{-9}$ ampere and $i_e = 1.27 \times 10^{-12}$ ampere rms. The total noise current (i_t) is given by

$$i_t = \left(i_j^2 + i_s^2 + i_e^2 \right)^{1/2}$$

and the signal-to-noise ratio (S/N) by

$$S/N = \frac{I_s}{i_t}$$

The results were summarized below (for 0.5% albedo).

Parameter	Channel 1	Channel 2
i_j (ampere)	3.97×10^{-12}	3.97×10^{-12}
i_s (ampere)	2.84×10^{-12}	1.37×10^{-12}
i_e (ampere)	1.27×10^{-12}	1.27×10^{-12}
i_t (ampere)	5.04×10^{-12}	4.39×10^{-12}
S/N	345:1	92:1

2.2.3.3   Digitization Limit

The uncertainty introduced by digitization of the signal is in the range between ±0.5 bit and the rms level of ±0.5 x $\sqrt{3}$. For the proposed dual slope amplification technique (see section 7.0) the low albedo levels between 0 and 25% will occupy 0 to 500 levels of the available 1000 levels (10 bits) in channels 1 and 2. Therefore there are 1,000 half-bit levels between 0 and 25% albedo so that ±0.5 bit corresponds to an albedo uncertainty of 25% ÷ 1, 000 or ±0.025%. The 0.5% albedo specification therefore corresponds to a S/N ratio of 0.5% ÷ 0.025% or 20:1 for ±0.5 bit uncertainty (35:1 for ±0.5 x $\sqrt{3}$ for the rms level). Since the S/N ratio due to digitization is much lower in channels 1 and 2 than the calculated S/N ratio due to detector, preamp

and shot noises, the AVHRR/3 output sensitivity should be limited by the digitization process and achieving the NASA-desired 9:1 value will not be difficult.

2.3   Performance Summary

All of the spectral and sensitivity goals stated in the Statement of Work can be met for AVHRR/3 by instituting the following changes:

a. Add filter glass, KG-4, to channel 1 relay optics.

b. Change spectral filter in channel 2.

c. Change size of silicon detector for both channels from 0.100 to 0.024 inches.

d. Change to "blue enhanced" detectors.

e. Increase feedback resistors to 15M ohm.

f. Operate detectors at zero bias.

g. Incorporate optical mods to add channel 3A (i.e. eliminate gold dichroic beamsplitter and neutral density beamsplitter).

Table 2.2-2 lists the performance of AVHRR/2 and summarizes the expected sensitivity performance for AVHRR/3.

Table 2.2-2. Comparison of AVHRR/2 and AVHRR/3 Sensitivity

SIGNAL/NOISE:

AVHRR/2

	$\Delta\lambda$ μm	Req'd	Signal/Noise Calc.[a]	Measured[b]
Ch. 1	0.58=0.68	3:1	11:1	13:1
Ch. 2	0.725-1.00	3:1	44:1	10:1

[a]At Design Margin = 3.2:1 (No Digitization)

[b]Quantization Noise Limited

AVHRR/3

	$\Delta\lambda$ μm	Desired	Signal/Noise Calculated w/o Digitization	w/Digitization
Ch.1	0.58-0.68	9:1	345:1	20:1 (34:1)
Ch.2	0.84-0.87	9:1	92:1	20:1 (34:1)

NOTE: All values are for 1/2% albedo at subsatellite, noon point.

S/N with digitizer gives peak variation (0.5 counts) and rms variation ($0.5/\sqrt{3}$ counts)

3.0   SOLAR CHANNEL STABILITY MONITOR

3.1   Requirements

        Add a stability monitoring source or target for Channels 1
and 2 in order to determine changes or degradation in the total optical
throughput of the instrument. Full aperture illumination is desired.

        This part of the study shall address, but not be limited
to, the following topics:

        1. Type and location of source

        2. Protection from contamination

        3. Size, weight, power, and instrument modification
           requirements

        4. Number of commands necessary to perform the "calibra-
           tion"

        5. Impact of "calibration" on the data stream/MIRP inter-
           face

        6. Radiometric performance and source output versus Channel
           1 and 2 dynamic range

        7. Define any impacts on test equipment (T/V chamber lay-
           out, software, calibration equipment, etc.)

        It is anticipated that the "calibration" sequence will be
performed every 1 to 3 months over the instrument lifetime.

        The conceptual design approach and rough order of magnitude
(ROM) costs to implement the design on the NOAA-Next AVHRR/2 instru-
ments shall be presented to GSFC and NOAA prior to the detail design of
the target in this study. Detail design of the target will not be
required if NOAA decides not to pursue this effort after the ROM costs
to implement the design has been presented to GSFC and NOAA.

3.2   Stability Monitor Concepts

        An outline of the complete study of a stability monitor is
given in Table 3.2-1. A complete monitoring of the instrument's opti-
cal throughput requires that the full aperture, full instantaneous
field of view (IFOV), and full optical train (i.e., all the optical
elements) be covered by the stability monitor. The monitor should
cover several IFOV's for ease of alignment. The primary requirement
for stability is that the monitor be more stable than the instrument by
a large factor (say 10:1). For the best performance, the monitor sta-
bility would be the order of the instrument noise level. The ability
to meet the requirement for a stable monitor is increased by the fact

that the monitor is used on an intermittent basis, i.e., at a duty cycle that is a small fraction of the instrument's duty cycle. A single measurement with the monitor should take no more than 5 minutes. The onground calibration of the monitors increases the ability to use them for inter-comparison of instruments (correlation of successive flight units). Finally, the monitor should operate in a non-interference basis with the normal instrument operation, in the manner of the existing in-orbit infrared calibration targets.

A list of solar channels stability monitors that have been used or proposed for use is given in Table 3.2-2. They may be divided into three types: A) direct view of the sun, B) lamp sources, and C) sunlight diffusers.

3.2.1   Direct View of the Sun

The sun provides a good spectral match to the nominal scene but its radiance level must be attenuated to serve as a stability moni-tor. One way to do this is by aperture-attenuation of a direct view of the sun. Such a monitor has been included on several instruments, includng the SCMR (Nimbus spacecraft), MSS (Landsat), and Thematic Mapper (Landsat). However, this is not a suitable technique for several reasons:

a) The radiance across the sun's disc is nonuniform.

b) It does not fill the aperture or even a significant fraction of the aperture.

c) It requires the introduction of optical elements within the instrument's clear aperture.

d) The sun travels through a sequence of optical elements, incidence angles, or both as the sun angle varies with the orbit and season.

Finally, this monitoring method has not proven to be suc-cessful. In fact, when the Landsat 1 MSS was activated on Orbit 21; it was found that the view mirrors were severely degraded by solar irra-diance.

The above problems can be eliminated by shining the sun's radiation onto a diffuser or into an optical integrator. We will therefore assume that a stability monitor that uses the sun for the source must be used in combination with a diffuser or integrating cavity.

25

Table 3.2-1. Outline: Study of a Stability Monitor for
The Solar Channels (AVHRR/3)

<u>USE</u>

To determine changes/degradations in the total optical throughput
of the solar channels in the AVHRR/3 Imager.

<u>DESIGN OBJECTIVES</u>

1. full aperture
2. cover several instantaneous solid angles of view
3. full optical train (end-to-end)
4. cover all solar channels at a useful signal level (10% albedo
   minimum)
5. preserve stability
   ● protect from contamination
   ● free of interface artifacts (reflections)
   ● monitor output
6. non-interference with instrument operation
   ● nighttime part of orbit
   ● outside of radiant cooler field of view
7. within available space
   ● lamp source of diffuser storage
8. monitor at 1-3 month intervals over instrument lifetime
9. calibrate on the ground

<u>IMPACT ON INSTRUMENT</u>

1. modifications: size, weight, power, location
2. command system
3. data stream/MIRP interface

<u>IMPACT ON TEST EQUIPMENT</u>

1. calibration
2. thermal-vacuum

Table 3.2-2. Stability Monitors for the Solar Spectral Region

Instrument	Sun	Lamp
1. MLA imager (SBRC) (P)	• deployable diffuser • end-to-end • no details given	• lamps in integrating cavity • aft optics only • multi-level • requires rotation of mirror in instrument optical train
2. TM	• direct view without diffuser • small, 4-faceted mirror for sun angle changes	• multi-level (linearity check) • moving cal. shutter injected during turn-around • aft optics only
3. MLA imager (EK)	• deployable diffuser • end-to-end • full aperture • Si PD monitor • multiple levels from change in sun angle	• integrating sphere • filtered for better spectral match to scene • detector arrays only • uniformity improved by transfer lens design
4. MLA imager (Honeywell)	• integrating sphere/diffuser • multi-level (aperture wheel) for SWIR non-linearity	
5. CZCS (BASD)		• aft optics only
(ITT-A/OD) (P)		• integrating cavity • collimator • end-to-end • full aperture • spectrally filtered
6. HRV camera (P)	• mirror or illuminated fiber optics • collimator • end-to-end	• collimator • end-to-end
7. OCI (BASD) (P)	• Ball diffuser (array of convex spheres) • designed for constant radiance over sun angle range	

Table 3.2-2. Stability Monitors for the Solar Spectral
              Region (cont.)

Instrument	Sun	Lamp
(ITT-A/OD) (P)		● integrating cavity ● collimator ● end-to-end ● large fraction of aperture ● spectrally filtered
8. ERBE	● MAM diffuser (array of concave spheres) ● in long baffle ● rotated for sunview	● not end-to-end ● multi-level for linearity check
9. SBUV	● diffuser ● stored against contamination seal (SBUV/2)	

```
   P = proposed
 MLA = multispectral linear array
  TM = thematic mapper
CZCS = coastal zone color scanner
 HRV = high resolution visible
 OCI = ocean color imager
ERBE = earth radiation budget experiment
SBUV = solar backscattered ultraviolet (instrument)

SBRC = Santa Barbara Research Center
  EK = Eastman Kodak
BASD = Ball Aerospace Systems Division
```

3.2.3 Lamp Sources

Except for two proposed techniques of our own and one proposed for the French SPOT HRV camera, there has been no use or proposed use of lamp sources in an end-to-end stability monitor. One reason may be that such a monitor requires the addition of a front-end collimator to provide a useful signal level. In addition, to avoid viewing the lamp filament directly (i.e., to produce a uniform and repeatable radiance source), some means must be used to scramble the emission from the lamp (e.g., a diffusely reflecting integrating cavity or a projection-type collimator). This is also true of lamp monitors that are restricted to the aft optics, where fiber bundles are commonly used for this purpose. The bundles can also be used to combine the outputs from several lamps and to transfer the source radiance to a point within the instrument's optical train.

Outside of the three proposed monitors cited above, all of the developed and proposed techniques restrict the lamp sources to the after or secondary optics, sometimes to just the direct illumination of the detectors themselves. Such partial monitors are provided in many instruments where they serve little practical purpose as demonstrated by the CZCS experience. The secondary optics are not exposed to contamination and other degradations: the real problem is in the fore optics (scan mirror and telescope). Multiple levels are used to check linearity even though the photodiode detectors used are inherently linear over the dynamic range of interest.

Finally, it should be a design objective to avoid the use of mechanical motion to inject the signal from a lamp stability monitor. In particular, we want to avoid the motion of any element that is a part of the instrument's optical train, an approach that has been proposed for the SBRC version of an MLA imager.

3.2.4 Sunlight Diffusers

As described above, stability monitors that use the sun as a source must be combined with a diffuser. If the diffuser is an ordinary Lambertian surface, the radiance level is a function of the sun angle. In some designs, this is taken to be an advantage because it provides multiple end-to-end radiance levels and should be acceptable as long as the sun angle is known to sufficient accuracy. On the other hand, some observers maintain that it fails to meet one of the design objectives of a stability monitor, viz., to provide a fixed and repeatable source of radiance. For this reason, diffusers have been designed to provide a radiance level that is constant over a range of sun angles. The BASD design of such a diffuser consists of a matrix of reflective, convex spheres. However, according to reports, this diffuser is not angularly independent in practice because of multiple reflections among the spheres that were not accounted for in its design. In addition, this diffuser design does not have a suitable baffle, so that it is illuminated by sunlight, reflected from adjacent instrument and spacecraft surfaces, which destroys its repeatability as

well as the ability to relate its radiance to the incident solar irradiance. These problems are avoided in the Mirror Attenuating Mosaic (MAM) diffuser used on the ERBE instrument, which employs concave spheres to avoid multiple reflections and is contained in a long baffle to eliminate extraneous sources of irradiance.

3.2.5   Determination of Electrical Output/Radiance Input

If the detectors are linear over the radiance range to be measured, a two-point radiance input combined with electronic calibration is sufficient to determine the electrical output/radiance input curve. The electronic calibration determines the electrical input/electrical output or gain curve; the two radiance points fix the curve with respect to the radiance input scale. The two radiance points are zero (cold space) and the stability monitor level. This approach is valid even when the gain curve is a bi-linear or other companded conversion of electrical input to electrical output. Such a conversion is used to enhance the measurement of low-level signals in the solar channels when the number of quantization levels is fixed (10 bits in the AVHRR/2).

On the other hand, if the detectors are nonlinear, the two-point, end-to-end radiance levels can be combined with a multi-level lamp radiance source in the aft optics. Such a source can also be used with linear detectors to supplement the electronic calibration measurements.

3.2.6   Conversion to a Calibration Source

For a stability monitor to serve as a calibration source, it must have a stable radiance output that is calibrated against a known standard prior to launch. In addition, the instrument itself must have a stable, known relative spectral response in each of the channels to be calibrated. Meeting this second condition can be a problem, especially in a wide-band spectral channel that goes down to short wavelengths.

This problem is illustrated by data from the Coastal Zone Color Scanner (CZCS) on the Nimbus 7 spacecraft. There is a large decay in signal level in Band 1 (0.443 μm), modest decays in Bands 2 and 3 (0.520 μm), and negligible decay in Band 4 (0.670 μm). On the other hand, the ability to correct this data for the change in channel response indicates that the degradation is reasonably uniform within a spectral band (0.020 μm wide). In this case, a stability monitor can be used to measure and correct for these changes.

With a wide spectral band, such as in the solar channel of an earth radiation budget instrument (e.g., 0.2 - 5 μm), however, such a correction is not possible. A stable and known relative spectral response is then a necessary condition for the measurement of total albedo with an acceptable accuracy, because no satisfactory method has been found to check the spectral response in orbit. This raises

serious questions about the validity of wide band measurements in the solar region that extend below about 0.6 μm.

Even without any change in the spectral response, different source spectral distributions of the same radiance can produce different outputs when that spectral response is non-uniform. In this case, there is no unique calibration factor but rather a set of calibration factors that depend on the type of source under observation. The AVHRR is in effect, calibrated on the ground for a source with the spectral distribution of sunlight outside the atmosphere.

One conclusion to be drawn from this is that measurements should be made in channels with narrow spectral bands, especially if they include the short wavelengths that are subject to in-orbit degradation. When a wide spectral band is to be measured, a continuous set of narrow spectral bands should be measured (e.g., with a spectrometer) rather than a single wide band.

3.2.7 Stability Preservation

If a source is to be used to monitor changes in the solar channels of the AVHRR/3, the stability of that source must be preserved throughout the life of the instrument. That is, we must be sure that any degradation observed is really in the instrument and not the result of changes in the stability monitor itself. The means used to preserve the stability of the source are outlined in Table 3.2-3 and described in detail below.

3.2.7.1 Contamination Control

The potential problem from contamination degradation of a stability monitor is illustrated by severe loss in signal level from the sun "calibration" mirrors used in the Multispectral Scanner (MSS) on Landsat-1. The reduction in signal level was attributed to the polymerization of organic material deposited on the mirrors during the spacecraft thermal test. The degradation was wavelength dependent, with the greater loss at the lower wavelengths, especially below 650 nm. A similar wavelength dependent loss in signal has also been observed in the solar channels of the Nimbus 7 Coastal Zone Color Scanner. In this case, however, the degradation was confined to the channels centered at 443 nm, 520 nm, and 550 nm. There was no detectable signal loss in the two channels centered at 670 nm and 750 nm.

According to Hass and Hunter*, contaminant films of even high molecular weight materials (such as lubricants and diffusion pump fluids) will evaporate away in a clean vacuum (with time) as long as

---

* G. Hass and W. R. Hunter, Laboratory Experiments to Study Surface Contamination and Degradation of Optical Coatings and Materials in Simulated Space Environments, Appl. Opt. 9, 2101 (1970).

Table 3.2-3. Stability Preservation

A. Contamination Control

   ● stored in protective container

   ● heated at all times

   ● infrequent exposure to local atmosphere

B. Radiation Damage

   ● changes induced in uncontaminated stability monitor
     limited to wavelengths below the solar channels

   ● infrequent exposure

   ● pre-irradiate optical elements

C. Interface Reflections (Diffuser)

   ● minimize by use of terminator location

   ● minimize direct sunlight reflection by use of intermediate
     or complex deployment mechanism

the film is not too thick ($< \sim 170$ Å for DC 705 diffusion pump oil). However, a contaminated surface will not be restored if it is irradiated with uv or oil-decomposing particles such as electrons and protons. Such irradiation increases the degradation and makes it permanent because the residue formed by the irradiation does not evaporate. Contaminants on a diffuser surface must therefore be removed prior to exposure to sunlight and energetic particles. Better yet, the contaminants should be prevented from accumulating in the first place.

To this end, the diffuser is stored in a protective receptacle when not in use and is not deployed until the spacecraft atmosphere has dissipated (~ 2 weeks after launch). In addition, the diffuser is heated moderately above the local ambient to prevent the condensation of atmospheric constituents. The temperature should be sufficiently high to prevent the condensation of water vapor, which is absorbed by some diffuser surfaces (e.g., $BaSO_4$). Water vapor has the lowest saturated vapor pressure (at a given temperature) of all the common gases. A higher (out-gassing) temperature may be desirable to remove any accumulated materials from the surface prior to deployment.

Finally, the accumulation of contaminants from the local atmosphere is limited by the short exposure time (low duty cycle) of the stability monitor.

If a lamp source is used as the stability monitor, exposure to direct sunlight and therefore the photolysis of contaminants can be avoided altogether. This is also true of any detectors used to measure the source, whether it is a sunlight diffuser or a lamp source.

3.2.7.2   Radiation Damage

As described earlier, the exposure of the diffuser surface itself to electromagnetic radiation is not a problem because the resulting degradation occurs at wavelengths below those of the AVHRR/3 solar channels. Moreover, even this degradation is limited by the short exposure time of the stability monitor and the shielding of the diffuser surface during storage. A lamp source can be protected by means of a radiation-resistant optical material, such as synthetic sapphire or fused quartz.

Exposure to energetic particles will be a continuous effect since minimum shielding will be employed. This effect is basically a short wavelength effect and can be minimized by pre-irradiating elements which may be susceptible. This process was used as the Earth Radiation Buget Experiment flown on NOAA-9 with some success.

The real problem with space radiation is its ability to convert surface contaminants into forms that cannot be outgassed and that absorb over an extended spectral range that inlcudes the solar channels of the AVHRR/2. The means of dealing with this problem have already been described above under Contamination Control.

3.2.7.3   Interface Reflections (Diffuser)

In the case of a diffuser, artifacts can be produced by the reflection of direct and earth-reflected sunlight from the spacecraft interface onto the diffuser surface. These artifacts are minimized by taking the stability measurement at a terminator position in the orbit. As shown in Appendix M, the first illumination of the diffuser by earth-reflected sunlight (albedo) is much less than the direct illumination by sunlight. And because the artifacts produced by reflection of albedo from the interface onto the diffuser will be much smaller still, we can conclude that earth-reflected sunlight artifacts are negligible.

However, it is not true that a terminator illumination of the diffuser eliminates the direct sunlight artifacts. In order to determine the magnitude of this effect, we need a specific, detailed interface (spacecraft configuration). The effect of diffuse interface reflections can then be determined by calculating the view factors from the diffuser to the unshaded interface reflectors, by the imaging technique (i.e., by specularly imaging the diffuser in the reflector and using the reflector area as a window for incident sunlight). The effect of both types of reflection is reduced if the diffuser is turned away from the body of the spacecraft.

The effect of interface reflections is also reduced by employing either of two techniques proposed for improving the repeatability of the signal level.

    a) Comparing signals only at the same sun angle (same incidence angle). This approach, in effect, incorporates the reflections into the stability source. However, it is only a first-order correction because we can expect the magnitudes of the reflections to change over the life of the spacecraft as a result of reductions in the solar reflectivities of the interface surfaces. As a consequence, it is still necessary that interface be a reasonably small fraction of the direct sunlight signal.

    b) Measure the radiance of the sunlight diffuser with detector/filter monitors for each of the three solar channels. This has the effect of transferring the stability function from the source of the detectors.

3.2.8   Stability Monitor Ground Calibration

The objective of a ground calibration of the stability monitor is to permit the inter-orbit and inter-instrument comparison of data. Combined with the determintion of changes over time, which is the basic function of the stability monitor, this allows the instrument to be used to track long-term, seasonal, and geographical variations in the features under observation.

3.2.8.1   Lamp Source

The calibration of a lamp source stability monitor is straightforward. The instrument itself is used to transfer the calibration from the working radiance standard to the lamp source. First, the instrument is calibrated in the usual manner against an integrating sphere source that employs quartz-iodine lamps. The equivalent radiance of the stability monitor is then determined from this calibration and the measured output produced by the lamp source.

3.2.8.2   Sunlight Diffuser

The calibration factor for the sunlight diffuser is the ratio of measured radiance determined by the instrument calibration to the irradiance of the beam incident on the diffuser. The method used to determine the incident beam irradiance is shown in Figure 3.2-1. The irradiance from a quartz-iodine standard of spectral irradiance is compared with that incident on the diffuser from a collimated tungsten source by means of a spectroradiometer. Because the comparison is between unlike sources (a lamp and a collimated beam), an integrating sphere is used as an averaging device to obtain an accurate ratio.

The calibration factor for the diffuser is given by

$$(C.F.) = \frac{\rho}{\pi} \cos \phi \left(\frac{A_d}{A_o}\right) \cos \zeta \frac{a_e}{\pi}$$

where
ρ = diffuser reflectivity,
ϕ = incidence angle,
ζ = viewing angle,
A_d = unobscured diffuser area,
A_o = unobscured instrument entrance pupil area,
and
a_e = equivalent scene albedo
for
a_o = 0.10 (10%), ρ - 0.98 (BaSO$_4$), and ϕ = ζ = 45° (complex deployment mechanism at its nominal position), we obtain $\frac{A_d}{A_o}$ = 0.2041

In addition,

$$A_o = \frac{\pi}{4} (8^2 - 2^2) \text{ in}^2,$$

and

$$A_d = \frac{\pi}{4} (d^2 - 2^2) \text{ in}^2,$$

where d is the actual diameter of a round diffuser plate. We then obtain

$$d = 4.0305 \text{ in.}$$

Figure 3.2-1   CALIBRATION OF SUNLIGHT DIFFUSER

AEROSPACE/OPTICAL DIVISION ITT
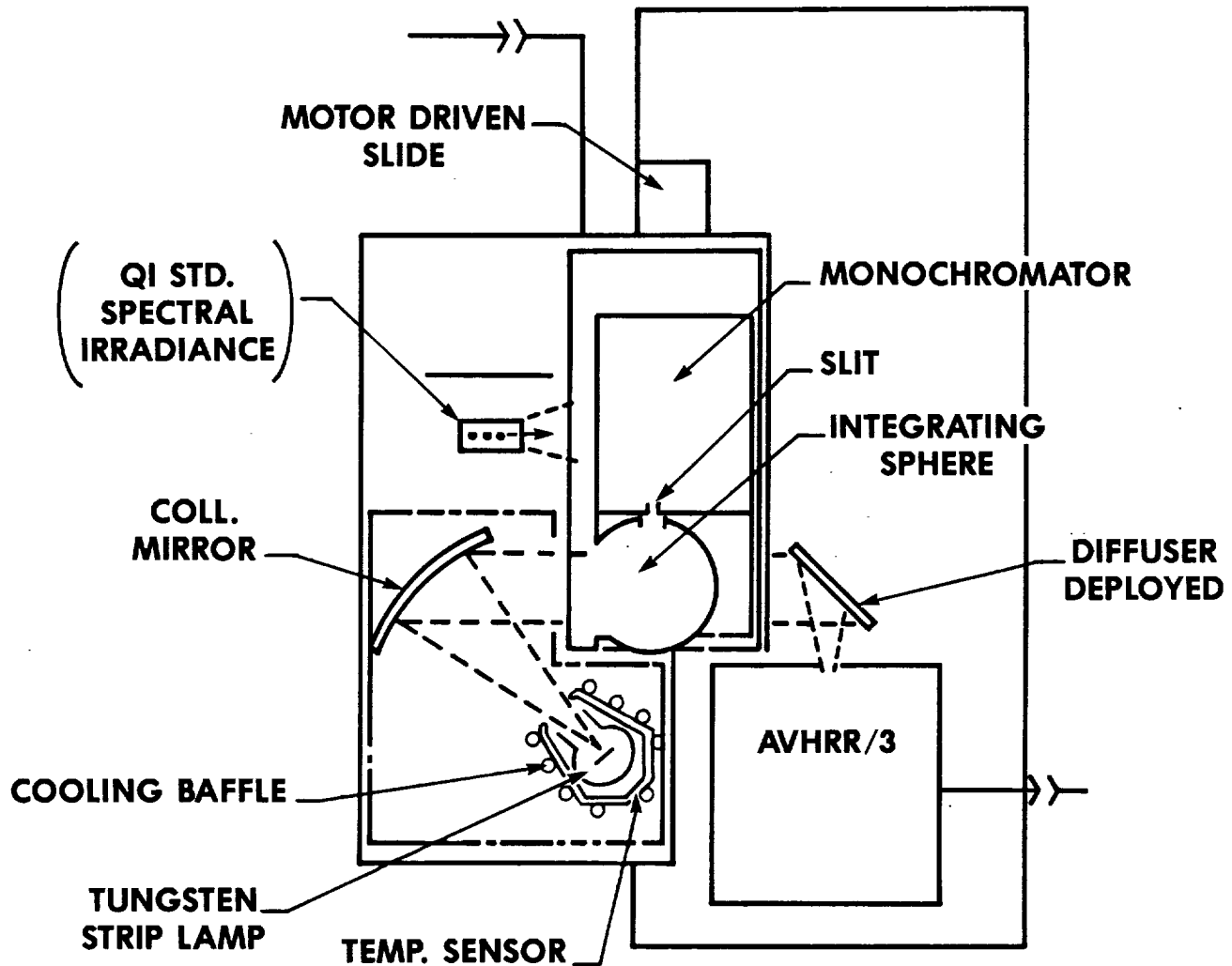
The calibration setup can also be used to measure the repeatability of the deployment mechanism and by mounting the instrument on a rotary table, the variation in stability monitor signal level with incidence angle can be determined. Finally, as shown by the above equations, the calibration serves to confirm that the diffuser signal will be at the desired albedo level.

3.2.9   Stability Monitor Using Lamp Source

3.2.9.1   Basic Concepts

All lamp sources used to monitor the full optical train (i.e., all the optical elements) of a radiometer must employ a front-end collimator to provide a useful signal level. Within this restriction, the source at the focal plane of the collimator that is viewed by the radiometer may take any of three forms:

    a) the exit port in an integrating cavity illuminated by a
       lamp source,

    b) the field diaphragm in a projection-type collimator
       (Koelher illuminator) illumated by a lamp and condenser
       optic,

and   c) the lamp filament itself.

These three approaches are listed in the order of decreasing uniformity and decreasing electrical power for a given signal level. All of them are covered by Maisonneuve and Dinguirard in their study of onboard calibration equipment for the HRV camera on the SPOT satellite. Based on a requirement for a signal level equal to that from the maximum scene radiance in the lowest SPOT wavelength channel (0.50 – 0.59 µm), they selected the third approach because of its low electrical power (< 5W), a choice that requires the design and construction of a special lamp.

However, in the case of the AVHRR/3, we can obtain useful signal levels at moderate power levels using an integrating cavity and a 3-inch diameter collimator, as shown in Table 3.2-4. The results are for a tungsten bulb at a 2800K color temperature in a 1.5-inch diameter BaSO$_4$ integrating sphere whose exit port is in the focal plane of the collimator. With a 5W bulb, the equivalent albedo ranges from 9.7% in Channel 1 to 64% in Channel 3A. A thin gold film (TGF) filter can be added to improve the spectral match to sunlight. This change provides equivalent albedos from 7.6% to 19%, all of which lie on the lower part of the bilinear gain curve (< 25% in Channels 1 and 2 and < 12-1/2% in Channel 3A). By increasing the bulb power to 20W and retaining the TGF filter, we can produce equivalent albedos that lie in the upper part of the gain curve.

The basic design of the lamp source stability monitor is shown in Figure 3.2-2. The monitor can be constructed as a separate

assembly that attaches to the side of the instrument mounting platform. Three detector/filter combinations are used to measure the output of the integrating sphere, one for each of the solar channels. The integrating sphere contains two bulbs, an active bulb and a redundant backup. Or the two bulbs may operate at two different power levels (5W and 20W) to provide monitoring in both parts of the bilinear gain curve. A collimating mirror could be used in place of the lens illustrated, although a lens seems to result in a better match to the available mounting surface. The lamp source is protected by a cover when not in use and can be heated to provide additional protection against the condensation of contaminants.

3.2.9.2   Analysis

The throughput of an integrating sphere, i.e., the ratio of exiting flux to that entering the sphere, is given by

$$T = \frac{f_x \, \rho}{1 - \rho \, (1 - f_p)}$$

where f_x = ratio of exit port area A_x to the total area A of the sphere surface,

f_ρ = ratio of the sum of all port areas (exit, bulbs, and detectors) to A

and ρ = reflectivity of A.

This equation is exact for a sphere, but, as can be shown by the use of the cavity theory, it is also a good approximation for any integrating cavity.

Approximately 90% of the electrical power P to the lamp is converted into radiant flux emitted over the entire spectrum, so that the flux (power) in a given spectral channel is given by

$$F = 0.9 \, KP,$$

where K is the fraction of the total flux emitted in the spectral channel. The radiance at the exit port of the integrating sphere is then given by

$$N_s = \frac{TF \, \tau}{\pi A} = \frac{0.9 KP\tau}{\pi A} \frac{\rho}{[1 - \rho \, (1 - f_p)]}$$

where τ is the transmittance of the collimating optics.

The total flux from the lamp source that is collected by the instrument is given by

$$\phi = N_s A_s \, \Omega,$$

Table 3.2-4. Equivalent Albedoes of Lamp Source
Stability Monitor

Channel	P = 5W w/o TGF	P = 5W w/TGF	P = 20W w/TGF
1	9.7%	7.6%	30.5%
2	29	19	75
3A	64	11	46

TGF = thin gold film

3-inch diameter collimator with a transmission
of 0.9

1.5-inch diameter, $BaSO_4$ integrating sphere

2800K color temperature bulb of electrical power P

Table 3.2-5. Factors in the Equation for the Equivalent Albedo
of a Lamp Source Stability Monitor

Channel	λ (μm)	ρ[a]	M[b]
1	0.63	0.95	15.35
2	0.855	0.95	15.35
3A	1.61	0.92	10.05

[a] $BaSO_4$ paint

[b] For $f_p = 1/80$

Channel	K[c]	H_{do}[d]	K/H_{do}[e]
1	0.0310	0.0164	1.89
2	0.0173	0.0302	5.74
3A	0.0255	0.00134	19.05

[c] For a 2800K color temperature

[d] Wcm^{-2}

[e] $W^{-1} cm^2$

Figure 3.2-2 BASIC DESIGN OF THE LAMP SOURCE STABILITY MONITOR

PROTECTIVE COVER

COLLIMATOR LENS

FOLDING MIRROR

LAMP SOURCE STABILITY MONITOR

INTEGRATING SPHERE

AVHRR/3

ELECTRONICS BOX

MOTOR POWER SUPPLY

52.5°

INSTRUMENT MOUNTING PLATFORM

TUNGSTEN BULB (2 PLACES)

DETECTOR/FILTER (3 PLACES)

INTEGRATING SPHERE

AEROSPACE/OPTICAL DIVISION **ITT**

40
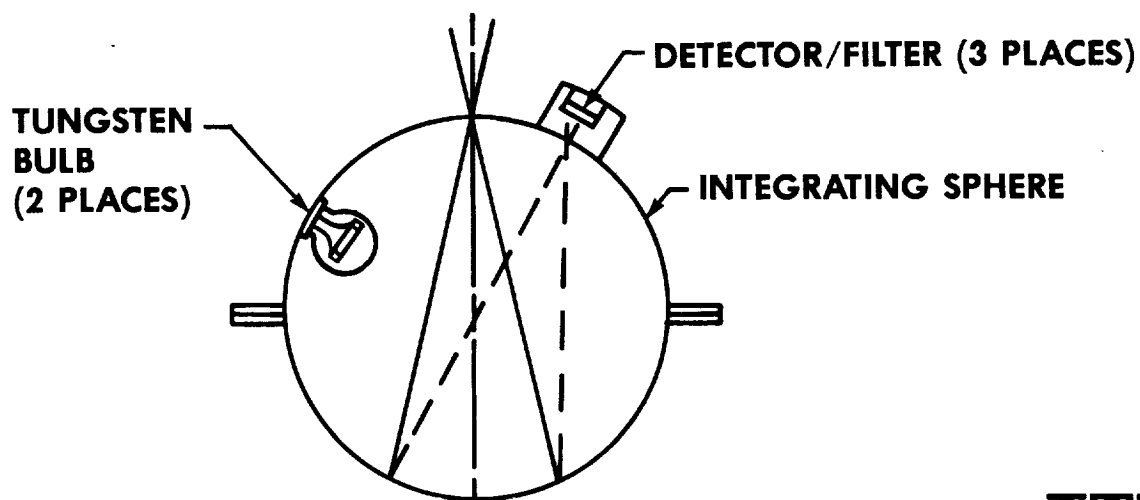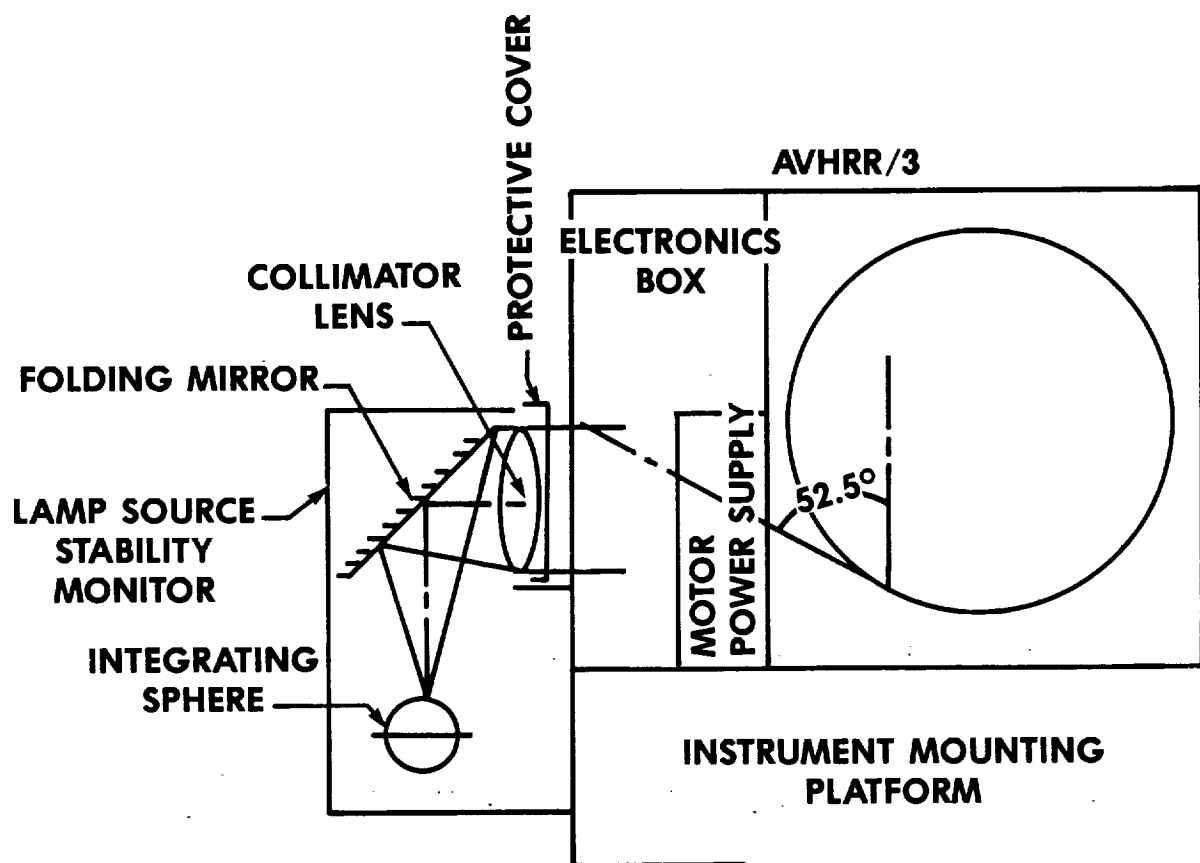
where A_s is the unobscured area of the source collimator and Ω is the solid angle of view of the instrument. This flux is equivalent to a scene albedo a_e that satisfies the equation

$$\phi = \frac{a_e}{\pi} H_{do} A_o \Omega,$$

where H_{do} is the solar irradiance (in the spectral channel) perpendicular to the sun's rays and A_o is the unobscured entrance pupil area of the AVHRR. We therefore have

$$a_e = \frac{\pi N_s A_s}{H_{do} A_o} = \frac{A_s}{A_o} \frac{0.9 K P \tau}{A H_{do}} \frac{\rho}{[1 - \rho(1-f_p)]}$$

For our preliminary design, we used a collimating optic that has a radius of 1.5 inches, which fits in the entrance pupil A_p without obscuration. This gives us

$$\frac{A_s}{A_o} = \frac{(1.5)^2}{8^2 - 2^2} = \frac{2.25}{60}$$

For an integrating sphere with a 1.5 inch diameter and 5 ports (2 bulbs and 3 detector/filter apertures) with an average area equal to a diameter of 0.15 inch, we also have

$$f_p = \frac{5}{4}\left(\frac{0.15}{1.5}\right)^2 = \frac{1}{80}$$

Compared with these ports, the area of the exit opening is small. For example, if the exit port covers a solid angle 5 AVHRR IFOV's in diameter, its diameter is $d_x = 5 \times 1.31 \times 10^{-3} \times 2 \times 3 = 0.039$ in. if the 3-inch collimator has a speed of f/2.

The values of ρ for a BaSo$_4$ diffuser are given in Table 3.2-5 for the three AVHRR/3 solar channels, together with the factor M $= \rho/[1 - \rho(1 - f_p)]$. We see that M is a strong function of ρ, i.e., small changes in p produce large changes in M. The values of K for a 2800K color temperature are also given in Table 3.2-5 together with the corresponding values of H_{do} and their ratio K/H. The resultant values of a_e have already been given in Table 3.2-4 for P = 5W with and without a thin golf film (TGF) spectral filter and for P = 20W with a filter. All these results are for a collimator transmittance τ of 0.9. Typical values were used for the transmittance of the TGF, namely 0.79 in Channel 1, 0.64 in Channel 2, and 0.18 in Channel 3A.

The use of a 2800K color temperature to determine the fraction K is only an approximation. For a tungsten strip lamp without cavities, the form of bulb we expect to use, a more accurate result can be obtained by spectrally integrating the product of the Planck equation and an analytic expression of the spectral emissivity of tungsten.

41

Table 3.2-6. Required Reflective Diffuser Surface
Properties

1. High reflectivity in all solar channels

    ● 0.58 – 0.68 μm (Channel 1)
    ● 0.84 – 0.87 μm (Channel 2)
    ● 1.58 – 1.64 μm (Channel 3A)
    ● Therefore, also low spectral selectivity

2. Stable Material

    ● mechanical
    ● Optical (reflectivity)
      – aging (time)
      – temperature and humidity
      – ultraviolet and particle radiations

3. Reflectivity independent of incidence angle

    ● as close as possible to a perfectly diffuse (Lambertian)
      reflector at the view angle of the instrument

The Schott KG series of glass filters can also be used to improve the spectral match between the tungsten source and the sun, in place of the TGF film.

The color temperature of a lamp source must be measured when there is a channel on the shortwave side of its spectral peak (1.0 μm for a 2800K source). The output in this spectral region is sensitive to changes in source temperature and the lamp output itself is not completely reproducible from one turn-on to the next. By way of example, a 5K or 0.18% increase in a greybody emitter at 2900K increases the exitance (emitted Wcm^{-2}) by 1.46% in channel 1, 1.08% in channel 2, and 0.59% in channel 3A. The color temperature can be determined from relative measurements in two shortwave side spectral channels and is therefore equivalent to monitoring the source output in Channels 1 and 2 of the AVHRR. For completeness, the source would also be monitored in Channel 3A, even though it is past the spectral peak of a tungsten lamp.

3.2.10   Reflective Diffuser Surface

The properties required of a reflective diffuser surface are listed in Table 3.2-6. Candidate surfaces are:

a. MgO (smoked or pressed powder).
b. $BaSO_4$ (pressed powder or spray).
c. Tetrafluoroethylene (TFE, Halon; pressed powder or spray)
d. Metallic coating (aluminum) on a rough surface
e. Arrays of reflective spheres (BASD and MAM diffusers).

All of these materials have high reflectivities in the solar channels and therefore meet the first requirement. However, MgO is mechanically fragile, difficult to prepare, and deteriorates with time. To obtain mechanically stable (strong) coatings, $BaSO_4$ and TFE powders are combined with a binder and applied by spraying.

The surface of $BaSO_4$ is polar and absorbs water, which produces absorption bands in the near infrared region. However, channel 3A (1.58 - 1.64 μm) is outside the absorption bands, the closest of which are centered at 1.4 μm and 1.85 μm. Moreover, the absorption of water can be controlled or prevented in air and eliminated in vacuum by heating the diffuser plate. Such heating is part of the stability preservation (contamination control) of the stability monitor. High humidity (water absorption) does not affect the reflectivity or diffusing properties of $BaSO_4$ in the visible region.

In contrast, TFE is hydrophobic and washable. However, coatings made from TFE show a very weak ultraviolet (wavelengths below 0.29 μm) fluorescence. On the other hand, the emission wavelengths (0.31 - 0.35 μm) are well below the solar channels in the AVHRR/3 and do not affect the suitability of TFE as a diffuser in a stability monitor.

The optical degradation of surfaces from ultraviolet and particle radiations in the space environment is also limited to wavelengths below the solar channels. In addition, such degradation is limited by the very small exposure time (very low duty cycle) of the diffuser.

Metallic coatings on rough surfaces approximate diffuse reflectors only at low incidence angles. The arrays of reflective spheres are non-diffuse by design and are used only over a limited range of incidence angles. As a result, neither of these candidate surfaces is suitable for our application. Having previously rejected the use of MgO, this leaves us with $BaSO_4$ and TFE. And based on the work of Young, et al., the closest approach to a perfect diffuser is a machined, thick sprayed deposit of Kodak $BaSO_4$ white reflectance paint viewed at an angle of 45°.

3.2.11 Geometry of a Sunlight Diffuser

One of the two types of stability monitors for the solar channels is a sunlit diffuser. The elements in a study of such a diffuser are listed in Table 3.2-7. Pertinent issues for this approach are discussed below.

3.2.11.1 Stability Preservation

A reflective diffuser has only one surface to protect from contamination and interface reflections. The storage receptacle can be much simpler and a heater can be attached to the rear surface to elevate its temperature. Artifacts produced by reflections off adjacent spacecraft and instrument surfaces are more easily controlled by surface orientation and/or the attachment of baffles.

3.2.11.2 Signal Level

The signal level from a diffuser of given size and orientation is greater from a reflective diffuser. A typical reflective diffuser has reflectivity of 90% or more, whereas a typical transmissive diffuser has a transmission of 35% to 40%.

The study of reflective diffuser geometry shows that:

A. The best location is at a terminator crossing during the orbit and at or near the nadir position in the scan field of the instrument.

B. The best orientation at nadir is with the diffuser normal at 45° to the scanner line-of-sight and in a vertical plane that makes an angle equal to the orbit normal to sun angle with the perpendicular plane to the orbit (nominal 24.0° a.m. and 67.8° p.m.).

C. The size of the diffuser must be such that its unobscured area is approximately 22% of the entrance pupil area in

Table 3.2-7. Stability Monitor: Sunlight Diffuser Study

1. Geometry

    ● location
      - in orbit
      - in instrument scan field
    ● orientation
      - adjustment for a.m./p.m. orbit
    ● size
      - for 10% (minimum) albedo
    ● shape
      - to cover several instantaneous fields of view

2. Surface Type

3. Stability Preservation

    ● contamination control
    ● interface reflections (artifacts)
    ● monitor

4. Storage Receptacle

    ● location
    ● size and shape
    ● contamination seal
    ● heater

5. Deployment Mechanism

    ● pre-launch adjustment for a.m./p.m. orbit

6. Ground Calibration

order to provide a minimum albedo signal of 10% (referred to normally incident sunlight outside the earth's atmosphere). Because of the 45° view angle from the scanner, the unobscured diffuser area needed to fill the entrance pupil is $\sqrt{2}x$ the pupil area.

D. The reflected sunlight from the diffuser will, of course, over-fill the instantaneous field of view (IFOV) of the AVHRR. However, in order to scan several IFOV's during each rotation of the scanner, the shape of the diffuser must be such that the fraction of the entrance pupil area it covers does not change during this scan. That is, the signal level must be constant over the IFOV's to be covered during the scan of the stability monitor.

The signal level can be measured by locating the diffuser off nadir in the space (anti-sun) side of the scan field. However, the distance from the scanner and therefore the length of the deployment mechanism must be increased to keep the diffuser fully illuminated at a terminator crossing. In addition, an extension too far in this direction will interfere with the space views of the scanner and passive cooler. And finally, there is an optimum scan-field position in an afternoon orbit (30° off nadir), beyond which the signal decreases.

The deployment mechanism can be simplified by setting the diffuser normal in a single, fixed vertical plane midway between the morning and afternoon positions. However, the size of the diffuser must be increased in order to maintain the minimum 10% albedo signal. The deployment mechanism can be further simplified by setting the diffuser normal in a vertical plane perpendicular to the orbit plane, a change that requires an additional increase in the diffuser size. This trade-off between the complexity of the deployment mechanism and the size of the diffuser is summarized in Table 3.2-7.

3.2.11.3   Location in Orbit

During an orbit, the sun describes a cone whose half angle is equal to the orbit normal to sun angle γ, as shown in Figures 3.2-3 and 3.2-4. The azimuth (angle μ) regions during which a deployed diffuser is in the sun are illustrated for both the nominal morning (7:30 a.m.) and afternoon (1:30 p.m.) orbits. During the nominal morning orbit, the spacecraft is in direct sunlight at all times, so that the shading of the deployed diffuser comes mostly during the daytime and is produced by the spacecraft structure, adjacent instruments, and the AVHRR itself. The exact location and extent of this shading region depends on the sun angle and the spacecraft/instrument configuration. During the afternoon orbit, the earth shades the spacecraft during most of the nighttime half of the orbit. Earth shading also occurs in the morning orbit whenever γ exceeds 27.8°, a condition that depends on both the crossing time and the time of year.

In order to cover all of the sun angles that may be encountered, deployment of the diffuser is therefore restricted to the nighttime part of the orbit when the sun is between the earth and the

Figure 3.2-3   SOLAR ILLUMINATION GEOMETRY, TIROS-N ORBIT

(DIFFUSER NORMAL)

$\vec{d}$

θ

ψ (SCAN ANGLE)

δ

γ

Y

(—VELOCITY, ROLL)

$\vec{s}$ (SUN VECTOR)

Z
ORBIT NORMAL,
PITCH)

μ

APPARENT
PATH OF SUN

X (NADIR, YAW)

AEROSPACE/OPTICAL DIVISION ITT

47
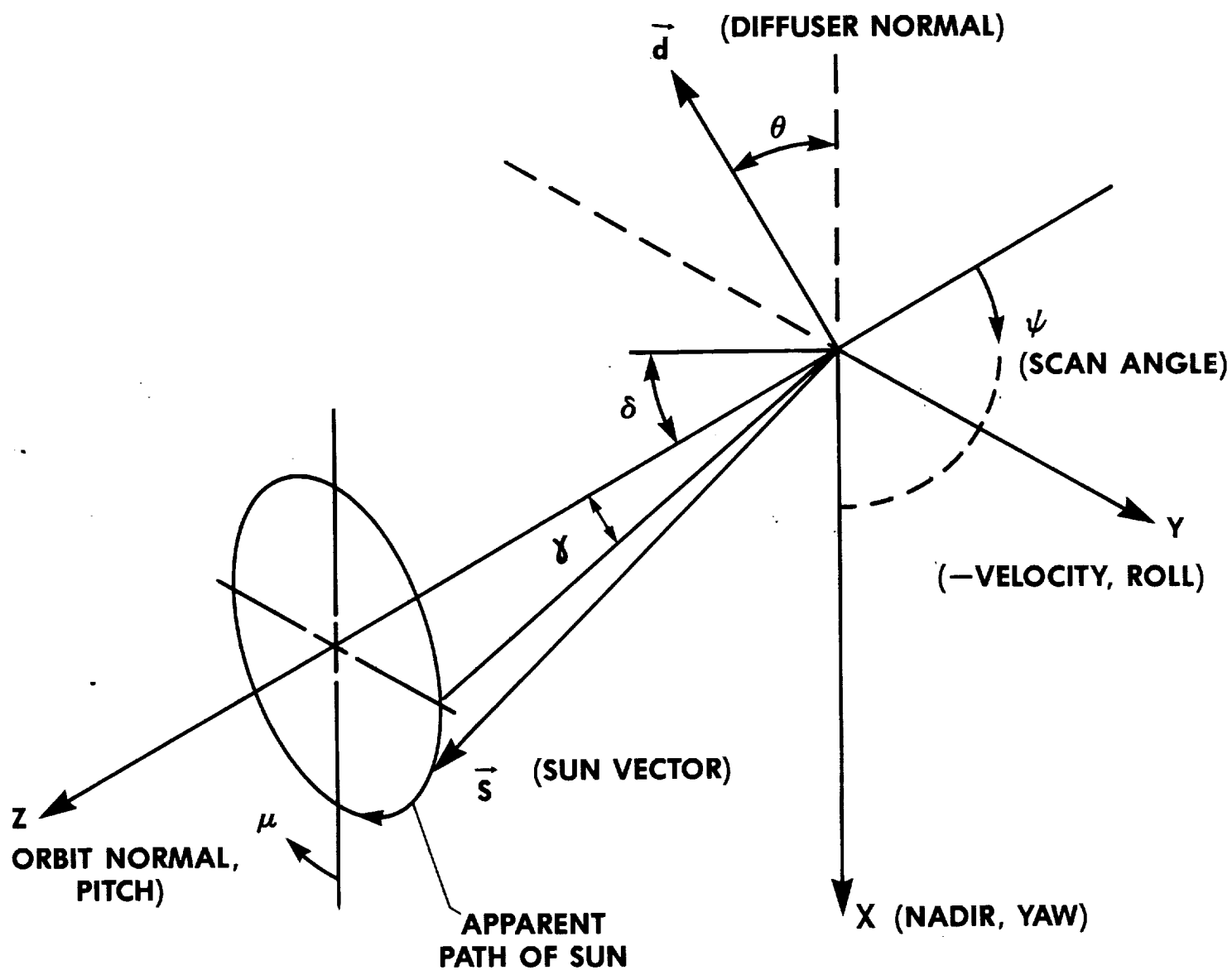
Figure 3.2-4 SOLAR ILLUMINATION DURING AN ORBIT

NORTH TERMINATOR

Y

B

A

EARTH SHADING

X

P.M. ORBIT

μ

ECLIPTIC, DAYTIME CROSSING

INTERFACE SHADING

SOUTH TERMINATOR

APPARENT PATH OF SUN

ECLIPTIC, NIGHTTIME CROSSING

Y

B

A

X

A.M. ORBIT

μ
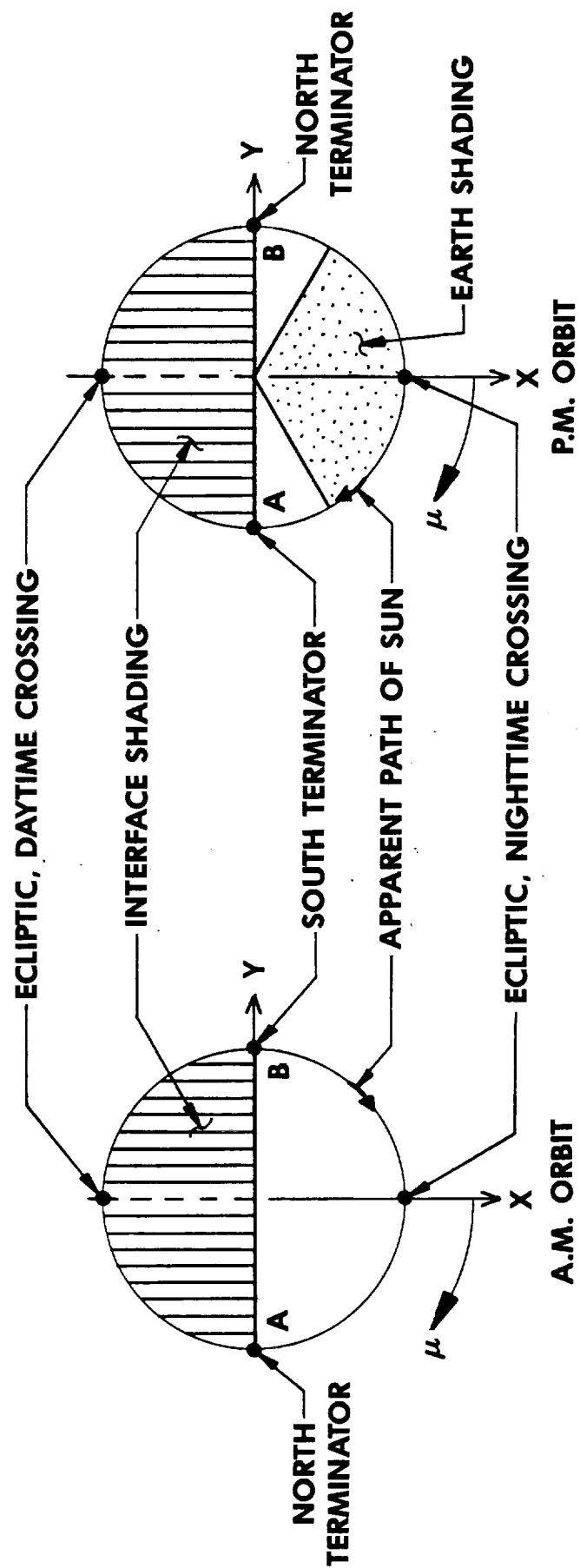
NORTH TERMINATOR

A = SUN ON TELESCOPE SIDE OF SCAN CAVITY
B = SUN ON MOTOR END OF SCAN CAVITY

AEROSPACE/OPTICAL DIVISION ITT

48

horizontal plane through the diffuser (terminator crossing in terms of orbital position). Because of the placement of the AVHRR on the spacecraft, this is the north terminator crossing in a morning orbit and the south terminator crossing in an afternoon orbit. Such a nighttime stability measurement is necessary if we do not want to interfere with the solar channel measurements, which are made during the daytime. A nighttime measurement is also necessary in order to avoid interference from the earth albedo (earth reflected sunlight), which could directly illuminate the diffuser, reflect off interface surfaces onto the diffuser, or combine with the stability signal when the diffuser is not large enough to fill the optical aperture of the AVHRR. The solar spectral signal from the nighttime earth is too weak to detect even with the enhanced signal/noise ratios. However, except at the terminator crossings, direct sunlight can reflect off interface surfaces onto the diffuser and thereby degrade its use as a stability monitor. In addition, the terminator (polar) regions are over-covered from a sun-synchronous orbit, so that the interruption of infrared data is minimized at this orbit position. As a consequence, the terminator crossing is the best orbital position at which to make stability measurements with a sunlit diffuser.

The only problem with this conclusion is that the spacecraft structure, notably the solar panel, may shade the diffuser at the (north)terminator crossing when the sun angle is sufficiently small. However, the time between stability measurements is relatively long (1 to 3 months), so that it may not be necessary to deploy the diffuser during the periods of low sun angle. Moreover, stability measurement exactly at the terminator crossing may not be necessary. Small extensions into either the nighttime or daytime half of the orbit are possible as long as the interfering signals are sufficiently small compared with the signal from the stability monitor itself.

3.2.11.4   Location in Instrument Scan Field

In addition to being located where it is illuminated by direct sunlight, the diffuser must also be located where it can be seen from the AVHRR, i.e., within the instrument scan field. The scan field geometry is illustrated in Figure 3.2-3. A reflective diffuser cannot be used in the vicinity of $\psi = 180°$; this region requires the use of a transmissive diffuser. In fact, a reflective diffuser becomes inefficient beyond $\psi = 90°$ because of the necessary increase in the solar incidence angle, the instrument view angle, or both. A diffuser in the vicinity of $\psi = 0°$ would interfere with the instrument space view (offset measurement/correction), be visible from the radiant cooler, and be shaded from sunlight in the vicinity of a terminator crossing.

The best location of the diffuser in the instrument scan field is therefore in the vicinity of nadir ($\psi = 90°$). Deployment within the earth region (i.e., outside of the space region) at $\psi < 90°$ is also possible. However, in this location, the diffuser must be at a greater distance from the scanner if it is to be fully illuminated at the terminator crossing.

3.2.11.5   Orientation

The solar irradiance of the diffuser is directly proportional to the cosine of the incidence angle,

$$\cos\phi = \vec{d} \cdot \vec{s},$$

where $\vec{d}$ = the unit vector along the diffuser normal,

and $\vec{s}$ = the unit vector pointed at the sun.

From Figure 3.2-3, we have

$$\vec{d} = (-\cos\theta,\ -\sin\delta\sin\theta,\ \cos\delta\sin\theta),$$

and $\vec{s} = (\cos\mu\sin\gamma,\ -\sin\mu\sin\gamma,\ \cos\gamma)$

which yield

$$\cos\phi = -\cos\mu\cos\theta\sin\gamma + \sin\mu\sin\delta\sin\theta\sin\gamma$$
$$+ \cos\delta\sin\theta\cos\gamma.$$

For a diffuser illuminated at a terminator crossing, $\mu = 90°$ and

$$\cos\phi = \sin\theta(\sin\delta\sin\gamma + \cos\delta\cos\gamma),$$

or $\cos\phi = \sin\theta\,\cos(\delta-\gamma).$

The maximum value of $\cos\phi$, i.e., the maximum solar irradiance, is than at $\delta = \gamma$, where

$$\cos\phi = \sin\theta.$$

Subject to the requirement that the diffuser be illuminated by the sun and, in particular, that it be outside the interface shadow, $\cos\phi$ is also a maximum at $\mu = 90°$. This result confirms our previous selection of a terminator crossing as the best orbit location for the diffuser.

For a diffuser that does not fill the optical aperture of the AVHRR, the signal from the diffuser is also directly proportional to the cosine of the view angle from the scanner,

$$\cos\zeta + \vec{d} \cdot \vec{v},$$

where $\vec{v}$ is the unit vector from the diffuser to the AVHRR. From Figure 3.2-3, we have

$$\vec{v} = (-\sin\psi,\ o,\ \cos\psi),$$

so that

$$\cos \zeta = \cos \theta \sin \gamma + \cos \delta \sin \theta \cos \psi,$$

With the diffuser located at the nadir position, $\psi = 90°$ and

$$\cos \zeta = \cos \theta,$$

i.e., the direction of view from the diffuser to the AVHRR is along the
-X axis.

Combining the two factors above, we find that the signal
from the sunlit diffuser is directly proportional to

$$\cos \phi \cos \zeta = \sin \theta \cos \theta = (1/2)\sin 2\theta.$$

The maximum value of this product is 1/2 at $\theta = 45°$. The optimum
orientation of a diffuser is therefore with its normal at $45°$ above the
horizontal in a vertical plane that contains the vector to the sun.
This result holds when the diffuser is located at the nadir position of
the instrument scan field and is illuminated during an orbit at a ter-
minator crossing.

We will now investigate how the signal from the diffuser
varies when it is located off nadir in the scan angle range $0° < \psi <
90°$. With μ still equal to $90°$ and δ still equal to γ, we now have $c =
\cos \phi \cos \zeta = \sin \theta \cos \theta \sin \gamma + \sin^2 \theta \cos \gamma \cos \psi$. The maximum value of c occurs
when $dc/d\theta = 0$, or at the angle θ that is the solution to

$$-\tan 2\theta = \tan (180° - 2\theta) = \tan \psi / \cos \gamma.$$

The optimum values for θ for ψ in the range from $0°$ to $90°$ are listed in
Table 3.2-8 for seven values of ψ and for the nominal morning ($\gamma =
24.0°$) and afternoon ($\gamma = 67.8°$) orbits, together with the resultant
values of c.

The results show that the signal level can be increased by
locating the reflective diffuser off nadir toward the shaded side of
the spacecraft. The highest level in a morning orbit occurs at $\psi = 0°$,
which is not a useful solution because it is within the space view of
the instrument and shaded from the sun at a terminator crossing. The
highest level in an afternoon orbit occurs at $\psi = 60°$ (to the nearest
degree). At this position, the increase in signal level compared with
the nadir position ($\psi = 90°$) is only 8.1%. In the morning orbit, the
relative increase at $\psi = 60°$ is much larger, namely 43.6%. However, as
described above, an off-nadir location requires that the diffuser be
deployed at a greater distance from the scanner in order to remain
fully illuminated at a terminator crossing.

3.2.11.6   Size of Diffuser

The radiance of a sunlit diffuser is given by

$$N_d = f_r H_d,$$

where f_r = reflection coefficient = fraction of total incident
flux reflected per unit projected solid angle
(steradian) in the view direction.

and H_d = solar irradiance = $H_{do} \cos \phi$, where H_{do} is the solar
irradiance on a plane perpendicular to the sun's rays.

The reflection coefficient f_r is equal to the bidirectional reflectance
distribution function (BRDF) described by Nicrodemus, et. al., it is
also equal to the scattering coefficient used by Leinert and
Klupelberg. In general, f_r is a function of the incidence and reflec-
tion angles (ϕ and ζ) and their respective azimuth positions about the
diffuser normal. However, we can assume that the diffuser surface is
isotropic, so that f_r is independent of the azimuth positions. In
addition, we will assume that the diffuser is selected so that f_r is
independent of the incidence angles (ϕ) over the range of sun angles
(γ) encountered in either an a.m. or p.m. orbit. Because the view
(reflection) angle (ζ) is fixed, we can now treat the diffuser as a
perfectly diffuse reflector of reflectivity ρ_d, in which case
$f_r = \rho_d / \pi$.

Table 3.2-8.   Relative Signal Level from a Sunlit Diffuser
in Off-Nadir Positions

Nominal a.m. orbit ($\gamma = 24.0°$)

ψ	optimum θ	$c = \sin\theta\cos\zeta$
0°	90°	0.9135
15	81.83	0.9010
30	73.85	0.8635
45	66.21	0.8018
60	58.90	0.7179
75	51.88	0.6154
90	45	0.5000

Nominal p.m. orbit ($\gamma = 67.8°$)

ψ	optimum θ	$c = \sin\theta\cos\zeta$
0°	90°	0.3778
15	72.33	0.4348
30	61.60	0.4623
45	55.35	0.5115
60	51.15	0.5405
75	47.89	0.5343
90	45	0.5000

The above radiance results in a radiant signal that is
given by

$$\phi_d = \frac{\rho_d}{\pi} H_{do} \cos \phi A_d \cos \zeta \Omega,$$

where A_d = diffuser area (maximum seen by the scanner),

and Ω = optical solid angle of view of the AVHRR.

This radiant signal is equivalent to a scene albedo a_e that satisfies
the equation

$$\phi_d = \frac{\rho_d}{\pi} H_{do} A_o \Omega,$$

where A_o is the entrance pupil (collecting) area of the AVHRR. We
therefore have

$$a_e = \rho_d \cos \phi \cos \zeta (\frac{A_d}{A_o}).$$

For $_d$ = 0.90 and $\cos \phi \cos \zeta$= 1/2, an equivalent albedo a_e =
0.10 requires an unobscured diffuser that satisfies

$$(\frac{A_d}{A_o}) = 0.2222.$$

Because of the geometry of the entrance pupil of the AVHRR (8.0 in
diameter with a central 2.0 in obscuration), the actual diffuser area
must in general be larger than that given by this ratio.

Instead of adjusting the orientation of the diffuser for a
morning or afternoon orbit, we could fixed it for the mean nominal sun
angle 45.9°. In this case, the cosine of the solar incidence angle at
the nominal sun angle in either an a.m. or p.m. orbit is reduced by
$\cos (\delta - \gamma)$ = cos 21.9°. In order to maintain the same signal level,
the unobscured diffuser area must then be increased by 1/cos 21.9°, to
0.2395x the entrance pupil area.

Instead of rotating the diffuser normal to the mean sun
position at the terminator, we could leave it in the vertical plane
perpendicular to the orbit plane. In this case, the unobscured dif-
fuser area must be increased by 1/cos 67.8°, to 0.5881x the entrance
pupil area, in order to maintain the signal level in the nominal p.m.
orbit.

3.2.11.7   Shape of Diffuser

In general, it is easy to meet the requirement that the
fraction of pupil area covered by a diffuser not change over the scan
of several IFOV's. First, the IFOV of the AVHRR is only 1.3×10^{-3}
radian on a side. And second, as shown in Figure 3.2-5, most ellip-

tical diffusers that project as a circle or ellipse onto the entrance pupil meet this requirement. However, as shown in Figure 3.2.5(b), a diffuser area that projects as a rectangle may not meet the requirement.

As an example of a specific design, consider an elliptical diffuser whose minor axis is 4 inches and whose major axis is $4\sqrt{2}$ inches. When viewed at 45°, this diffuser appears as a 4 in diameter circle. The resultant ratio of unobscured diffuser area to entrance pupil area is

$$\frac{A_d}{A_o} = \frac{\sqrt{2}(4^2 - 2^2)}{8^2 - 2^2} = \frac{\sqrt{2}}{5} = 0.2828.$$

3.2.11.8   Problems with Deployable Diffuser

There are two principal objections to the use of a deployable sunlight diffuser as a stability monitor, the potential for failure and the potential for contamination degradation. A reflective diffuser must be deployed within the active scan region of the AVHRR. And even with fail safes and backups, there is still the possibility that the mechanism will become stuck in the deployed position, which effectively destroys the usefulness of the AVHRR. In fact, the very use of a deployable reflective diffuser violates one of our design objectives, namely that the stability monitor be used in a manner that does not interfere with normal instrument operation. Furthermore, the deployed diffuser may also interfere with the operation of other instruments, notably the microwave sounder.

Contamination degradation is a potential problem because the deployed diffuser must be exposed to ultraviolet and energetic particle radiations. Such exposure increases the degradation from a contaminant and makes it permanent because the residue formed absorbs over a wider spectral band and does not evaporate. Moreover, past experience in this area is not encouraging. Apparently it is very difficult to maintain a clean surface throughout the construction, testing, spacecraft integration, and launch of an instrument. On the other hand, provided the degradation is not too severe, a useful source can still be provided by monitoring the diffuser signal with detectors protected from sunlight.

For these reasons, ITT does not recommend implementation of the deployable reflective diffuser as a stability monitor.

3.2.12   Transmissive Diffuser Source

3.2.12.1   Location and Material

Use of a transmissive diffuser source allows the source to be fixed in location and out of the normal earth scan region of AVHRR. Figure 3.2-6 shows the proposed location of a transmissive diffuser plate. As shown it is on the sun side of the scan cavity and is located to clear the active scan region.

Figure 3.2-5 **EFFECT OF DIFFUSER GEOMETRY
ON ENTRANCE APERTURE**

1,2 **BOUNDARY OF
ENTRANCE PUPIL**

**DIFFUSER AREA
(PROJECTED)**

(B) UNACCEPTABLE

**DIFFUSER AREA
(PROJECTED)**

(A) ACCEPTABLE
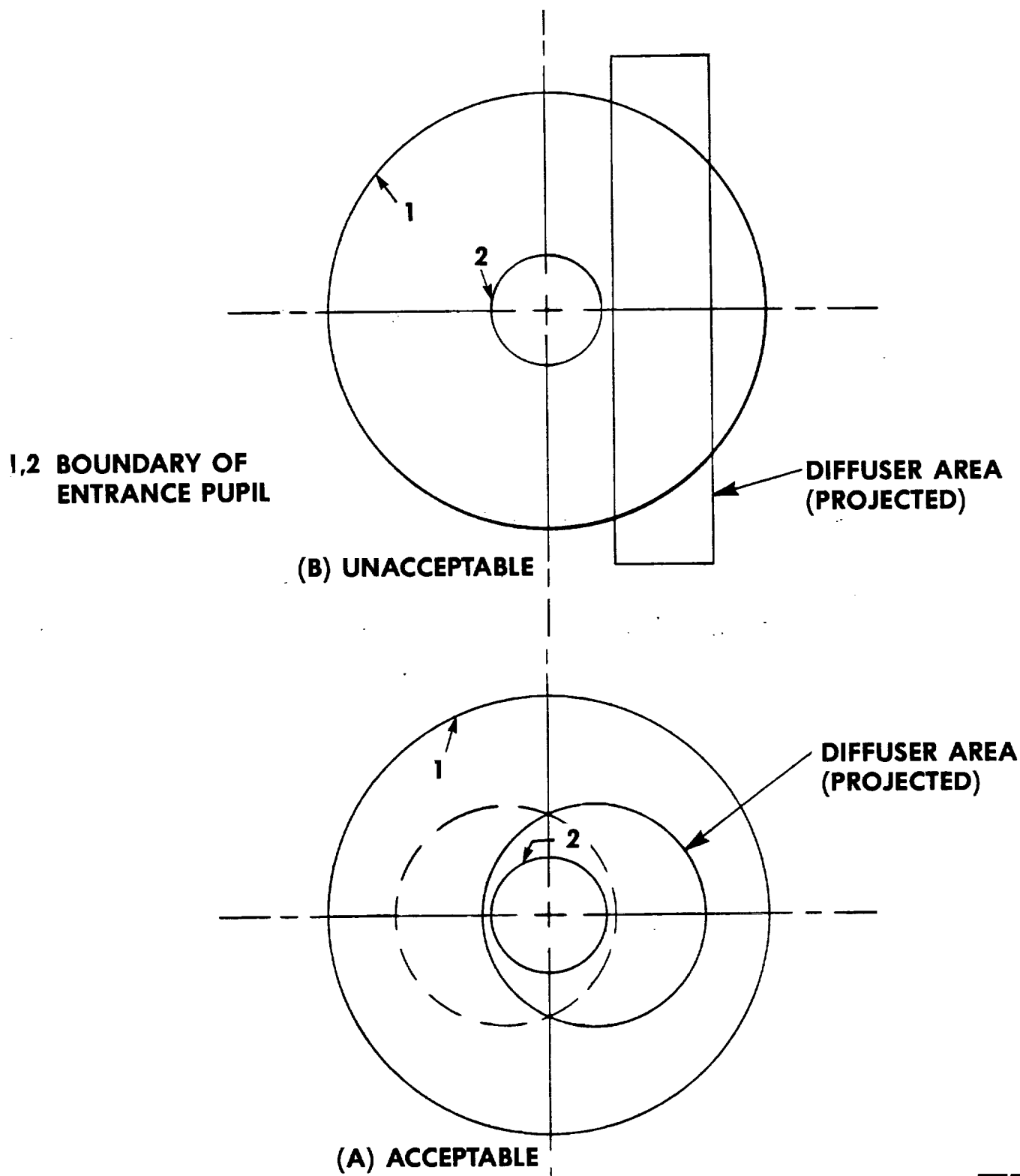
AEROSPACE/OPTICAL DIVISION ITT

Figure 3.2-6   LOCATION OF TRANSMISSIVE DIFFUSER IN SCAN

EARTH SCAN
125°

62° 30'

8° 39'
DEEP SPACE SCAN

Z

PITCH AXIS

+X

YAW AXIS

NADIR

O.A.

8.0"

17° 30'

90°

27° 30'   5.0"

5° 10'

IN FLIGHT IR
CALIBRATION

0° 42'

9.5"

15.0"

TRANSMISSIVE
DIFFUSER

FULL APERTURE DIFFUSER

AEROSPACE/OPTICAL DIVISION   ITT

56
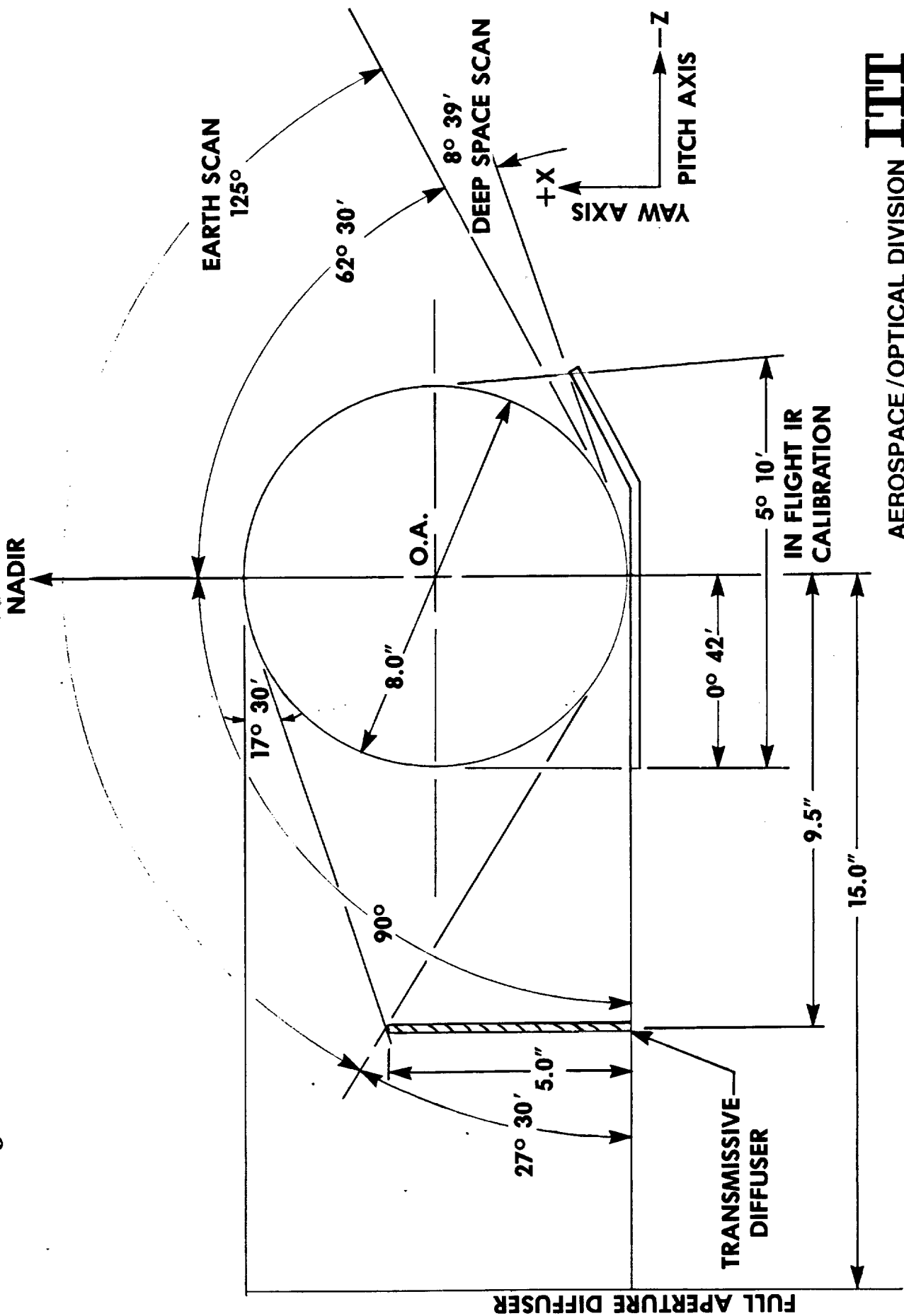
The diffuser material will probably be Schott opal glass. Opal glass is made by precipitating inclusions of a material with different refractive index into a host material. Typical inclusion diameters are in the 0.4 to 1.3 micron range and typical inclusion density is 10^{10} to 10^{14} per cm^3. These inclusions cause scattering which increases the optical path by about 4 to 8 times. This scattering gives opal glass its very excellent Lambertian radiance characteristic.

Table 3.2-9 lists Schott published data on the transmission of opal glass. The data does not cover the Channel 3A. Using a sample provided by the Schott factory, we set up an experiment to measure the diffuse characteristics of a 0.25 mm thick white flashed opal glass at 1.6 microns. The set up is shown in Figure 3.2-7. A chopped light source was used to normally illuminate the sample. A filter and lens was placed over an InGaAs detector which was moved to measure the angular radiance of the sample.

Figure 3.2-8 gives the test results. The sample shows a very good diffuse characteristic of all angles except in the direction where the detector is in direct view of the source (0° in this case). This is typical for these types of diffusers and was not unexpected.

Since the proposed application of this diffuser places it off axis to the illumination (sun) and the AVHRR optics, and since the sun is never in direct view of the AVHRR optics during calibration, this diffuser material will provide the diffuse target required.

Table 3.2-9. Transmission of Two Thicknesses of Schott Opal Glass

Wavelength (nm)	Transmission .28mm	.68mm	Absorption Length
300	2.0	1.0	.577 mm
350	26.8	16.0	.775 mm
400	29.0	19.0	.946 mm
450	29.8	19.8	.978 mm
500	30.4	20.6	1.028 mm
600	32.0	22.3	1.108 mm
700	33.5	24.0	1.199 mm
800	34.8	25.2	1.239 mm
900	36.0	26.7	1.338 mm
1000	37.5	28.0	1.369 mm
1100	39.0	29.2	1.599 mm

Figure 3.2-7 TEST CONFIGURATION TO MEASURE 1.6 μm OPAL GLASS CHARACTERISTICS
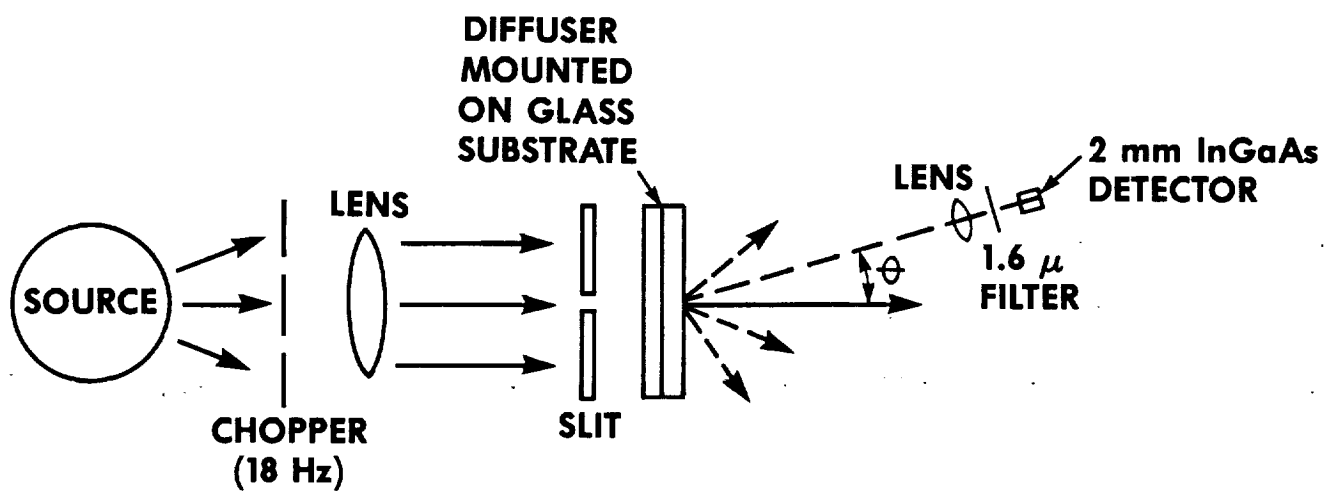
Figure 3.2-8 *TRANSMISSION CHARACTERISTICS OF A .28 mm SCHOTT OPAL GLASS DIFFUSER AT 1.6 μm*

1.0
.9
.8
.7
.6
.5
.4

40°
50°
60°
70°
80°
90°

TRANSMISSION SPIKE

PERFECT DIFFUSER

PEAK (0°) TRANSMISSION

$\tau = 29.7\%$ APPROX

RANGE OF GOOD DIFFUSION

AEROSPACE/OPTICAL DIVISION ITT
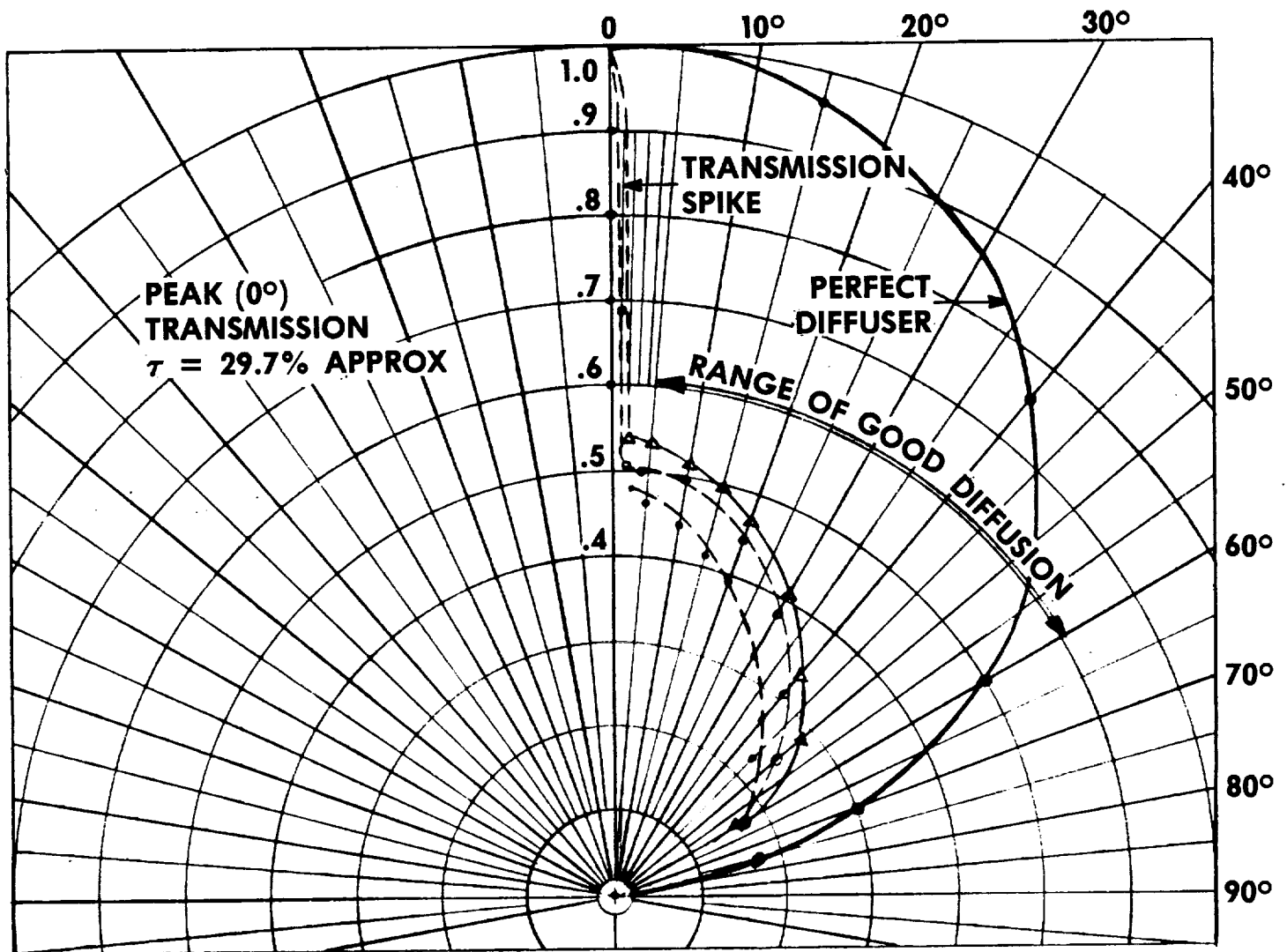
3.2.12.2   Orientation and Signal Level

If the prime use of solar data is in the afternoon orbit, the transmissive diffuser must be tilted toward the pm sun position to avoid very large incidence angles, where both the signal level and degree of diffuseness are low. Such a tilt also reduces the diffuser's sensitivity to interface reflections and the variation in its transmittance with incidence (sun) angle.

A transmissive diffuser deviates somewhat from a perfect diffuser, i.e., its transmittance is not independent of the incidence and view angles. This was shown in the previously reported test data. However, since the diffuser is used at a constant view angle, it is more important that the radiance in this fixed direction be independent of the incidence angle. According to the data given by Walsh (Ref. 1), the radiance of opal glass changes very little at a view angle of 30° for incidence angles in the range from about 10° to 60°. The configuration for the AVHRR/3 comes close to providing a 30° view angle. For a diffuser tilted 20° toward the pm sun at the terminator position and for an instrument that views the diffuser at a scan angle of 17.5°, we have

$$\cos \zeta = \cos 20° \cos 17.5°,$$
$$\text{or} \qquad \zeta = 26.3°.$$

Increasing the tilt angle to 25° increases the view angle to 30.2°.

The equivalent albedo of a transmissive diffuser is given by

$$a_e = \tau f \cos \phi,$$

where

τ = diffuser transmittance = 0.35 (opal glass),

f = fraction of the clear aperture filled by the diffuser at the view angle of the scanner = 0.60 for the configuration proposed,

and

ϕ = incidence angle = $\gamma - 20°$, where γ is the orbit normal to sun angle (terminator position).

The resultant levels of a_e are listed in Table 3.2-10 for both the morning and afternoon orbits. The sun angle ranges are taken from the previous discussion for reflective diffusers. We see that all the albedo levels exceed 10% and that the variation with sun angle is small in the morning orbit ($\pm 4.2\%$) and large in the afternoon orbit ($\pm 22.2\%$).

As stated above, the most likely material for use as the transmissive diffuser is opal glass manufactured by Schott Glass Co. This is a well-known material with considerable information available on transmission and "diffuseness" in the visible region. Little is known about its characteristics at 1.6 microns (Channels 3A). Contacts with the Schott Company continue. They indicate that the diffuse characteristics can be varied by processing; however, a minimum buy may be invoked for a non-standard product.

References

1. J. W. T. Walsh, Photometry (Constable and co., 1985; Dover 1965),
    p. 381.

Table 3.2-10. Equivalent Albedo of the Transmissive
Diffuser Design

Orbit	γ	a_e
am	$29° \pm 15°$	0.207; 0.192; 0.209
pm	$69° \pm 11°$	0.138; 0.105; 0.165

3.3   Mechanical Implementation Approaches

In this section of this report, the following conceptual design parameters for each approach will be addressed. The type of calibration source or target and its orientation to the scanner and earth scan view will be discussed. One method to provide input to the instrument is via a target which utilizes solar radiation as the source. By using either a reflective or transmissive diffuser, the solar energy can be directed into the scan cavity. A second source is a lamp which employs a diffused reflective surface which reflects the lamp energy through a collimated lens assembly into the scan cavity and telescope. Each method requires a means to provide protection from contamination when not in use. Once the TIROS spacecraft is located in orbit and functioning, the spacecraft will outgas particles for a duration of time. Due to the sensitive nature of optical components like the reflective/transmissive diffuser or collimator lens it is important not to allow any particle contamination to condense onto these surfaces. A means must be provided for each stability monitor to protect the critical components when the unit is either not functioning or deployed. The use of this monitor is limited. It will be commanded to operate once every three months. Thus the method for protection is critical if a constant source is to be maintained.

The physical size, weight, electrical power impacts and modifications to the AVHRR present instrument configuation will be present in this report. The size of the unit must integrate readily with both the individual AVHRR instrument and TIROS spacecraft. Its location will be governed by its operation and size. It is imperative that the unit does not dimensionally interfere with any adjacent hardware. The additional weight of the stability monitor must be considered. Each additional pound of equipment added to the spacecraft adds to the total launch cost of the TIROS program. With cost as a governing parameter, the packaging of the stability monitor must be efficient in both weight and size.

The electrical requirements, both power and operational circuits must be an efficient design to optimize the overall design of the stability monitor. The power and operational commands will be directed through the AVHRR instrument. The number and sequence of commands to perform the stability calibration will be defined. It is desirable not to impact the current data/stream MIRP interface.

As with all spaceborne instrumentation, be it electrical, mechanical or optical, it must be simple and highly reliable. These are the two basic parameters governing the stability monitor design. The unit must survive the vibrational input placed on it during the ground test and final launch of the spacecraft. The major design parameter restriction placed on the stability monitor unit is that it is not to interfere with the earth scan or deep space scan views of the AVHRR instrument. The method of deploying or projecting either the target or artifical source into the scan cavity shall not interfere with the normal operational functions of the AVHRR instrument. The

fail safe requirement imposed by ITT engineers at the onset of the study effort was that the stability monitor was transparent to the AVHRR instrument. The addition of the stability monitor was not to impact the AVHRR instrument as to effect the present operation of the instrument. Thus, in either the stored or deployed state of the stability monitor; the instrument's operation and views would not be effected. If the stability monitor is to fail when positioned in the deployed state, it shall not impact the normal scan function of the AVHRR instrument.

3.3.1   Reflective Diffusers

          The initial conceptual approaches utilizing the sun as an energy source employed a reflective diffuser surface. This scheme would emmulate the diffused cloud scene which the AVHRR instrument views during normal operations. The mechanism to deploy the diffuser panel was located on the "bottom" of the instrument, above the telescope housing. The means to deploy the panel, used an arm which pivoted the panel into the field of view and oriented the panel normal to the sun angle. The orientation would be orbit configuration dependent. This scheme was in concept form only. It was rejected since it was in direct obscuration of the earth scan when deployed (Figure 3.3-1). If the arm would fail when in the deployed state, the AVHRR instrument would be useless. Also, the mechanism to deploy and store the diffuser panel was complex and comburesome. The arm was complex in that it had to be able to accommodate both orbit parameters. It was conceived that the linkage would be set before launch to the corresponding setting for either a morning or afternoon orbit. This made the mechanism difficult to design. The need to make the linkage accommodate two different orbit positions was to allow for a smaller diffuser panel.

          A large panel for both orbits orientated nominal for both orbits tended to make the packaging a problem. Several types of reflective diffusers were proposed. Size and deployment being the driving factors in each concept design. Due to the two different orbit configurations and the reflective nature of the diffuser surface, tradeoffs were considered to optimize size and performane of the panel. To understand the requirement to optimize the view of the panel as seen by the scan mirror we first must define the nature of the diffuser surface. The diffuse surface reflectivity is a cosine function. Figure 3.3-2 illustrates this characteristic. From the standpoint of energy reflected, a direct, normal view of the panel yields the best results. For this reason, the orientation of the diffuser panel must be such that the scan mirror view of the surface is sufficient to receive enough energy for the AVHRR instrument to use.

          The first approach of a pivotinig diffuser panel was modified by replacing the small panel with a larger panel which need not be positioned unique to the morning of afternoon orbit, but rather was position at half the difference of the two orbit angles. As was the first approach, this larger panel concept was rejected since it interfered with the operational view of the instrument.

DIFFUSER NORMAL TO SCAN PLANE.

45°

Figure 3.3-1

AEROSPACE/OPTICAL DIVISION **ITT**

Figure 3.3-2

$\tau H_o \cos\theta \cos\phi$

ϕ

θ

DIFFUSE SURFACE
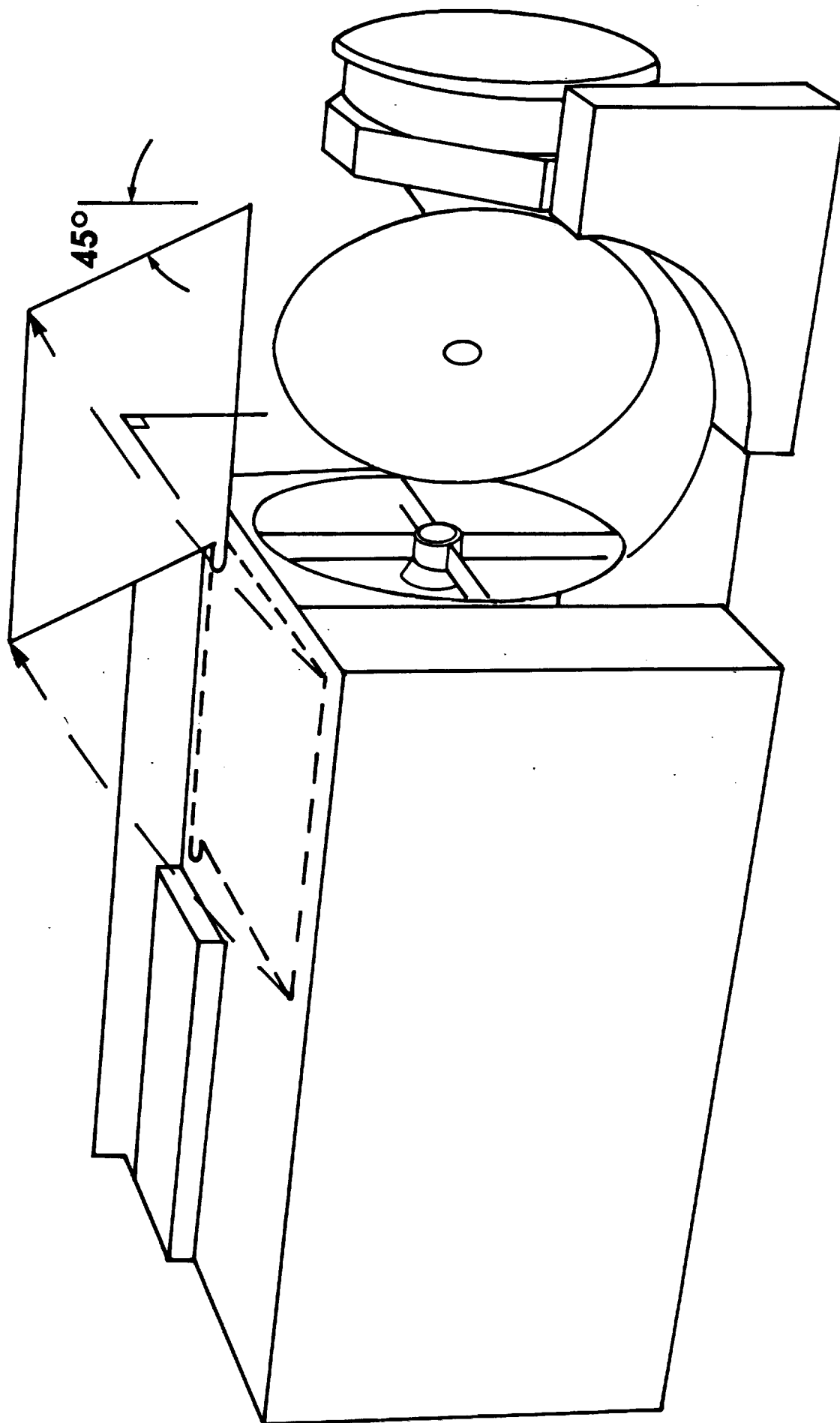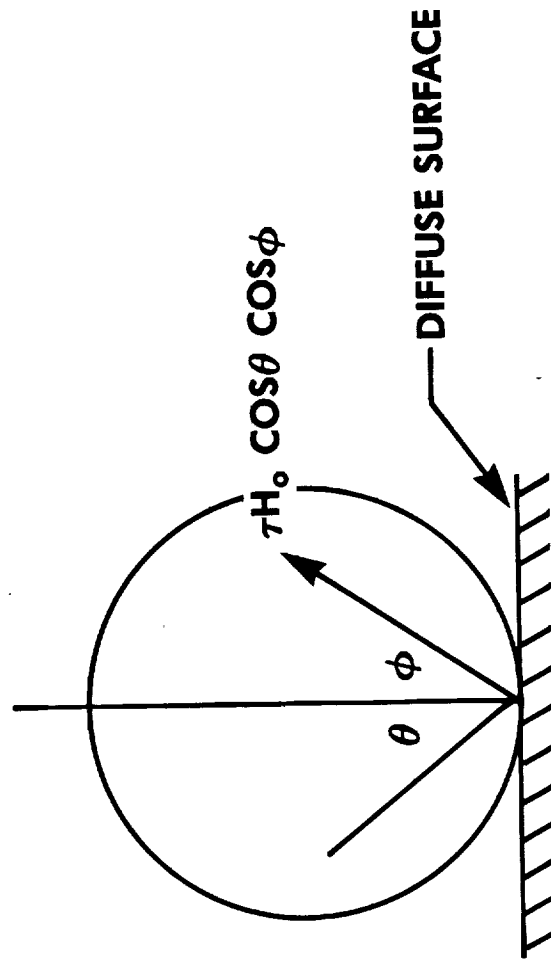
3.3.2   Tranmissive Diffusers

An alternative approach to the reflective diffuser is the use of a transmissive diffuser. This concept utilizes the solar energy and transmissive diffuser with the same cosine view function as the reflective diffuser. The key reason for investigating this approach is that this scheme does not require the use of the earth scan. Due to the orientation of the TIROS spacecraft with respect to the sun, during certain portions of the orbit, the sun is incident into the scan cavity across the motor power supply. Figures 3.3-3 and 3.3-4 illustrate this approach. During the deployed operations of the transmissive diffuser, the sunlight would pass through the diffuser and into the scan cavity where the scan mirror would divert the energy into the optics of the AVHRR instrument. As illustrated, the stability monitor diffuser is orientated outside the scan envelope. Thus, in the deployed condition, the monitor will not impair the normal operations of the AVHRR instrument.

Like the reflective diffuser, the morning and afternoon orbit conditions must be accounted for. The orientation of the transmissive diffuser with respect to the scan cavity and instrument is limited. Due to geometry and diffuser view angle properties, the transmissive diffuser cannot be orientated normal to the afternoon orbit. For this reason, the transmissive diffuser is positioned a nominal 20 degrees off the normal scan view. This angle is a mean angle for the incident sunlight of both the morning and afternoon orbits and is an acceptable view angle for the scan mirror to view.

Two mechanisms to deploy the transmissive diffuser are illustrated in Figures 3.3-5 and 3.3-6. The first method pivoted the panel into position. The diffuser was stored captive in the box which mounted on the electronic side of the AVHRR instrument. The enclosure provides the necessary contamination protection when the diffuser is not deployed. As illustrated, the lid has four bumpers which hold the diffuser panel captive to the enclosure when the lid is closed. These bumpers act as clamps to restrain the panel's motion during ground base vibration test and launch. This approach is simple in that only dc stepper motors and simple rotary motion is required to deploy the panel. The only design concern is the size of the panel and it's protection against fracture during vibration. The complete unit will impact the AVHRR instrument by requiring the relocation of several instrument/IMP electrical connectors.

After Goddard Space Flight Center had defined the location and view of the AMSU, it was found that the pivoting transmissive diffuser approach could not be used. The required envelope to swing the diffuser panel is in excess of the space between the AVHRR and AMSU on the TIROS spacecraft. For this reason, this approach was dropped.

The second alternative is to slide the transmissive diffuser into the field of view. This concept utilized the 20 degree offset with respect to the scan normal of the transmissive diffuser panel.

Figure 3.3-3

SCAN ASSEMBLY

VEL

SUN, P.M. ORBIT

MOTOR POWER SUPPLY

EARTH

SUN, A.M. ORBIT

SCAN NORMAL

AEROSPACE/OPTICAL DIVISION ITT

67
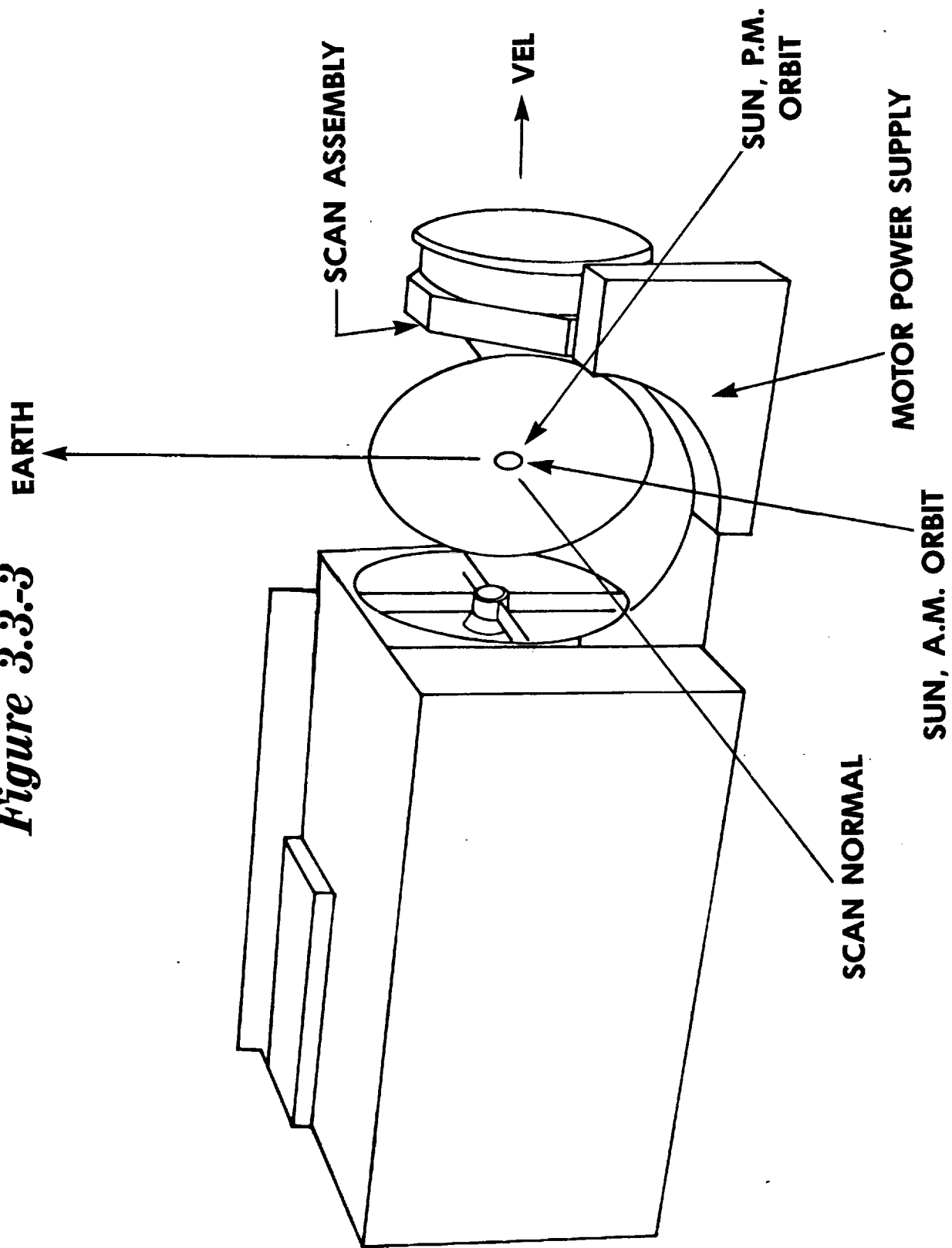
Figure 3.3.-4 AVHRR/3 SCAN ANGLES DIAGRAM

EARTH SCAN 125°

8° 39'

DEEP SPACE SCAN

—Z

PITCH AXIS

+X

YAW AXIS

62° 30'

O.A.

8.0"

17°30'

90°

5° 10'

IN FLIGHT CALIBRATION

0° 42'

9.5"

27° 30'

AEROSPACE/OPTICAL DIVISION

ITT

68
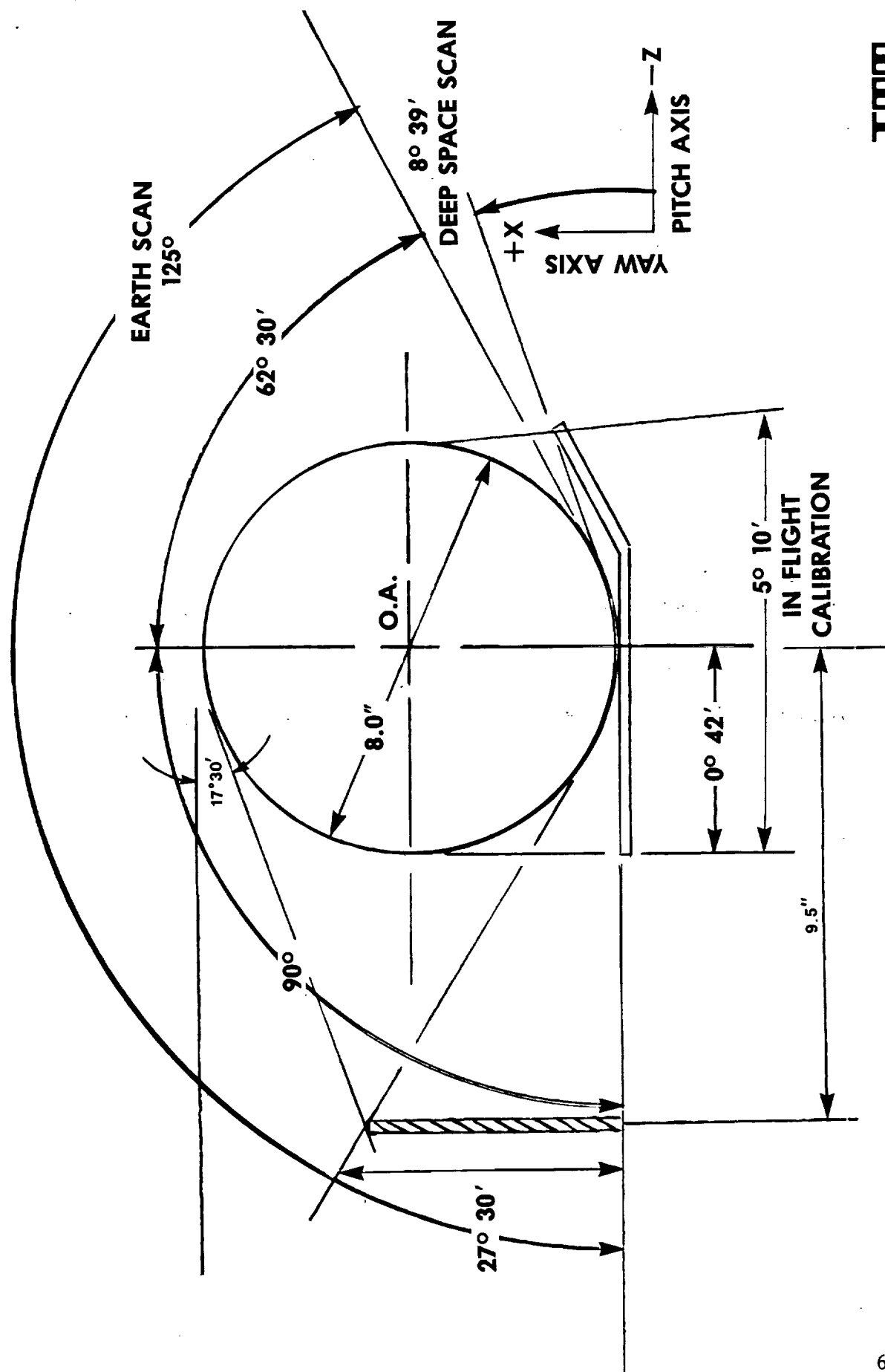
Figure 3.3-5 AVHRR/3 ROTATING TRANSMISSIVE DIFFUSER STABILITY MONITOR—WORKING ENVELOPE

69
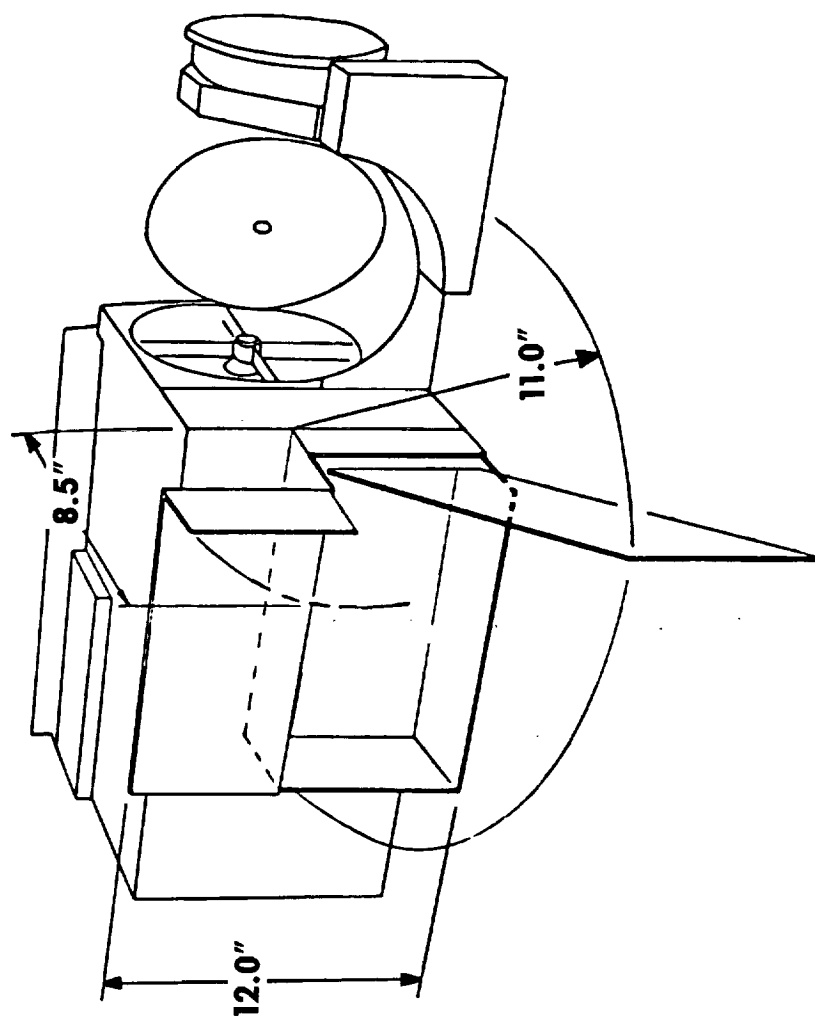
Figure 3.3-6 AVHRR/3 SLIDING TRANSMISSIVE DIFFUSER STABILITY MONITOR—DEPLOYED

AEROSPACE/OPTICAL DIVISION ITT

70
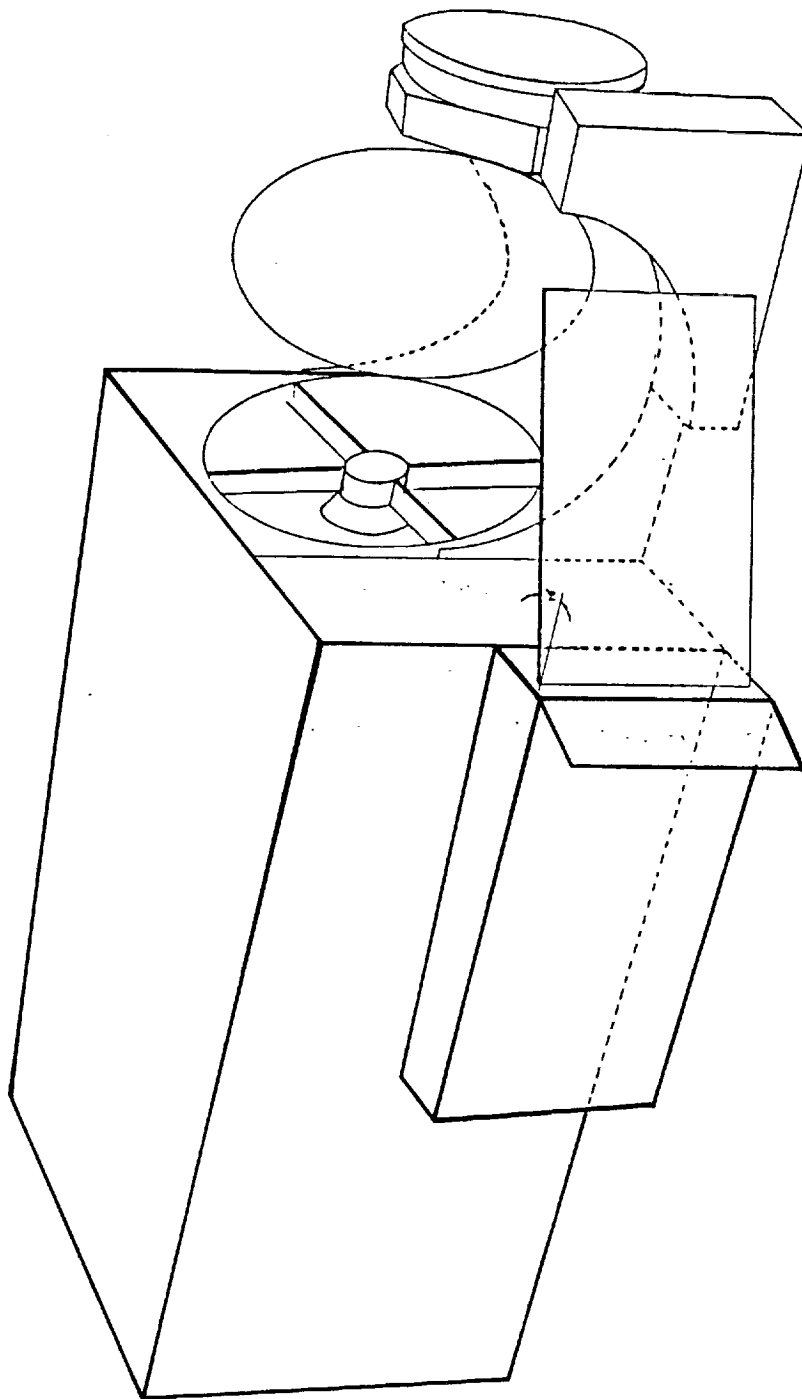
The mechanism for deployment slides the diffuser out from the protective enclosure mounted on the electronic side of the AVHRR instrument. The diffuser is held captive inside of the enclosure for protection from particle contamination and vibrational restraint during test and launch. Figure 3.3-6 illustrates the method of deployment. The side door of the enclosure would swing open and allow the diffuser panel to translate into position, then pivot the diffuser panel to obtain the correct 20 degree offset.

A variation to the second approach positioned the complete enclosure 20 degrees offset. This scheme eliminates the complete cam motion required by the second approach. Instead of sliding the diffuser then rotating into correct orientation the complete diffuser is held fix at the correct position. The enclosure is a box structure with a large aperture opening. When the stability monitor is commanded to function the diffuser is slid into position along guide tracks. This method is similar to the previous concept, but eliminates the need to pivot to acquire the 20 degree orientation. From a scientific standpoint, the transmissive diffuser provides the optimal stability source for the AVHRR instrument to view. From a mechanical viewpoint, the use of a large glass "window" poses some mechanical problems. Mainly, the survivability of the glass diffuser during vibration ground test and launch. The size of the glass diffuser in turn dictates the size of the protective enclosure. As illustrated, the enclosure for this conceptual approach is large, which in turn means additional weight.

3.3.3   Collimated Bulb Stability Monitor

Another means to provide onboard stability monitoring uses an artifical lamp source. Figure 3.3.3-1 illustrates this approach. In this concept, a lamp illuminates the reflective surface of a diffuse surface which in turn acts as the focus to a three inch diameter collimating lens assembly. The collimator presents a three inch diameter beam of energy to the scan mirror. Calculations indicate that a 3 inch diameter collimated artifical light source will be sufficient as an energy input for the AVHRR instrument to use as a stability monitor. This unit is mounted on the electronic side of the AVHRR instrument. It is a small compact unit with no adverse impacts on the present instrument design. As illustrated, the unit will not effect the location of the electrical connectors. As with all diffusers, the optical surfaces will require protection to keep contamination from condensing on the exposed surface of the outboard lense. A shutter is placed over the lense port when the unit is not operational. When the unit is commanded on, the shutter is rotated out of the optical path and the lamp is illuminated. A redundant lamp is employed as a means of guarantee. Before each stability operation, internal outgas heaters are commanded on.

A detailed weight estimate has been prepared for the collimated lamp stability monitor assembly.

ORIGINAL PAGE IS
OE POOR QUALITY

Figure 3.3.3-1

The weight estimate is given in Table 3.3.2-1. To this must be added the weight of the monitor detector box (not shown). It is estimated to weight 8 ounces.

Table 3.3.3-1. Weight Estimate for Collimated Lamp Stability Monitor

Focusing Lens Assembly
Glass Elements	13.7 oz
Housing	11.8 oz
Folding Mirror	9.5 oz
Monitor Housing	36.5 oz
Integrating Sphere & Shutter	<u>12.0 oz</u>
	83.5 oz
10% Misc.	<u>8.5 oz</u>
	92.0 oz
	5 lbs 12 oz

This drawing also illustrates the location of the adjacent spacecraft hardware, the AMSU. The stability monitor unit must intergrate with the current TIROS spacecraft. The spacecraft instrumentation defines the stability monitors package size. The stability monitor is to be a complete self supporting add-on unit with no spacecraft impact, other than onboard power and commands.

3.3.3.1   Stability Monitor Detectors

The monitor will provide the energy input to the AVHRR instrument. An array of four (4) diode detectors will be packaged as an additional unit to support the stability monitor. The function of this detector assembly (Figure 1.4-1) is to monitor the output level of the stability monitor. In effect, the diode detectors become the stability monitor. This unit is located on the deep space side of the scan cavity. It is positioned to view across the scan cavity, under the scan mirror and at the stability monitor.

The diode package will note any degradation in the stability monitor output. Both the sun source and artifical lamp source approaches are performance/time dependent. Both the reflective and transmissive diffuser performance properties degrade with exposure to sunlight. The lamp source filament will degrade with time as well. Thus, both the approaches must be monitored to determine each effect of the determination as to the total AVHRR optical throughput performance variance. The actual monitor of the instrument using either the sun or lamp source approach is the four diode detectors. Section 9.0 describes the electronics portion of the diode information handling.

4.0   CHANNEL 3A ADDITION

4.1   Requirements

4.1.1   Spectral Requirements

        Add Channel 3A (1.61 μm) to the AVHRR/2 instrument. The
desired Channel 3A characteristics are as follows:

        The total instrument response characteristics of Cahnnel 3A
shall be symmetric about 1.61 μm ± 0.01 μm as follows:

        1. 50% of maximum response points:

           1.58 ± 0.01 μm, and

           1.64 ± 0.01 μm.

A separation between the 50% points of 0.06 μm shall not be exceeded.

        2. 5% response points: 0.02 μm or less from the 50% points.

        3. 80% response points: 0.01 μm or less from the 50% points.

        4. The response between the 80% response points on opposite
           sides of the center frequency shall always exceed 80%.

        5. The 50% response point tolerance of 0.01 μm may be
           extended to TBD if the above requirements cannot be met.

        6. The total out-of-band response shall be less than 2% of
           the total integrated response within the bandpass region
           when viewing a solar source which simulates the solar
           spectral energy distribution.

        7. The desired signal-to-noise requirement is 20:1 at 0.5%
           Albedo.

        We acknowledge the fact that Channel 3A and the redefined
Channels 1 and 2 spectral tolerance values are state-of-the-art filter
capabilities as well as the Channel 2 and 3A signal-to-noise ratios.
Therefore, we have expressed these requirements as desired. ITT-A/OD
shall indicate those areas which are not achievable or those require-
ments which will escalate cost prior to the final design.

4.1.2   Implementation Requirements

        It shall be possible to select either Channel 3A or 3B (3.7
μm) output for transmission and/or storage on-board the satellite.
Both need not be available at the same time. Selection will be
accomplished either by ground commands or use of the on-board stored
command table. It is desired that the 1.6 μm output be selected during

the Earth illuminated or daylight portion of the orbit while the 3.7 μm
output will be selected for the night time portion.

Note: No changes to the MIRP are allowed. Channel
switching between 3A and 3B shall occur in the instrument and be
transparent to the MIRP. But, some type of flag in the data stream will
be required in order to identify which channel is being outputted.

4.2   Optical Design

The addition of a 1.6 micron channel to AVHRR is best
accomplished by using an uncooled photodiode detector rather than a
cooled detector. This allows the optical modifications to be limited
to a redesign of the relay optic assembly. It also allows the thermal
IR channels' optical design to remain unchanged.

The redesign of the solar channels' relay optics allows a
redesign of the channels 1 and 2 relay optics. This redesign allows the
optical throughput to be increased in these channels. This results in
improved signal to noise ratios in channels 1 and 2.

The following optical discussion covers channels 1 and 2 as
well as the new channel 3A.

4.2.1   AVHRR Relay Optic Redesign

The incorporation of the new Channel 3A and the changes in
Channel 1 and 2 S/N and spectral responses require the relay optic
design of these channels to be redone. The present albedo channel
relay optic was designed when channels 1 and 2 overlapped spectrally.
For that reason a very inefficient neutral density beamsplitter is used
to separate these two channels. Since the overlap no longer exists, we
can eliminate this element, use a more efficient multilayer dichroic
beamsplitter and increase the amount of signal available to both chan-
nels.

Figure 4.2-1 shows two of many relay optic configurations
which were studied. Figure 4.2-1a incorporates a channel 1/2
beamsplitting arrangement similar to that used on the radiant cooler
patch to separate channels 4 and 5. A common relay optic feeds the
beam to the dichroic beamsplitter which separates channels 1 and 2. It
has the advantage of eliminating one set of lenses, saving space and
weight.

The disadvantages of doing this are mainly associated with
the optical problems of doing beamsplitting and filtering in a focussed
beam. This would tend to reduce the steepness of the spectral cut-on
and cut-off slopes in each channel. The design of the beamsplitter
becomes more complicated in a non-parallel optical beam. In summary,
it would be difficult to predict by calculation the extent of polariza-
tion effects, changes in spectral response, in-band ripple etc. result-
ing from placing the beamsplitter and filters in the focused beam. We

Figure 4.2-1a   *POSSIBLE RELAY OPTICS DESIGN*
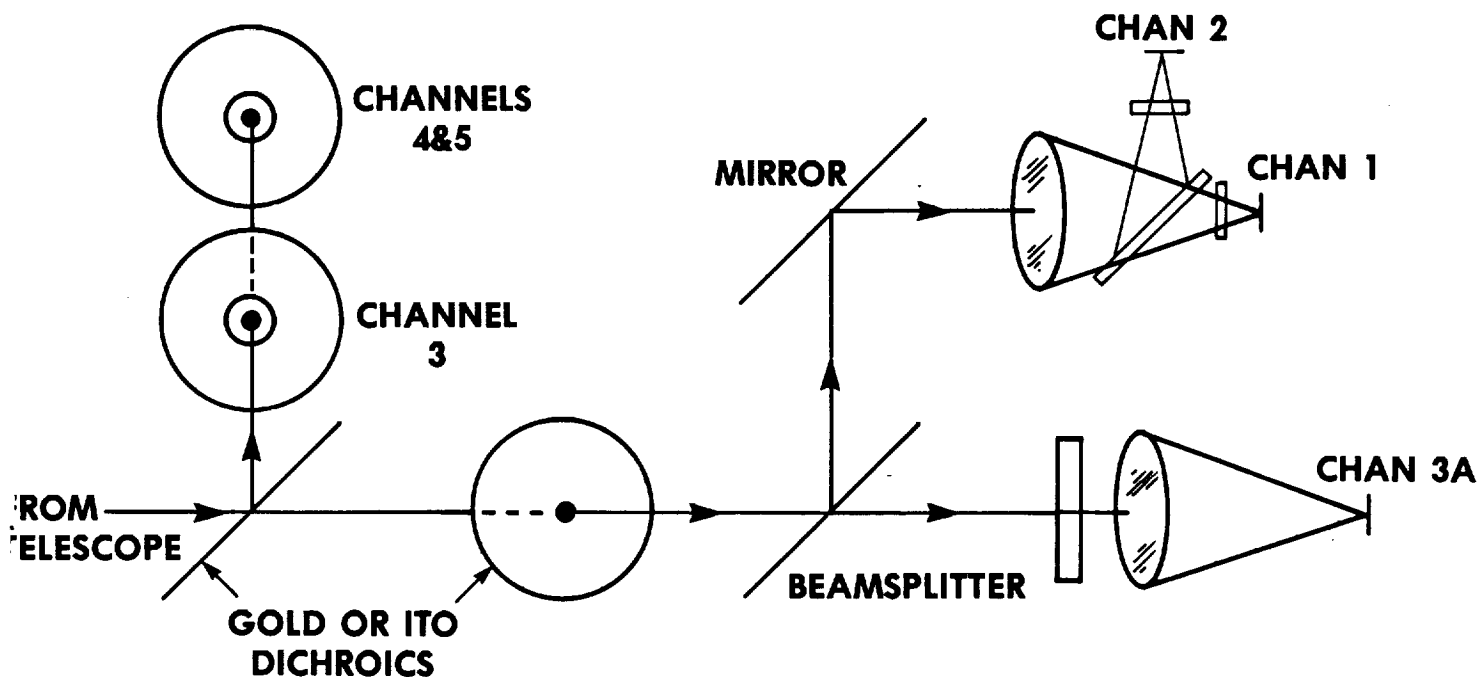
Figure 4.2-1b   *INCORPORATION OF CHANNEL 3A*
INTO AVHRR/3
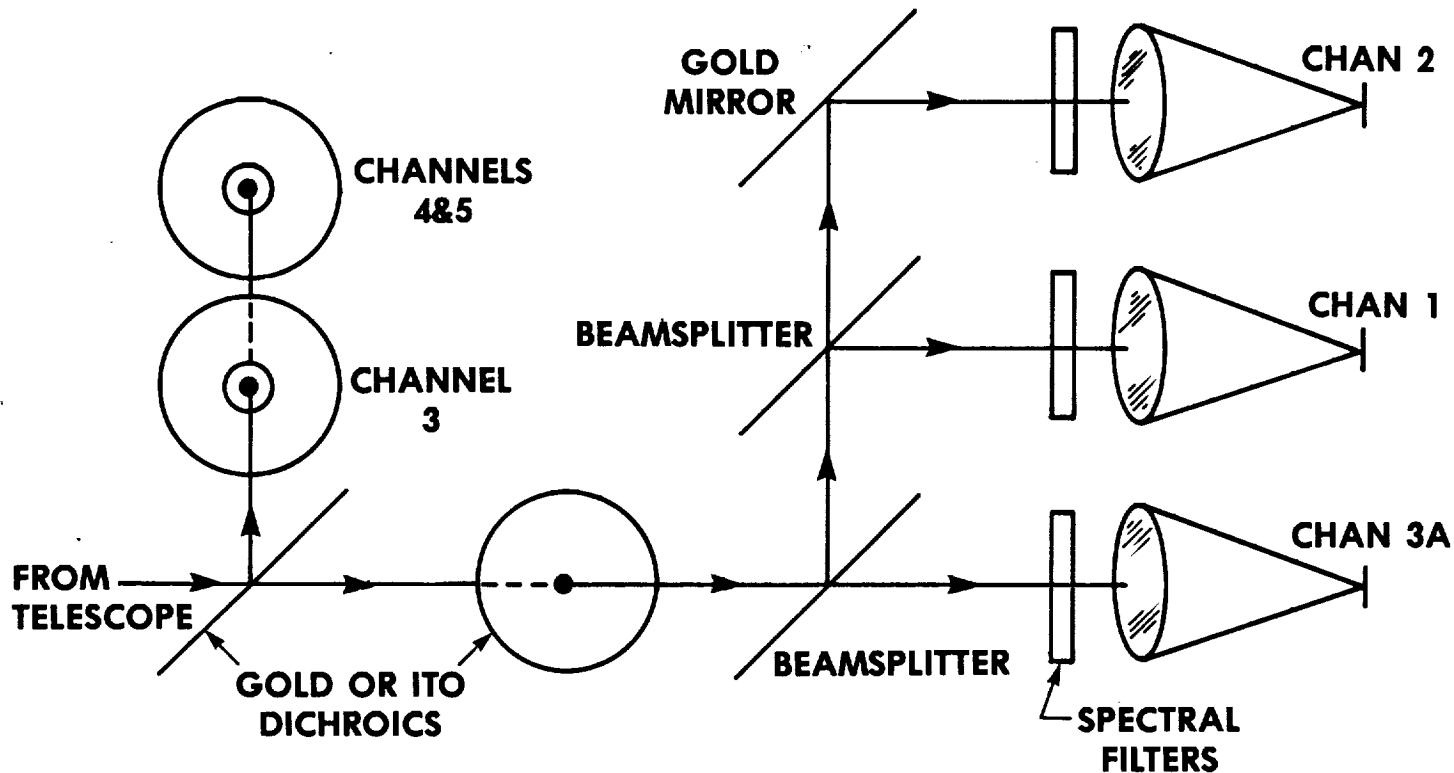
AEROSPACE/OPTICAL DIVISION ITT

therefore do not recommend this approach. We recommend that all
beamsplitters and spectral filtering be done in collimated optical
beams in Channels 1, 2 and 3A. A typical approach is shown in Figure
4.2-1B.

4.2.1.1   Review of AVHRR Optics Design

The AVHRR optics were originally designed to cover a field
of view larger than required by the IGFOV (instantaneous geometric
field of view) in order to allow some lateral adjustment of detectors
to accomplish registration without vignetting the optical beam. The
AVHRR/O (i.e. original design) contained two "visible" and one thermal
(10.5-12.5μm) channels with IGFOV widths of 0.55mr (milliradian) as
well as the 6.5-7μm water vapor channel with IGFOV of 2.2mr. The
telescope and infrared channels were therefore designed for an EFOV
radius (extended field of view) of 2.2mr and the visible channels for
only 1.1mr radius. When the spacecraft orbital altitude was decreased
(to its present 833 km value) the visible and thermal channel IGFOVs
were increased to 1.31 mr and the 6.5 μm channel was replaced with the
3.5 μm channel with an IGFOV of 1.31 mr. The EFOVs of the infrared
channels were adequate to accept the new IGFOVs of those channels since
adequate margin had been allowed in the original design. In the
visible channels the maximum allowable IGFOV was 1.3 + 0.2 = 1.5 mr so
that the angle from the optical axis to the corner of the maximum
square IGOFV was 1/2 (1.5 x $\sqrt{2}$) mr or 1.06 mr.

4.2.1.2   AVHRR/3 Relay Optics EFOV

In order to incorporate the 1.6 μm channel using an
uncooled detector, additional beamsplitters must be incorporated into
the relay optics. Furthermore, the configuration is required to meet
the polarization specifications. The clear aperture sizes of the
beamsplitters, folding mirrors and focus lenses (first curved surface)
are determined by their location along the optical axis and the radius
of the EFOV we select. In addition to the maximum IGFOV noted above
(1.06 mr to the corner) we should add the assembly alignment tolerance
of ±0.3mr (maximum) and also add a boresight error for alignment of the
test collimator to the boresight mirror on the AVHRR. This latter
allowance is estimated to be no more than ±0.1 IGFOV or 0.13 mr. The
minimum design EFOV for the relay elements should therefore be

$$EFOV_{minimum} = 1.06 + 0.30 + 0.13 = 1.49 \ mr$$

It is therefore recommended that an EFOV _radius_ of 1.5 mr
(in object space) be used to determine clear aperture sizes of all
beamsplitters, fold mirrors and focus lenses (front elements) in the
relay optics for channels 1, 2 and 3A. The only exception to this is
the beamsplitter which reflects the three cooled infrared channels; it
is presently designed to cover the 2.2 mr EFOV radius and this will be
retained in the AVHRR/3 optics design.

4.2.2   Final Design of Relay Optics

          Figure 4.2-2 is a layout of the selected relay optic
approach. The collimated beam from the telescope comes from the left
side and is incident on Dichroic, D1, which reflects channels 3B, 4 and
5 (thermal IR) and transmits channels 1, 2 and 3A (solar channels).
Dichroic D1 is an Indium Tin Oxide dichroic which replaced the thin
film gold dichroic used previously. Reason for this change is
discussed later.

          Dichroic, D2, is identical to D1 and is used for polariza-
tion compensation. Its major axis is rotated 90° to D1 to accomplish
this.

          Dichroic, D3, reflects channels 1 and 2 and transmits chan-
nel 3A. Its characteristics are discussed later.

          Dichroic, D4, reflects channel 1 and transmits channel 2.
M1 is a gold mirror which reflects channel 2 to its relay optic.

          Filters F1, F2 and F3A are the spectral bandpass filters
for those respective channels. They are used in a collimated beam as
previously discussed.

          The channel 1 and 2 relay lenses are identical to each
other and focus their respective signals onto silicon photodiode detec-
tors located at the focal planes.

          Channel 3A relay lenses are faster than the channels 1 and
2 and focus the energy onto the InGaAs detector located at the focal
plane.

          The specific lens designs and relay optic performance for
each channel can be found in Appendix B to this report.

          A discussion of each of the dichroic beamsplitters follows.
Copies of preliminary procurement specifications for the dichroics are
enclosed in Appendix C to this report.

4.2.2.1   ITO Dichroics D1 and D2

          In order to combine the three solar channels (i.e., treat
the 1.6 µm channel as an uncooled solar channel) the present thin gold
film (TGF) dichroic that separates the solar and thermal channels will
be replaced with a dichroic that transmits well at 1.61 µm. This can
be done by using either a thinner gold film or an indium-tin-oxide
(ITO) film. Such a change will increase the sensitivity (signal-to-
noise ratio) in Channels 1 and 2. However, in order to obtain a
dichroic transmission high enough to meet the signal-to-noise objective
at 1.61 µm, the optical transmission (dichroic reflection) in Channel
3B (3.7 µm) may be reduced significantly.

Figure 4.2-2 INCORPORATION OF CHANNEL 3A INTO AVHRR/3

AEROSPACE/OPTICAL DIVISION **ITT**
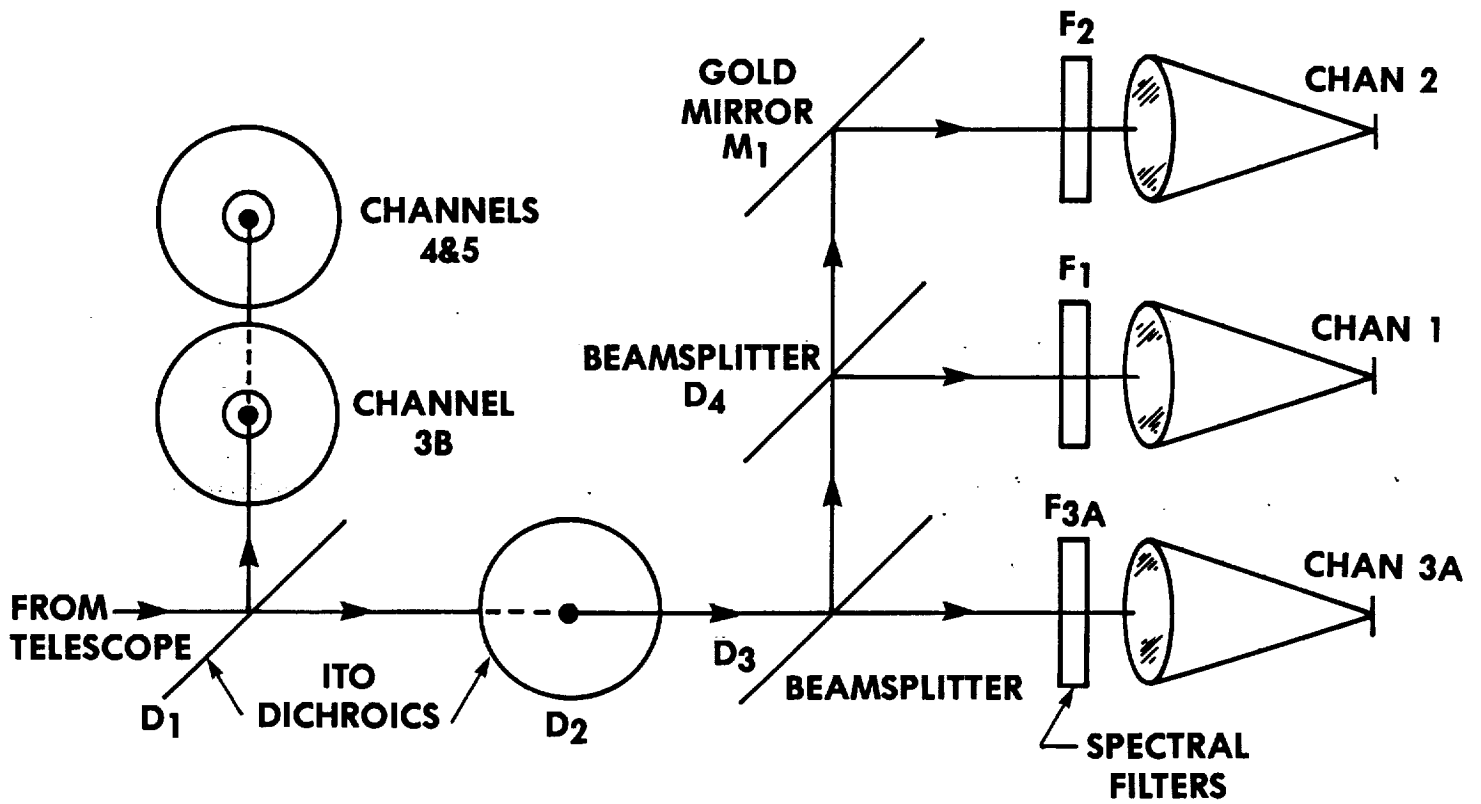
In theory, there is sufficient sensitivity (design margin) in Channel 3B to allow for this reduction in transmission. In practice, however, the margin is much smaller because of the noise degradation factor seen during normal operation. Moreover, much larger degradations have been observed during in-orbit operation (15 to 20 X normal). As a result, we must conclude that the signal-to-noise objective in Channel 3A can only be met when it is combined with Channels 1 and 2.

The ITO dichroic has been in use as a thermal control coating in space applications for many years. It is manufactured by OCLI, Santa Rosa, California, and is considerably more durable than the gold dichroic used previously.

As part of this study, ITT gave OCLI a subcontract to design and fabricate three samples of an ITO dichroic. The primary reason is to allow OCLI to verify that coatings can be fabricated to meet AVHRR/3 needs. The AVHRR requires a thinner coating than OCLI normally uses for non-optical purposes.

The results of this subcontract are shown in Figures 4.2-3 and 4.2-4. Figure 4.2-5 is the typical gold dichroic characteristic from AVHRR/1 and /2. The coating samples made by OCLI meet all of the requirements set by ITT in terms of transmission and reflection. Adhesion and abrasion tests by OCLI showed that the samples met these requirements as well.

The major concern with this dichroic is its reduced reflectance in channel 3B compared to the gold dichroic. This reduced reflectance will reduce the sensitivity margin in this channel and will require that extraneous pick up and noise degradations (which are exhibited in this channel in orbit) be reduced or eliminated.

A separate effort is underway to change channel 3B detector and preamp design to accomplish this. For this reason ITT recommends that the ITO coating be incorporated in AVHRR/3.

As stated previously, two identical dichroics are used with crossed axes to eliminate the polarization contribution of this element. A discussion of polarization sensitivity is found later in this report.

4.2.2.2   Channel 3A Dichroic, D3

Barr Associates has performed an analysis to determine the design and expected transmission and reflection for the beamsplitter required to transmit channel 3A and reflect channels 1 and 2.

Figure 4.2-6 is the expected reflectance of the dichroic in the channels 1 and 2 spectral bands. Figure 4.2-7 is the same on an expanded scale. This figure shows the S and P polarization responses. According to this data, this dichroic beamsplitter will not be a

Figure 4.2-3 OCLI ITO DICHROIC TRANSMITTANCE

SCAN #1 — TRANSMITTANCE

WAVELENGTH IN NM

%T

T ≥ 99%

T ≥ 87%

T ≥ 86%

1.65 μm
1.57 μm
.875 μm
.835 μm
.69 μm
.57 μm

ITT

AEROSPACE/OPTICAL DIVISION

81
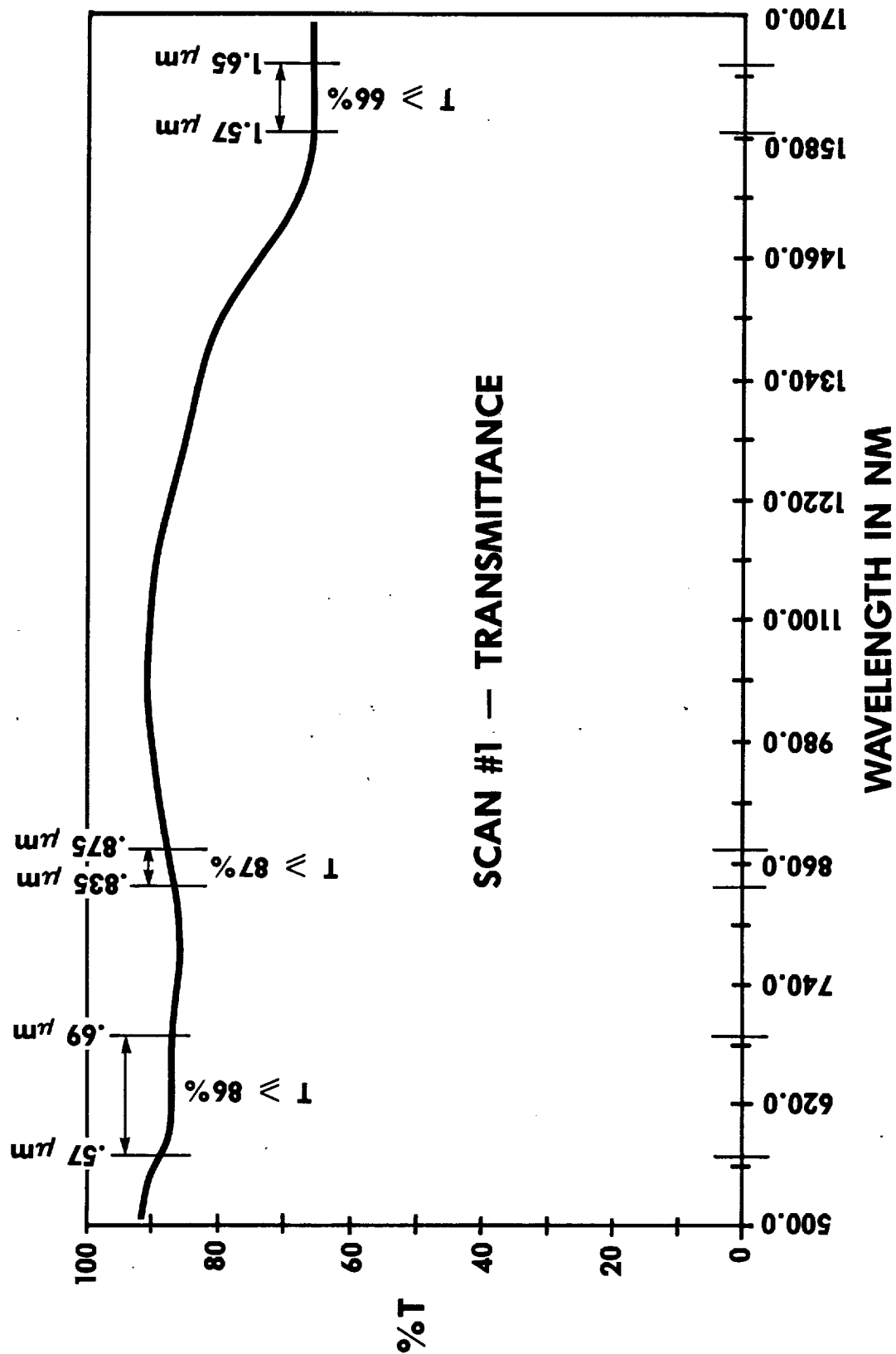
Figure 4.2-4 OCLI ITO DICHROIC REFLECTANCE

SCAN #2 — RELFECTANCE

WAVELENGTH (NM)

AEROSPACE/OPTICAL DIVISION ITT

82
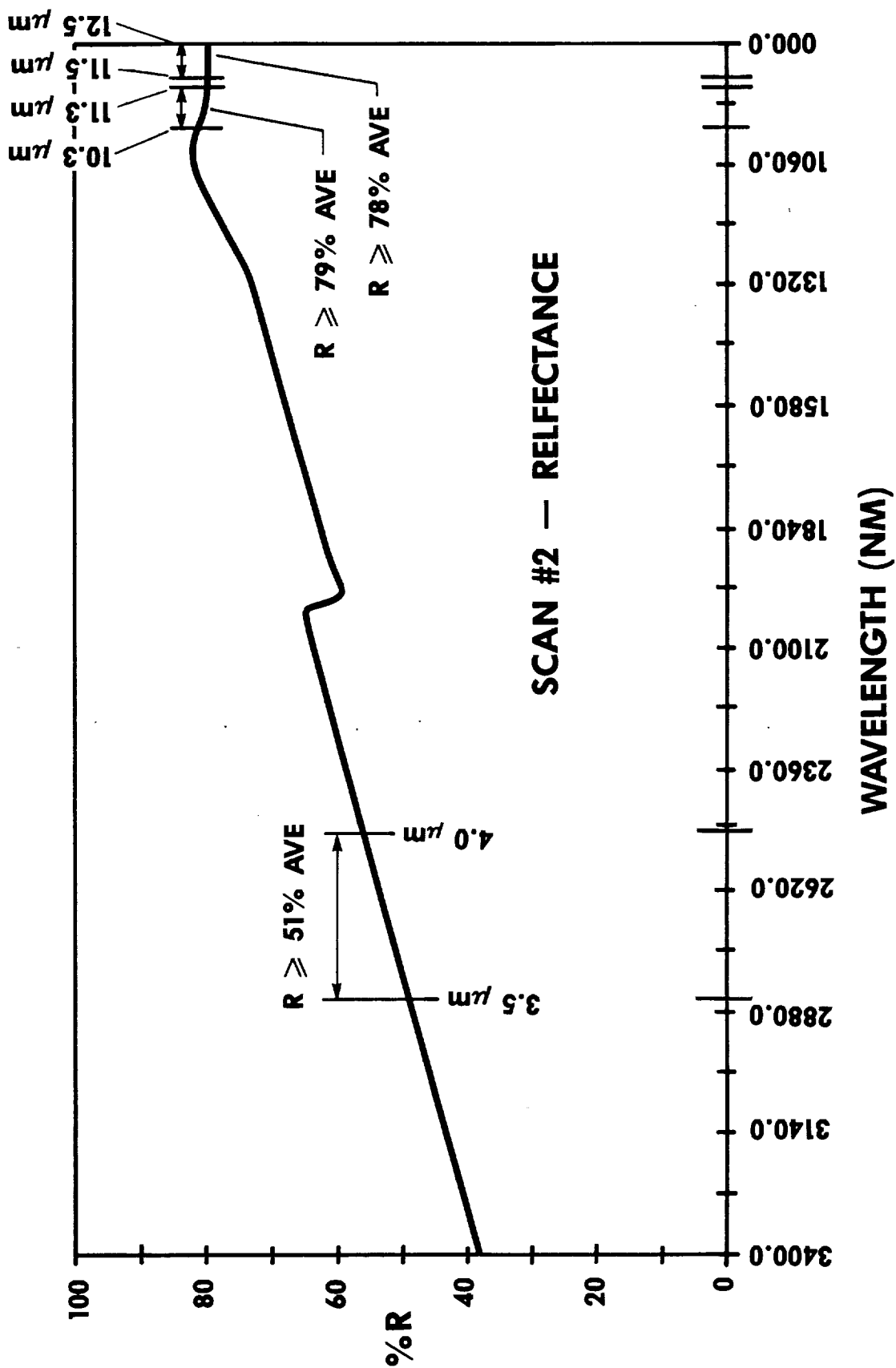
Figure 4.2-5 TYPICAL GOLD DICHROIC COATING RESPONSE
(AVHRR/3 CHANNELS SHOWN)

T = TRANSMISSION

R = REFLECTION

WAVELENGTH IN MICRONS

AEROSPACE/OPTICAL DIVISION **ITT**
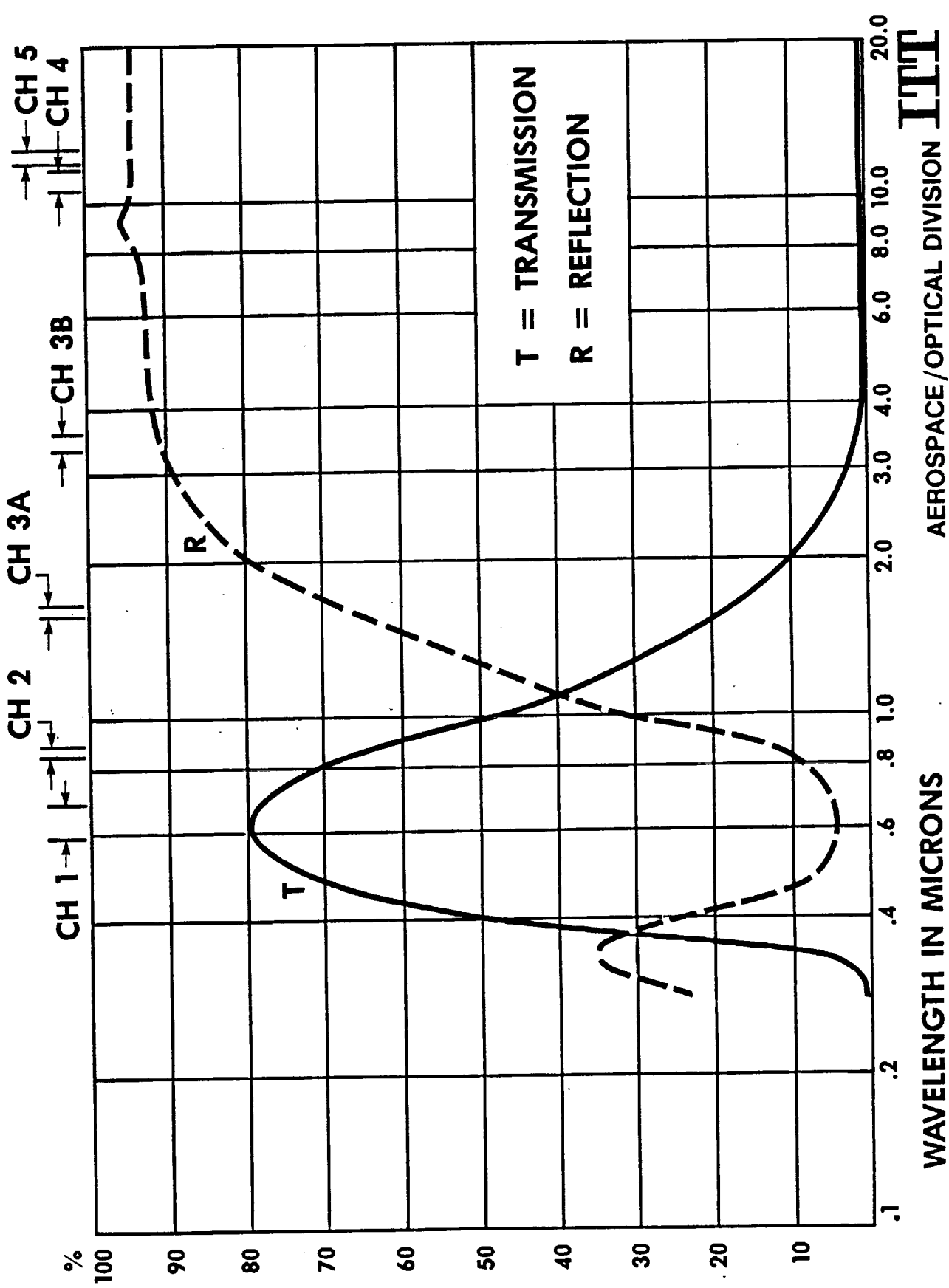
Figure 4.2-6 EXPECTED REFLECTANCE OF CHANNEL 3A BEAMSPLITTER

ITT

AEROSPACE/OPTICAL DIVISION

C-2

84
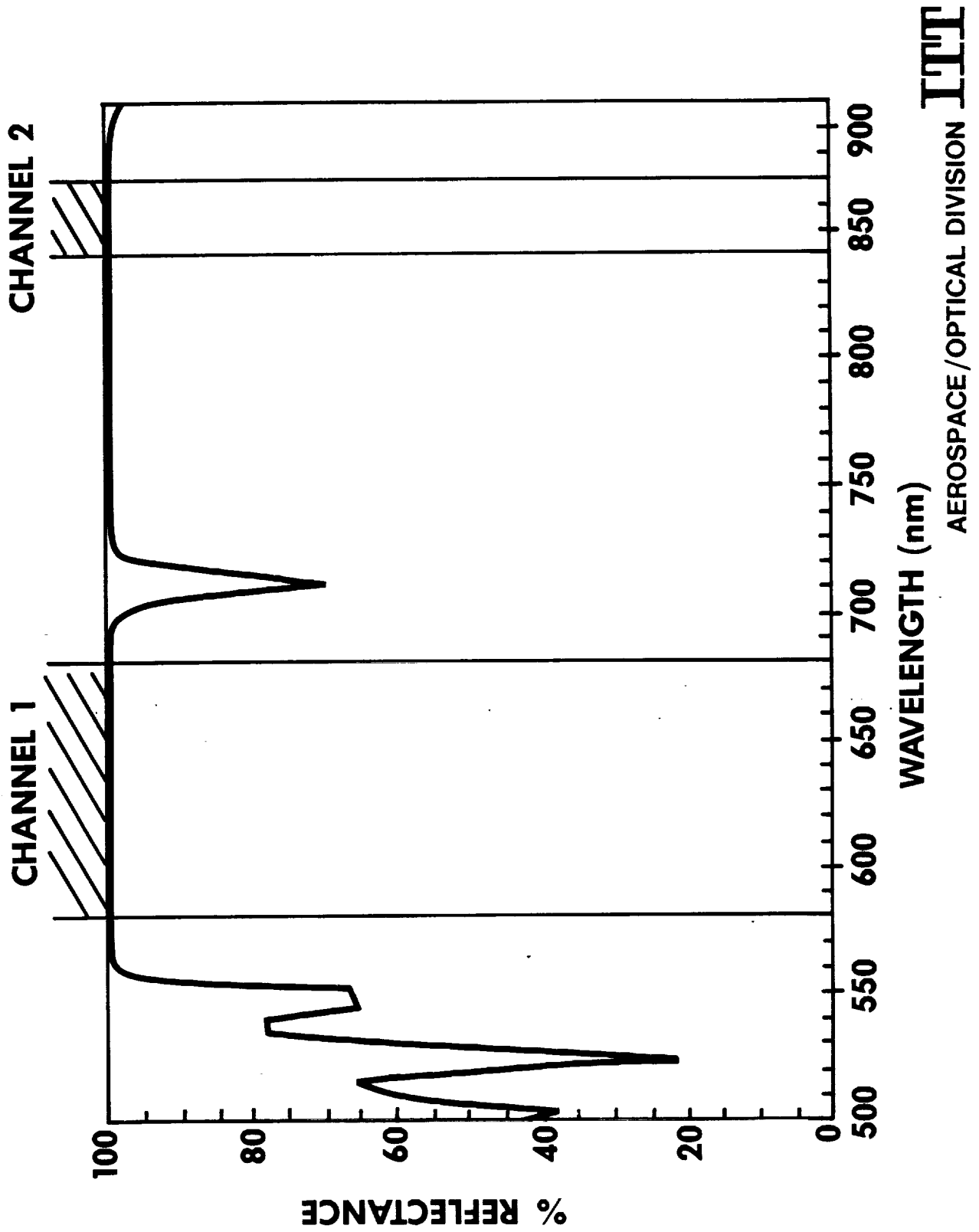
Figure 4.2-7 EXPANDED REFLECTANCE, CHANNEL 3A BEAMSPLITTER

CHANNEL 2

CHANNEL 1

P,S-pol
AND AVERAGE

WAVELENGTH (nm)

% REFLECTANCE

AEROSPACE/OPTICAL DIVISION

ITT

85
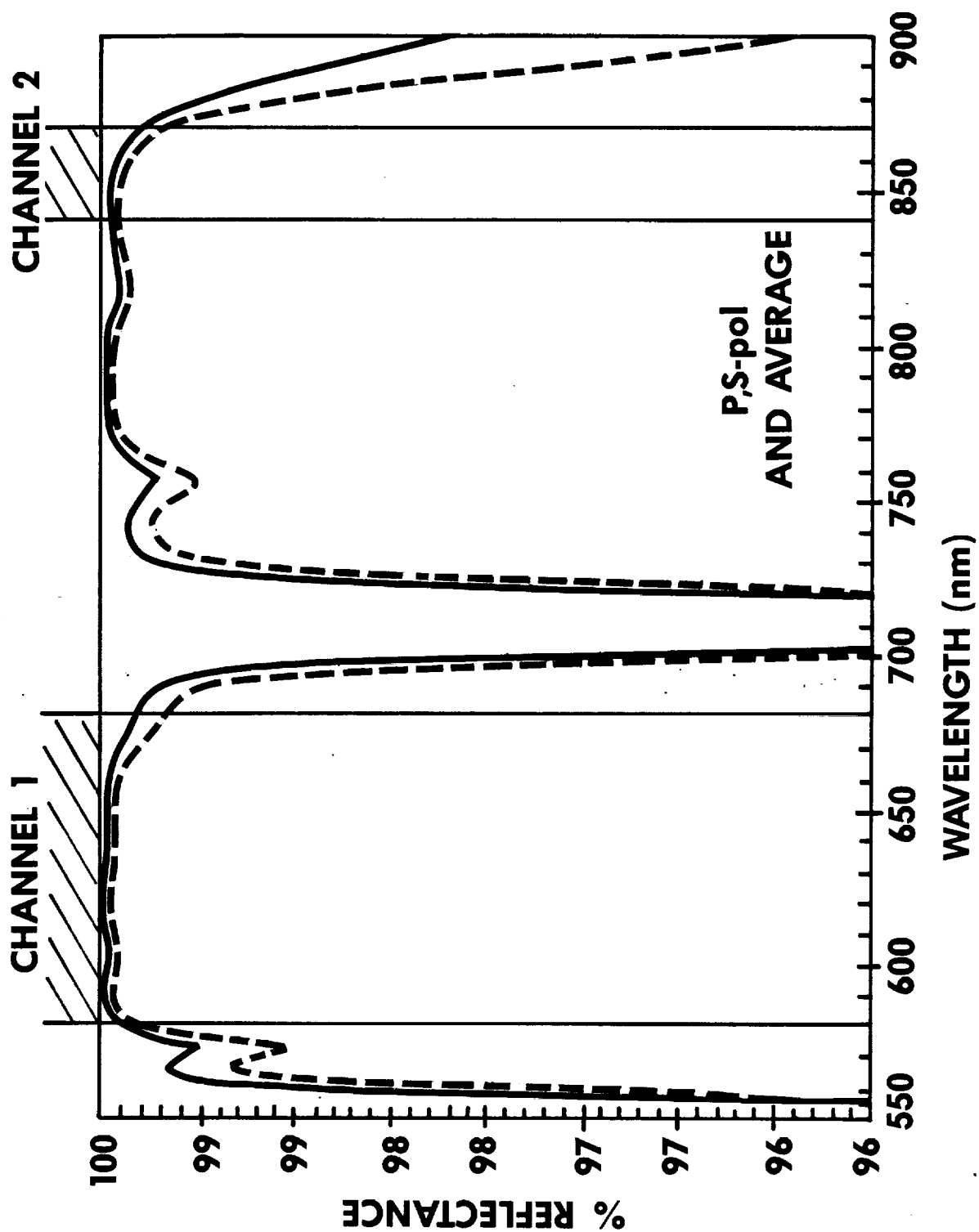
contributor of polarization sensitivity in channels 1 and 2 and will
provide extremely high efficiency.

Figure 4.2-8 gives the transmittance characteristics of
this beamsplitter in channel 3A. Values for P and S polarization are
shown along with the average. There is some polarization effect in
channel 3A; however, on an integrated in-band basis, this element
contributes very little (almost an insignificant amount) to the overall
instrument polarization sensitivity.

According to Barr Associates, this dichroic beamsplitter is
of straightforward design and should present no manufacturing problems.
Materials are all typial optical materials which should all be accep-
table for spaceflight use.

4.2.2.3   Channel 1/2 Dichoric, D4

The present AVHRR uses a neutral density inconel
beamsplitter to separate the Channel 1 and Channel 2 energy. This is a
hold over from the time when channels 1 and 2 had overlapping spectral
responses. The optical efficiency of this beamsplitter is extremely
low and so we are proposing to change the neutral beamsplitter to a
multilayer dichroic beamsplitter.

Figures 4.2-9 thru 4.2-13 give predicted transmission and
reflection for the proposed dichroic. These curves were run by Barr
Associates, Inc., Westford, MA. The curves show the overall transmit-
tance from 500 to 900 nm followed by curves for P and S polarization
transmittance and reflectance in channels 1 and 2. Channel 1 (580 -
680 nm) is reflected from the beamsplitter while channel 2 (840 - 870
nm) is transmitted.

The curves show first that the proposed beamsplitter will
have very high efficiency in both channels 1 and 2. Second, the
polarization sensitivity contribution of this element will be
exceedingly small (again because the efficiency is so high).

According to Barr Associates, materials are all common
materials which should be totally acceptable for use in space.

4.2.2.4   Beamsplitter Sources

Since uniformity of spectral response and minimum polariza-
tion are prime concerns to NASA and NOAA, phone contacts were made with
six different beamsplitter manufacturers to find out what performance
can reasonbly be achieved (this information is not normally given in
catalogs except for typical examples).

Of the six vendor contacts, by far the best response was
obtained from Barr Associates, Inc. (Westford, MA, Mr. Tom Mooney).
The following general information was obtained from them:

Figure 4.2-8 EXPECTED TRANSMITTANCE OF CHANNEL 3A BEAMSPLITTER

CHANNEL 3A

S-pol

P-pol

ON BK7 @ 45 deg

% TRANSMITTANCE

WAVELENGTH (nm)

AEROSPACE/OPTICAL DIVISION

ITT

87
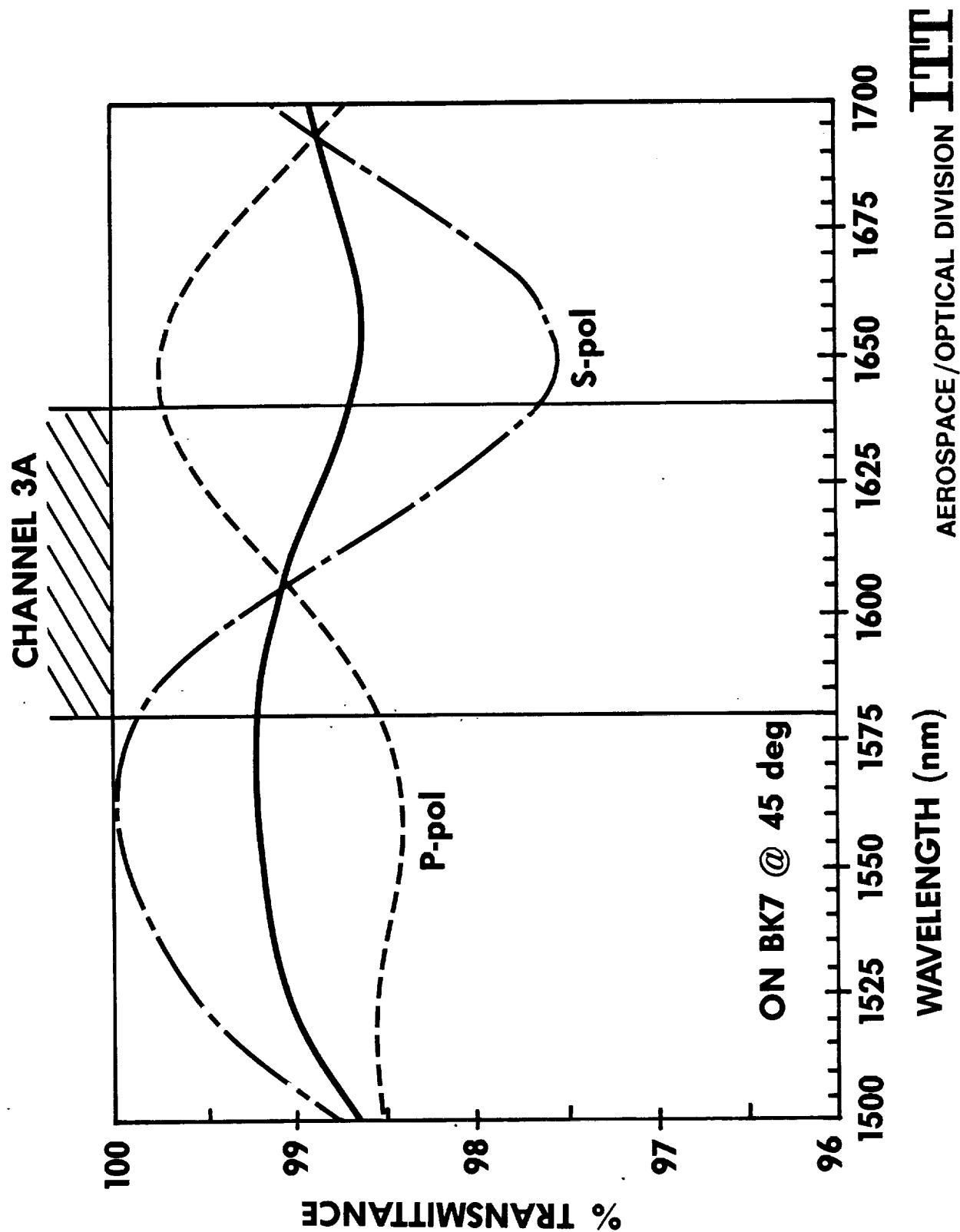
Figure 4.2-9 SPECTRAL TRANSMITTANCE OF NEW CHANNEL
1/2 DICHROIC BEAMSPLITTER

AEROSPACE/OPTICAL DIVISION IT'I'

88
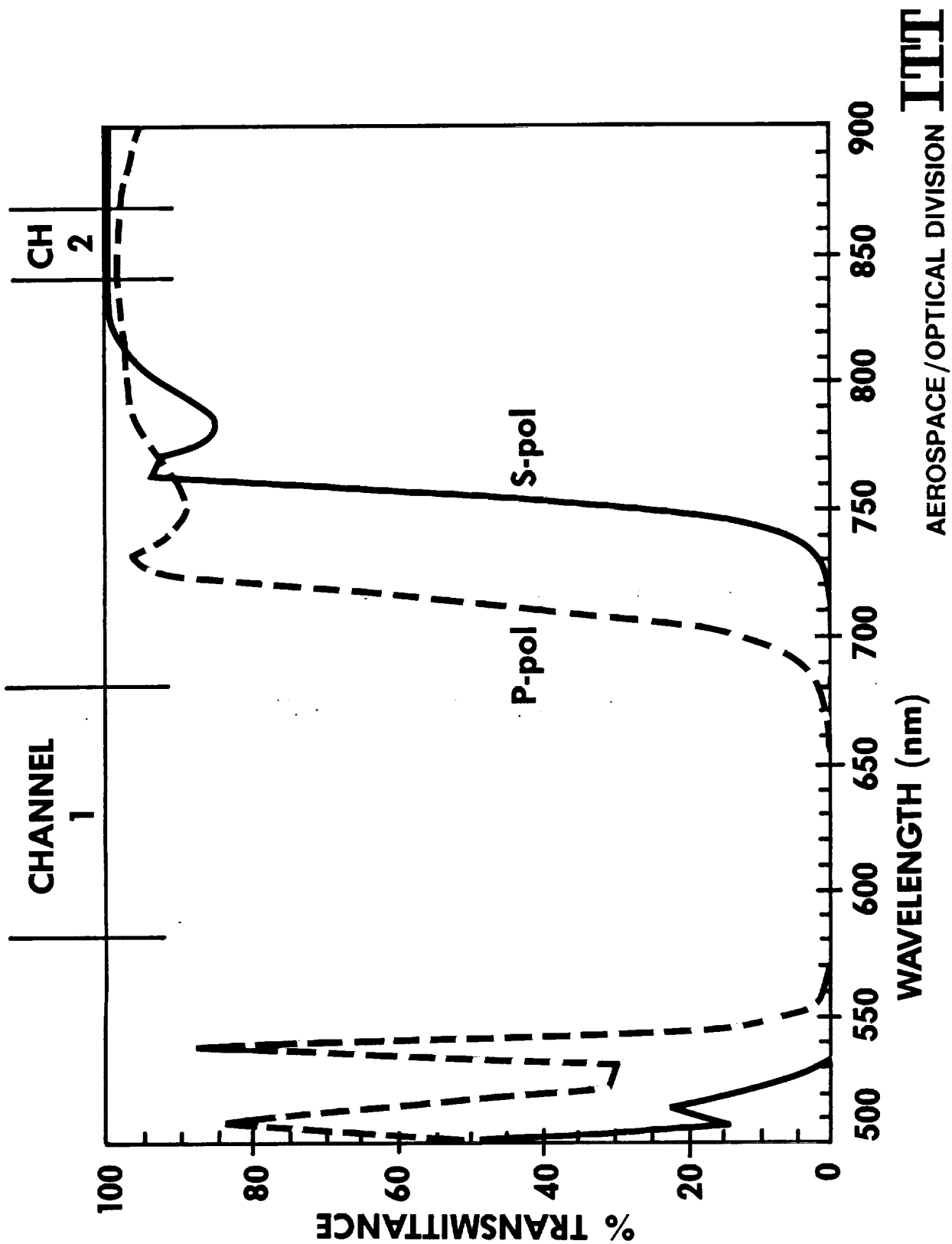
Figure 4.2-10 P-POLARIZATION REFLECTANCE OF CHANNEL 1/2 BEAMSPLITTER

RMIN 98.323%   RMAX 99.906%   RAVE 99.671%   (560 - 680 nm)

AEROSPACE/OPTICAL DIVISION   ITT
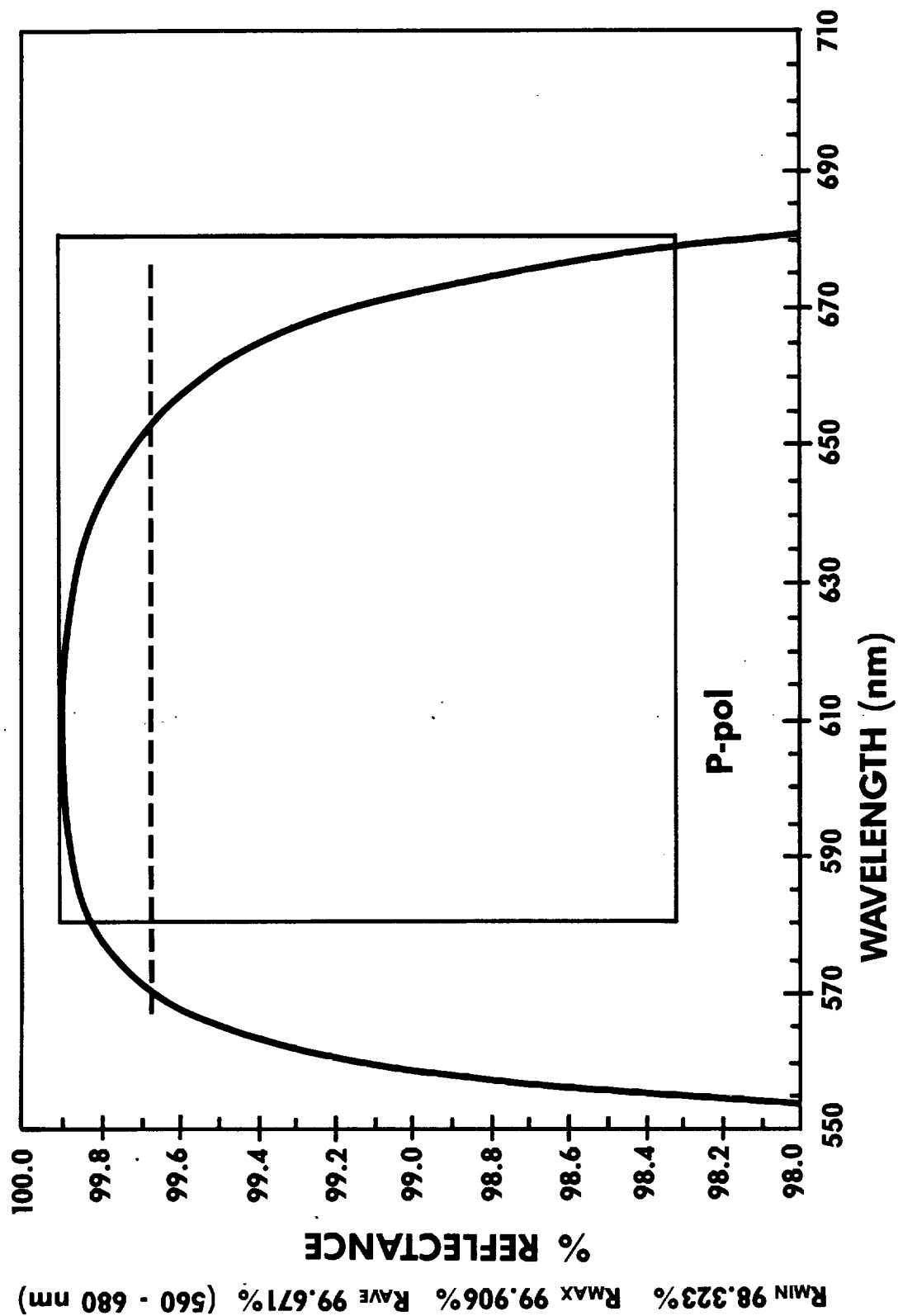
Figure 4.2-11 S-POLARIZATION REFLECTANCE OF CHANNEL 1/2 BEAMSPLITTER

S-pol

% REFLECTANCE

100.0
99.98
99.96
99.94
99.92
99.90
99.88
99.86
99.84
99.82
99.80

550   570   590   610   630   650   670   690   710

WAVELENGTH (nm)

RMIN 99.982%   RMAX 99.997%   RAVE 99.994%   (560 - 680 nm)

AEROSPACE/OPTICAL DIVISION ITT

90
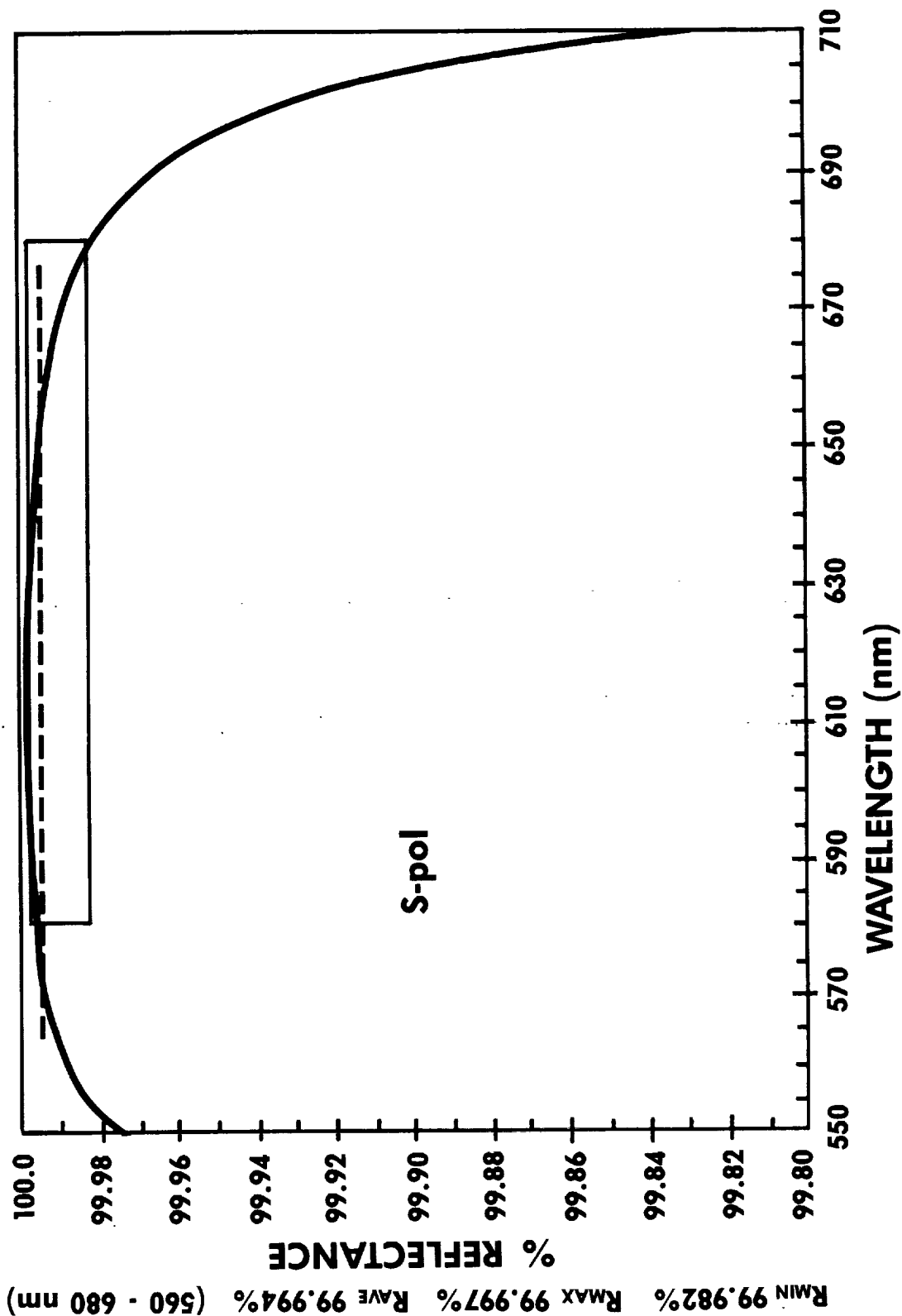
Figure 4.2-12 P-POLARIZATION TRANSMITTANCE OF CHANNEL 1/2 BEAMSPLITTER

WAVELENGTH (nm)

% TRANSMITTANCE

P-pol

T_Min 99.411%   T_Max 98.988%   T_Ave 98.792%   (825 - 865 nm)

AEROSPACE/OPTICAL DIVISION ITT

91
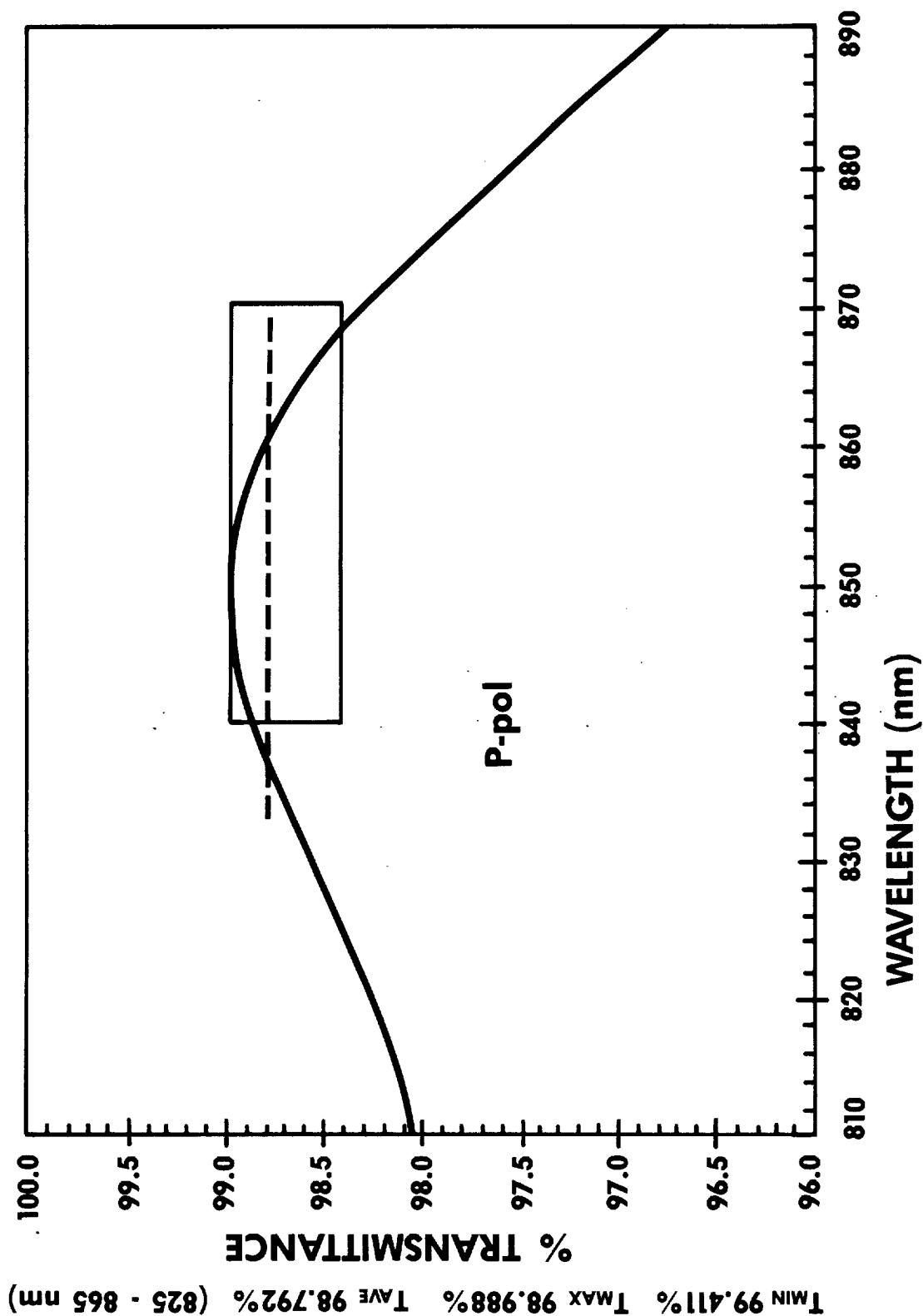
Figure 4.2-13 S-POLARIZATION TRANSMITTANCE OF CHANNEL 1/2 BEAMSPLITTER

TMin 99.331%   TMax 99.881%   TAve 99.741%   (825 - 865 nm)

S-pol

% TRANSMITTANCE

WAVELENGTH (nm)

AEROSPACE/OPTICAL DIVISION ITT
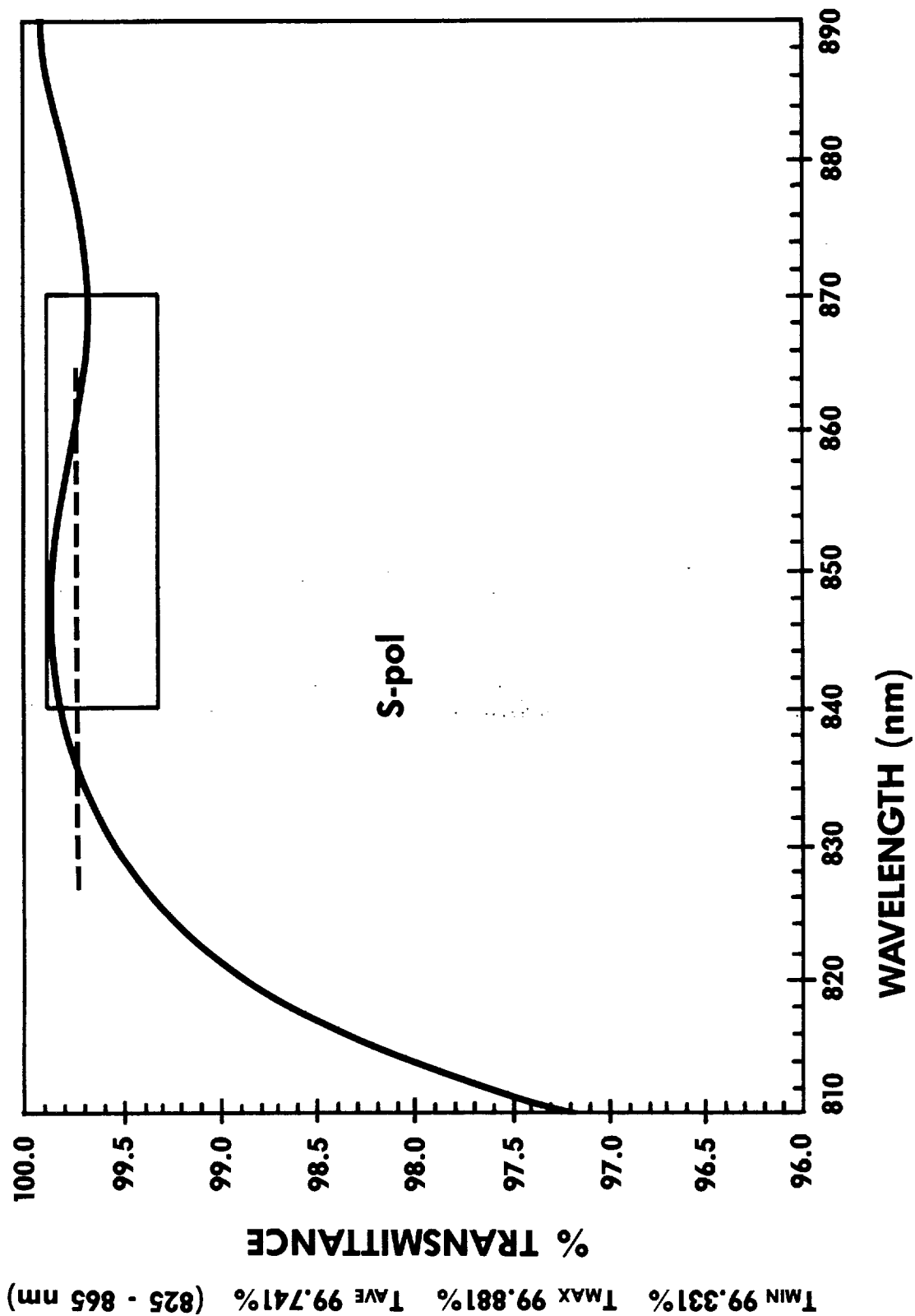
1) it is usually better to transmit the longer wavelengths because less in-band ripple (variation in transmission) and polarization are obtained.

2) the spectral separation between channels 1 and 2 is probably sufficient so that most of the ripple will be gone by the time we get to the passbands (the transition would be designed to occur about midway between the two bands, i.e. at 760 nm.)

3) polarization gets worse as the angle of incidence increases, however they can minimize this effect for a 45° incidence angle if we have a collimated beam (they do not have a computer program for designing beamsplitters in a focused beam; also, they have no standard measurement capability for focused beams although this has been done for one vendor who supplied the lens).

4) if we reflect the shorter wavelength band (i.e. 580 to 680 nm) then the average reflectivity will be 99 + % so very little in-band ripple or polarization would be caused by this beamsplitter in this spectral band.

5) for the transmitted beam (840 to 870 nm for the channel 1 and 2 beamsplitter) they can design for both maximum transmission and minimum ripple; the calculated values will be less than 1% ripple and average transmission >99%. In actual practice they find approximately 1% loss due to scattering in the dielectric coating layers, average transmission of about 93 to 95% and peak-to-valley ripple from +1% to +5%. The amount of ripple is a yield effect depending on operator skill, equipment, number of coating runs, etc. The achievable ripple is therefore determined to a large extent on how much we are willing to pay.

The above five comments also apply in general to the beamsplitter which will reflect channels 1 and 2 and transmit channel 3A (1.54 to 1.64 μm), however, Mr. Mooney felt that it would probably not be as difficult to manufacture as the one separating channels 1 and 2.

Other vendors contacted and any pertinent comments are listed below:

1) Microcoatings, Inc., Westford, MA (Louise Deveau)

For minimum polarization they would recommend an incidence angle of about 15° with 30° being the maximum. They will send us some spectral transmission curves for typical dichroic beamsplitters.

2) Balzers Optical Group, Marlborough, MA (Michael Pearlmutter)

   For a long wavelength pass (LWP) design the average transmission would be 90 to 94%.

3) Omega Optical, Inc., Brattleboro, VT (Robert Johnson)

   After much reflection and thought Mr. Johnson stated a LWP design would be best for minimum ripple and polarization. He would expect about 99% average reflectance in channel 1 and about 85% average transmission in channel 2 with 5% absolute ripple ($T_{max} - T_{min}$).

4) Trans World Optics, Inc., Hauppague, NY (Dr. Robert Leshne)

   For a 45° incidence angle (LWP design) the S polarization normally reflects very well and the P polarization likes to transmit through the beamsplitter; a lower angle of incidence would be helpful. Dr. Leshne also said there would be little ripple in the reflected beam.

5) Corion Corp., Holliston, MA (Robert Quellette)

   Mr. Quellette said that on large production runs of LWP beamsplitters most of the parts will pass a ripple specification of ±10% in the transmitted beam. As the ripple specification is reduced the cost increases exponentially because the yield goes down. They could achieve ±1% ripple if we can afford the cost, all we need to do is specify what amount of ripple we will accept.

There are several other manufacturers who were not contacted but we would include them in a list of potential suppliers. These include Ditric Optics, Herron Optical Co., Optical Coating Labs Inc., Esco Products Corp., Pomfret Research Optics Inc., Spectron Optical Systems Inc. and Newport Thin Film Labs Inc.

4.2.2.5   Gold Mirror, M1

This element is a folding mirror and will have a protected gold reflective coating. No significant problems are expected with this element.

The present AVHRR/2 uses an aluminum folding mirror for channel 2. It was selected so that its polarization effects would help to compensate those of other elements. In the AVHRR/3 design this compensating polarization is not needed and the high efficiency gold can be used.

4.2.2.6   Spectral Filters

        According to filter manufacturers contacted during this
study, all three of the spectral filters are straight-forward in design
and manufacture. All NASA bandwidths, slopes, in-band ripples and out-
of-band blocking requirements can be met.

        Preliminary procurement specifications were generated for
review by the vendors. These are included in Appendix C to this
report.

4.2.2.7   Optical Transmission

        The estimated nominal optical transmission for all optical
elements in channels 1, 2 and 3A are given in Table 4.2-1. The
spectral balance filter for channel 1 is a KG-4 Schott color glass
filter used to eliminate a response at 0.90 microns.

        By way of comparison, the total system transmission for
AVHRR/2 is 0.05 in channel 1 and 0.06 in channel 2.

Table 4.2-1.   AVHRR/3, Optical Transmission, Nominal
               Average In-Band

Comkponent	Ch. 1	Ch. 2	Ch. 3A
SCAN MIRROR	0.94	0.91	0.89
TELESCOPE PRIMARY	0.94	0.91	0.89
TELESCOPE SECONDARY	0.94	0.91	0.89
OBSCURATION	0.92	0.92	0.92
ITO DICHROIC, D1	0.86	0.87	0.66
ITO DICHROIC, D2	0.86	0.87	0.66
DICHROIC D3	0.99	0.99	0.98
DICHROIC D4	0.99	0.98	N.A.
FOLD MIRROR, GOLD	N.A.	0.96	N.A.
FILTER, BANDPASS	0.75	0.75	0.75
FOCUS LENS #1	0.98	0.98	0.98
FOCUS LENS #2	0.98	0.98	0.98
FOCUS LENS #3	0.98	0.98	0.98
SPECTRAL BALANCE FILTER	0.85	N.A.	N.A.
TOTAL	0.33	0.34	0.20

4.2.3   Polarization Design

        The degree of polarization is defined by

$$P = \frac{O_{max} - O_{min}}{O_{max} + O_{min}}$$

Where O is the output for a linearly polarized input. Because the
detectors are not polarization sensitive, O can be replaced by τ, the
transmittance of the optical train. In fact, a component is (at least
theoretically) insensitive to polarization when the incident beam is a
cone of radiation symmetrical about the 0° incidence angle. As a
result, we can also exclude the telescope mirrors and focusing lenses
from the polarization design. Or, stated another way, we can limit the
polarization design to those elements that are at an angle to the optic
axis.

        The polarization design requirement (for channels 1, 2, and
3A) is P < 0.053, where the 0.053 maximum is the current limit imposed
on the AVHRR/2. The original AVHRR polarization design was carried out
for the nadir position, because that is the only position at which the
specification applies. In fact, however, the AVHRR meets this require-
ment throughout the useful range of scan angles (±50° about nadir). We
will therefore assume that this performance must be preserved in the
spectrally modified imager, i.e., that the degree of polarization must
be <0.053 at all useful scan angles.

        The major contributors to residual polarization sensitivity
are the scan mirror, the dichroic beamsplitters and the channel 2
folding mirror. The scan mirror will be an enhanced aluminum coating
(nearly identical to the present scan mirror coating). Figure 4.2-14
is the expected reflectivity in channels 1, 2 and 3A for two orthogonal
polarizations and the average. This is at a 45° incidence angle. This
data was provided by Evaporated Metal Films, Inc., manufacturer of the
present scan mirror coating. The curves represent calculated values of
absolute reflectivity and will be about 1% lower overall in reality.
However, the polarization effects are reported to be reasonable.
According to the previous definition, the mirror will contribute a
polarization sensitivity as given in Table 4.2-2.

        The ITO dichroics will not contribute measurable polariza-
tion since the two ITOs used (D1 and D2) will compensate each other.
The dichroics will be coated in the same batch to assure maximum simi-
larity in properties.

        The channel 3A dichroic, D3, and the channel 1/2 dichroic,
D4, will have very high efficiency for both transmission and reflec-
tion. The contributions for these elements are given in Table 4.2-2.
These values were obtained from Barr Associates, Massachusetts.

        Note that the sense of the channel 2 polarization from D4
is reversed with respect to the other elements. According to Barr

Figure 4.2-14 SCAN MIRROR POLARIZATION (ENHANCED ALUMINUM)

REFLECTANCE (%)
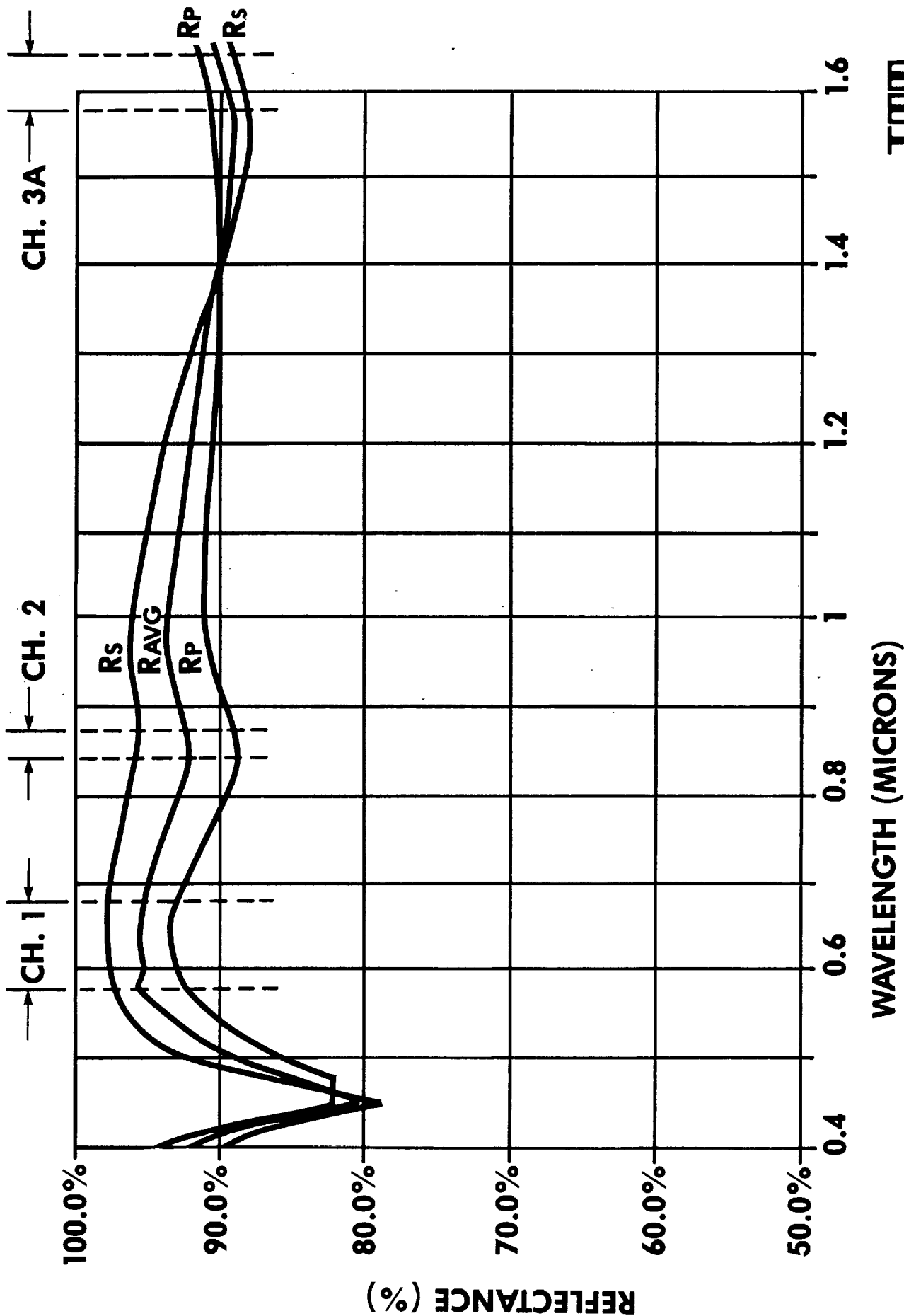
WAVELENGTH (MICRONS)

AEROSPACE/OPTICAL DIVISION ITT

Table 4.2-2. Polarization Contributors in AVHRR/3 Channels 1, 2 and 3A

Component	Channel 1	Channel 2	Channel 3
Scan Mirror	2.4%	3.6%	1.2%
ITO Dichroic (D1, D2)	Negligible	Negligible	Negligible
Ch. 3A Dichroic D3	<1.5%	<1.5%	<3.0%
Ch 1/2 Dichroic D4	<1.0%	-3.0%*	---
Gold Mirror M1	---	<1.0%	---
Total	<4.9%	<3.1%	<4.2%

* Note sign

Table 4.2-3. AVHRR Polarization Comparison

AVHRR/1 & 2

	Req'd*	Measured**
Ch. 1	<7%	3.7%
Ch. 2	<7%	5.3%

* IFOV at Nadir; design goal <5.3%
** PFM Model AVHRR/1

AVHRR/3

	Desired*	Present Estimate
Ch. 1	Minimum*	<4.9%
Ch. 2	Minimum*	<3.1%
Ch. 3A	Minimum*	<4.2%

* Assumed to be <5.3%

98

Associates, they can adjust the coating to give a wide range of polarizations. He suggested that the residual polarization of this element can be used to partially offset the contribution of the scan mirror.

The gold mirror, M1, also has a very high reflectance. Its contribution to channel 2 is estimated to be 1.0% or less.

Table 4.2-3 lists the expected AVHRR/3 polarization sensitivities and compares them to the present AVHRR/1 and /2 values.

4.3   Channel 3A Detector

Two candidates were considered as the most likely materials for use in this channel. They are a Germanium (Ge) photodiode or an Indium Gallium Arsenide (InGaAs) photodiode. These are considered as the most likely candidates due to their high performance without cooling. Of the two, the InGaAs is considered to be the best choice, even though it is a relatively new material with no known spaceflight history.

4.3.1   Detector Noise Performance

The chosen detector will be a photodiode; hence, the noise discussion found in section 2.2.3.1.1 of this report applies. The amplifier noise discussion of section 2.2.3.1.3 is also relevant.

4.3.1.1   Germanium Noise Characteristics

In this channel, we would not only use the detector as the field stop, we would also reduce the f-number. In particular, we will assume that the detector sensitive area (field stops) has been reduced to 0.25 mm x 0.25 mm, which corresponds to an f-number of 0.96 in the AVHRR. The reduction in f-number is possible because of the higher index optical materials that can be used in this channel, such as $Si(n = 3.5)$, $ZnSe(2.4)$, $ZnS(2.3)$, and $GaAs(3.3)$.

For a 0.25-mm square Ge detector, Judson Infrared lists a typical peak (1.5 μm) D^* of 8×10^{10} cm $Hz^{1/2}W^{-1}$ at zero bias. The corresponding noise current, i_n, can be calculated from

$$D^* = \frac{RA^{1/2}}{i_n} = \frac{0.75 \times 2.5 \times 10^{-2}}{i_n}$$

where R is the peak responsivity ($0.75AW^{-1}$). The result is $i_n = 2.34 \times 10^{-13}$ $AHz^{-1/2}$. Equating this noise current to $(2qId)^{1/2}$, we obtain an equivalent dark current of

$$I_d = 1.71 \times 10^{-7} \text{ A} = 171 nA$$

or 2.74×10^{-4} Acm^{-2}. By comparison, the Johnson noise current from a 15 megohm feedback resistance R_f is equal to that from a dark current $I_f = 3.45nA$. The noise from R_f is therefore negligible compared with

that from the Ge photodiode, which is exactly opposite the situation
for the Si photodiodes.

Hammamatsu lists Ge photodiodes with higher D*'s (to 2 x
10^{11}) but only in larger sizes (1 mm x 1 mm and larger) and at a lower
responsivity) ($0.70AW^{-1}$). If this performance could be obtained in a
0.25-mm square element, the corresponding dark current would be 138nA.

The application of a reverse bias to a Ge photodiode
increases the dark current by a factor of approximately 10. The detec-
tors studied by Conradi had a dark current density of 2.5 x 10^{-3} Acm^{-2}
which is in the range given by Van Muoi of (0.64 - 6.4) x 10^{-3} Acm^{-2}.

4.3.1.2   Indium Gallium Arsenide Characteristics

A much lower dark current and therefore a higher signal-to-
noise ratio can be obtained by using a InGaAs in the 1.61 μm channel.
The photodiode in the InGaAs alloy system cover wavelengths from 0.9 μm
to beyond 2.1 μm using InGaAs epitaxially grown on GaAs substrates.
The best choice for our application is probably the alloy with 57%
Indium that has a peak response at approximately 1.7 μm. The Plessy
detectors of this type have a typical dark current of 3nA and a best
dark current of 1nA in the 0.25-mm diameter size. If we scale this up
to 0.25-mm square detector (on an area basis), the typical dark current
becomes 3.8nA. This is much less than the dark current from a Ge pho-
todiode of the same size (~150 nA without bias) and comparable to the
equivalent dark current from a 15 megohm feedback resistor (3.5 nA).

The above typical dark current for a 1.7 μm InGaAs photo-
diode corresponds to a density of 6.1 x 10^{-6} Acm 2. Comparison with
other data indicates that this is at low or zero bias voltage. The
data of Van Muoi yield dark current densities with bias of (1.3-6.4) x
10^{-5} Acm^{-2}, and the data of Epitaxx Inc. show 7.6 x 10^{-5} to 1.9 x 10^{-4}
Acm^{-2}.

4.3.2   Amplifier Noise

The amplifier noise in this channel is not completely
negligible for a InGaAs photodiode. This amplifier noise voltage
introduces a small degradation factor (1.06X).

4.3.2.1   Germaniuum Amplifier Noise

For a Ge photodiode at zero bias the Hamamatsu data yield
C_d/A_d = 550pF/mm^2 or 34pF for a 0.25 mm square element. This is
somewhat larger than the 20pF quoted to us by Judson. For C_i = 34 pF,
the equations of section 2.2.3.1.3 yield I_e = 1.0nA, which is negli-
gible compared with the dark current I_d from the unbiased Ge (~150nA).

4.3.2.2   Indium Gallium Arsenide Amplifier Noise

For an InGaAs photodiode at zero bias, the Plessey data yield C_d/A_d - 200pF/mm^2 (best) to 500 pF/mm^2 (typical). Using the typical value, a 0.25-mm square detector has a capacitance of 31pF. For C_i = 31pF, we obtain I_e - 0.83nA. This is small compared with the combined dark currents of the detector and 15 megohm load resistance, $I_d + I_f$ - 3.8 + 3.45 - 7.25nA. The addition of 0.83 nA to 7.25nA increases the rms noise by a (degradation) factor of $(7.5 + 0.83)/7.25^{1/2}$ = 1.06X.

4.3.3   Sensitivity Design Channel 3A

The objective of the sensitivity design at 1.61 μm (Channel 3A) is to achieve a minimum signal-to-noise ratio of 20:1 for a 0.5% Albedo scene. This objective can be met by using an uncooled InGaAs photodiode as the detector. In order to meet the minimum signal-to-noise ratio with a Ge photodiode, it would be necessary to cool the detector to 245K (-28°C) by means of a thermoelectric or single-stage passive cooler. The calculated signal-to-noise at 0.5% Albdo for a InGaAs photodiode is 33.8:1, which gives us a design margin of 1.69. The calculated signal-to-noise for an uncooled Ge photodiode is 8.1:1 and for a cooled Ge photodiode, 28.7:1.

4.3.3.1   Signal Current

The signal current from the photodiode is given by

$$I_s = \frac{AS_\lambda \Delta\lambda}{\pi} \times A_o \, \theta^2 \tau R.$$

where

A = Albedo = 5×10^{-3} (0.5%)

S_λ = spectral irradiance of normally incident sunlight at 1.61 μm = $2.23 \times 10^{-2} Wcm^{-2}\mu m^{-1}$

$\Delta\lambda$ = spectral bandwidth = 0.06 μm

A_o = optical (telescope) collecting area = $\pi (8 \times 2.54)^2/4 cm^2$,

θ = instantaneous field of view - 1.3×10^{-3} radian,

τ = optical transmission in Channel 3A - 0.20,

and R = responsivity of photodiode (AW^{-1}).

The spectral irradiance data of Neckel and Labs., which is considered the standard, ends at a wavelength of 1.25 μm. We have therefore used the data given by Allen (spectral radiance of $3.28 \times 10^2 Wster^{-1}cm^{-2}\mu m^{-1}$ times the solid angle subtended by the sun of $6.80 \times 10^{-5} ster$). Allen's data yields a result halfway between that derived from Gast (2.07×10^{-2}) and interpolated from Thekaekara (2.41×10^{-2}. The optical transmission was calculated from the transmission and reflection of the elements in the optical train, as shown previously in Table 4.2-3.

The specified responsivity,R,of Ge at its peak wavelength (1.5 to 1.55 μm) is 0.70AW^{-1} to 0.75AW^{-1}. However, by anti-reflection coating, the responsivity at 1.6 μm can be increased to 0.90AW^{-1},

which corresponds to a quantum efficiency of 0.70. The same quantum efficiency can be obtained in a InGaAs photodiode. For either detector, the resultant signal current is then

$$I_s = 2.10 \times 10^{-10} A.$$

4.3.3.2   Noise Currents

The rms noise current can be calculated from the sum of the signal and noise dark currents. For a InGaAs photodiode, we have:

signal	I_s = 0.21nA
detector dark current	I_d = 3.8nA
feedback resistance	I_f = 3.45nA (15 x 10^6 ohms)
amplifier	I_e = 0.83nA
	I = 8.29nA

The rms noise current is then

$$i_n = (2qI\Delta f)^{1/2} = 6.21 \times 10^{-12} A,$$

where q = charge on a electron = $1.602 \times 10^{-19}C$, and Δf = electronic bandwidth = $14.5 \times 10^3 Hz$.

The signal-to-noise ratio at 0.5% Albedo using a InGaAs detector is therefore

$$\frac{S}{N} = \frac{2.10 \times 10^{-10}}{6.21 \times 10^{-12}} = 33.8:1.$$

The corresponding design margin with respect to the minimum objective is 33.8/20 = 1.69.

For an uncooled Ge photodiode, the currents that contribute to the noise are:

$$I_s = 0.21nA$$
$$I_d = 138nA \text{ (Hamamatsu detector)}$$
$$I_f = 3.45nA$$
$$I_e = 1.0nA$$
$$I = 143nA$$

The resultant rms noise current is $2.58 \times 10^{-11}A$ and the signal-to-noise ratio,

$$\frac{S}{N} = \frac{2.10 \times 10^{-10}}{2.58 \times 10^{-11}} = 8.1:1.$$

This is well below the minimum objective of 20:1. In order to meet the objective with a Ge detector, we must cool it to a temperature of 235K (-28°C). According to the Judson specifications, this increases the D* from 0.8×10^{11} to 4×10^{11}cmHz$^{1/2}$W^{-1}, so that the photodiode dark current (at zero bias) is reduced to

$$I_d = \frac{171nA}{(4/0.8)^2} = 6.84nA,$$

where the dark current of 171nA corresponds to a D* of 0.8×10^{11}cmHz$^{1/2}$W^{-2}. This reduces I to 11.5nA and i_n to 7.31×10^{-12}A. The resultant signal-to-noise ratio is

$$\frac{S}{N} = \frac{2.10 \times 10^{-10}}{7.31 \times 10^{-13}} = 28.7:1.$$

This result neglects the fact that the spectral response shifts to shorter wavelengths when the photodiode is cooled, so that it may not be possible to maintain a quantum efficiency of 0.70 at 1.6 μm.

4.3.3.3   Detector Choice

There are at least three reasons for using an InGaAs photodiode detector rather than a Ge detector in Channel 3A:

a) The minimum signal-to-noise objective can be met without cooling the detector.

b) The signal-to-noise ratio with an uncooled InGaAs detector is greater than that with a cooled Ge detector.

c) The spectral response can be varied by varying the alloy composition.

The optimum choice of alloy composition is arrived at by ensuring that the center wavelength corresponds to the peak of the spectral response at the lowest operational temperature. On this basis, a InGaAs photodiode containing 57% In appears to be near optimum for our application.

4.3.4   InGaAs Detector Sources

Several InGaAs manufacturers were contacted and the preliminary AVHRR/3 InGaAs specification was sent to them for review. The vendors contacted were:

E-O Systems Specialists, Inc., Malvern, PA
PlessCor Optromics, Inc., Chatsworth, CA
Ford Aerospace, Newport Beach, CA
Epitaxx, Inc., Princeton, NJ
Optoelectronics, Inc., Petaluma, CA
Texas Optoelectronics, Inc., Garland, TX
RCA, Lancaster, PA

Of these only Epitaxx expressed an interest in working on a low quantity, high reliability device for spaceflight use. Other vendors either were not interested due to the specifications or because of the low quantity required.

The primary commercial application for these devices is in the optical communications industry. When coupled to fiber optic systems, these devices offer stable, reliable performance with the highest sensitivity available for this spectral region without cooling.

Epitaxx is unique in this field in that it uses the vapor phase epitaxy (VPE) method of crystal growth. Using this technique thin films of semiconductor materials are deposited from gases (as opposed to Liquid Phase Epitaxy or LPE).

4.3.4.1   Visit to Epitaxx

R. Harber (design physicist) and Ed Erginsoy (components engineer) visited Epitaxx, Inc. during September 1985. Purpose of the visit was to review the procurement specification generated by ITT for a channel 3A detector and to learn about the processes they use to fabricate the InGaAs detectors proposed for the new Channel 3A.

Epitaxx manufacturers InGaAs detectors for a variety of commercial uses. They have no space flight history since the detector material (and the company itself) is relatively new. They have reviewed the preliminary specs for an AVHRR detector and agreed that they could meet all requirements except an NEP specification (because they do not normally measure this parameter).

They claim that their dynamic impedance measurement shows that the detectors have low noise; but, they will not accept (at this time) a corresponding NEP specification where

$$NEP = \frac{1}{R} \left(\frac{4kT\Delta f}{R_d}\right)^{1/2}$$

where R = responsivity of the detector in amps watt^{-1}

k = Boltzmann constant

T = temperature in Kelvin

Δf = electrical bandwidth = 1.0 Hz

R_d = dynamic impedance.

(ITT is asking for $R_d = 15 \times 10^6$ ohms and NEP = 3.7×10^{-14} watt Hz$^{1/2}$; they would like to lower the R_d spec to 5 M ohms and NEP to 5 $\times 10^{-13}$.) We were unable to resolve this issue although Greg Olsen (president) said he felt that the NEP should be measured with an identical preamp that we plan to use in the AVHRR.

104

They showed the equipment used to fabricate the InGaAs detectors and explained the process, and distributed copies of fabrication flowcharts and Q.A. specifications for review and comments. Their evaluation process and testing procedures were shown and explained.

They took exception to the spectral response requirement given in the specification which states that the peak response be at 1.75 ± 0.05μm. Although this could be done by modifying the alloy composition, it would cause many problems; they prefer that we specify an allowable variation (e.g. ±10%) in the responsivity within our spectral band (1.58 to 1.64 μm). If we really need the longer wavelength response they could supply us with a separate cost estimate to do so.

They have no objections to running any of the screening tests proposed in the specification. They did point out that they do not normally perform such tests since their prime market is commercial. They are constantly improving their test equipment and facilities and expect to be able to perform most of our required electrical tests on their premises. The InGaAs crystals are grown in-house. All processing is done in-house as are the majority of standard tests.

The company is essentially where other detector vendors (SDC and IR Associates for example) were when ITT started dealing with them. Some effort will be required to upgrade their systems to provide flight worthy detectors.

4.3.4.2   Detector Tests

As part of the evaluation of this new detector material, ITT has purchased several samples including a standard 0.3 mm diameter detector for noise and spectral response tests. These initial tests were run in ambient at room temperature. Figure 4.3-1 shows the measured spectral response of this detector. This curve basically confirms the "standard" InGaAs response.

Figure 4.3-2 shows the ITT measured spectral response of another Epitaxx device also received for evaluation (on a loan basis).

Note that the cutoff is very sharp below 1.0 micron. Epitaxx also sells an InGaAs detector with better shortwave response. It is this detector that would be used in the wideband HIRS/3 channel 20 if implemented.

The noise voltage from a 300 μm diameter Indium-Gallium-Arsenide photodiode (SN1456) made by Epitaxx Inc. was measured and the corresponding D* was calculated (ITT plans to use a 250 μm by 250 μm detector in channel 3A of AVHRR/3 so the sensitive area of the tested detector is close to what is needed). A transimpedance amplifier using an OP15 operational amplifier with 15 megohm feedback resistor (precision film carbon resistor made by Caddock Electronics Co.) was used to amplify the photodiode noise voltage which was then measured with an HP Spectrum Analyzer (Model 3580A). No bias voltage was applied to the photodiode, however the pre-amplifier may have produced

Figure 4.3-1 MEASURED SPECTRAL RESPONSE EPITAXX InGaAs DETECTOR, SN1456
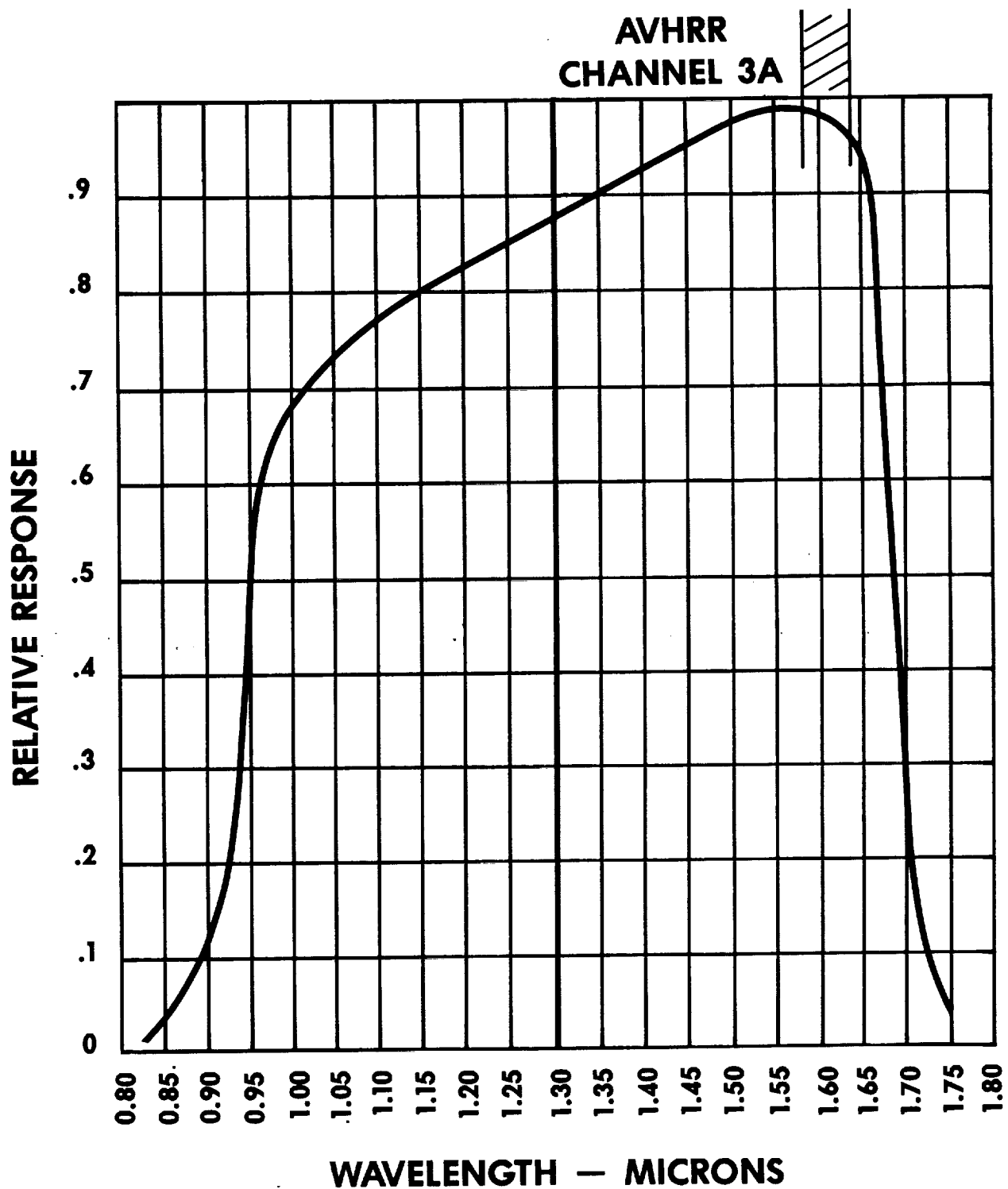
MEASURED InGaAs SPECTRAL RESPONSE (EPITAXX 0.3 mm DIA. STANDARD RESPONSE)

RELATIVE RESPONSE

WAVELENGTH-MICRONS
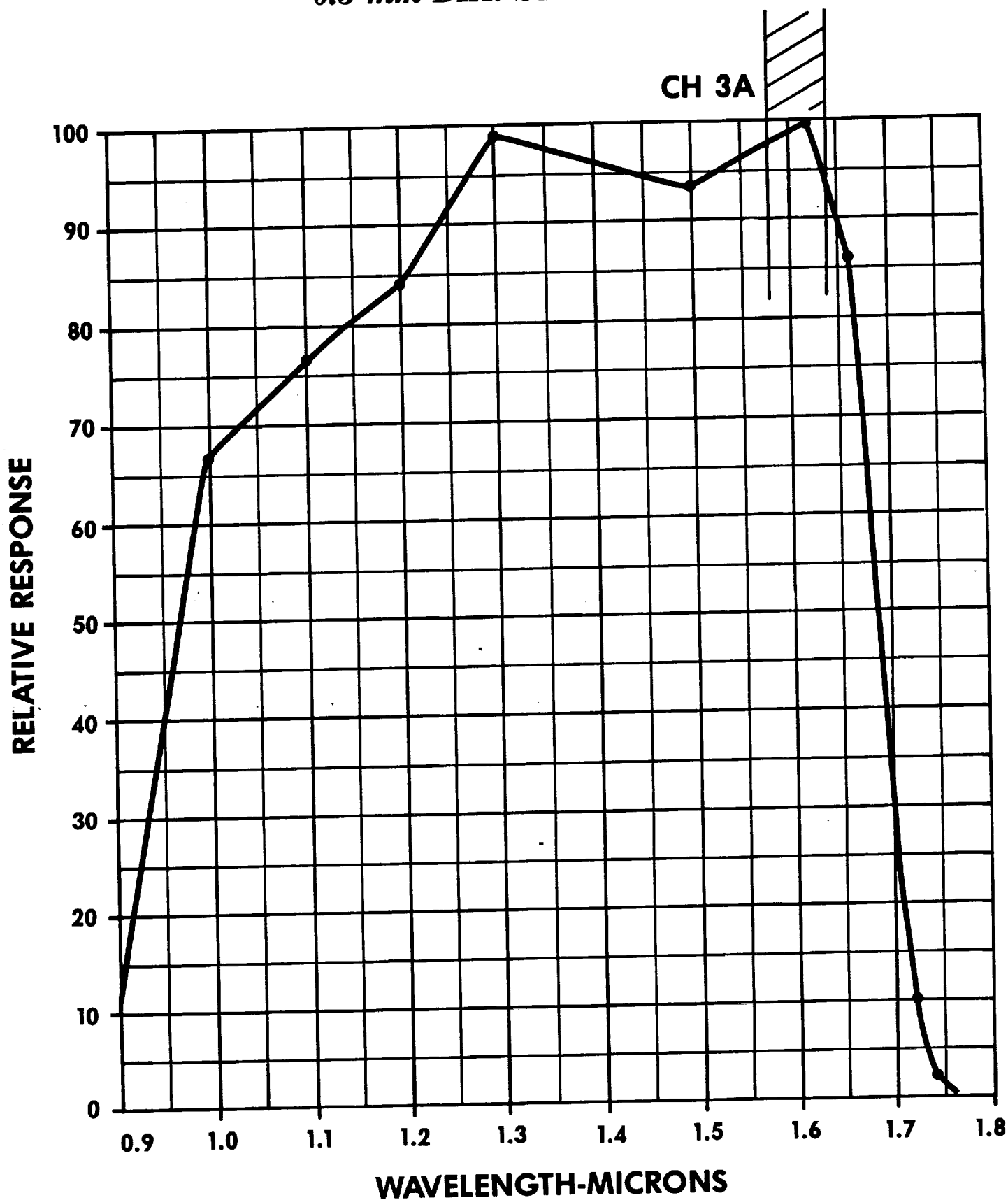
AEROSPACE/OPTICAL DIVISION **ITT**

a small offset voltage. The measured noise voltage (per $Hz^{1/2}$) was converted into an equivalent noise current at the preamp input by dividing by the feedback resistance. With the photodiode disconnected from the preamp the measured noise current was equal to the calculated Johnson noise current from the feedback resistance which verified that the noise contributed by the OP15 was negligible. The InGaAs photodiode was then connected to the preamp and the total output noise remeasured; the detector noise current (i_d) was then calculated using the equation

$$i_d = \sqrt{(i_{d+f}^{\;2} - i_f^{\;2})}$$

where I_{d+f} = noise current from detector + feedback resistor

i_f = noise current from feedback resistor only.

The detector noise current was determined to be 1.75 x 10^{-14} ampere $Hz^{1/2}$ and was constant from about 25 Hz to 2,000 Hz. The detector NEP (noise equivalent power) is given by

$$NEP = \frac{i_d}{R}$$

where R = responsivity (ampere/watt); we assumed a value of 0.90 for a wavelength of 1.6μm. This gave NEP = 1.94 x 10^{-14} watt $Hz^{1/2}$. The D* is calculated from the equation

$$D* = \frac{\sqrt{A_d \cdot \Delta f}}{NEP}$$

where A_d = detector sensitive area = $\frac{\pi}{4}$ (0.03 cm)^2

Δf = electrical bandwidth = 1.0 Hz.

This gives D* = 1.37 x 10^{12} cm $Hz^{1/2}$ watt^{-1}.

For the signal-to-noise calculations for channel 3A ITT assumed a detector D* of 6.8 x 10^{11}; therefore, the Epitaxx detector appears to be about twice as good as needed to produce a S/N ratio of 34:1 for 0.5% albedo scene.

If we calculate the photodiode dynamic impedance from the measured noise current using the Johnson noise equation given previously we obtain 53.5 megohms. Unfortunately, Epitaxx did not measure this parameter for this detector but they have stated that measurements on many of their other 300μm diameter detectors range from 40 to 50 megohms.

Since the dynamic impedance of the photodiode is significantly greater than the feedback resistance in the preamp there was

only a small increase in output noise when the photodiode was connected to the preamp. The accuracy in determining the noise current from the photodiode was therefore not very good.

Finally, a wideband noise measurement was made between 5 Hz and 1600 Hz (3 dB frequencies) using an Ithaco Variable Electronic Filter and a Ballantine RMS Voltmeter (the same preamp was used). The measured result was basically the same as determined by using the Spectrum Analyzer.

The linearity (responsivity versus signal level) was measured on a sample InGaAs detector obtained from Epitaxx, Inc. This was compared to the responsivity curve provided by Epitaxx as typical for these devices.

Figure 4.3-3 shows the Epitaxx-measured response for one of their detectors. It shows excellent linearity. Curve A is the measured response. It includes a preamp limited non-linearity at the lower end of the curve. When the preamp effect is taken out the curve becomes very close to B, the perfect linearity curve. The expected signal level in AVHRR/3 channel 3A is from -40 dBm to about -65 dBm.

Figure 4.3-4 is the measured response for SN1456 detector. The measured range of input signals ran above and below the expected channel 3A range and covered 3 orders of magnitude. The measured points are accurate to about 0.1% in terms of input signal and output current levels. The ITT measurement was made with an input wavelength of 1.6 microns.

Epitaxx claims excellent response linearity for their devices and states that their InGaAs is being considered for use as a near-IR "standard detector."

Tests were also performed on this detector and on an RCA device to determine change in response versus temperature. The detectors were placed in a dry nitrogen environment (to prevent condensation) and illuminated with the AVHRR test monochromator while the detector temperature was varied.

Figure 4.3-5 is the measured response of the Epitaxx detector at 21.4°C and 0°C. Very little difference is seen except for a change in the longwave cutoff response. Additional tests were performed measuring the response changes in the proposed channel 3A spectral region. These were run at 10°C increments from -10 to +40°C. These are shown in Figure 4.3-6. From -10 to +40°C the response change at the longwave side of the channel 3A is somewhat less than 20%. In the test range of the AVHRR (+10°C to +20°C) the longwave response change is about 3%. On an integrated total response basis the overall response change is much less than 1%.

Figure 4.3.5 LINEARITY TEST DATA OF THE EPITAXX

InGaAs DETECTOR

EPITAXX

InGaAs LINEARITY

DATE: 10/23/85
SERIAL #: EPITAXX
WAVELENGTH: 1295 nm
RESPONSE: .63

1 mW

A

B

DETECTOR POWER [dBm]

20
10
1 mW 0
−10
−20
−30
−40
−50
−60
−70

ATTENUATION [dB]

10
0
−10
−20
−30
−40
−50
−60
−70
−80

AEROSPACE/OPTICAL DIVISION

ITT

110
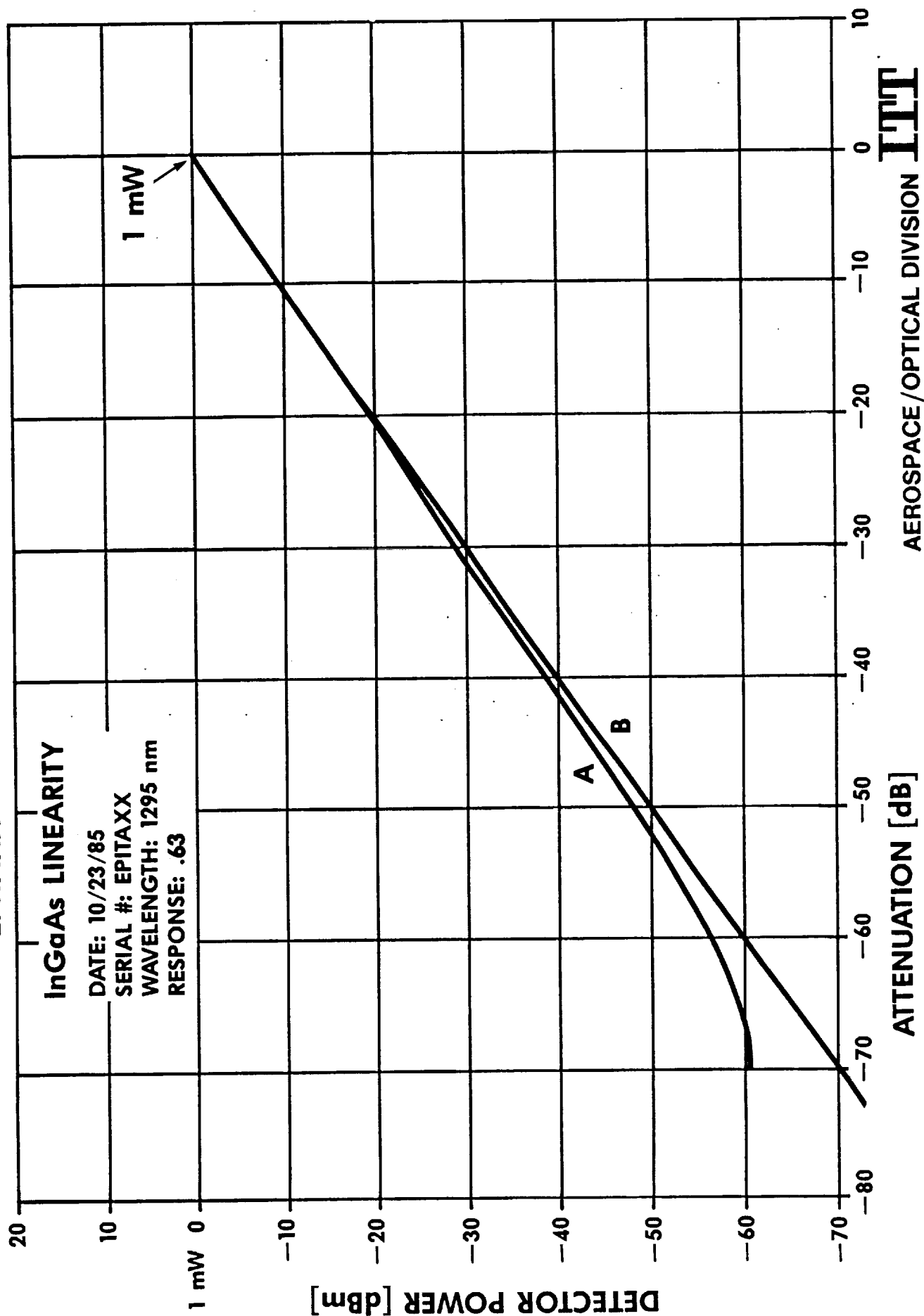
Figure 4.3-4 ITT MEASURED InGaAs DETECTOR RESPONSE LINEARITY

AEROSPACE/OPTICAL DIVISION ITT

111
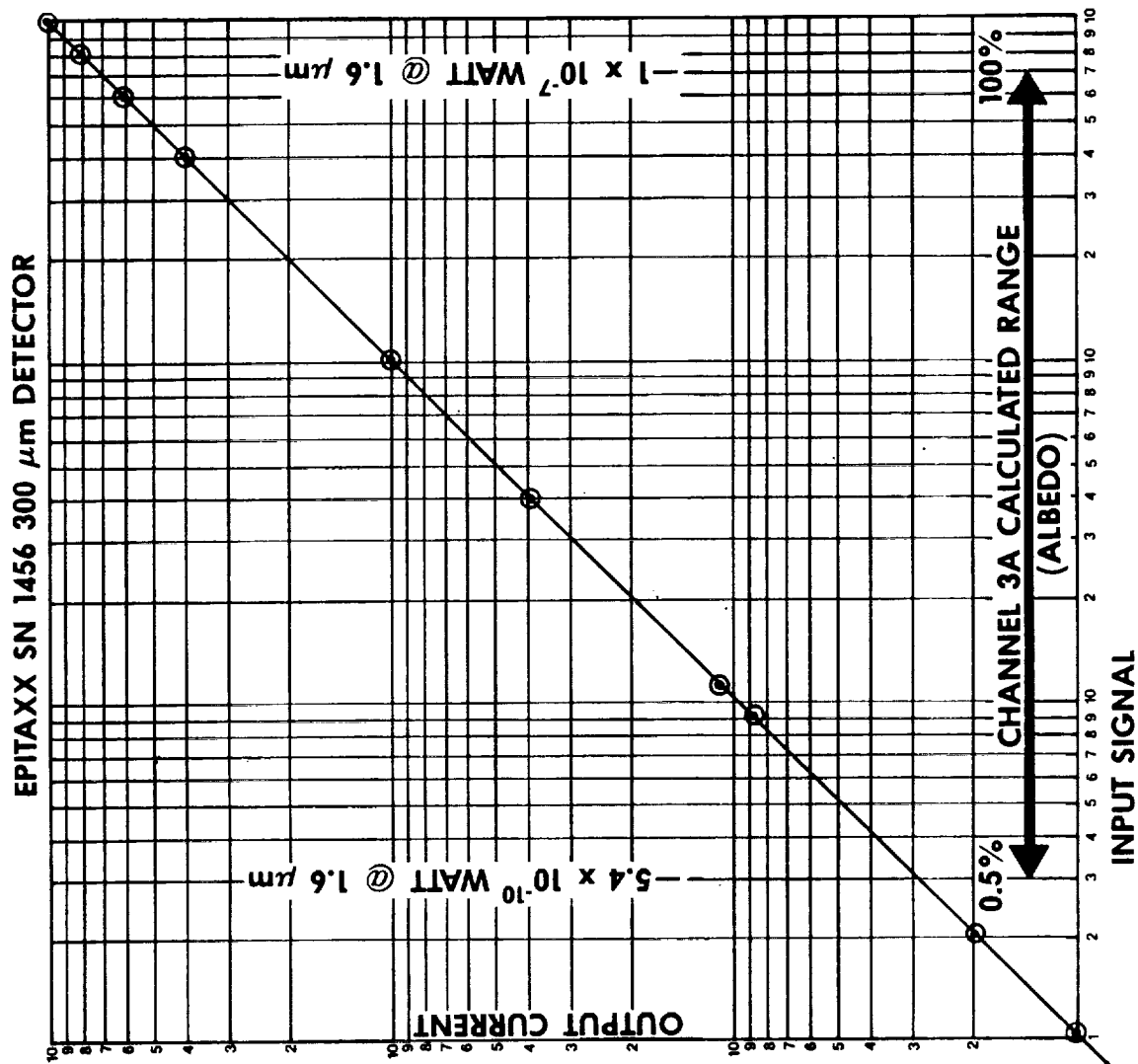
Figure 4.3-5   InGaAs SPECTRAL RESPONSE VERSUS TEMPERATURE (TOTAL RESPONSE)

112
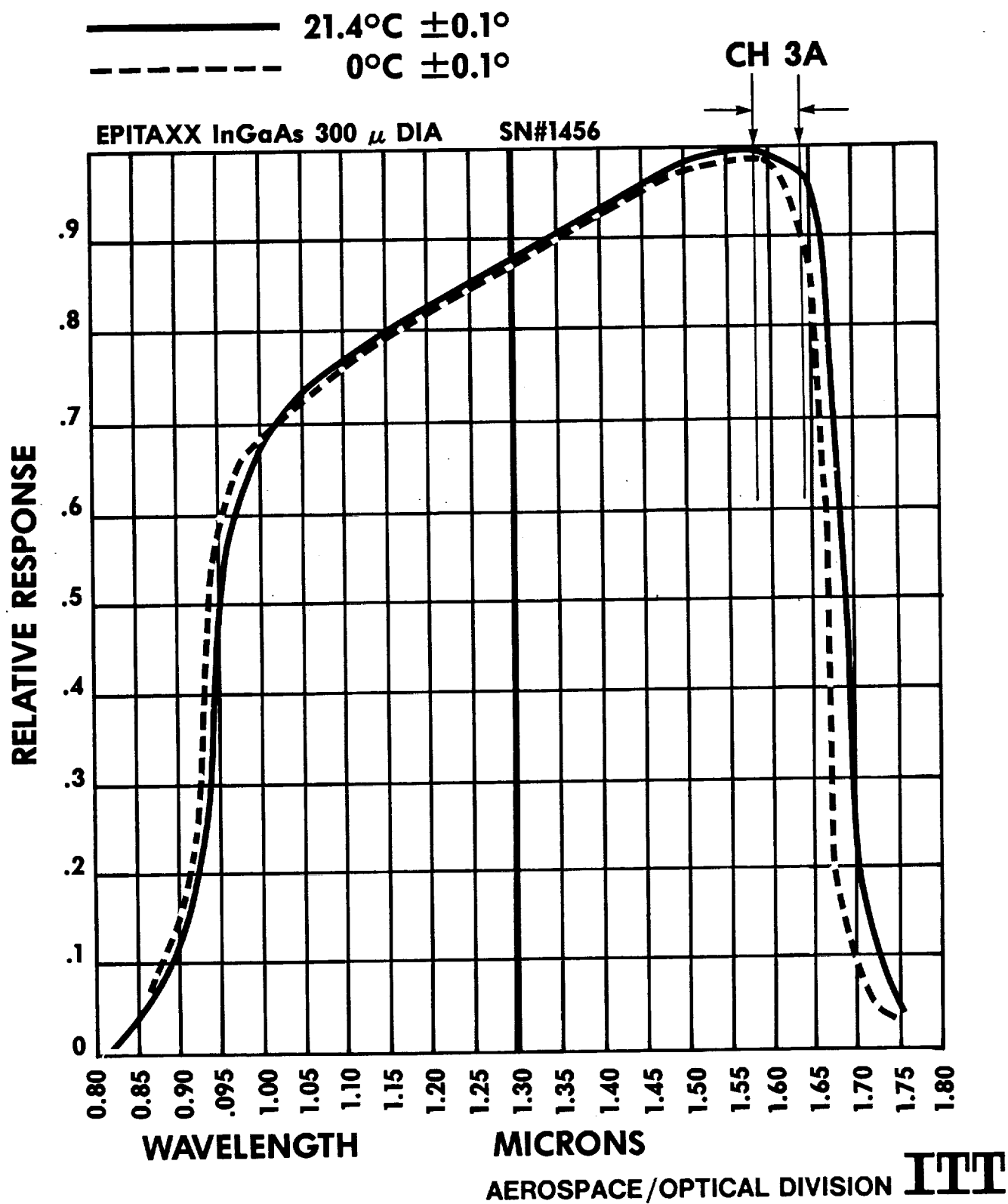
Figure 4.3-7 presents the results of similar tests on an RCA InGaAs photodiode. Interestingly, this device has a longwave cutoff far enough beyond channel 3A that temperature does not affect the realtive response. However, the absolute response changes significantly. If this detector is typical of RCA fabricated InGaAs, some sort of temperature control may be needed to keep a constant response over the AVHRR baseplate operating range (about $\pm 1°C$).

Figure 4.3-8 is the typical uniformity of response of the Epitaxx InGaAs. This figure was provided by Epitaxx. The active area of this device was larger than that to be used for AVHRR/3 channel 3A; however, Epitaxx feels that this data reflects that expected for an AVHRR detector.

4.3.4.3   Detector Selection Summary

ITT believes that the Epitaxx InGaAs photodiode is the detector of choice for the new channel 3A. The vendor is a relatively new one and effort must be expended to upgrade the product to flight quality.

Table 4.3-1 gives the present state of the D* question. A D* of 4.0×10^{11} is needed to meet the NASA S/N goal of 20:1 at 0.5% albedo. ITT requested 6.8×10^{11} in our specification; Epitaxx delivered (according to ITT test data) 1.37×10^{12} but guarantees only 5.3×10^{10}.

Most of the Epitaxx reticence is due to their inexperience with the performance of high reliability devices. They have considerable InGaAs experience but only for commercial products.

ITT expects to work with Epitaxx to allow both them and ITT to gain confidence in their product. ITT has worked with detector vendors in the past to upgrade their processes and quality to spaceflight standards.

Other vendors will again be contacted to verify their interest (or lack) at the time detectors will be purchased. It is conceivable that changes in business climate and technology will make another vendor the preferred source.

A copy of the preliminary specification for the InGaAs photodiode is given in Appendix D.

Figure 4.3-7 EXPANDED TEMPERATURE RESPONSE OF RCA InGaAs DETECTOR

CHANNEL 3A

RELATIVE RESPONSE

−10°C
±0°
+10°
+20°
+30°
+40°C

−10
0
+10
+20
+30
+40

WAVELENGTH MICRONS

AEROSPACE/OPTICAL DIVISION ITT

115
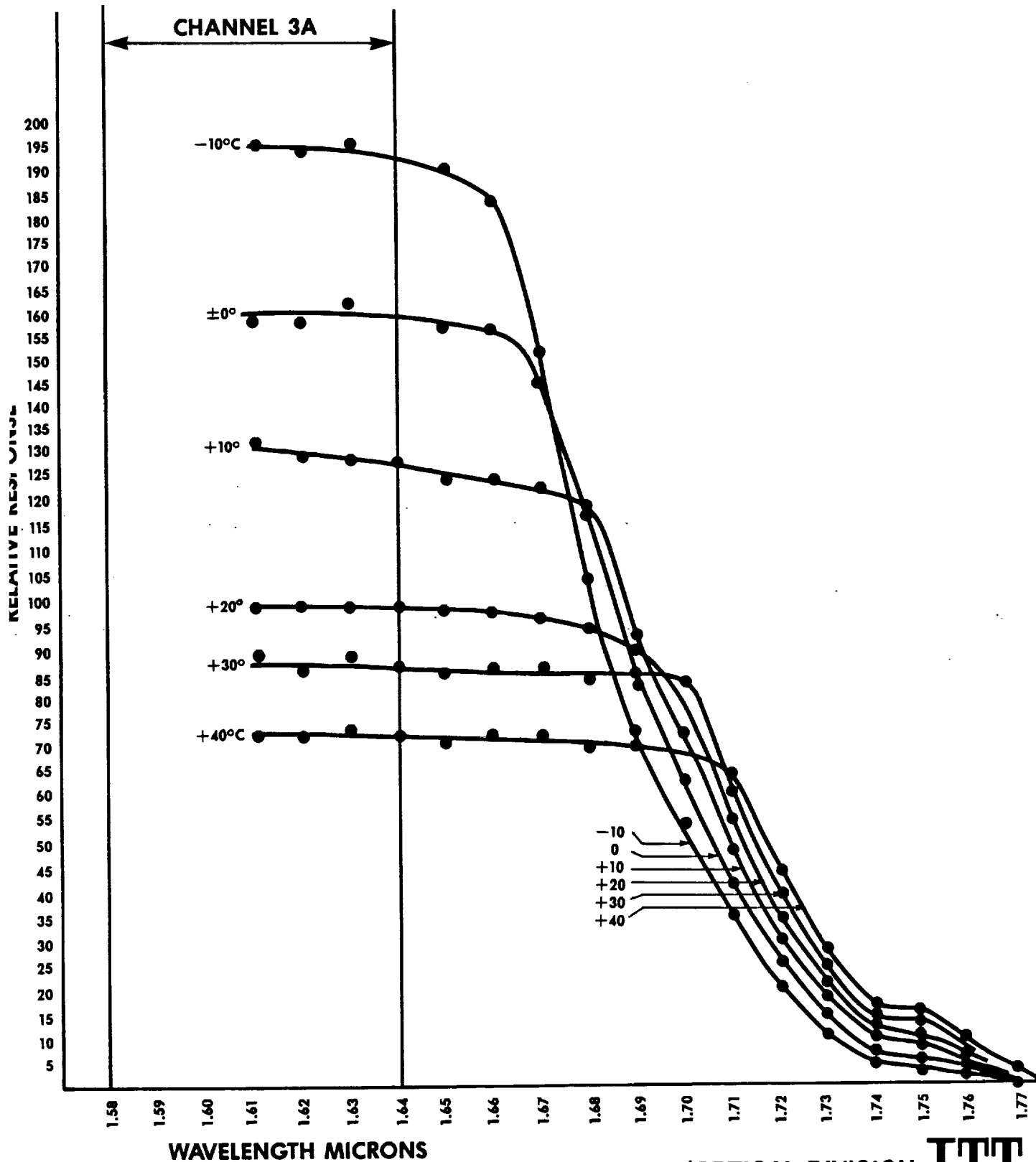
Figure 4.3-8   UNIFORMITY OF RESPONSE OF EPITAXX InGaAs DETECTOR

DETECTOR SURFACE SCAN

WAVELENGTH: 1300 nm
FILE   : INGA11
CHIP TEMP : 25 C
POWER   : 200.0 uW

AEROSPACE/OPTICAL DIVISION ITT
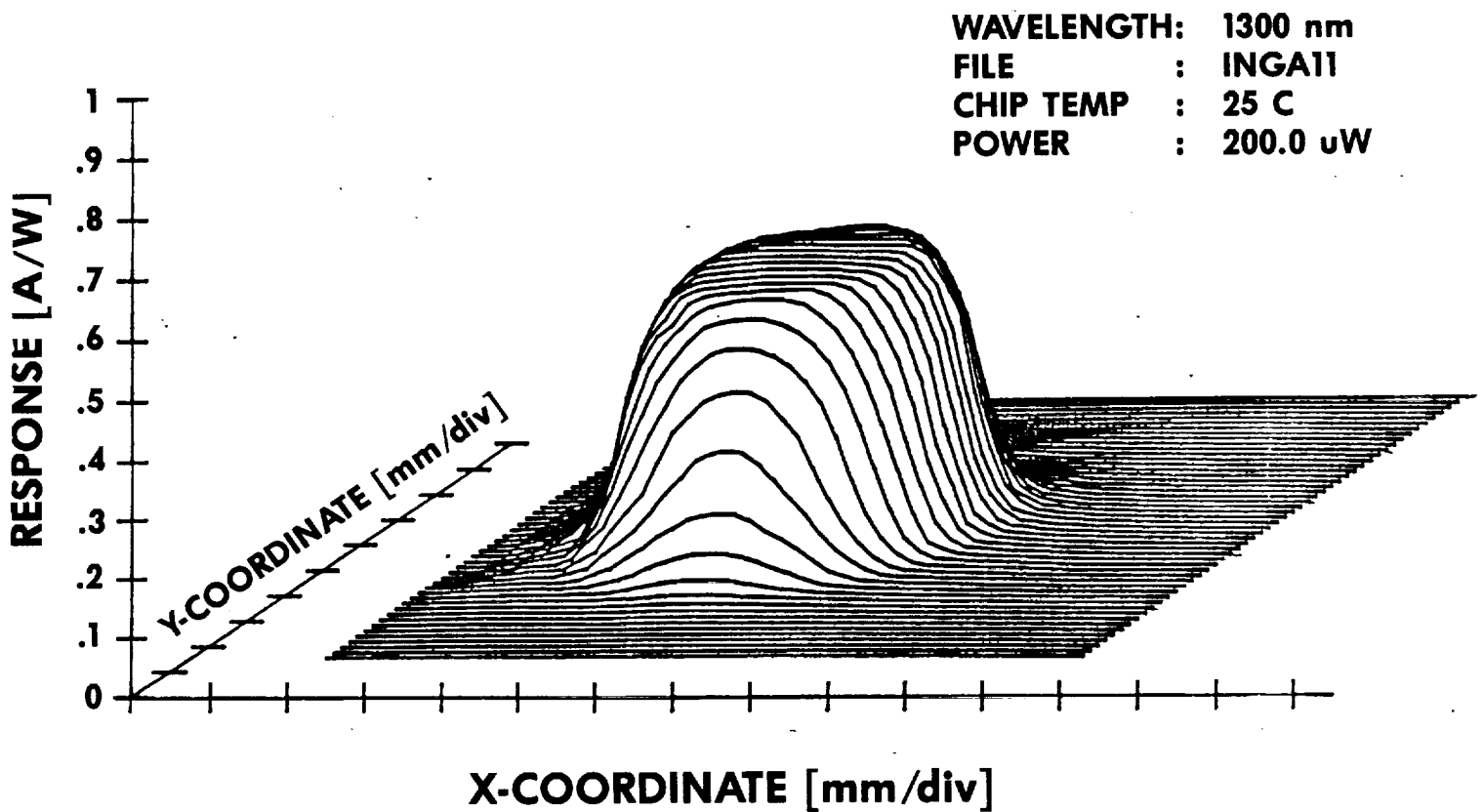
Table 4.3-1. InGaAs Sensitivity

	$\dfrac{D^* \ (\text{CmHz}^{1/2})}{\text{Watt}}$	S/N
ITT Spec to Vendor	6.8×10^{11}	34:1
NASA Spec Requires	4.0×10^{11}	20:1
ITT Test Results	1.37×10^{12}	68:1
Vendor Guarantees	5.3×10^{10}	3:1

4.3.5   Mechanical Implementation

As stated previously, the addition of channel 3A to the AVHRR/2 was achieved while limiting direct mechanical changes to the relay optic housing, the electronic box and the baseplate. No changes were made to the telescope, radiant cooler or scanner.

The new relay optic housing is shown conceptually in Figure 4.3-9. It is identical in concept with the existing housing except that there are three uncooled channels rather than two. The optical and mechanical details for the three IR channels has not changed. The interface to the radiant cooler is also unchanged.

The relay optic housing is mounted to the telescope primary mirror cell using the same three point mounting approach as AVHRR/2. The support structure was strengthened somewhat to accommodate the heavier housing. A detailed weight analysis was performed to determine the weight of the new relay optic assembly. This estimate is given in Table 4.3-2. It includes all optical elements, mounting sleeves, shims, etc. The new relay optic assembly weighs about 1 pound (15%) more than the AVHRR/2 assembly.

Table 4.3-2. AVHRR/3 Relay Optic Assembly Weight Estimate

Relay Optics Housing		3 lbs
Glass Elements		
Beam Splitters & Folding Mirrors		9.4 oz
Channel 1 glass		5.3 oz
Channel 2 glass		5.9 oz
Channel 3A glass		4.6 oz
Channel 3 & 5 Glass & housing		5 oz
Channel 4 Glass & housing		5 oz
Channel 1, 2 & 3A housing		12 oz
Support Brackets		14 oz
	6 lbs	13 oz
10% Misc.		11 oz
	7 lbs	8 oz

AVHRR/2 Relay Optics Assembly 6 lbs 8 oz

Figure 4.3-9 *AVHRR/3 RELAY OPTIC ILLUSTRATION*

OPTIC AXIS

CH 2

CH 1

CH 3A

CH 4&5

CH 3B

AEROSPACE/OPTICAL DIVISION **ITT**
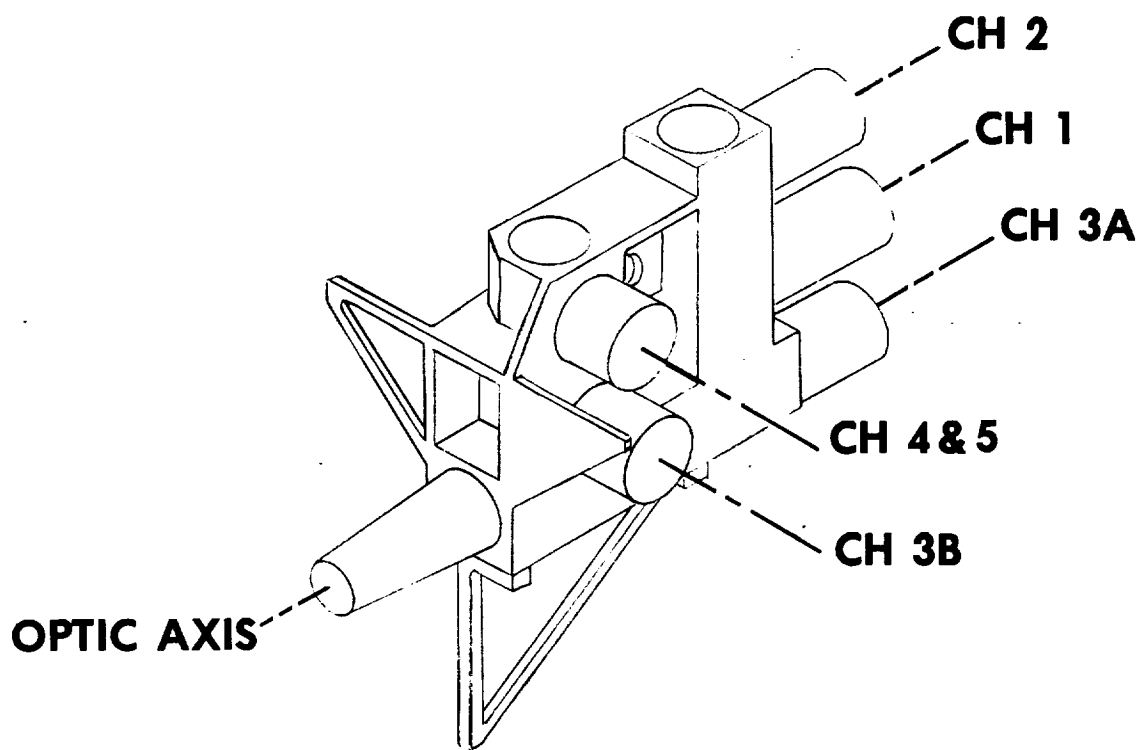
4.3.5.1 Structural Analysis

Figure 4.3-10 is a side view cutaway layout of the AVHRR/3 relay optic assembly. The telescope mounting plane is on the left and the three detector mounting assemblies are on the right.

The primary function of the relay optics is to divide the total incoming focused energy into various discrete wavelengths and focus these filtered wavelengths onto the detectors. As a structure, the relay optics must hold the various optical elements properly aligned during vibration. If the structure is to deform during vibration, it must not permanently affect optical alignment and registration. The relay assembly in its most general representation can be modeled as a cantilevered beam simply supported at one end. Thus, the structure must be extremely lightweight, yet rigid to support the various optical elements and itself.

A finite element model utilizing the computer software code NASTRAN was used to analyze the replay optics design. The intent of using computer analysis was to determine the resonance frequencies at which the structure and/or various parts of the structure would stress in worst case conditions. The computer analysis generates deformed structural mode shapes for each resonance. The deformed shape can be either beam modes, rigid body modes or bending/torsional modes. The beam mode is self explanatory in that the beams in the structure deform. Rigid body mode is a shift in the entire structure. The bending/torsional mode is the complex distortion of the structure. It is in this mode that the worst case stresses and strains are developed.

Table 4.3-3 is the vibration input levels which are placed on the AVHRR instrument during system test. For the relay optics assembly, it is desirable for the modes of deformation not to occur between 5 - 2000 Hz. If a mode does occur in this range, it should occur where the g's level is lowest. Table 4.3-4 lists the computer generated output of the modal frequencies of the relay optics assembly model.

Figure 4.3-10 illustrates the basic structural shape of the new relay optics assembly. The housing is square with cylindrical bores for the optical paths. In analysis using NASTRAN, the structure was modeled as a box using .200 thick plates. The determination of the plate thickness was to match the area moment of inertia of the model to the designed assembly. The tripod mounting frame which mounts the relay optics to the primary mirror cell is comprised of beams and a plate.

The analysis consists of extracting the resonant frequencies of the structure by first calculating the structural stiffness,

Figure 4.3-10 SIDE VIEW AVHRR/3 RELAY OPTICS

AEROSPACE/OPTICAL DIVISION ITT
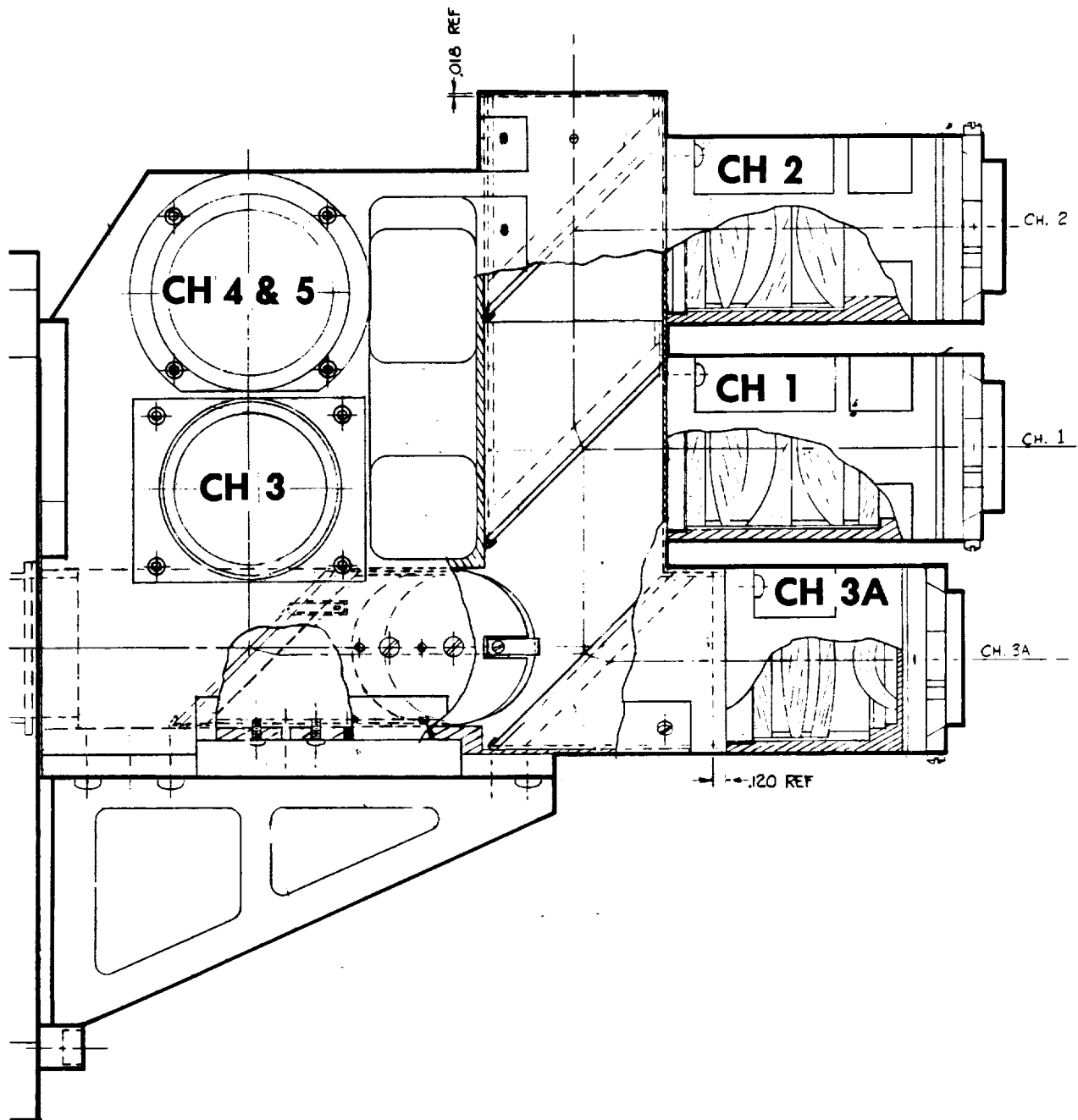
mass, and associated eigenvectors. The eigen value is a scalar frequency value at which the resonant deformation occurs. The eigenvector is the matrix vector which defines the structural mode shape. Table 4.3-4 lists the modal resonant frequencies of the relay optics. Three computer analyses were made of the model. The second two incorporate modifications done to change the output frequencies. Figure 4.3-11 is the graphical output of the first computer analysis at 74 Hz. The first two modes are a combination of rigid body and beam deflection. The structure is shifting only due to the deflection of the tripod mounting frame beams. The third and fourth modes are torsional deformation, but at a high enough frequency where low g levels and displacements are minimal.

The second modeling iteration stiffened the mounting frame beams by doubling the the cross sectional area and doubling the cross sectional area moment of inertia. This was done to raise the first model's first resonance from 74 Hz. The 74 Hz resonance is close to the 5 g level between 60 - 70 Hz in the lateral (x) direction, and should be increased as means to induce a margin of safety into the design.

The third and final iteration again doubled the cross sectional moment of inertia of the tripod mounting beams to further increase the rigidity of the system. The first two modes again are predominately beam/rigid body modes. The third and fourth modes do have slight bending deformation. However, these modes occur at a high frequency where the g level is low yielding minimal distortion.

The conclusion drawn from this analysis is the relay optics housing is a sound mechanical design with sufficient structural stiffness and rigidity, such that the first resonant frequency mode is outside the frequency range of high g levels. The lack of torsional bending at the lower frequencies lessens the concern of stressing the optical components. As a result of this model the mounting beams used to attach the relay assembly to the primary cell will be modified. The beam on the underside of the relay housing is being replaced with a plate to improve the mounting frame's rigidity.

4.3.5.2   Relay Optic Drawings

A complete set of layout, assembly and piece part drawing were generated for the AVHRR/3 relay optic assembly. These drawings and a preliminary drawing tree for the assembly are found in Appendix E to this report.

Table 4.3-3. AVHRR Vibration Input Levels

<u>Test Levels FM's</u>

(a) <u>Sinusoidal Vibration</u>

Axis	Frequency Range (Hz)	Flight (Acceptance) Level (g's, 0-Peak)	Sweep Rate (oct./min.)
Lateral (X)	5-14	0.33" d.a.	
	14-40	3.3	
	40-60	10.0	4.0
	60-70	5.0	
	70-110	2.0	
	110-2000*	2.0	
Lateral (Y)	5-14	0.33" d.a.	
	14-60	3.3	4.0
	60-110	2.0	
	110-2000*	2.0	
Thrust (Z)	5-21	0.33" d.a.	
	21-60	7.6	4.0
	60-70	4.0	
	70-110	2.0	
	110-2000*	2.0	

(b) <u>Random Vibration</u>

Flight (all axes)

FREQUENCY RANGE (Hz)	POWER SPECTRAL DENSITY (g2/Hz)	G-RMS	DURATION MIN./AXIS
20-2000	0.020	6.3	1.0

Table 4.3-4. NASTRAN Finite Element Analysis

-1-

MODE	FREQUENCY
1	74
2	393
3	635
4	757

-2-

MODE	FREQUENCY
1	107
2	412
3	679
4	809

-3-

MODE	FREQUENCY
1	130
2	426
3	711
4	851

Figure 4.3-11 FIRST ITERATION RELAY MODEL DEFORMATION AT 74 Hz

AEROSPACE/OPTICAL DIVISION ITT
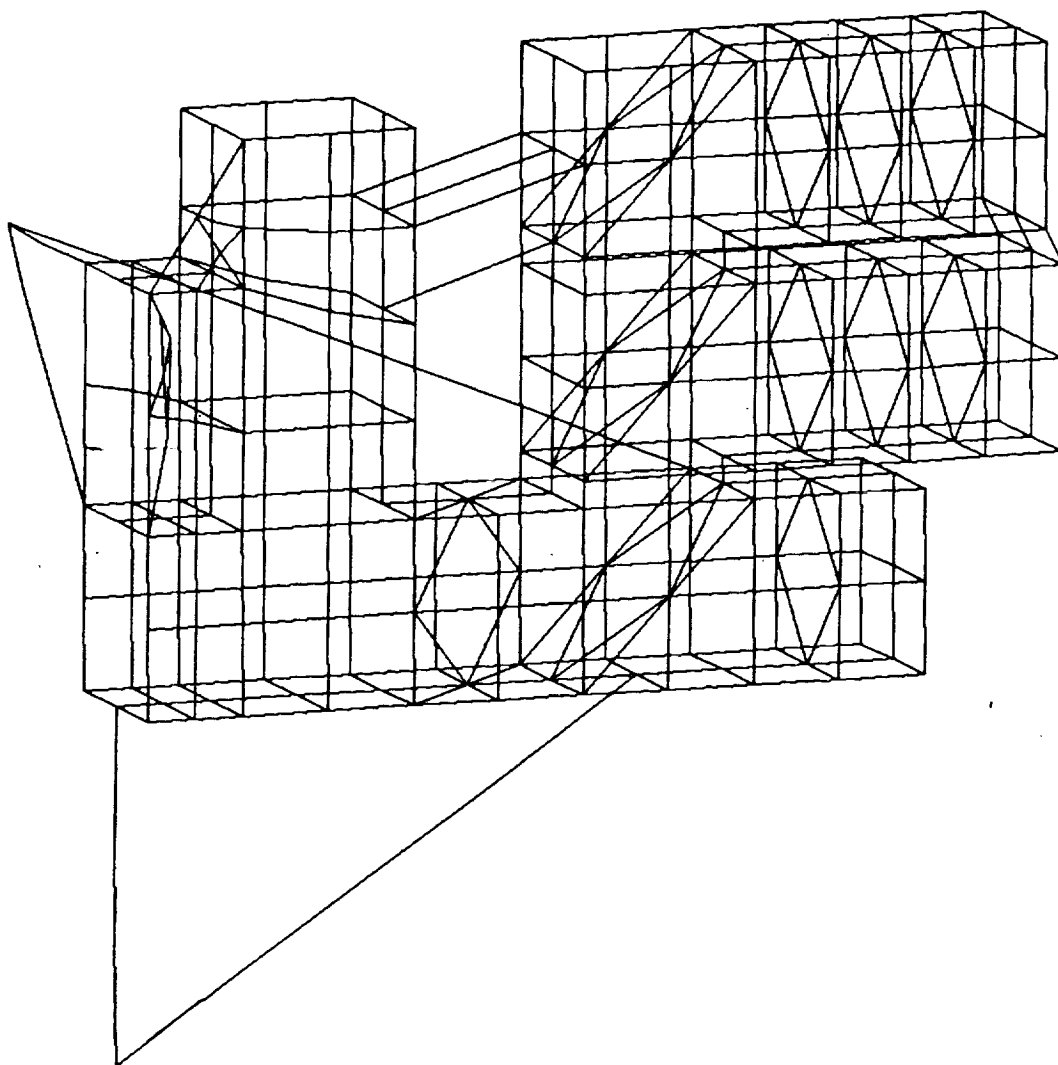
5.0   AVHRR INFRARED CALIBRATION TARGET STUDY

5.1   Requirements

          This part of the study shall address, but not be limited
to, the following topics:

          A.   Establish in-orbit performance of the NOAA-6(A),
                NOAA-7(C), and NOAA-9(F) AVHRR infrared calibration
                target.

                1. Define gradients
                2. Define orbital inputs and transients

          B.   Try to correlate target temperature gradients to solar
                input, baseplate and scan motor temperatures, and
                instrument emitting area.

          C.   Calculate radiometric effect of target gradients and
                transients.

          D.   Establish possible ways to reduce calibration target
                gradients and transients.

5.2   IR Calibration Target Uniformity

          Gradients in the target are defined and plotted as a func-
tion of sun angle in Figure 5.2-1. Attempts to correlate the thermal
model with the in-orbit data were mediocre (qualitative) at best,
apparently because of the poor performance of the AVHRR thermal control
system (TCS) on the spacecraft. The baseplate (TCS louvered radiator
under the telescope assembly and electronics box) in the AVHRR does not
act as a constant temperature (or nearly constant temperature) heat-
sink, in sharp contrast with the baseplate on the HIRS/2.

          The radiometric effects of target gradients were calcu-
lated. Target transients are not radiometrically detrimental per se,
although they may be inconvenient or annoying to the user. Possible
ways to reduce calibration target temperature gradients and transients
are described below.

5.2.1   Sensor Location Effects

          Temperature gradients in the in-flight, infrared calibra-
tion target produce radiometric errors only to the extent that they
produce an average measured temperature that is different from the
average temperature seen by the instrument. And, as shown below, this
difference is much less than the measured maximum gradient. A maximum
measured gradient of 3.0K produces a radiometric error of only about
0.2K. Moreover, the radiometric error can be reduced to a negligible
value (<0.05K) by relocating the temperature sensors on the calibration
target so that they produce a better measure of the area viewed by the
instrument.

FIGURE 5.2-1   MAXIMUM CALIBRATION TARGET TEMPERATURE GRADIENT VS. SUN ANGLE

AEROSPACE/OPTICAL DIVISION ITT

126
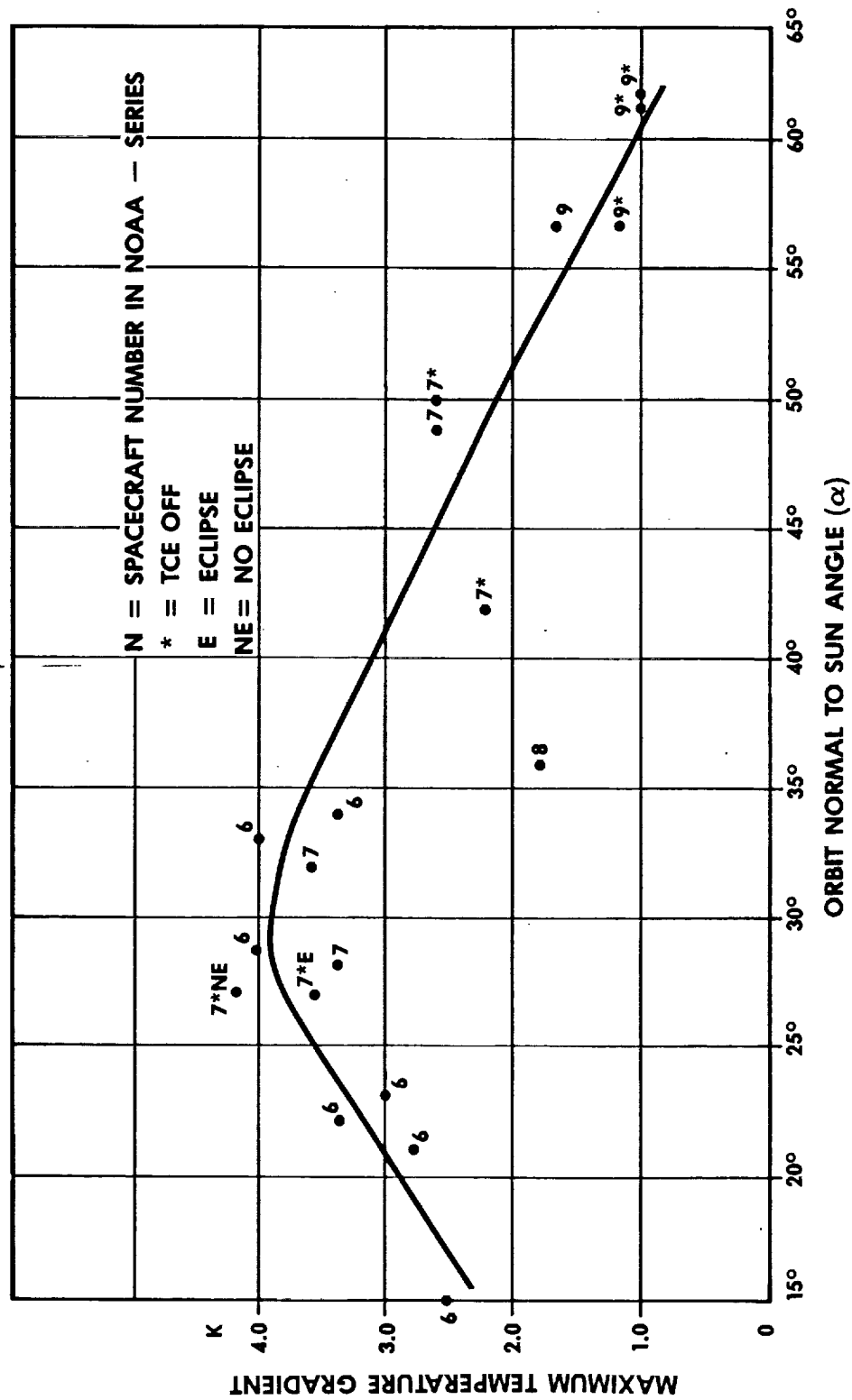
A typical worst-case, in-orbit temperature gradient is illustrated in Figure 5.2-2. Temperature differences are shown with respect to the average of the four sensors on the calibration target. The gradients are rounded to the nearest 0.1K and are assumed to be linear between the four measurement points. The area between the two concentric circles is the target area viewed by the instrument aperture (neglecting the small beamspread from the entrance pupil). The effective radiant exitance (emitted W cm^{-2}) seen by the instrument in the spectral band $\Delta\lambda$ is

$$W_e = \sum \frac{A_i}{A} W (T_i, \Delta\lambda)$$

where,

A_i/A = fraction of the viewed area at a temperature T_i, and

$W_i (T_i, \Delta\lambda)$ = blackbody exitance at a temperature T_i in the spectral band $\Delta\lambda$.

The input data for the calculation of W_e for each of the three AVHRR thermal channels (3B, 4, and 5) are shown in Table 5.2-1 for the gradient pattern in Figure 5.2-2. The radiometric error produced by use of the average temperature $\overline{T}$ of the four sensors is then

$$\Delta W = W (\overline{T}, \Delta\lambda) - W_e$$

This error can also be expressed as an equivalent temperature error ΔC. The errors for the gradient pattern of Figure 5.2-2 are listed in Table 5.2-2 for the three thermal bands. We see that the radiometric error is only a small fraction (0.13x) of the measured maximum temperature gradient.

This error can be further reduced to a very small level if the temperature sensors are relocated as shown in Figure 5.2-2. These locations are 90° apart in polar angle and positioned radially to divide the area viewed by the instrument into two equal parts. With this change, the average reading of the four sensors is increased from 290.9K to 291.05K and the radiometric error is reduced to less than 0.05K as shown in Table 5.2-3.

The conversion from radiant exitance to counts was made on the basis of the nominal count at the maximum scene temperature. For Ch. 3B, we used the values for the AVHRR/2; 6.200 mV at a maximum scene temperature of 320K, 300 mV at 0K, and 6.394 mV at 1024 counts. This yields 945 counts at 320K (1.182 877 x 10^{-4} W cm^{-2} in Ch. 3B). Because of the tolerance on the voltage settings at 320K and 0K, the count can be as high as 969. For Chs. 4 and 5, the nominal count is 998 at the maximum scene temperature of 335K (4.861 056 x 10^{-3} W cm^{-2} in Ch. 4 and 4.315 071 x 10^{-3} W cm^{-2} in Ch. 5), which corresponds to a maximum count of 1023.

FIGURE 5.2-2 MAXIMUM IR CALIBRATION TARGET GRADIENT

SENSOR #4   290K

SENSOR #3   289.4K

−1.6K

−0.8K

NOAA-6 (A)
YR   1984
DAY   255
$\gamma = 23°$

+0.8K

+1.6K

SCAN
MOTOR

SENSOR #2
292.4K
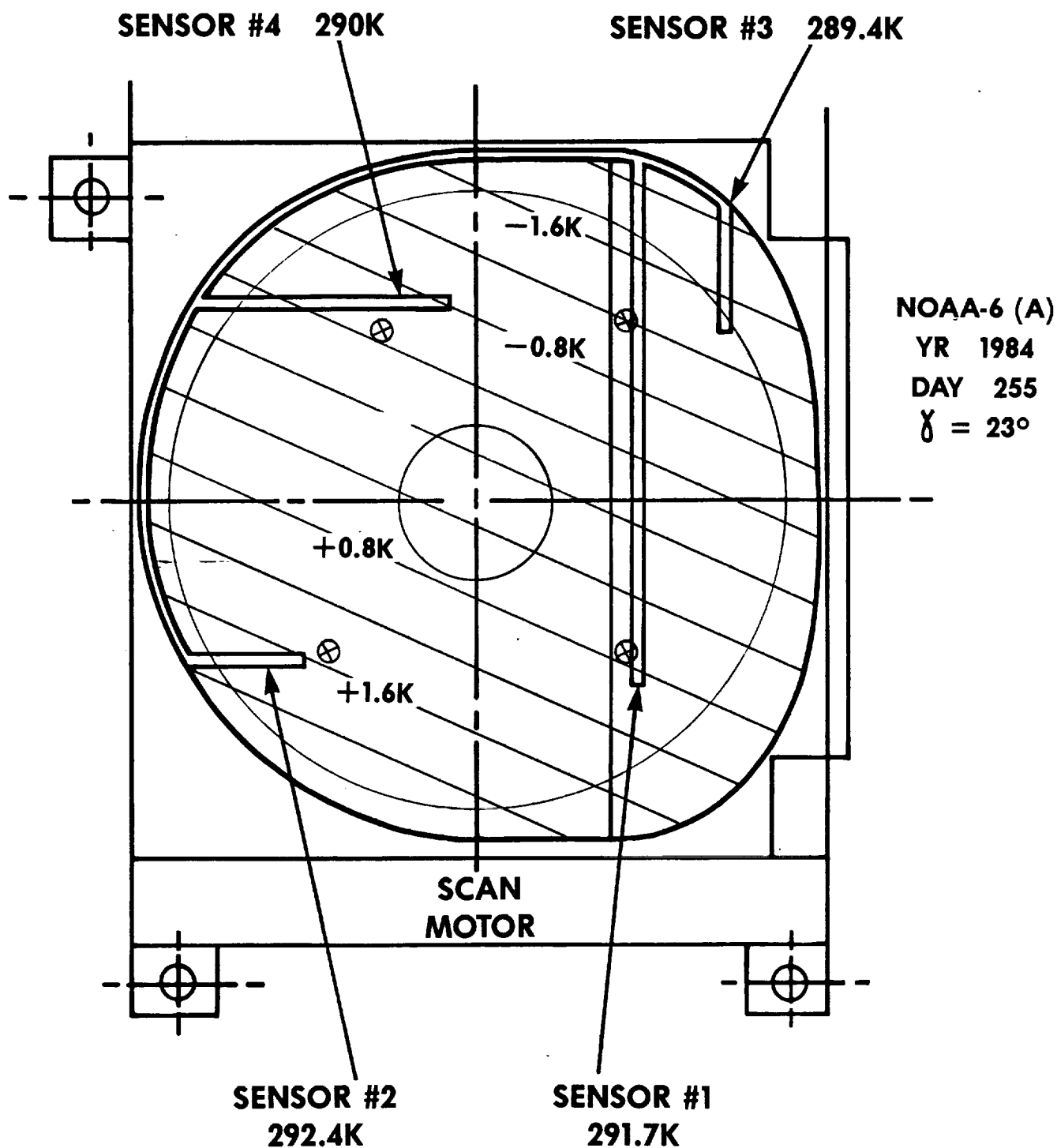
SENSOR #1
291.7K

⊗ IMPROVED SENSOR LOCATIONS

SCALE ≃1/2

AEROSPACE/OPTICAL DIVISION ITT

Table 5.2-1. Input Data for the Calculation of
Effective Target Radiant Exitance

i	T_i	A_i/A
1	289.1K	0.033
2	289.5	0.087
3	289.9	0.112
4	290.3	0.115
5	290.7	0.121
6	291.1	0.097
7	291.5	0.123
8	291.9	0.119
9	292.3	0.105
10	292.7	0.075
11	293.1	0.013

$$W\ (T_i,\ \Delta\lambda) \qquad (W\ cm^{-2})$$

i	Ch. 3B (3.55-3.93 μm)	Ch. 4 (10.3-11.3 μm)	Ch. 5 (11.5-12.5 μm)
1	$3.296\ 333 \times 10^{-5}$	$2.560\ 556 \times 10^{-3}$	$2.412\ 924 \times 10^{-3}$
2	3.357 121	2.577 093	2.427 029
3	3.418 859	2.593 692	2.441 179
4	3.481 558	2.610 353	2.455 373
5	3.545 230	2.627 075	2.469 611
6	3.609 888	2.643 860	2.483 894
7	3.675 544	2.660 706	2.498 221
8	3.742 210	2.677 614	2.512 593
9	3.809 899	2.694 585	2.527 009
10	3.878 623	2.711 617	2.541 470
11	3.948 396	2.728 711	2.555 975

Table 5.2-2. Radiometric Errors from Use of Average Target
             Temperature in Presence of 3.0K Measured
             Gradient (Figure 5.2-1)

Ch.	$\Delta W = W\,(\overline{T}) - W_e$ (W cm^{-2})	$\Delta\ \Delta T$ (K)	ΔC (Counts)
3B	-2.552×10^{-7}	-0.16	-2.0
4	-5.939×10^{-6}	-0.14	-1.2
5	-5.025×10^{-6}	-0.14	-1.2

$\overline{T} = 290.9K$

Table 5.2-3. Radiometric Errors with Temperature Sensors at
             Areal Centers of Four Quadrants (Figure 5.2-1)

Ch.	ΔW (W cm^{-2})	ΔT (K)	ΔC (Count)
3B	-1.201×10^{-8}	$-0.0074K$	-0.10
4	$+3.592 \times 10^{-7}$	$+0.0086$	$+0.07$
5	$+3.341 \times 10^{-7}$	$+0.0094$	$+0.08$

$\overline{T} = 291.05K$

130

This analysis has been extended to two additional conditions, the minimum gradient at a low sun angle and the maximum gradient at a high sun angle (low sunlight exposure). The results are shown in Figure 5.2-3 and Table 5.2-4 for the former condition and in Figure 5.2-4 and Table 5.2-5 for the latter condition. The analyses for these two conditions was limited to Channel 3B (3.55-3.93 μm).

The results for all three conditions are summarized below:

Condition	@ Present Locations	Radiometric Error in Ch. 3B for Temperature Sensors @ Areal Centers
max. ΔT, low γ	-0.16K (-2.0 ct)	-0.0074K (-0.10 Ct)
min. ΔT, low γ	-0.082 (-1.2)	+0.018 (+0.26)
max. ΔT, high γ	-0.086 (-1.0)	-0.011 (-0.13)

We see that the average of the four temperature sensors in the target is an accurate measure of the effective temperature seen by the radiometer even with the sensors located at their present positions. That is, the use of the average temperature removes most of the radiometric error introduced by temperature gradients across the target. In addition, errors from the use of these average temperatures are reduced to a negligible level by relocating the temperature sensors to produce a better measure of the area viewed by the radiometer. Finally, these conclusions hold for all the orbital conditions encountered onboard a NOAA spacecraft in either a morning (low sun angle) or afternoon (high sun angle) orbit.

5.2.2   Scan Motor and Baseplate Temperature Effects

The data in Table 5.2-6 indicate that the temperature gradient does not correlate well with the scan motor temperature, the baseplate temperature, or the temperature difference between the scan motor and baseplate. Between sun angles of 15° and 28.7°, there is little change in the scan motor and baseplate temperatures at the point where the calibration target temperature is a maximum, although there is a marked increase in the gradient itself. The scan motor temperature at the maximum gradient point is the same at sun angles of 32° and 36°, but the maximum gradient is much different. The same holds true for the baseplate temperature at sun angles of 28.7° and 57°. Finally, at one orbit point at 36° and two orbit points at 57°, the scan motor and baseplate are at the same temperature (see Figure 5.2-5) so that the target gradient is approximately perpendicular to the motor-to-baseplate line (telescope optic axis).

FIGURE 5.2-3 MINIMUM IR CALIBRATION TARGET GRADIENT AT LOW SUN ANGLE (TYP.)

MINIMUM ORBITAL GRADIENT
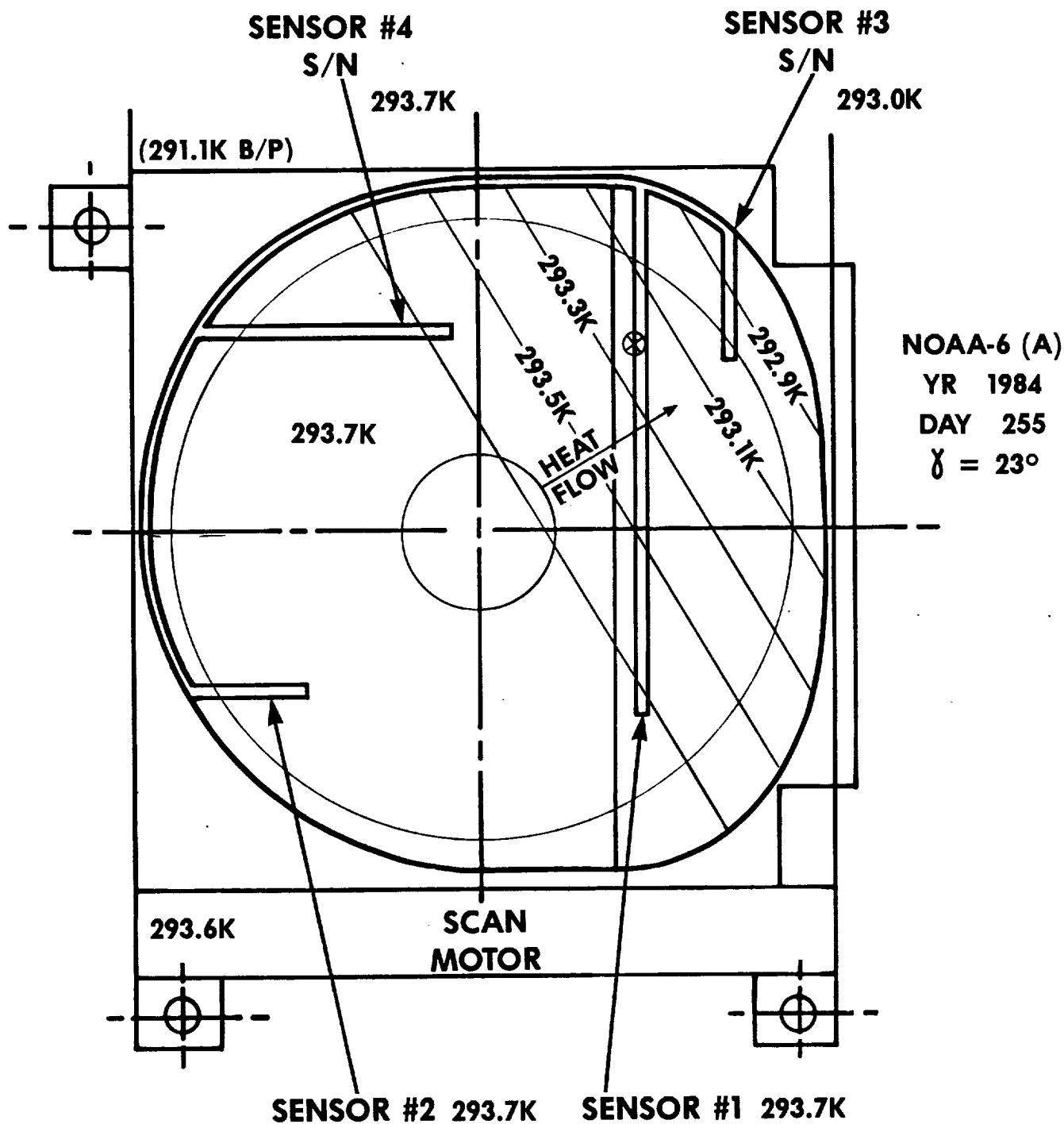
SENSOR #4
S/N
293.7K

SENSOR #3
S/N
293.0K

(291.1K B/P)

293.3K

293.5K

292.9K

293.1K

HEAT FLOW

293.7K

NOAA-6 (A)
YR 1984
DAY 255
$\gamma = 23°$

293.6K

SCAN MOTOR

SENSOR #2 293.7K   SENSOR #1 293.7K

⊗ IMPROVED SENSOR LOCATIONS

SCALE: 1/2

AEROSPACE/OPTICAL DIVISION **ITT**

132

FIGURE 5.2-4 MAXIMUM IR CALIBRATION TARGET GRADIENT AT HIGH SUN ANGLE (TYP.)

MAXIUM ORBITAL GRADIENT

SENSOR #4
S/N

SENSOR #3
S/N

288.4K

289.0K

(290.0K B/P)

+0.9K

+0.7K

+0.5K

+0.3K

HEAT FLOW

+0.1K

0K

−0.1K

−0.2K

−0.3l

−0.4K

−0.5K

−0.6K

NOAA-9 (F)
YR 1985
DAY 173
$\chi = 61.5°$

288.9K

SCAN MOTOR

SENSOR #2 288.5K

SENSOR #1 288.0K
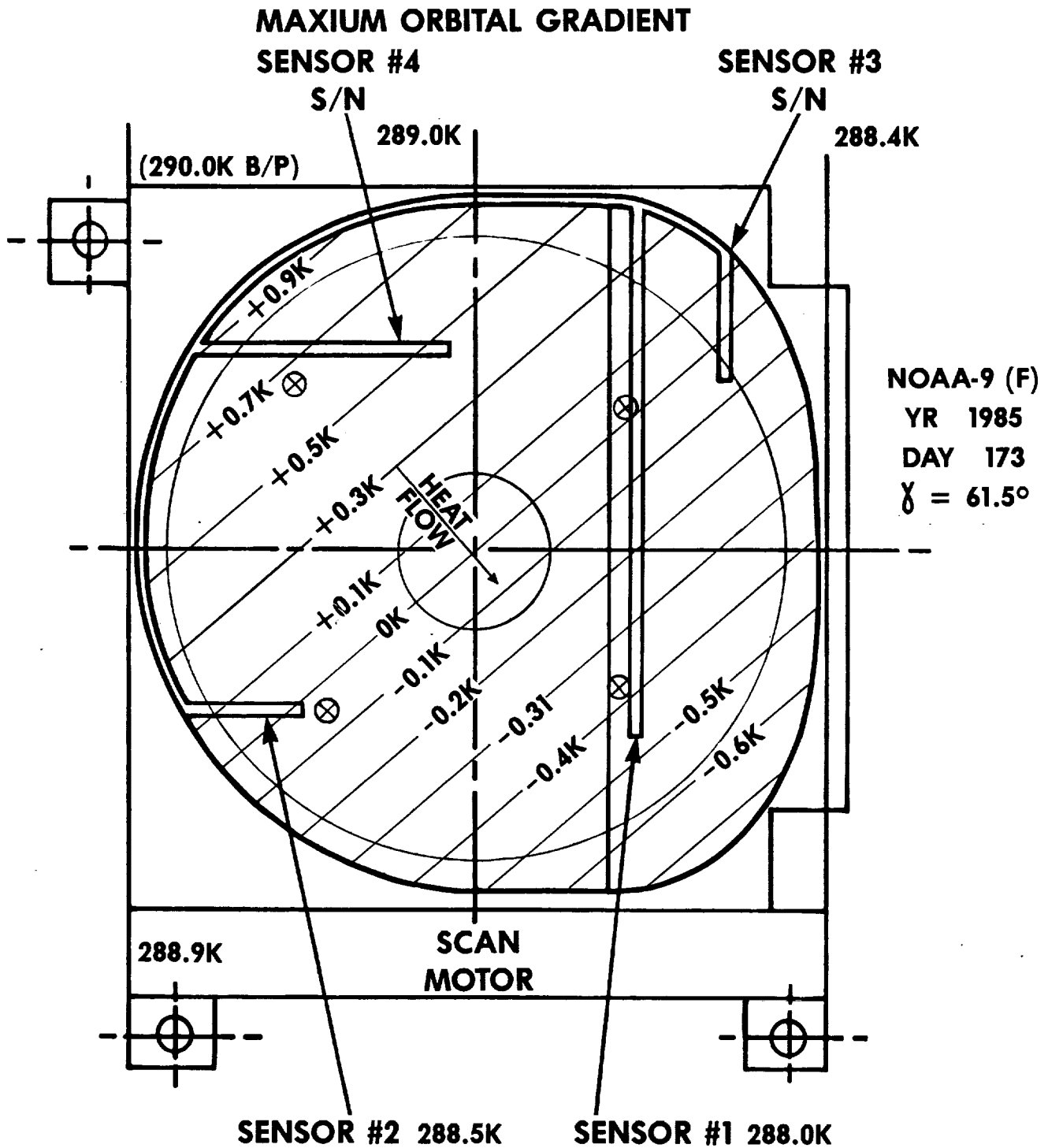
⊗ IMPROVED SENSOR LOCATIONS

SCALE: 1/2

AEROSPACE/OPTICAL DIVISION **ITT**

Table 5.2-4. Radiometric Errors from Use of Average Target Temperature in Presence of Minimum Gradient at Low Sun Angle (Figure 5.2-3)

i	T_i	A_i/A	W (T_i, 3.55 - 3.93 μm)
1	293.7K	0.612	$4.055\ 047 \times 10^{-5}$ W cm^{-2}
2	293.6	0.141	4.037 105
3	293.4	0.123	4.001 421
4	293.2	0.096	3.966 004
5	293.0	0.028	3.930 854

$$W_e = \sum \frac{A_i}{A} W\ (T_i,\ \Delta\lambda) = 4.033\ 896 \times 10^{-5} \text{ W cm}^{-2}$$

	$\overline{T}$	W ($\overline{T}$, $\Delta\lambda$)
Present locations	293.5K	$4.019\ 229 \times 10^{-5}$ W cm^{-2}
at areal centers	293.6	$4.037\ 105 \times 10^{-5}$

	radiometric	errors
Present locations	-0.082K	-1.2 counts
at areal centers	+0.018	+0.26

134

Table 5.2-5. Radiometric Errors from Use of Average Target Temperature in Presence of Maximum Gradient at High Sun Angle (Figure 5.2-4)

i	T_i	A_i/A	W (T_i, 3.55 - 3.93 μm)
1	289.5K	0.004	3.357 121 x 10^{-5} W cm^{-2}
2	289.3	0.074	3.326 609
3	289.1	0.113	3.296 333
4	288.9	0.128	3.266 292
5	288.7	0.116	3.236 483
6	288.55	0.050	3.214 279
7	288.45	0.074	3.199 548
8	288.35	0.088	3.184 874
9	288.25	0.106	3.170 258
10	288.15	0.099	3.155 699
11	288.05	0.092	3.141 197
12	287.95	0.050	3.126 751
13	287.9	0.006	3.119 549

$$W_e = \sum \frac{A_i}{A} W (T_i, \Delta\lambda) = 3.215\ 857 \times 10^{-5} \text{ W cm}^{-2}$$

	$\overline{T}$	W ($\overline{T}$, $\Delta\lambda$)
Present locations	288.475K	3.203 255 x 10^{-5} W cm^{-2}
at areal centers	288.55	3.214 279 x 10^{-5}

	$\Delta T(K)$	radiometric errors ΔC (count)
Present locations	-0.086K	-1.0
at areal centers	-0.011	-0.13

135

Table 5.2-6. Maximum Temperature Gradient Versus Sun Angle
(Data Plotted in Figure 5.2-1)

Spacecraft	Date	γ	Max. ΔT	
NOAA-6	4 Feb 85	15°	2.5K	
	15 Oct 84	21°	2.8	
	27 Aug 84	22°	3.4	
	14 Nov 84 and	23°	3.0	
	9 Sep 85			
	13 Aug 84	28.7°	4.0	
	29 Apr 83	33°	4.0	
	6 May 83	34°	3.4	
NOAA-7	5 Nov 84	27°	4.2K	No earth eclipse, TCE off
	15 Oct 84	27°	3.6	Small earth eclipse, TCE off
	14 Nov 84	28°	3.4	
	4 Feb 85	32°	3.6	
	9 Aug 84	42°	2.2	TCE off
	29 Apr 83	49°	2.6	
	6 May 83	50°	2.6	TCE off
NOAA-8	19 Jul 85	36°	1.9K	
NOAA-9	8 Mar 85	57°	1.7K	
	3 Mar 85	57°	1.2	TCE off
	20 Jun 85	61.5°	1.0	TCE off
	18 Jul 85	62°	1.0	TCE off

γ = orbit normal to sun angle
TCE = thermal control electronics

Table 5.2-6. Variation of Scan Motor and Baseplate
Temperature with Sun Angle

γ	Max. ΔT	(SM)	(BP)	(SM) - (BP)	Max. (SM) - (BP)
15°	2.5°C	19.6°C	15.1°C	4.5°C	4.5°C
28.7°	4.0	19.7	15.6	4.1	5.6
32°	3.6	18.2	13.9	4.3	5.3
36°	1.9	18.2	15.3	2.9	3.2
57°	1.7	15.0	15.6	-0.6	1.9

γ = orbit normal to sun angle
Max. ΔT = maximum measured gradient in IR target
(SM) = scan motor temperature
(BP) = baseplate temperature

TCE on in all cases

FIGURE 5.2-5 MOTOR AND BASEPLATE TEMPERATURES AT $\gamma = 36°$

The fact that the scan motor temperature is below the baseplate temperature during part of the 57° orbit suggests that the target gradient is not the result of motor heat, even at the high sun angles where the solar input is small.

Except at a sun angle of 15°, the maximum target gradient does not occur at the same orbital point as the maximum temperature difference between the scan motor and baseplate. And between sun angles of 15° and 28.7°, this difference goes down at the point of maximum target gradient, whereas the gradient itself goes up. The opposite occurs between sun angles of 28.7° and 32°. Finally, the target gradient does not go to zero when the scan motor to baseplate temperature difference is zero during points in the 36° and 57° sun angle orbits.

5.2.3 Solar Input

On the other hand, the data in Figure 5.2-1 and Table 5.2-6 suggest that the maximum calibration target gradient is associated with the amount of solar input. Both the maximum target gradient and the solar input to the scan cavity peak in the vicinity of a 28° sun angle, where the solar shading of the earth begins. To explore this relationship in greater detail, we studied the temperature profiles of the four target temperature sensors at the five sun angles listed in Table 5.2-6. These profiles are shown in Figures 5.2-6 through 5.2-8. Note that the thermal control electronics (TCE) was on in all cases. Temperature Sensors 1 and 2 are at the scan motor end of the target and Sensors 3 and 4 are at the baseplate (telescope) end. Sensors 2 and 4 are on the sun side and 1 and 3 are on the space side.

At the sun angle of 15°, the spacecraft is in the sun for the entire orbit, but the instrument is shaded by the interface for half of the orbit (during daytime on the earth). Here, the maximum target gradient occurs at the end of the solar heating, i.e., at the nighttime-to-daytime terminator. The solar input is not as large on the motor end of the scan cavity as on the telescope end because of the partial shading by spacecraft appendages and other instruments. This shading increases as the sun angle increases and when combined with the cutoff produced by the earth's shadow, results in a sharp solar input pulse, as shown in Figures 5.2-7 and 5.2-8. These pulses produce the maximum target gradients during these 28.7° and 32°, the maximum target gradient correlates well with the solar input to the motor end of the scan cavity.

As the sun angle increases further, the shading of the motor end increases until the solar exposure of this end of the scan cavity disappears completely, as shown in Figure 5.2-9. At this sun angle (36°), the maximum target gradient occurs during the daytime and therefore does not correlate with the solar input. Solar exposure is now limited to the telescope end of the scan cavity and has been reduced to the point where the temperatures are higher during the daytime input from the increased earth albedo (which increases with the
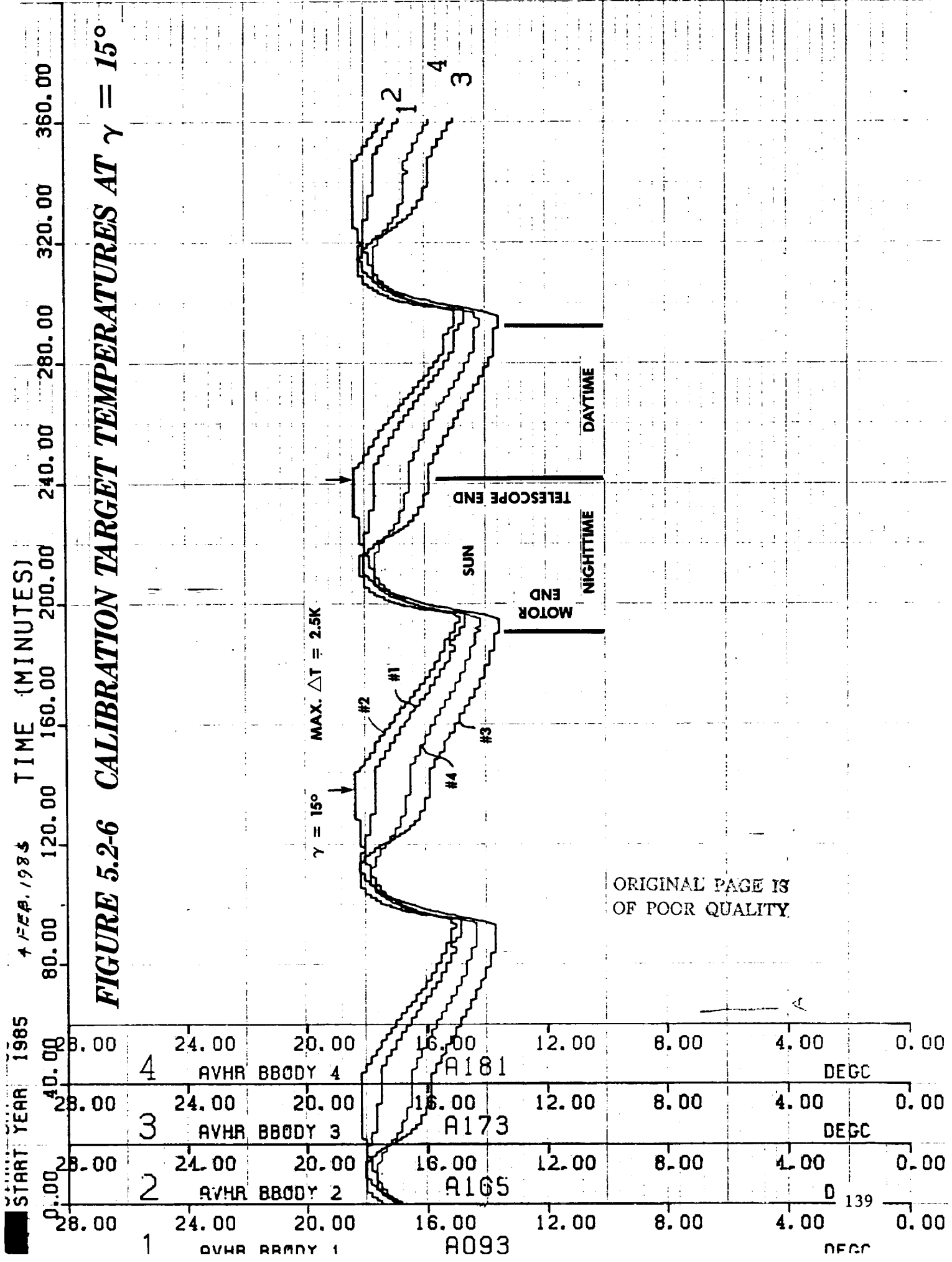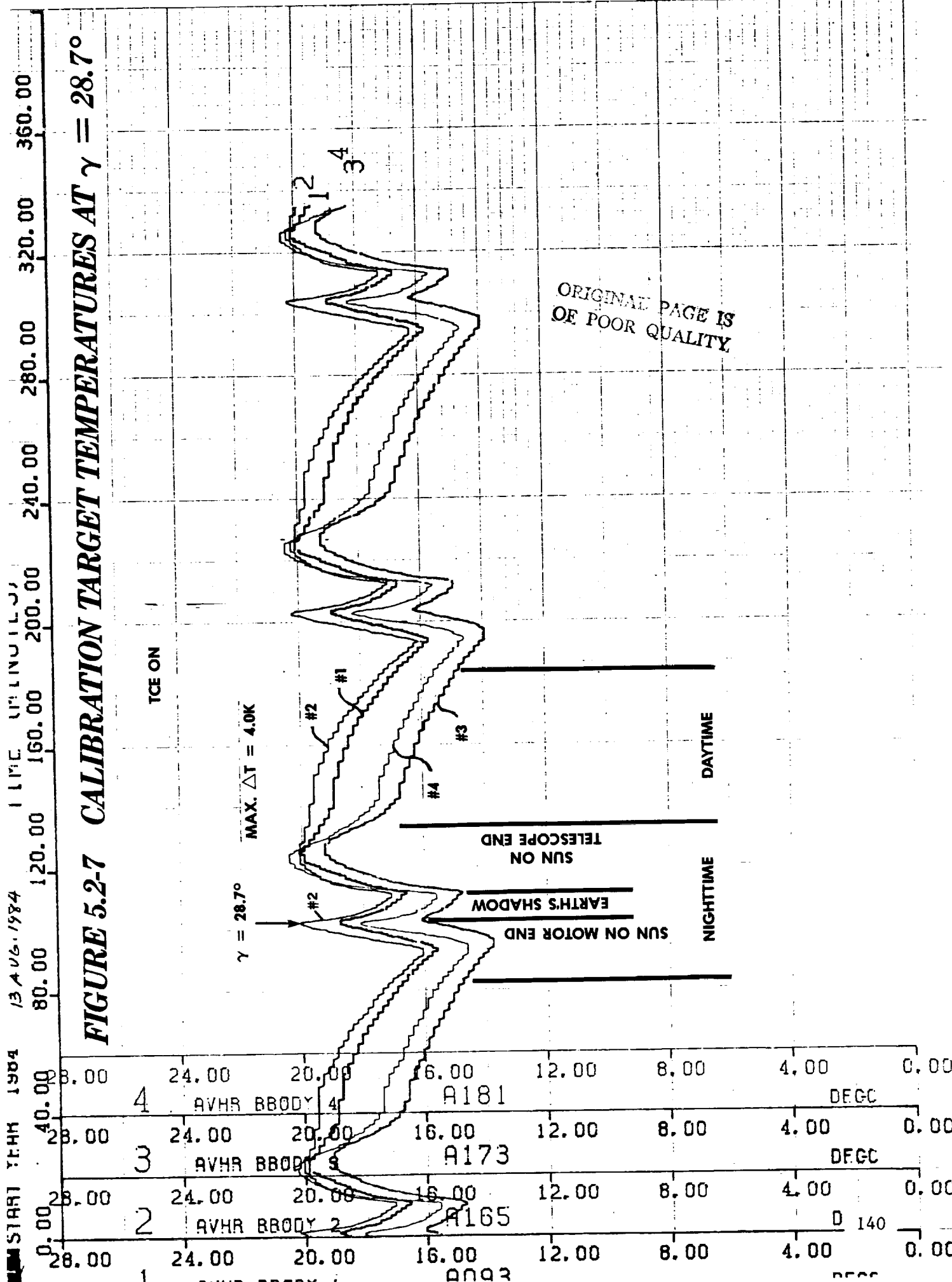
FIGURE 5.2-6 CALIBRATION TARGET TEMPERATURES AT $\gamma = 15°$

ORIGINAL PAGE IS
OF POOR QUALITY

139

FIGURE 5.2-7 CALIBRATION TARGET TEMPERATURES AT $\gamma = 28.7°$

FIGURE 5.2-8 CALIBRATION TARGET TEMPERATURES AT $\gamma = 32°$

FIGURE 5.2-9 CALIBRATION TARGET TEMPERATURES AT $\gamma = 36°$

19 JULY 1985

TIME (MINUTES)

80.00   40.00   160.00   200.00   240.00   280.00   320.00   360.00

TCE ON

$\gamma = 36°$

MAX. $\Delta T = 1.9K$

#1   #2   #3   #4

2 4
1 3

DAYTIME

SUN ON
TELESCOPE END

NIGHTTIME

EARTH'S
SHADOW

0301 = 1ST MIN. OF SUN

28.00   24.00   20.00   16.00   12.00   8.00   4.00   0.00

4   AVHR BBODY 4   A181   DEGC

28.00   24.00   20.00   16.00   12.00   8.00   4.00   0.00

3   AVHR BBODY 3   A173   DEGC

28.00   24.00   20.00   16.00   12.00   8.00   4.00   0.00

2   AVHR BBODY 2   A165   D 142

28.00   24.00   20.00   16.00   12.00   8.00   4.00   0.00
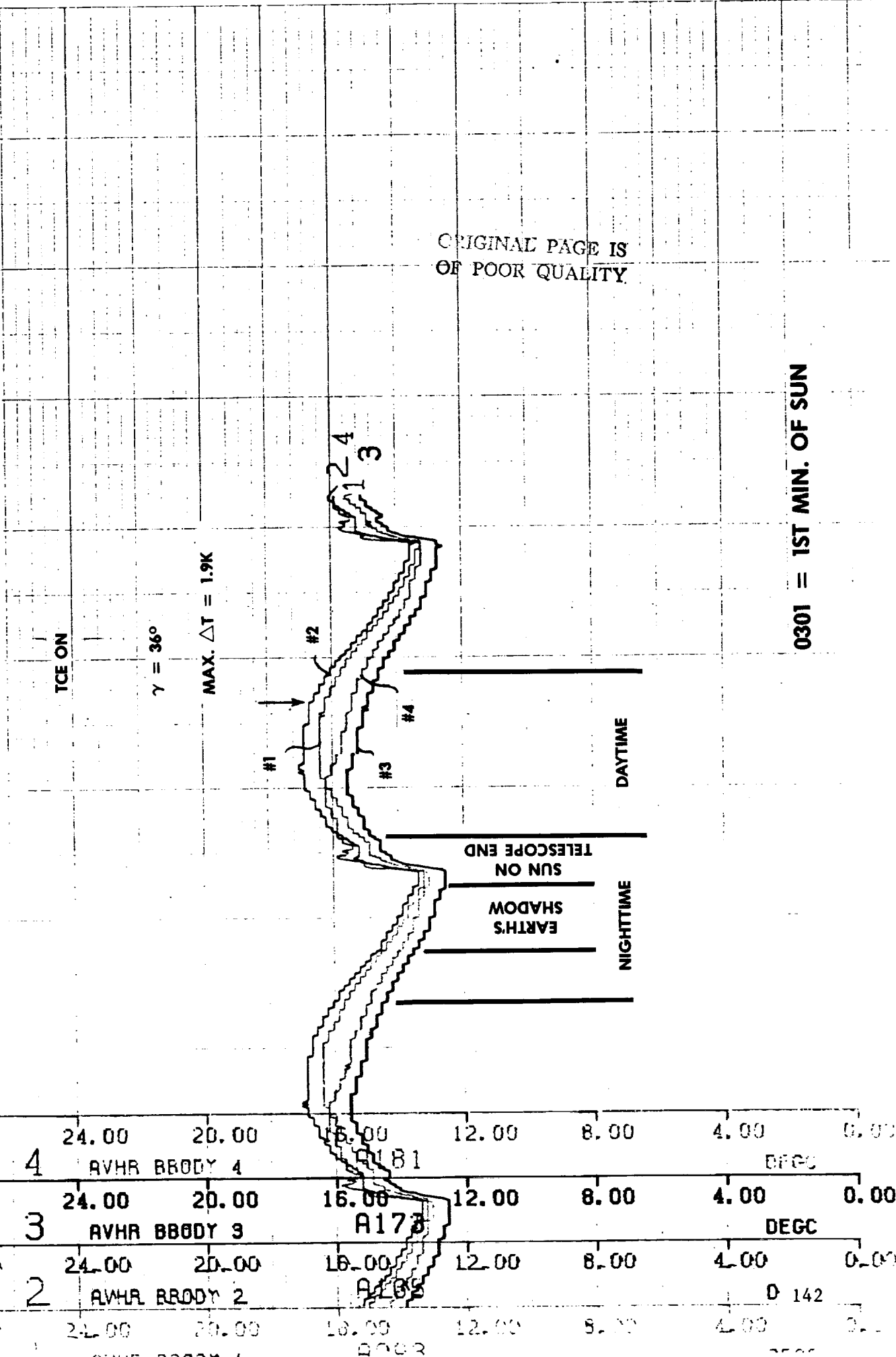
sun angle). On the other hand, there is not much difference between the maximum gradient and the gradient that occurs during the solar input or, for that matter, during the entire daytime half of the orbit. This situation persists up to a sun angle of 57° (Figure 5.2-10), except that the gradient during the small solar exposure is now slightly greater than the daytime maximum.

5.3   Gradient Reduction

We have shown that the radiometric error produced by temperature gradients can be reduced to a low level by a) using the average temperature measured by the four sensors, and b) relocating the sensors so that their average reading is a more accurate measure of the effective target temperature seen by the instrument. On the other hand, the Statement of Work suggests that we reduce the error by reducing the gradient itself. In particular, we are to establish possible ways to reduce calibration target gradients and transients.

An obvious way is to:

1. Increase the thermal conductance and heat capacity of the target by increasing the thickness of the baseplate wall across the scan cavity. This modification will reduce both the temperature gradients and the temperature transients (rates of change in temperature).

Other ways may be revealed by a study of the HIRS/2 whose warm infrared calibration target has both small gradients and small transients. This is shown by the following comparisons:

	AVHRR @ γ = 23°	HIRS/2 @ γ = 28°
Gradients	0.7K - 3.0K	0.02K - 0.34K
Total variation	7.2K	2.2K
Max $\Delta T/\Delta t$	0.79K/min	0.080K/min

Both the maximum gradient and the maximum transient are nearly an order of magnitude smaller in the HIRS/2 than in the AVHRR.

From a review of the HIRS/2 design, we have established the following additional possible ways to reduce AVHRR/3 calibration target gradients and transients.

2. Locate the target off the baseplate on the sun side of the instrument, with its surface tilted at an angle to the baseplate. (This angle is 50° in the HIRS/2). This eliminates exposure of the target to direct sunlight, reduces its view to space, and increases its view to surfaces at or near the temperature of the target. In addition, it moves the target off the baseplate and out of the conduction path across the scan cavity.

143

FIGURE 5.2-10 CALIBRATION TARGET TEMPERATURES AT γ = 57°
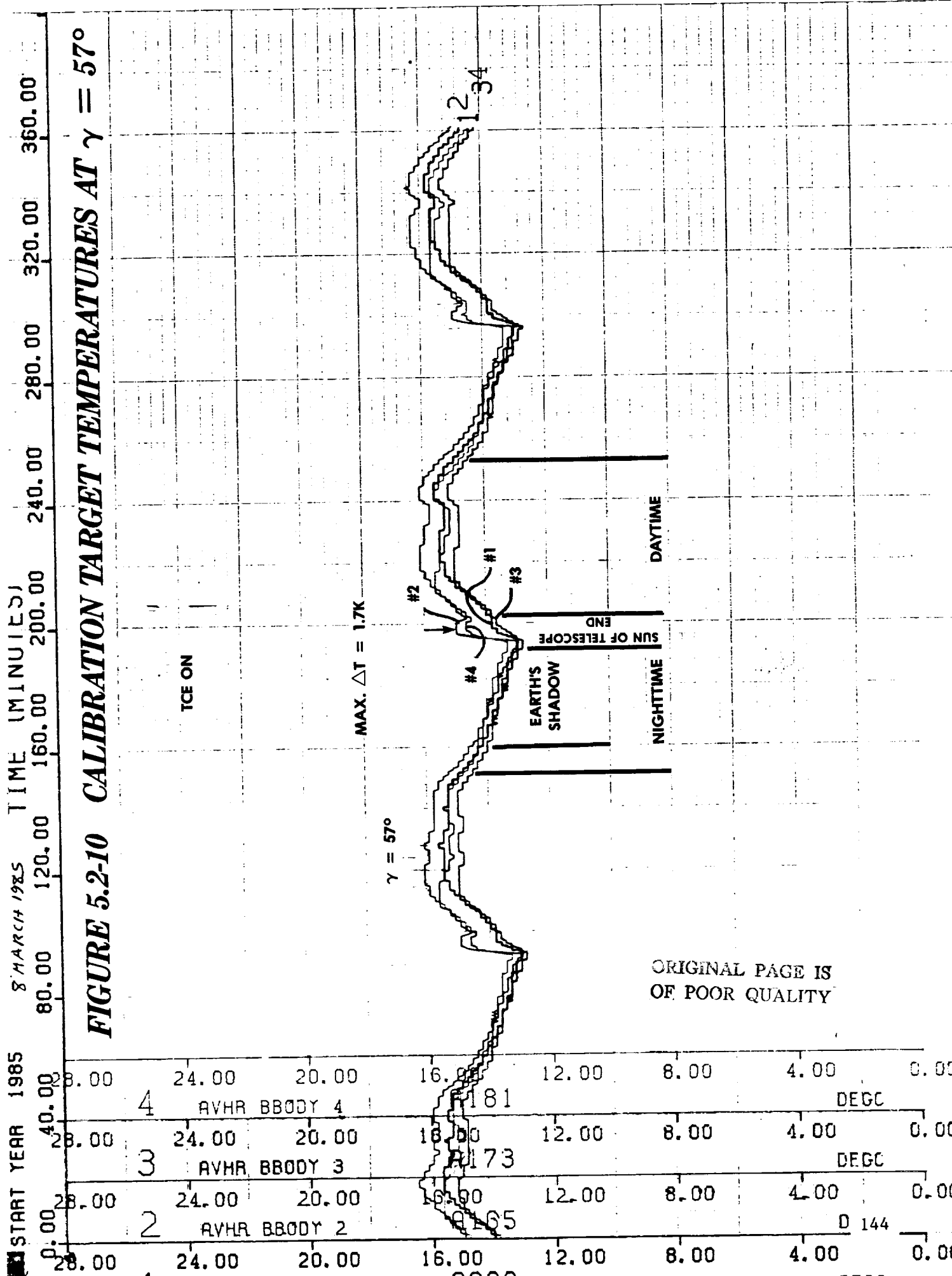
On the other hand, relocation of the AVHRR infrared target in this fashion uses the same space that would be occupied by a transmissive diffuser or bulb source stability monitor.

3. Extend the thermal-control louvers to the area under the scan cavity. With this modification, not all of the heat will have to flow across the scan cavity to reach a baseplate radiating area.

4. Add a radiating area to the scan motor housing. This radiator eliminates the flow of motor power into or through the scan cavity and calibration target.

5. Improve the thermal control of the baseplate (TCE operation). The control of the HIRS/2 is much better than that of the AVHRR, as shown by the following data from NOAA-9 (immediately after launch, at a sun angle of about 55°):

	Baseplate temperature over an orbit
HIRS/2	12.8°C $\pm$ 0.05°C
AVHRR	15.1°C, +1.3°C, -1.0°C

Moreover, the temperature variations in the AVHRR increase as the sun angle decreases (exposure to sunlight increases). For example, the baseplate of the AVHRR on NOAA-6 varied between 13.4°C and 17.9°C at a sun angle of 23° (1984, day 255).

Finally, previous study has shown that sunshades added to the instrument are not effective in reducing the exposure of the calibration target to direct sunlight if they are located outside the scan field of the radiometer. However, if this constraint is removed, we can add a sunshade within the scan field on the sun side of the instrument but outside the active (earth) scan field. This is the region that would be occupied by a relocated target or a solar channel stability monitor. In fact, a stability monitor permanently mounted in this location would also serve as a sunshade for the infrared calibration target.

5.4   Recommended Changes

ITT recommends the following changes be incorporated into AVHRR/3.

1. Reposition the PRTs so that they record an average temperature closer to that recorded by the instrument.

2. Increase baseplate mass under the target by three pounds. This will reduce the gradient by about half.

3. Install a sunshade in the scan field beyond the earth
    edge on the sun-side of the scanner. This shield can
    either be the solar channel stability monitor or an
    aluminum plate.

4. Review the spacecraft thermal control system to deter-
    mine if the AVHRR baseplate can be held more nearly
    constant.

6.0   AVHRR/2 SCAN MOTOR CHANGE

6.1   Requirements

Examine the instrument modification which are required to increase the instrument operation/performance life from 2 years to 3 to 5 years; specifically in the area of scan motor operation. It appears that the present nominal scan motor operation is limited to approximately 2 1/2 years because of the lubrication constraints which have been imposed in order to meet the jitter requirements. The study will address, but not be limited to, the anticipated changes relating to power, structure, thermal, and scan motor operation.

This study shall be a conceptual design approach rather than a detailed examination. The study shall also present the anticipated effort and ROM cost associated with proposing a separate detailed study.

Note that the AVHRR scanner has never failed in orbit. Operation of over 7 years has been experienced. The increased jitter anomaly which occurs around 30 months after launch is completely reversable by heating and then cooling the scanner back to normal operating temperature. To date the AVHRR scanner is not a life-limiting subsystem (unlike the HIRS/2 filter wheel).

6.2   Scan Motor

A significant amount of investigation was conducted into the scan motor area in an effort to understand past motor performance and recommend motor improvements for the AVHRR/3. Included in the Appendix H to this report is design information report #48 which historically documents AVHRR scan motor efforts and provides the baseline for an AVHRR/3 scan motor.

Appendix I is the new specification for the scan motor proposed for AVHRR/3. The motor is the Schaeffer Magnetics, Inc. hysteresis motor used previously; however, the testing and torque requirements have changed somewhat.

Testing requirements have been changed to minimize variation in torque performance from motor to motor. Torque will be specified and measured as sync torque not 1% slip torque. Sync torque will be defined as the torque the motor puts out with no measurable slip (less than 10 microseconds in 20 minutes).

The specified shaft sync torque is specified as no less than 3.0 inch ounces. Since the bearing load has been measured to be in the 1 to 2 inch ounce range, the total motor freebody output torque will be 4 to 5 inch ounces.

A meeting was held between ITT and Schaeffer perosonnel. As a result of the meeting this specification will be modified. the torque requirement will be specified as a free body output synchronous torque of 5.0 inch ounces minimum.

In addition to investigations at ITT, a consultant, Dr. Gordon R. Slemon of the University of Toronto, was engaged to study the AVHRR scan motor design in an effort to define possible causes of scan motor long term "slip" and to recommend changes in our design. Dr. Slemon's report is included in Appendix J.

6.2.1   Use of DC Servo Drive for AVHRR Scanner

A requirement of this investigation was to conduct a study to determine the effects of redesigning the scan system to use a DC servo to drive the scanner instead of the present 80 pole hysteresis synchronous motor. A block diagram of the dc servo drive is shown in Figure 6.2-1. The servo design was reviewed by Mr. John Sudey of NASA-GSFC. His review and comments are included in Appendix K.

Comparison factors were considered in replacing the scanner with a DC servo drive system.

There are four major factors to be considered in comparing scanner drive systems on the AVHRR. They are:

1. Performance
2. Circuit Complexity
3. Weight
4. Power Drain

Following are preliminary estimates concerning each of the four factors.

1. Performance

Performance parameters to be considered are torque capability, jitter, long term phase constancy.

Type of Motor Drive	Torque Max. at 2, 2.5V, 6Hz	Jitter/Rev. (Microseconds)	Long Term Phase Change (Microseconds)
Synchronous	≥ 3.0 oz-in (usually ≥ 3.2 oz-in)	0 to +17	Usually 0
DC Servo	8.1 oz-in	Goal is ≤ 5	0

Running torque is nominally about 1.6 oz-in for the AVHRR bearing system. This leaves a torque margin of greater than 1.6 oz-in in the case of the synchronous motor drive and 6.5 oz-in with the dc servo motor drive.

WITH VOLTAGE DRIVE:
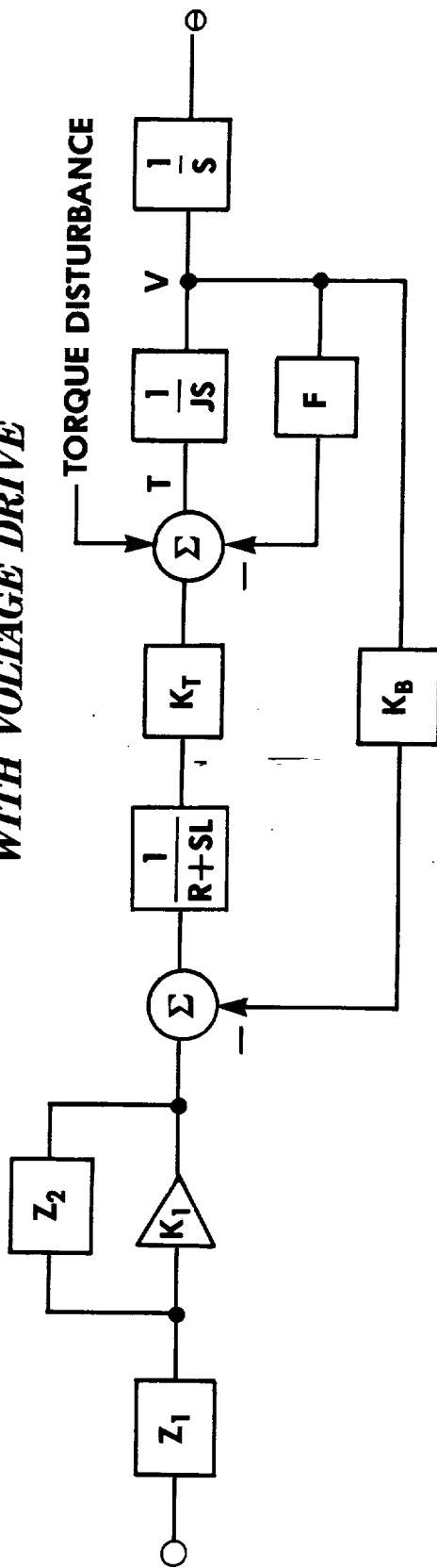
FIGURE 6.2-1b VOLTAGE/POSITION MODEL OF DRIVER/MOTOR/LOAD
WITH CURRENT DRIVE

NOTE THAT THE EFFECT OF K_B AND $\frac{1}{R+SL}$,
MINIMAL AS LONG AS THE OPERATION IS IN A LINEAR MODE
(I.E., NOT IN A LIMIT CONDITION).
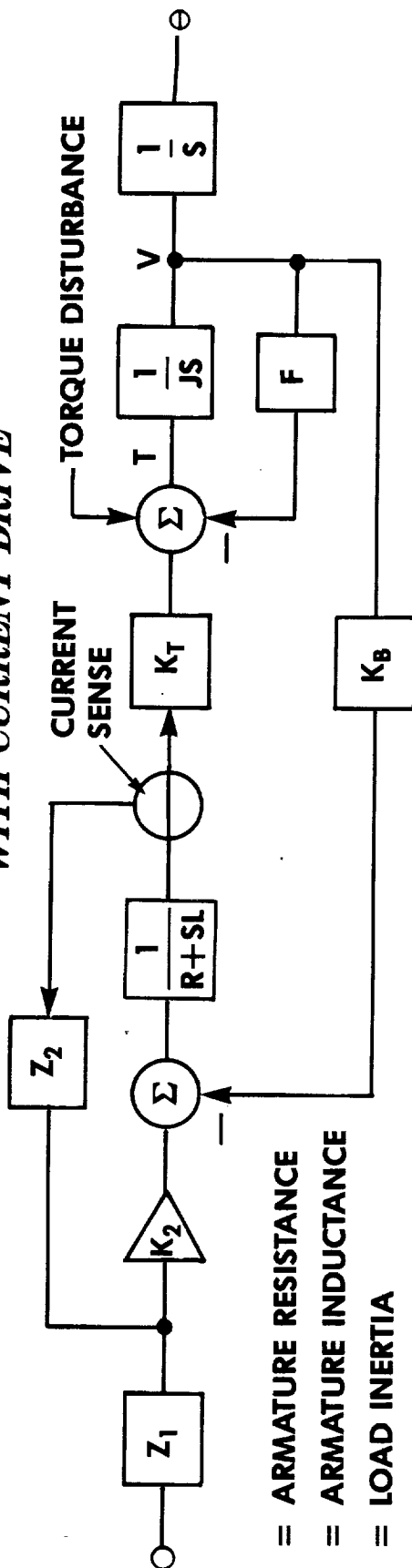
R = ARMATURE RESISTANCE
L = ARMATURE INDUCTANCE
J = LOAD INERTIA
F = LUBE VISCOUS DAMPING
K_T = MOTOR TORQUE CONSTANT
K_B = BACK EMF CONSTANT
K_1 = DRIVER VOLTAGE GAIN
K_2 = DRIVER CONVERSION AMPS/VOLT

$\left(\dfrac{Z_2}{Z_1} \; / \; \text{VOLTS/AMP OF CURRENT SENSOR} \right)$

AEROSPACE/OPTICAL DIVISION **ITT**

149

Driving frequency of the synchronous motor is 240 Hz; band-width of the dc servo loop is expected to be about 400 Hz.

Combination of wider bandwidth and greater torque reserve justifies confidence in predicting a low jitter value for the dc servo drive.

By using a true integrator in the loop of the dc servo system, gain can be increased to bring long term phase variations to essentially zero, even if bearing/lube drag change significantly.

2. Circuit Complexity

The dc servo motor drive requires much more complex circuitry than the synchronous motor drive, due to the fact that it must be controlled by a closed control loop for synchronous operations, whereas the ac hysteresis motor is already synchronous with open loop drive configuration.

Following is a listing of the circuitry required for each type of drive system. It is estimated that the dc servo system will require two additional circuit boards.

Synchronous Motor Drive

(1) Switching Regulator
(2) Bridge inverters/drivers (with transformers)
(3) Synchronous ac hysteresis motor

DC Servo Motor Drive

(1) Switching Regulator
(2) Inverters/rectify and filter ($\pm$scan supplies)
(1) Optical incremental rate generator
(1) Commutation counter/control/switches
(1) Reference generator
(1) Synchronous frequency/phase detector
(1) Start-up logics and control circuitry
(1) Analog dc servo amplifier (includes integrator, gain vs. frequency compensation and two motor current drivers)
(1) Quadrature winding brushless dc motor

3. Weight

The brushless dc motor has a weight of about 16 oz. However, the incremental rate generator weights 13 oz. This is a total of 29 oz. compared to the weight of the synchronous motor which is 53 oz.

This is a net difference of 24 oz., the synchronous motor being the heavier unit.

4. Power Drain

    The power required for the synchronous motor drive system
is nominally 3 watts. This is low due to the minimum of circuitry
required.

    The dc servo motor drive system requires a total of 5.4
watts, estimated nominal power. This consists of:

Motor drive power	2.4 watts
Control electronics power (54LS family)	1.2 watts
Encoder power	.8 watts
TOTAL POWER	5.4 watts

    This estimated total power is nominally 2.4 watts more than
that required for synchronous motor drive system.

6.3   Lubrication

    The purpose of lubrication is to extend bearing life. To
better understand the purpose we need to define the function of
lubrication.

    The function of the lubrication is to separate the asperi-
ties of the ball and race contacting surfaces. The balls travel over
the raceway on a lubrication hydrodynamic film. Spalling, a surface
breakdown, occurs when the lubrication film thickness depletes,
allowing the surface asperities to contact. During the manufacturing
of bearing races and balls surfaces, irregularities are introduced onto
the surfaces. The magnitude of these irregularities are controllable;
however, they will always exist. These asperities are typically a few
millionths of an inch peak to valley. In an unlubricated bearing, the
asperity peaks of the ball contact the asperity peaks of the raceway.
As the peaks contact, micro-welding occurs, followed by a shear separa-
tion. The separation results in the removal of the peak of either con-
tacting surface. Once this occurs, the nature of the failure mode
propagates to a surface pit. If a separation can be achieved and main-
tained, the bearing will function until the separation is lost.

    Once a micropit has developed, the surface has been damaged
irreversibly. As the successive contacting surface passes over the
micropit, the lubrication film thickness drops, and the trailing edges
contacts with instantaneous microwelding followed by separation;
yielding further surface degradation. If the pit is in the wear track,
each successive pass of a ball over the pit will further damage the
raceway and ball.

6.3.1   Elastohyrodynamic (EHD) Film Thickness; AVHRR Scanner
           Bearings

          The primary task of this section is to predict the film
thickness between the ball and inner race of the AVHRR scan bearing.
The calculation will compare KRYTOX 143AB (present AVHRR scanner lubri-
cant) to APIEZON C (present HIRS/2 filter wheel lubricant) in a
operating environment between 0-40°C. The rotational speed will be the
scanner's operating angular velocity of 37.7 rad/sec (360 rpm).

          In calculating the L_{10} service life of a ball bearing, the
bearing is assumed to have adequate lubrication to prevent surface
degradation. The lubrication is used to maintain a separation between
the surface of the balls and races.

          Since, the materials in contact are of high elastic modu-
lus, the elastohydrodynamic (EHD) film thickness is governed by the
elastic deformation and pressure-viscosity effects of the lubrication.
The behavior of the EHD film thickness is very dependent on the
geometry of the two contacting surfaces, relative motion, and fluid
viscosity. The contact area between the ball and race is small, but
becomes significantly larger with increased load. The lubrication's
viscosity between the point contact of the two surfaces increases as
the pressure increase.

          The variables governing the elastohydrodynamic lubrication
theory are:[1]

E'   effective elastic modulus, $\dfrac{1}{\dfrac{1-v_a^2}{E_a} + \dfrac{1-v_b^2}{E_b}}$, psi

F   applied load, lbs

h   film thickness, in

R_x effective radius in x (motion) direction, $\dfrac{1}{\dfrac{1}{r_{ax}} + \dfrac{1}{r_{bx}}}$,in

R_y effective radius in y (transverse) direction, $\dfrac{1}{\dfrac{1}{r_{ay}} + \dfrac{1}{r_{by}}}$,in

u   mean surface velocity in x direction, $(u_a + u_b)/2$, in/s

---

[1] Hamrock, Bernard J. Elastohydrodynamic Lubrication, National
    Aeronautics and Space Administration, Lewis Research Center

a pressure-viscosity coefficent, in^2/lbs

n_o atmospheric viscosity, $lb - s / in^2$

The calculation of the EHD film thickness is a function of five dimensionless parameters using the above variables;

Dimensionless film parameter

$$H = \frac{h}{R_x} \tag{1}$$

Dimensionless load parameter

$$W = \frac{F}{E'R_x^2} \tag{2}$$

Dimensionless speed parameter

$$U = \frac{n_o\, u}{E'R_x} \tag{3}$$

Dimensionless material parameter

$$G = aE' \tag{4}$$

Ellipticity parameter

$$k = (R_y / R_x)^{2/\pi} \tag{5}$$

The dimensionless minimum film thickness can be written as a function of;

$$H_{min} = f(k,U,W,G) \tag{6}$$

where the minimum-film-thickness formula is given by;

$$H_{min} = 3.63U^{0.68}G^{0.49}W^{-0.073}(1-e^{-0.68k}) \tag{7}$$

The minimum-film-thickness h(inches) is obtained by solving the dimensionless film thickness parameter (1). The central-film-thickness is given as;

$$H_c = 2.69U^{0.67}G^{0.53}W^{-0.067}(1-0.61e^{-0.73k}) \tag{8}$$

153

The central-film-thickness is the EHD thickness under the central protion of the ball/race interface.

The EHD equations 7 and 8 calculate the expected film thickness generated between the ball and inner race for a given bearing geometry, speed, material type, radial load, temperature and lubrication. these equations are for the inner race-ball interface since the Herzian contact is greatest at this interface in a bearing. In Table 6.3-1 are the calculated film thickness values for KRYTOX 143AB and APIEZON C at 0, 20 and 40 degrees centigrade. Figure 6.3-1 graphically illustrates the data in Table 6.3-1, and shows that the film thickness generated by KRYTOX is very temperature dependent.

Viscosity is a function of kinematic viscosity, density and temperature. Table 6.3-2 compares the three parameters for the two lubricants. Density appears to be the driving parameter which governs the variations between the film thickness of the KRYTOX and APIEZON.

We now can compare the EHD results to the needed calculated film thickness. The EHD lubrication theory shows that the required film thickness needed to keep the asperities from contacting is a function of the surface finishes of the parts. Thus, the film thickness is expressed by a film parameter Λ.

$$\Lambda = \frac{h_{min}}{s}$$

The service life of a bearing is dependent on the lubrication factor F. If this value is less than optimal, then the L_{10} life of a bearing will be limited. The lubrication factor, F should be between 1.5 to 2.0. See Figures 6.3-2 and 6.3-3.

The surface finish of the AVHRR scanner bearing balls is specified to be 1 microinch, with the raceways being 1.5 microinch. The composite surface roughness (rms) becomes;

● ●

Table 6.3-1. Temperature Vs. Kinematic Viscosity

TEMP °C	log viscosity (centistokes)	
	KRYTOX 143AB	APIEZON C
0	3	–
20	2.36	2.45
40	1.93	1.95
100	1.01	1.03

FIGURE 6.3-1 EHD MINIMUM–FILM–THICKNESS

AEROSPACE/OPTICAL DIVISION ITT

155
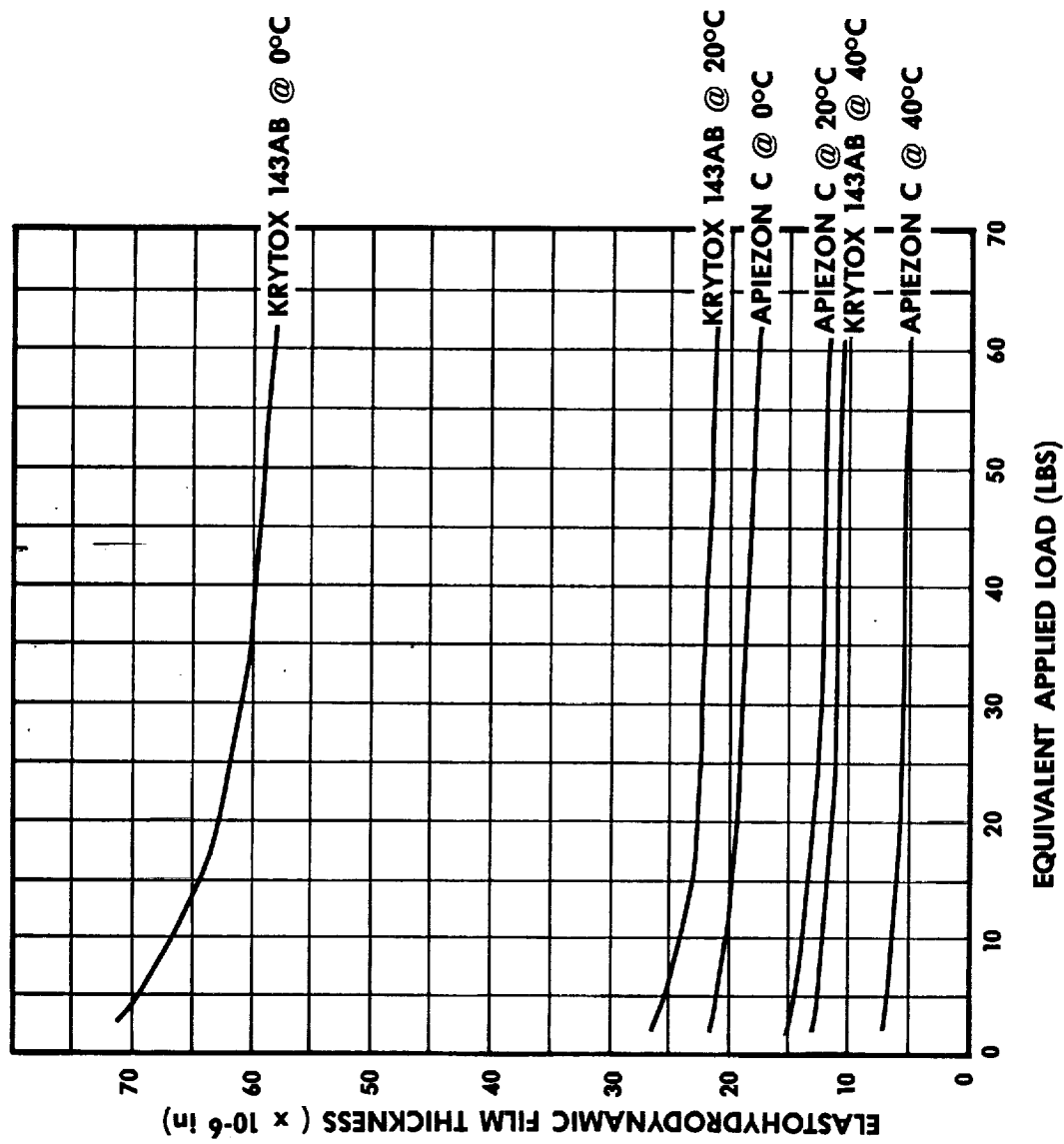
FIGURE 6.3-2   LUBRICATION FACTOR AS A FUNCTION OF
FILM PARAMETER

AEROSPACE/OPTICAL DIVISION **ITT**

156
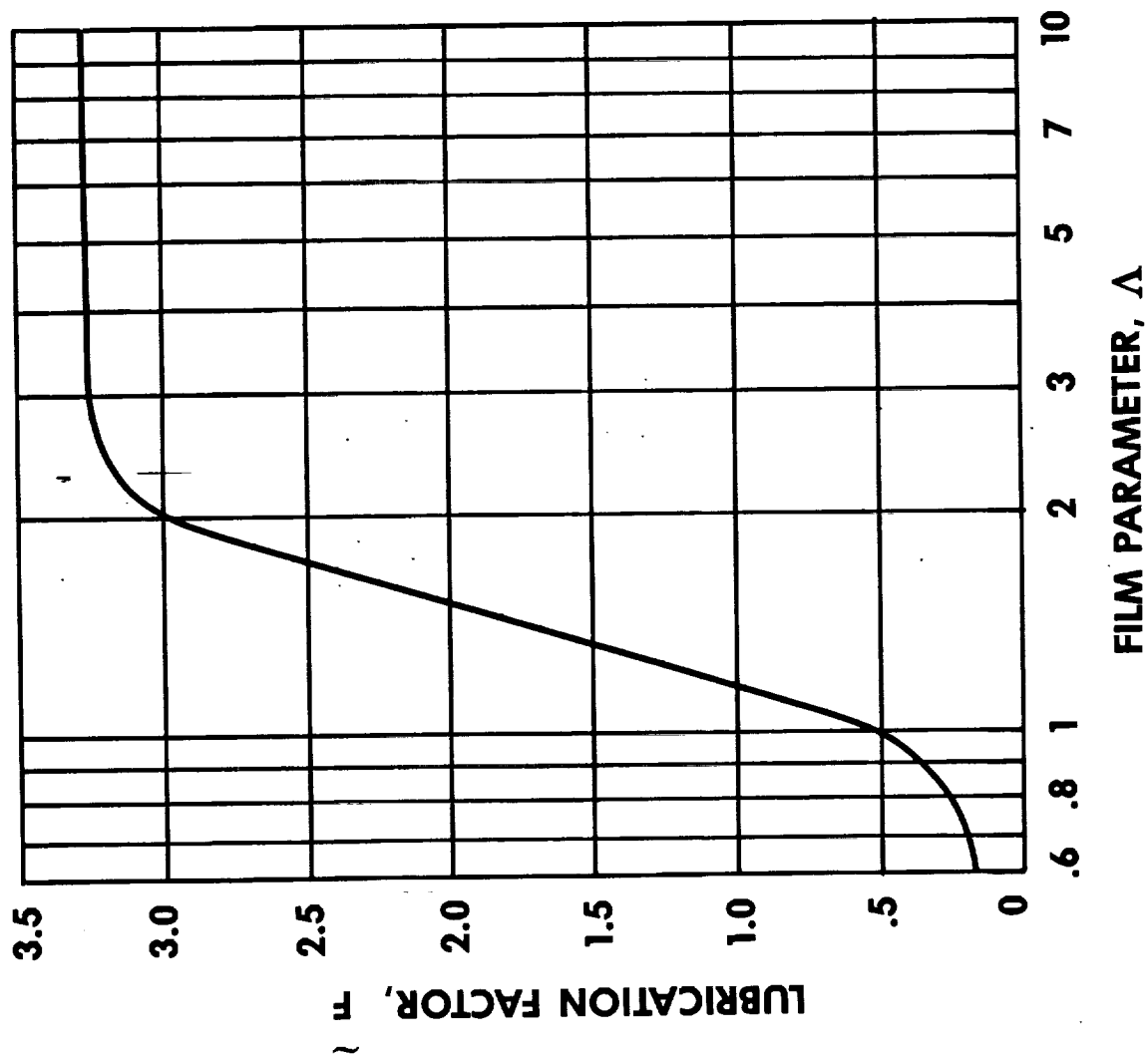
FIGURE 6.3-3

—HOW FILM THICKNESS AFFECTS SERVICE LIFE. RATED SERVICE LIFE CAN BE EXPECTED IF Λ IS BETWEEN 0.9 AND 1.5. ABOVE THAT VALUE, GREATER THAN RATED LIFE CAN BE EXPECTED. (REPRINTED BY PERMISSION OF SKF INDUSTRIES, INC.)

FUNCTION OF FILM THICKNESS AND SURFACE ROUGHNESS, Λ

$$\Lambda = \frac{H_0}{Q} \left(\frac{\text{FILM THICKNESS}}{\text{SURFACE ROUGHNESS}} \right)$$

AEROSPACE/OPTICAL DIVISION ITT

157
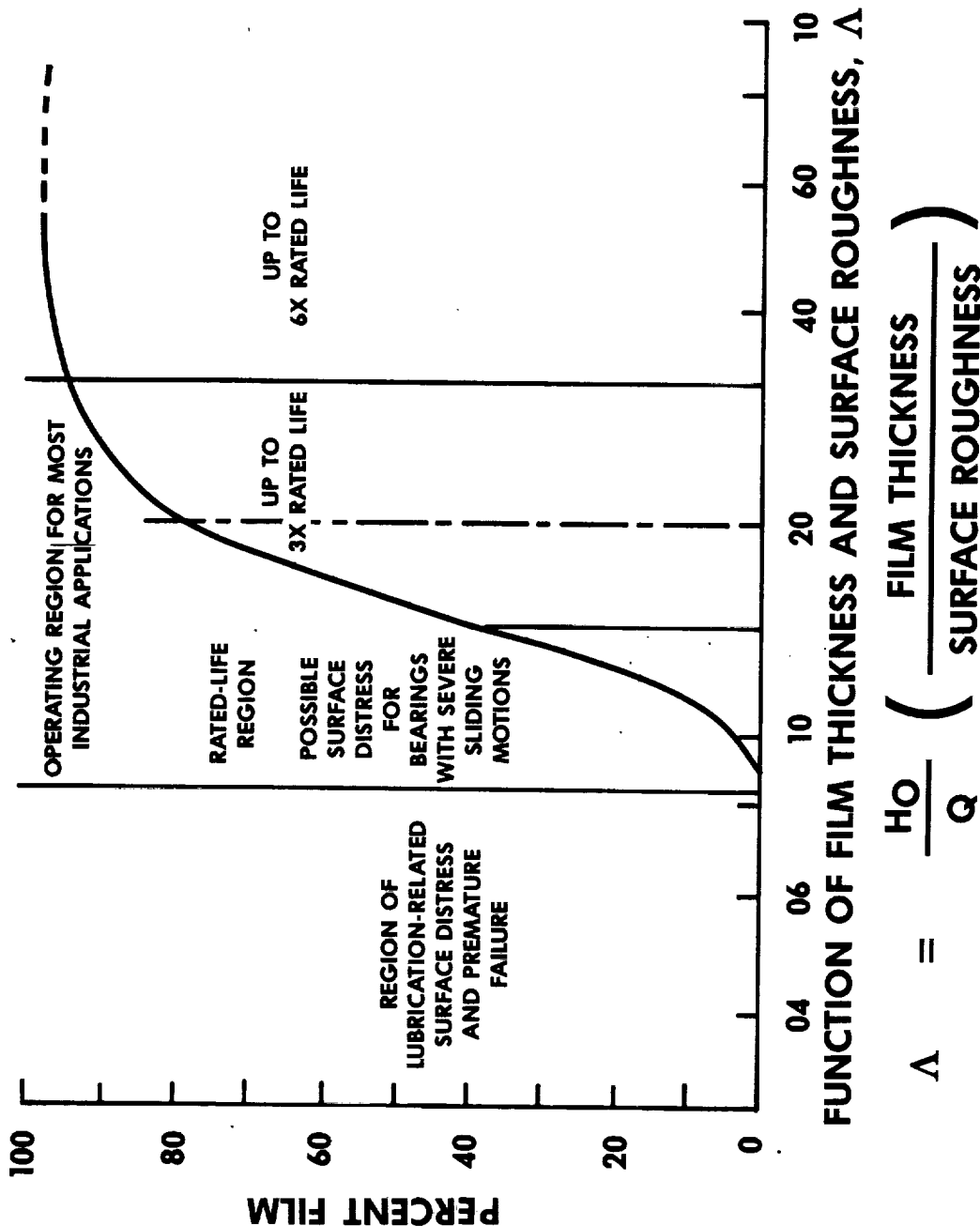
Table 6.3-2. Temperature Vs. Density

TEMP °C	density (g/ml)	
	KRYTOX 143AB1	APIEZON C2
0	1.938	.887
10	1.92	.881
20	1.902	.875
30	1.884	.869
40	1.886	.863

$$S = \sqrt{S1^2 + S2^2} \qquad = \sqrt{1^2 + 1.5^2}$$

S = 1.80 microinch rms

Using F between 1.5 and 2.25 the required film thickness is;

$$hmin \begin{bmatrix} 2.7 \text{ microinch} \\ 4.1 \text{ microinch} \end{bmatrix}$$

In comparing the generated film thickness of Hamrock's equations to the film parameter Λ , it appears that the AVHRR scanner bearings are generating sufficient film thickness to maintain asperity separation.

Attached are data sheets used in the above calculations:

FIG. 6.3-4 VISCOSITIES OF KYRTOX® 143
FIG. 6.3-5 PHYSICAL PROPERTIES OF APIEZON
FIG. 6.3-6 KINEMATIC VISCOSITY VS TEMP APIEZON "C"
FIG. 6.3-7 AVHRR BEARING LOADS
FIG. 6.3-8 E.H.D. FILM THICKNESS PROGRAM LISTING

FIGURE 6.3-4   VISCOSITIES OF ARKTUA? 143 FLUORINATED OILS

143AD

143AC

143AX

143AB

143AY

143AA

143AZ

ITT

AEROSPACE/OPTICAL DIVISION

TEMPERATURE, °F

KINEMATIC VISCOSITY, CENTISTOKES

50,000
20,000
10,000
5000
3000
2000
1000
500
300
200
100
75
50
30
20
10
5.0
4.0
3.0
2.0
1.5
1.0
0.70

-50   0   50   100   150   200   250   300   350   400   450   500
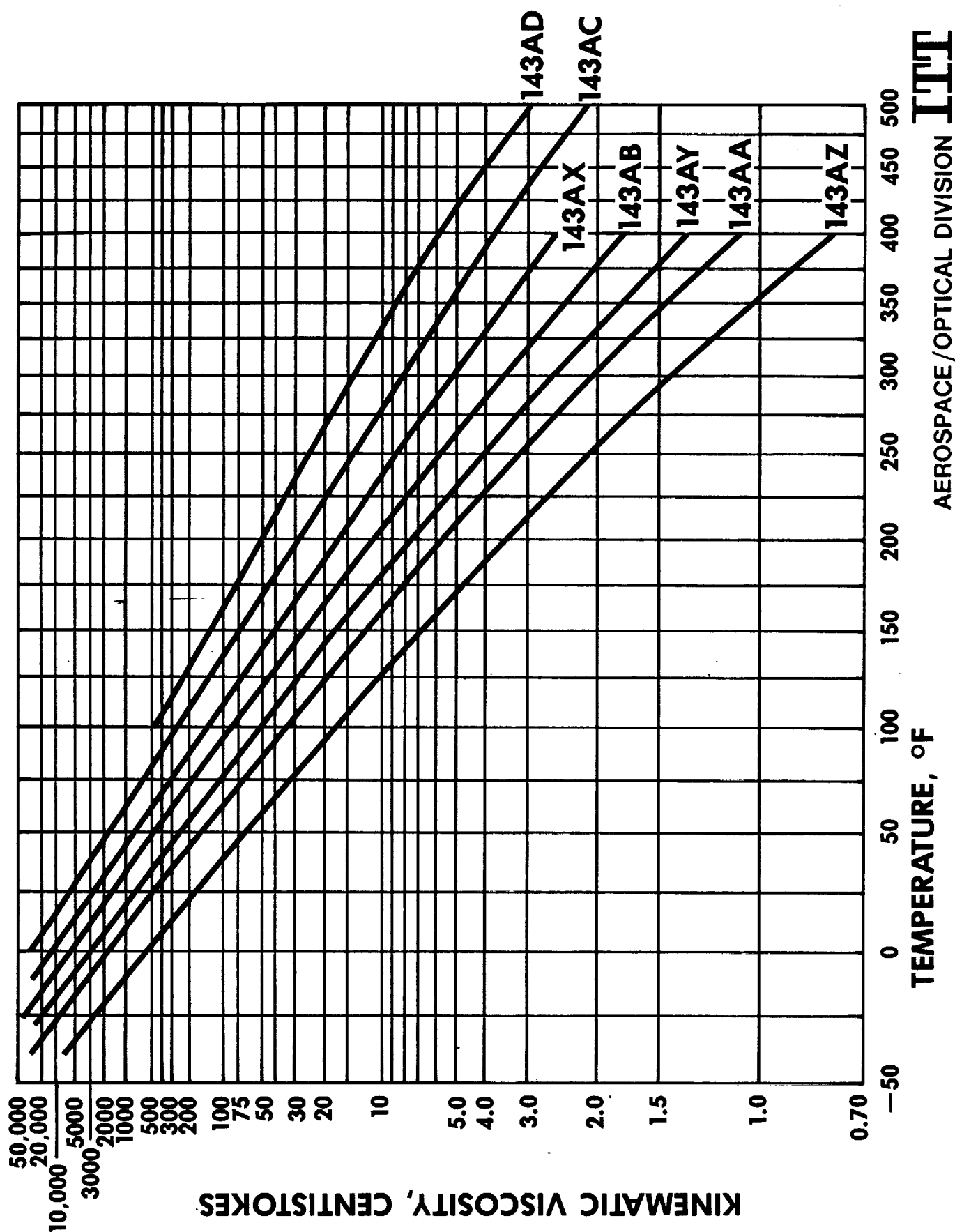
FIGURE 6.3-5 PHYSICAL PROPERTIES OF APIEZON OILS

	APIEZON DIFFUSION PUMP OILS			LUBRICATING AND SEALING OILS	
	OIL A	OIL B	OIL C	OIL J	OIL K
ULTIMATE PRESSURE OBTAINABLE, TORR (a)	5×10^{5}	10^{6}	10^{7}		
AVERAGE BOILING POINT, °C, AT 1 TORR PRESSURE	190	220	255		
SPECIFIC GRAVITY AT: 20°C/15.5°C	0.865	0.873	0.876	0.918	0.919(a)
30°C/15.5°C	0.859	0.869	0.869	0.911	0.914(a)
DENSITY, g/ml AT: 10°C	0.871	0.878	0.881	0.923	0.921
20°C	0.865	0.872	0.875	0.918	0.916
30°C	0.859	0.866	0.869	0.909	0.912
40°C	0.852	0.859	0.863	0.903	0.904
FLASH POINT, PENSKY-MARTENS, °F, CLOSED (ASTM D 93 AND IP 35/63)	410	470	475	590	645
OPEN	410	470	510	665	660
FIRE (IP 190/64)	450	505	560	OVER 700	OVER 700
VISCOSITY, KINEMATIC, cS AT: 20°C (ASTM D 445:65)	59	142	283	3330	5710(b)
40°C	23.4	49.3	90	107	177
100°C	4.5	7.0	10.6		
VISCOSITY, ENGLER (°E) AT: 20°C	7.8	18.8	37.3	198	330(b)
50°C	2.44	4.21	7.3	14.2	23.4
100°C	1.35	1.56	1.90		
VISCOSITY, DYNAMIC (cP) AT: 40°C	19.9	42.4	77.2	3005	5160
POUR POINT, ASTM, °F (D97/66)	20	15	5	30	30
COEFFICIENT OF EXPANSION PER °C OVER 20°C-30°C (ASTM D 1903/61T)	0.00070	0.00073	0.00069	0.00070	0.00062(a)
COEFFICIENT OF EXPANSION PER °C OVER 10°C-40°C (b)	0.00083	0.00080	0.00080	0.00083	0.00070
AVERAGE MOLECULAR WEIGHT	354	420	479	1130	1355
REFRACTIVE INDEX AT 20°C (ASTM D 1807-62T SODIUM D LINE)	1.4780	1.4815	1.4830		
THERMAL CONDUCTIVITY Btu in/ft2.h.°F	0.91	0.91	0.96	1.16	1.17
w/m.°C	0.132	0.132	0.139	0.167	0.169
SPECIFIC HEAT AT 25°C: CAL/g	0.46	0.49	0.46	0.48	0.46
JOULE/g	1.9	2.0	1.9	2.0	1.9

IIT

AEROSPACE/OPTICAL DIVISION

160

FIGURE 6.3-6 **KINEMATIC VISCOSITY VS. TEMPERATURE**

APIEZON 011 C

AEROSPACE/OPTICAL DIVISION ITT

161
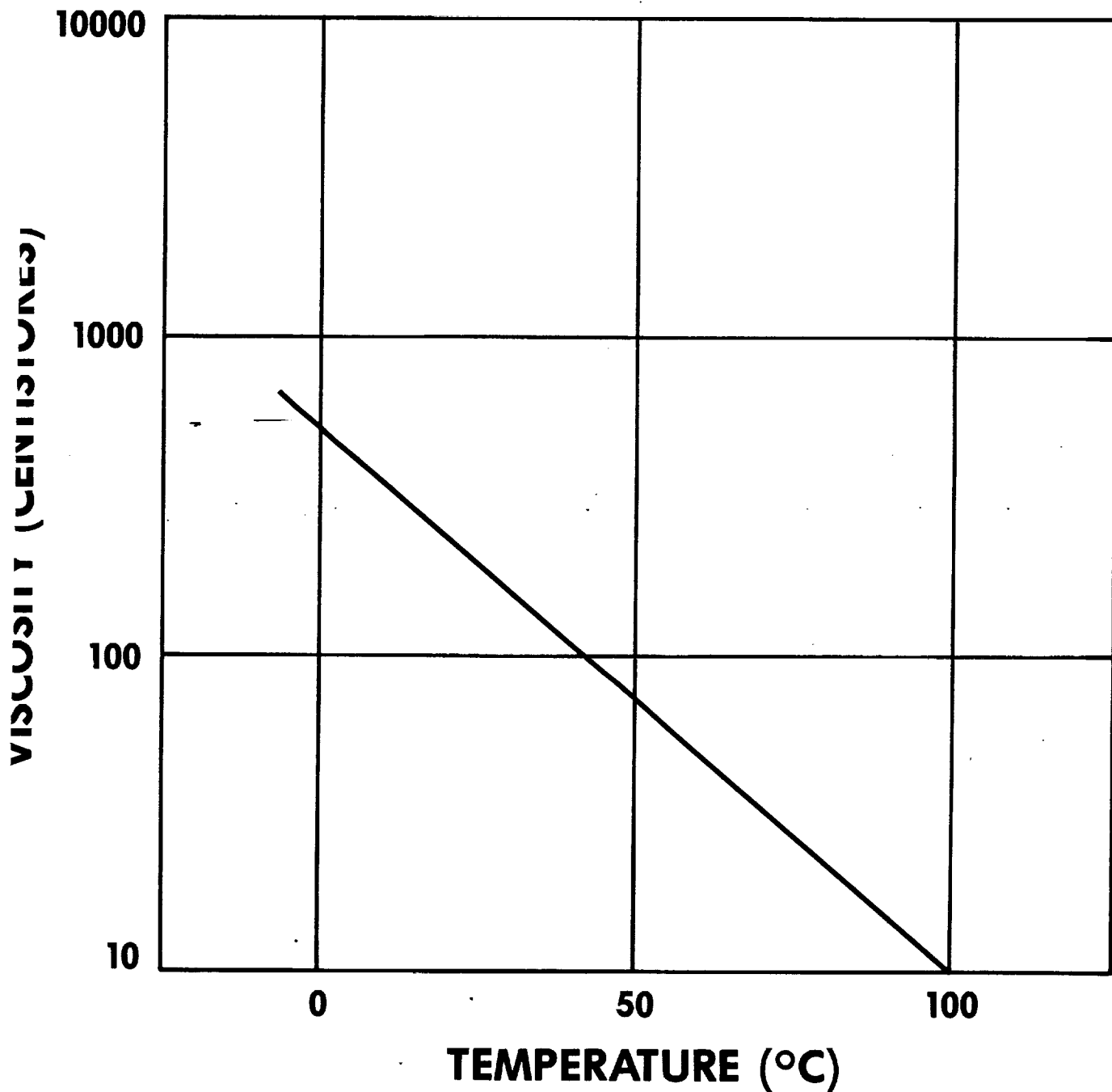
FIGURE 6.3-7   LEVELS g'S

	X-AXIS	Y-AXIS	Z-AXIS
$\ddot{X}$	10.0	3.3	7.6
$\ddot{X}_{RMS}$	6.3	6.3	6.3

$$W = W_{MIRROR} + W_{ROTOR}$$

$$W = 769 grm + 745\ grm =$$

$$1514\ grm$$

$$3.33\ LBS$$

X-AXIS

$Fr = W/2 + W/2(10.0)Qsin(wt)$	84.9 LBS
$= W/2 + W/2(6.3)QRMS$	54.1 LBS
$Fa = PRELOAD$	2.0 LBS

Y-AXIS

$Fr = W/2 + W/2(7.6)Qsin(wt)$	64.9 LBS
$= W/2 + W/2(6.3)QRMS$	54.1 LBS
$Fa = PRELOAD$	2.0 LBS

Z-AXIS

$Fr = W/2$	1.6 LBS
$Fa = PRELOAD + W(3.3)Qsin(wt)$	29.5 LBS
$= PRELOAD + W(6.3)QRMS$	56.1 LBS

$**Q = 5$

AEROSPACE/OPTICAL DIVISION **ITT**

```
1010 REM *
1020 REM *         PROGRAM EHD.BAS
1030 REM *         WRITTEN BY A. BELL
1040 REM *         ITT AEROSPACE/OPTICAL DIVISION
1050 REM *         E/O SYSTEMS
1060 REM *         NOVEMBER 1985
1070 REM *
1080 REM *   PROGRAM CALCULATES THE HARD ELASTOHYDRO-
1090 REM *   DYNAMIC LUBRICATION (EHL) FILM THICKNESS
1100 REM *   FOR A GIVEN BEARING.
1110 REM *
1120 REM ********************************************
1130 REM
1140 REM THIS PROGRAM INPUTS THE VARIOUS GEOMETRY OF A BALL BEARING AND THE
1150 REM CHARACTERISTICS OF THE LUBRICATION TO CALCULATE A ELASTOHYDRO-
1160 REM DYNAMIC FILM THICKNESS.  THE FILM THICKNESS EQUATIONS WERE DEVELOPED
1170 REM BY HAMROCK AND DOWSON.
1180 REM THE EQUATIONS ARE:
1190 REM    Hmin = 3.63 U^.68 G^.49 W^-.073 (1-e^-.68k)
1200 REM    Hc   = 2.69 U^.67 G^.53 W^-.067 (1-.61e^-.73k)
1210 REM WHERE THE THE FILM THICKNESS IS DERIVED FROM :
1220 REM    H = h/Rx    DIMENSIONLESS FILM THICKNESS
1230 REM
1240 REM VARIABLE DEFINITION:
1250 REM D = BALL BEARING DIAMETER
1260 REM DE = BEARING PITCH DIAMETER
1270 REM BETA = CONTACT ANGLE
1280 REM FI = BEARING RACE CONFORMITY RATIO
1290 REM RAX = RADII OF CURVATURE OF CONTACTING SOLID A IN X DIRECTION
1300 REM RAY = RADII OF CURVATURE OF CONTACTING SOLID A IN Y DIRECTION
1310 REM RBX = RADII OF CURVATURE OF CONTACTING SOLID B IN X DIRECTION
1320 REM RBY = RADII OF CURVATURE OF CONTACTING SOLID B IN Y DIRECTION
1330 REM RX = EFFECTIVE RADIUS IN X (MOTION) DIRECTION
1340 REM RY = EFFECTIVE RADIUS IN Y (TRANSVERSE) DIRECTION
1350 REM EA = MODULUS OF ELASTICITY OF MATERIAL A (RACE)
1360 REM EB = MODULUS OF ELASTICITY OF MATERIAL B (BALL)
1370 REM VA = POSSION RATIO OF MATERIAL A (RACE)
1380 REM VB = POSSION RATIO OF MATERIAL B (BALL)
1390 REM E = MODIFIED MODULUS OF ELASTICITY
1400 REM TEMP = TEMPERATURE OF SYSTEM
1410 REM RHO = DENSITY OF LUBRICATION
1420 REM V = KINEMATIC VISCOSITY OF LUBRICATION
1430 REM VIS = VISCOSITY OF LUBRICATION AT TEMPERATURE, TEMP
1440 REM ALPHA = PRESSURE-VISCOSITY COEFFICIENT OF LUBRICATION
1450 REM WI = ANGULAR VELOCITY OF INNER RACE
1460 REM UAI = MEAN SURFACE VELOCITY IN X DIRECTION OF CONTACTING SOLID
1470 REM W = DIMENSIONLESS LOAD PARAMETER
1480 REM U = DIMENSIONLESS SPEED PARAMETER
1490 REM G = DIMENSIONLESS MATERIAL PARAMETER
1500 REM K = ELLIPTICITY PARAMETER
1510 REM HMIN = MINIMUM-FILM-THICKNESS
1520 REM HC = CENTRAL-FILM-THICKNESS
1530 REM
1540 REM
1550 CLS
1560 INPUT"ENTER THE BEARING BALL DIAMETER , D inches >>",D
1570 INPUT"ENTER THE BEARING PITCH DIAMETER , De inches >>",DE
1580 INPUT"ENTER THE BEARING RACE CONFORMITY , f1 >>",FI
1590 INPUT"ENTER THE BEARING CONTACT ANGLE , B degress>>",BETA
1600 BETA = BETA *3.14159/180
1610 REM
1620 RAX = D/2 : RAY = D/2
1630 RBX = (DE - D*COS(BETA))/(2*COS(BETA))
1640 RBY = -FI*D
1650 RX = 1 / ( (1/RAX) + (1/RBX) )
1660 RY = 1 / ( (1/RAY) + (1/RBY) )
1670 REM OUTPUT
1680 LPRINT"BEARING GEOMETRY"
1690 LPRINT" "
1700 LPRINT"BEARING BALL DIAMETER >>",D
1710 LPRINT"BEARING PITCH DIAMETER >>",DE
1720 LPRINT"BEARING RACE CONFORMITY >>",FI
1730 LPRINT"BEARING CONTACT ANGLE, B radians >>",BETA
1760 LPRINT"ray >>",RAY
1770 LPRINT"rbx >>",RBX
1780 LPRINT"rby >>",RBY
1790 LPRINT"Rx >>",RX
1800 LPRINT"Ry >>",RY
1810 REM
1820 PRINT"ENTER BEARING MATERIAL PARAMETER'S"
1830 INPUT"RACE MATERIAL MODULUS OF ELASTICITY , E psi >>",EA
1840 INPUT"RACE MATERIAL POSSION RATIO , v >>",VA
1850 INPUT"BALL MATERIAL MODULUS OF ELASTICITY , E psi >>",EB
1860 INPUT"BALL MATERIAL POSSION RATIO , v >>",VB
1870 REM
1880 E = 2 / ( ((1-VA^2)/EA) + ((1-VB^2)/EB) )
1890 REM
1900 LPRINT"MODIFIED MODULUS OF ELASTICITY , E' >>",E
1910 REM
1920 PRINT"ENTER LUBRICATION PROPERTIES"
1930 INPUT"TYPE OF LUBRICATION >>",LUB$
1940 INPUT"TEMPERATURE OF LUBRICATION , T centigrade >>",TEMP
1950 INPUT"DENSITY OF LUBRICATION , p kg/m^3 >>", RHO
1960 INPUT"KINEMATIC VISCOSITY , v m^2/S >>",V
1970 INPUT"PRESSURE-VISCOSITY COEFFICIENT , square in/lb >>",ALPHA
1980 REM
1990 VIS = RHO*V*.0001499
2000 LPRINT" "
2010 LPRINT"LUBRICATION PARAMETERS"
2020 LPRINT"NAME OF LUBRICATION >>",LUB$
2030 LPRINT"TEMPERATURE OF LUBRICATION , centigrade >>",TEMP
2040 LPRINT"DENSITY OF LUBRICATON , kg/cubic m >>",RHO
2050 LPRINT"KINEMATIC VISCOSITY , square m/s >>",V
2060 LPRINT"VISCOSITY , lb-s/square in >>",VIS
2070 LPRINT"PRESSURE-VISCOSITY COEFFICIENT , square in/lb >>",ALPHA
2080 REM
2090 LPRINT""
2100 LPRINT"THE FILM CALCULATION IS FOR THE INNER RACE - BALL INTERFACE"
2110 PRINT"CALCULATION ASSUMES THE OUTER RACE IS HELD FIXED."
2120 INPUT"ENTER THE ANGULAR VELOCITY OF INNER RACE , rad/s >>",WI
2130 WO = 0
2140 WIR = ((DE + D*COS(BETA))/2*DE)*(WI-WO)
2150 UAI = ((DE - D*COS(BETA))/2)*WIR
2160 LPRINT"MEAN SURFACE VELOCITY IN X DIRECTION , in/s >>",UAI
2170 LPRINT""
2180 INPUT"ENTER MAX FORCE , FMAX >>", FMAX
2190 REM
2200 REM MAIN PROGRAM
2210 REM
2220 LPRINT"FORCE lbs      MINIMUM-FILM-THICKNESS in    CENTRAL-FILM THICKNESS in"
2230 FOR F = 1 TO FMAX
2240 F=F+4
2250 REM CALCULATION OF DIMENSIONLESS PARAMETERS
2260 REM LOAD
2270 W = F/(E*(RX^2))
2280 REM SPEED
2290 U = (VIS*UAI)/(E*RX)
2300 REM MATERIAL
2310 G = ALPHA*E
2320 REM ELLIPTICITY
2330 K = (RY/RX)^(2/3.14159)
2340 REM CALCULATE MINIMUM-FILM-THICKNESS
2350 REM CALCULATE MINIMUM-FILM-THICKNESS
2360 HMIN = 3.63*(U^.68)*(G^.49)*(W^-.073)*(1-2.718^(-.68*K))
2370 REM CALCULATE CENTRAL-FILM-THICKNESS
2380 HC = 2.69*(U^.67)*(G^.53)*(W^-.067)*(1-.61*2.718^(-.73*K))
2390 LPRINT F, HMIN*RX, HC*RX
2400 NEXT F
2410 LPRINT ""
2420 INPUT"DO YOU WANT TO DO ANOTHER CALCULATION Y OR N?",K$
2430 IF K$ = "Y" THEN CLS : GOTO 1910
2440 END
```

Figure 6.3-8

AEROSPACE/OPTICAL DIVISION ITT

6.3.2   HIRS/2 and AVHRR Bearing Lubrication and Life Correlation

This data is the result of an investigation to correlate bearing lubrication to performance/service in the HIRS/2 and AVHRR programs. The intent was to compare the amount of lubrication in the bearing retainer and free lubrication of the bearings per individual flight models to orbital operations.

Table 6.3.2-1 is a list of bearing lubrication for the HIRS/2 and AVHRR instruments. Retainer Wgt. is the clean dry weight of the retainer; Retainer Lub. is the amount of impregnated lubrication in the clean retainer; Free Lub. is the amount of lubrication added to the assembled bearing. All amounts are in grams.

The AVHRR/1 lubrication data is incomplete since recording the lubrication process was not incorporated into the assembly procedure. The only available information is on the AVHRR/2 bearings. Some of the data is incomplete since some of the AVHRR/2 bearings were carry overs from the earlier AVHRR/1 program.

Table 6.3.2-2 and 6.3.2-3 are simple statistical calculations which may assist in analyzing the distribution of lubrication in each bearing group (duplex, single; scan, filter/chopper). The deviation of each bearing is the amount positive or negative from the mean (average) value. The mean deviation is the average of the absolute value of deviation of each bearing. the standard deviation is the root-mean-square of the deviations.

A correlation between the amount of lubrication in the bearings with the achieved life to date can be made with the aid of Table 6.3.2-4. This table is status of the spacecraft as of this date. By comparing the amount of lube in each instrument bearing with the time since launch one can get an idea of the success of the lubrication achieved in the HIRS/2 and AVHRR Instruments.

Table 6.3.2-1

FM	S/N	RETAINER WGT.	RETAINER LUB.	FREE LUB.	
HIRS/2 SCAN DUPLEX BEARINGS					
1	7	.22830	.06485	.00750	09-23-77
	7B	.25915	.02960	.00735	
2	14	.26080	.03375	.00765	11-12-77
	14A	.22960	.03135	.00790	
3	27	.23910	.05005	.00720	02-06-78
	27A	.27890	.04485	.00720	

TABLE 6.3.2-1 (cont'd)

FM	S/N	RETAINER WGT.	RETAINER LUB.	FREE LUB.	

HIRS/2 SCAN DUPLEX BEARINGS

FM	S/N	RETAINER WGT.	RETAINER LUB.	FREE LUB.	
		.24490	.03620	.00740	05-24-78
		.28060	.03480	.00700	
4	12	.25730	.03710	.00780	05-24-78
	12A	.27860	.02730	.00720	
5	26	.27130	.02680	.00715	02-29-78
	26A	.23755	.03305	.00755	
		.27030	.03280	.00720	05-15-78
		.24080	.02700	.00760	
6	25	.28535	.03735	.00710	02-29-78
	25A	.24585	.02760	.00730	
		.28410	.03080	.00710	05-15-78
		.24670	.03590	.00760	
7	23	.26085	.04260	.00745	02-27-78
	23A	.28175	.02970	.00770	
		.25880	.04000	.00710	05-15-78
		.27980	.03060	.00710	

HIRS/2 SCAN SINGLE BEARINGS

FM	S/N	RETAINER WGT.	RETAINER LUB.	FREE LUB.	
1	007	.27240	.03200	.00720	09-23-77
2	001	.24735	.04800	.00730	11-12-77
3	011	.27610	.02450	.00730	05-17-78
		.27390	.02820	.00785	02-26-78
4	004	.25380	.05245	.00715	02-27-78
		.25310	.04170	.00770	05-17-78
5	009	.24310	.04780	.00795	02-29-78
		.24350	.03180	.00730	05-17-78
6	006	.27620	.03266	.00705	02-29-78
		.27470	.02070	.00740	05-17-78
7	010	.26715	.03010	.00735	03-06-78
		.26800	.02860	.00730	05-17-78

TABLE 6.3.2-1 (cont'd)

FM	S/N	RETAINER WGT.	RETAINER LUB.	FREE LUB.	

HIRS/2 FILTER/CHOPPER DUPLEX BEARINGS

FM	S/N	RETAINER WGT.	RETAINER LUB.	FREE LUB.	
1	7-023A	.35430	.01805	.02125	08-18-77
	7-023B	.36630	.02170	.02010	
2	7-053A	.36000	.01310	.02220	03-30-78
	7-053B	.35490	.01150	.02000	
		.37260	NA	.02001	04-22-78
		.36870	NA	.01985	
		.37260	.02001	.02048	06-05-78
		.36873	.01985	.02081	
3	7-021A	.36610	.01710	.02140	08-18-77
	7-021B	.35950	.01535	.02265	
		.37700	.02145	.02150	03-22-79
		.37920	.02230	.02105	
4	7-043A	.34185	.01225	.02135	09-27-77
	7-043B	.35655	.01180	.02105	
		.35695	.02040	.02120	07-20-79
		.37043	.02020	.02073	
5	7-044A	.36490	.01445	.02125	09-27-77
	7-044B	.34815	.01420	.02125	
		.38140	.02090	.02050	1Q-18-79
		.36260	.02110	.02075	
6	7-022A	.36585	.01885	.02055	08-18-77
	7-022B	.35340	.01915	.02060	
		.37976	NA	.02190	02-26-80
		.36560	NA	.02060	
		NA	NA	.02035	03-08-80
		NA	NA	.02060	
7	7-051A	.35490	.01190	.02090	09-27-77
	7-051B	.34320	.01290	.02065	
		.36950	.02015	.02075	06-17-80
		.35900	.02110	.02110	

TABLE 6.3.2-1 (cont'd)

FM	S/N	RETAINER WGT.	RETAINER LUB.	FREE LUB.
AVHRR/2 SCAN DUPLEX BEARING				
SN 201	5-018	.48249	.02633	.0073
	5-018A	.48972	.02432	.0073
SN 202	5-009	NA	NA	.0069
	5-009A	NA	NA	.0070
SN 203	5-017	.48584	.01796	.0071
	5-017A	.49237	.01388	.0072
SN 204	5-016	NA	NA	.0072
	5-016A	NA	NA	.0073
SN 205	5-010	.48260	.02725	.0075
	5-010A	.50456	.01441	.0076
SN 206	2-006	.51466	.01204	.0071
	2-006A	.51412	.01219	.0072

TABLE 6.3.2-2

HIRS/2 SCAN DUPLEX BEARINGS RETAINER DRY WEIGHT

GRAMS	DEVIATION
.2283	-3.025356E-02
.25915	5.964339E-04
.2608	2.24644E-03
.2296	-2.895357E-02
.2449	-1.365356E-02
.2806	2.204645E-02
.2573	-1.253575E-03
.2786	2.004644E-02
.2703	-1.174644E-02
.2408	-1.775357E-02
.2841	2.554643E-02
.2467	-1.185356E-02
.2588	2.464354E-04
.2798	2.124643E-02

MEAN :	.2585536
MEAN DEVIATION :	1.481735E-02
STANDARD DEVIATION :	1.799336E-02

HIRS/2 SCAN DUPLEX BEARINGS RETAINER LUBRICATION

GRAMS	DEVIATION
.06485	2.970357E-02
.0296	-5.54643E-03
.03375	-1.396429E-03
.03135	-3.796429E-03
.0362	1.053572E-03
.0348	-3.464297E-04
.0371	1.953568E-03
.0273	-7.84643E-03
.0328	-2.34643E-03
.027	-8.14643E-03
.0308	-4.346431E-03
.0359	7.535704E-04
.04	4.853569E-03
.0306	-4.54643E-03

MEAN :	3.514643E-02
MEAN DEVIATION :	5.47398E-03
STANDARD DEVIATION :	8.990461E-03

TABLE 6.3.2-2 (cont'd)

HIRS/2 SCAN SINGLE BEARINGS RETAINER DRY WEIGHT

GRAMS	DEVIATION
.2724	1.054999E-02
.24735	-1.449999E-02
.2739	.01205
.2531	-8.749992E-03
.2435	-1.835001E-02
.2747	1.284999E-02
.268	6.150007E-03

MEAN	:	.26185
MEAN DEVIATION	:	1.188571E-02
STANDARD DEVIATION	:	1.243833E-02

HIRS/2 SCAN SINGLE BEARINGS RETAINER LUBRICATION

GRAMS	DEVIATION
.032	-9.999983E-04
.048	.015
.0282	-.0048
.0417	8.700002E-03
.0318	-1.199998E-03
.0207	-.0123
.0286	-.0044

MEAN	:	.033
MEAN DEVIATION	:	6.771428E-03
STANDARD DEVIATION	:	8.424624E-03

TABLE 6.3.2-2 (cont'd)

HIRS/2 FILTER/CHOPPER DUPLEX BEARINGS RETAINER DRY WEIGHT

GRAMS	DEVIATION
.3543	-1.451218E-02
.3663	-2.512187E-03
.3762	3.787816E-03
.36873	-8.2165E-05
.377	8.187831E-03
.3792	1.038784E-02
.35695	-1.186216E-02
.37043	1.617819E-03
.3814	1.258782E-02
.3626	-6.212175E-03
.37976	1.094782E-02
.3656	-3.212184E-03
.3695	6.878376E-04
.359	-9.812176E-03

MEAN : .3688122
MEAN DEVIATION : 6.886429E-03
STANDARD DEVIATION : 8.338867E-03

HIRS/2 FILTER/CHOPPER DUPLEX BEARINGS RETAINER LUBRICATION

GRAMS	DEVIATION
.01805	-2.322143E-03
.0217	1.327857E-03
.02001	-3.621429E-04
.01985	-5.221423E-04
.02145	1.077857E-03
.0223	1.927856E-03
.0204	2.785772E-05
.0202	-1.721438E-04
.0209	5.278569E-04
.0211	7.278566E-04
.01885	-1.522143E-03
.01915	-1.222143E-03
.02015	-2.221428E-04
.0211	7.278566E-04

MEAN : 2.03714E-02
MEAN DEVIATION : 9.064284E-04
STANDARD DEVIATION : 1.123331E-03

Table 6.3.2-3.

HIRS/2 SCAN DUPLEX BEARINGS FREE LUBRICATION

GRAMS	DEVIATION
.0075	1.071426E-04
.00735	-4.285714E-05
.00765	2.571428E-04
.0079	5.071424E-04
.0074	7.142779E-06
.007	-3.92857E-04
.0078	4.071426E-04
.0072	-1.928574E-04
.0072	-1.928574E-04
.0076	2.071429E-04
.0071	-2.928572E-04
.0076	2.071429E-04
.0071	-2.928572E-04
.0071	-2.928572E-04

MEAN	:	7.392857E-03
MEAN DEVIATION	:	2.428571E-04
STANDARD DEVIATION	:	2.770102E-04

HIRS/2 SCAN DUPLEX BEARINGS FREE LUBRICATION

GRAMS	DEVIATION
.0072	-1.571425E-04
.0073	-5.714223E-05
.00785	4.928573E-04
.00715	-2.071424E-04
.0073	-5.714223E-05
.0074	4.28576E-05
.0073	-5.714223E-05

MEAN	:	7.357143E-03
MEAN DEVIATION	:	1.530609E-04
STANDARD DEVIATION	:	2.145236E-04

Table 6.3.2-3. (cont'd)

HIRS/2 FILTER/CHOPPER DUPLEX BEARINGS FREE LUBRICATION

GRAMS	DEVIATION
.02125	4.521441E-04
.0201	-6.978568E-04
.02048	-3.178567E-04
.02081	1.214445E-05
.0215	7.021446E-04
.02105	2.521444E-04
.0212	4.021432E-04
.02073	-6.785616E-05
.0205	-2.978556E-04
.02075	-4.785694E-05
.02035	-4.478563E-04
.0206	-1.978558E-04
.02075	-4.785694E-05
.0211	3.021434E-04

MEAN :	2.079786E-02
MEAN DEVIATION :	3.032654E-04
STANDARD DEVIATION :	3.722363E-04

Table 6.3.2-4. TIROS-N/NOAA History

SATELLITE	LAUNCH DATE	AVHRR		HIRS/2		REMARKS
		UNIT	DELIVERY	UNIT	DELIVERY	
TIROS-N	10-13-78	PFM	12-22-76	PFM	5-1-78	AVHRR had electrical failure after 25 months. HIRS/2 functional at S/C deactivation 3-1-81.
NOAA-6/A	6-27-79	103	4-17-78	FM-1	8-23-78	AVHRR had intermittent elect. problem starting in 1982, but continued operational until S/C deactivated in 1983. HIRS/2 filter wheel stopped 10-83. S/C reactivated 7-4-84 when NOAA-8 failed. AVHRR was ok. AVHRR still running 5-86.
NOAA-B	5-28-80	104	11-20-78	FM-2	2-17-79	Launch failure.
NOAA-7/C	6-23-81	201	1-8-79	FM-4	2-25-80	AVHRR operational thru 5-86. Some scanner jitter increase after 31 months. HIRS/2 filter wheel stopped 2-6-85.
NOAA-8/E	3-28-83	102	9-11-78	FM-3	10-15-79	AVHRR and HIRS/2 operational. S/C clock failure in 7-1-84.
NOAA-9/F	12-11-84	202	4-22-80	FM-6	1-19-81	AVHRR and HIRS/2 operational
NOAA-G		101	1-31-78	FM-5	4-15-84	Next expected launch. Oldest AVHRR and first HIRS/2I.
NOAA-D		203	9-22-81	FM-7	4-20-81	Launch date unknown.

6.3.3   AVHRR Scanner-Oil Reservoir

At the beginning of this study effort the direction of improvement was through the use of an active lubrication source. This improvement provided a method to supply a constant supply of oil in the bearings. Two approaches were developed to maintain a constant oil supply. The first utilizes an external reservoir place in an existing scanner housing cavity. In this cavity, a bi-metallic container would retain the oil. A thermal gradient (via electric command) placed on the container will cause a reduction in volume forcing the displacement of the oil to the bearing raceway via a wick. The problem with such an active reservoir is the control and containment of the oil in the bearing assembly. An oil atmosphere of some partial pressure in the bearing assembly will tend to migrate toward the vacuum of space. This outgassing tendency needs to be controlled to prevent the contamination of the oil onto the various exposed optical elements in the instrument. To contain the oil, labyrinth seals are required. The present AVHRR/2 scan assembly has limited labyrinth seals.

This is not the first time that an active reservoir has been considered for the AVHRR scan bearing set. Figure 6.3.3-1 is a partial drawing of the AVHRR scan assembly. There is a cavity surrounding the scan bearing (as marked). In the previous SCMR and early AVHRR designs, a nylasint ring occupied this cavity. The original AVHRR design incorporated a nylasint porous oil retention ring located between the two bearings. The retainer was impregnated with F-50 Versalube oil. The nylasint was chosen due to its porosity and dismissed, due to the uncontrollable nature of the system. There was no containment control of the oil. Once the reservoir was under vacuum, the partial pressure of the oil in the nylasint allowed the oil to migrate. The amount of outgassing oil was sufficient to cause optical problems.

For the AVHRR/3 study the addition of a reservoir will have little impact on the current scan assembly. We might consider a reservoir using the nylasint retainer. A possible reservoir design would utilize a nylasint or similar porous material to hold the oil. The retainer would be encapsulated to prevent uncontrollable fluid flow and subsequent contamination. A heater would outgas the oil via a wick to the race lands of the bearings. This is a possible scheme to extend the life of the bearings.

However, based on past experience, ITT does not recommend consideration of this approach without detailed analysis and test.

FIGURE 6.3.3-1

SPACER

HOUSING

BEARING

ROTOR/SHAFT

8009201

2.380

1.500

1.510

RESERVOIR CAVITY
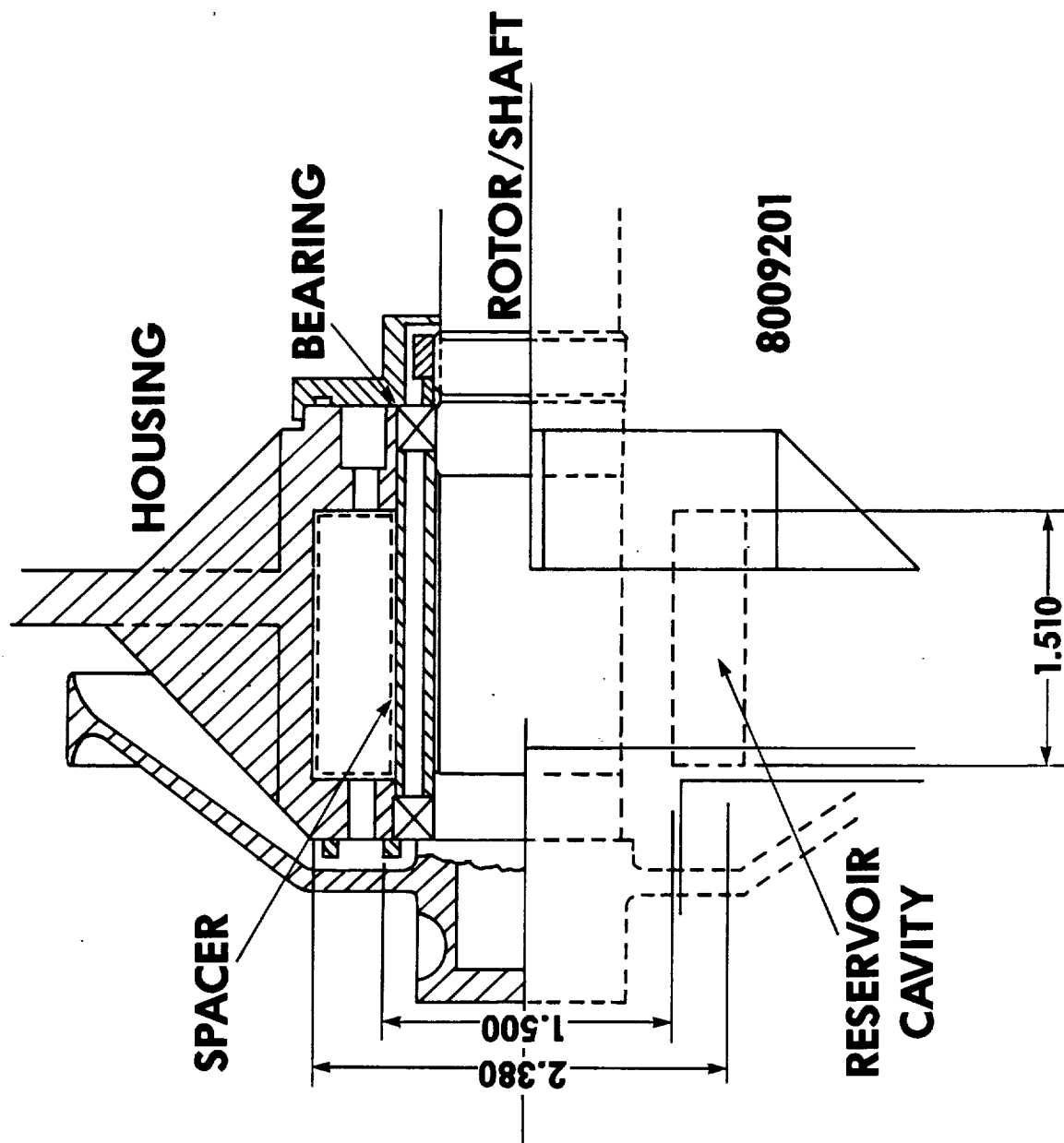
6.3.4   AVHRR Scanner Lube Investigation

A second approach to adding lubricant to the bearing is to modify the lubrication of the bearing. The current lubrication scheme vacuum impregnates oil into the retainer and adds approximately 7 mg. directly into the raceways of the assembled bearings. This 7 mg. free lube is the heart of the elastohydrodynamic film thickness developed in the running bearing. As pointed out previously, the reduction/depletion of the EHD film degrades the performance of the bearing. The alternative approach to the active lubrication reservoir is to add to the quantity "free lube" added to the bearing when processed.

In an effort to improve the scanner life of the AVHRR instruments, a series of tests were run on the AVHRR ETM scanner to evaluate the effect of additional free lube in the bearing at the beginning of life. The theory is that the failure mechanism is an eventual loss of lubrication and adding more free lube in the beginning would increase the life of the scan system. Adding free lube, however, has some negative effects on the performance of the scanner. The major effect is an increase in bearing load with an accompanying decrease in scan motor torque margin and a corresponding increase in system jitter. The attached chart, Table 6.3.4-1, outlines the effect of free lube vs. scan motor performance as measured on the ETM motor during this study.

6.3.4.1   Test

The nominal free lube is presently 7 mg. The amount of free lube was increased in increments of 4 mg steps while measuring system performance. The amount of running torque was also measured at each lubrication level to determine the change in bearing load due to this increase. At each level the power was increased in an effort to determine the change in power required to reach the jitter spec level at that quantity of the lube. In some cases (19 mg and 23 mg) the power supply regulator did not have enough range to apply more power to the scan motor.

6.3.4.2   Results

The data is fairly consistent with results as expected. As the amount of lube is increased the bearing load increases and jitter becomes worse. By increasing the torque output of the motor (power input), scanner jitter can be improved and brought within specifications, if enough motor synchronous torque and supply power is available. From the data it appears as though the amount of free lube could be doubled (7 mg to 15 mg) without much loss in system performance. With a corresponding increase in power (approximately 1W) system jitter performance can be maintained. An alternative would be to keep power constant and open up the jitter specification.

Table 6.3.4-1. Free Lube Jitter Test

Free Lube Level mg.	Jitter %	Running Torque oz. in.	Motor Power Watts	Increased Power Watts	Jitter @ Pwr. Increase oz. in.
7	95%	1.3	3.4	-	-
11	80%	1.6	3.6	4.5	97%
15	80%	1.5	3.7	4.6	95%
19	60%	1.6	3.8	5.0	77%
23	50%	1.8	4.0	5.2	63%
4	92%	.25	3.5	4.3	98%
7	100%	-	3.7	-	-

NOTE: These tests were run in early 1986 on the
Engineering Test Model AVHRR.

Jitter is defined as the percentage of scanner rotation periods which are within ±16 microseconds of the nominal rotation period over a 20 minute test duration. A higher number indicates more constant rotation.

6.4   AVHRR Scanner Bearings

The life of the scanner is limited by the performance of
the bearings. Once the bearings cannot maintain proper constant rota-
tional period, the usefullness of the instrument is lost. In this
study one area considered to improve scanner life is bearing
improvements.

6.4.1   Vendor Visit Results

Trips were made to Charles Stark Draper Laboratories,
Cambridge, Massachusetts, and Miniature Precision Bearings, Keene, New
Hampshire. These visits were taken to bring the specification up to
date with current industry standards of the spaceborne satellite
industry. The information gained by these trips and later follow up
trips layed the frame work for the new specifications defining the
scanner bearings and lubrication methods.

The initial visit with Draper Labs and MPB alerted ITT to
the requirements of proper assembly of bearings into the scanner. The
bearings in the scanner are thin section torque tube bearings. Because
of the dimensions of the bearing, the bearings have a natural tendency
to deform under pressure. The bearings must be installed properly as
not to destroy/deform shape. The best way to insure and preserve the
form of the bearing when assembled in the scan housing is to emulate
the manufacturing conditions of the bearing. This is done to alleviate
potential distortion of the thin section bearing.

The piece part drawings of the scanner shaft and housing
were given to MPB for critiquing. This allowed the manufacturer to
review the tolerances of the various parts which interface with the
bearing. After MPB's review, the control on concentricity of the shaft
and housing bearing surfaces was recommended improved from 0.001 to
.00015. The thin section slender bearing are delicate and the amount
of axial compression exerted by the shaft nut should be reduced from 50
+5 in. lb. to 10 +2 in. lb. as not to axially crush the bearing set.

One of the most crucial concerns to come from Draper Labs,
and later emphasized by MPB, was the impact of excessive handling on
performance. Thin section bearings are especially susceptible to
deformation during disassembly and assembly. The very best that can
happen during handling is for nothing to happen. Each time ITT
disassembles and reassembles a bearing, a risk of damage to the balls
and race increases.

One unique method to avoid damaging the bearing, is to use
a separatable bearing. A separatable bearing has no internal dam to
hold the balls captive when an axial load is not present. During the
disassembly of the current AVHRR/2 non-separatable bearing, the outer
race is heated and the inner race cooled to provide the necessary ther-
mal expansion and contraction to allow the balls to clear the raceway
dam. To reassemble the bearing, the same technique is employed.

During both processes, axial force is applied to assist the balls over the raceway dam. As the balls are forced over the dam, point contact is placed on the balls surface, resulting in a flat or brinelled surface on the ball. The now imperfect ball will adversely effect the performance of the bearing. Once assembled, the dam serves no useful function. ITT lubrication process entails the multiple disassembly and reassembly of a bearing. Each time this occurs, the bearing is open to damage. Both Draper Labs and MPB recommend that ITT configure to separatable bearings.

Separatable bearings are complete fall-apart assemblies, and eliminate the need for potential destructive handling. The separatable bearing will allow ITT to have post-manufacturing process control without the damage risk. The separatable bearing will be a significant cost saver. In changing the bearing to a separatable type the scrap rate should decrease.

6.4.2   Effects of Bearing Handling

A special series of tests were run on a set of AVHRR/2 scanner bearings to evaluate the effect of lubrication and stabilization process on the scanner performance. A particular interest was placed on the effect that bearing disassembly has on system jitter. It was felt that bearing damage could be occurring due to repeated disassembly.

In the normal processing of a set of bearings, the bearings and retainers are initially cleaned and the retainers vacuum impregnated with lubricant. In order to stabilize the amount of lubrication in the retainers, the bearings are assembled, weighed, installed, and run in for a period of approximately 100 hours. The bearings are then removed from the scanner, disassembled, and reweighed for loss of lubricant. This procedure is repeated until the amount of lubricant loss in the retainer is "0". This generally takes three to four iterations of the process. At this point the retainers are saturated with lubrication and considered stabilized. Free lube is finally added and the bearing installed in the scanner for the final time. Following final scanner assembly the scanner subassy is subjected to a low level vibration to "seat the bearings." This is done to remove any built-in stresses due to bearing/mounting system misalignments.

6.4.2.1   Test Setup

The setup for this test used the AVHRR jitter/drift test equipment to monitor scanner performance. The scanner was tested as a subassembly in a TV environment with a controlled temperature baseplate. All bearing processing was followed as outlined in the above procedure. A set of flight quality new buy bearings were used in the LTM Scanner (SN 4.012). Scanner performance was monitored after each step in our assembly process.

6.4.2.2   Bearing Test Summary

        The most significant degradation in scanner performance
occurred at the fourth disassembly and re-lube in the bearings to check
the effect of retainer orientation. This produced a reduction in
jitter from 100/100% to 89/61%. These numbers are the jitter (as
defined in Tale 6.3.4-1) for ± 16 Msec and ± 8 Msec. The unit was then
subjected to an assembly level vibration which improved jitter to
99/93%. This improvement implies that this vibration causes some
dimensional changes in the bearings (settling-in) to a condition where
the bearings fit better within the scanner. This effect has been
observed in the past on the completed instruments but the improvement
was typically less dramatic than this time.

        This fact seems to support the bearing manufacturer's (MPB)
analysis that for our bearing design we need to improve our mechanical
fit tolerances and the dimensional specs of the bearing itself.
(AVHRR/3 design improvement recommendations.)

        The data also seems to imply that as careful as we control
our assembly process, we can still install the scanner bearing with
built-in stresses that create distortional loads within the bearing
resulting in excessive jitter.

        The data also indicates that the assembly vibration was not
sufficient to cause the scanner to return to the most optimum condition
but a significant improvement was made in jitter performance.

6.4.3   New Bearing Specification (Appendix L)

        Discussions with MPB yielded the separatable bearing along
with a new bearing specification. In this new specification, par-
ticular attention is placed on the bearing tolerances and geometry.
Previously, the purchase of a spaceflight bearing was done to the ABEC
call outs. The ABEC specifications are not sufficient for spaceflight
bearings. The spacecraft bearing technology requires very careful
tailoring of the bearing requirements and the lubricant system to the
particular applications. It cannot be done using a bearing catalog or
handbook. Stock bearings do not have tight enough controls.

        In this new specification the controls needed to assure a
quality bearings are defined. The balls are respecified from standard
grade 10 to grade 3. The overall raceway roundness, lobing and cross
raceway curvature controls are noted as to define the geometry of the
raceway on which the balls orbit. These controls are changed to
improve the quality of the bearing and its performance. The surface
finish and surface irregularities at the contact angle (zone of contact
between the ball and race) are held to the tightest reasonable
tolerance. This insures that the lubrication needed to maintain sur-
face separation is minimal. If the outgassing rate of the Krytox 143AB
lubrication scheme remains the same (AVHRR/2) and the improved surface
requires less oil separation, the developed EHD thickness is extended.
This extension corrolates to an increased bearing life.

Run-out and parallism controls are placed on the bearing to assure optimal bearing performance. Raceway parallism controls the two raceways of a duplex bearing from being slightly skewed to one another. This skew will cause a binding condition and an increase in running torque. After a period of time the uneven wear would affect the bearing. One method to alleviate potential non-parallel alignment of the two bearings is with a one-piece outer raceway. Both outer raceways would be ground on the same piece in the same setup and eliminate the potential nonparalism. This one piece bearing has unique assembly problems in trying to keep the bearing together during assembly. However, the advantages of the bearing outweigh the assembly problem.

6.4.4 Additional Bearing Investigation

In preparing a set of scanner bearings for use, 7 mg. of free lubrication in addition to a vacuum impregnated retainer is used to oil the bearing. In orbit after two years, heat is applied to the scanner housing. It is believed that the heat outgasses the oil out of the retainer which lubricates the bearing. Draper Labs contends that ITT's scenario is nothing more than a dimensional thermal change which relieves a binding condition due to wear generated in orbit.

Draper's studies in bearing research detailed the function of the retainer. The single purpose of the retainer is to lubricate the bearing. Draper Labs has developed "retainerless bearings" thus, they now contend that the bearing retainer's primary function is to lubricate the balls. As the ball contacts the retainer, the retainer material compresses, resulting in the wicking of the suspended oil onto the ball. As the ball rolls, the oil is carried back around (surface tension) to the retainer, to be reabsorbed back into the retainer. This pump action supplies the lubrication to maintain the EHD raceway/ball interface separation.

The current AVHRR bearing retainers are made of cotton base phenolic which holds approximately 3.5% oil by weight. MPB suggested that ITT investigate the merits of paper base phenolic and polyimide retainers. The oil retention of these materials is approximately double that of linen base. Retainers made of the paper base have less strength than the linen base; however, due to the low operational rotational speed, MPB feels that the strength reduction will not be a problem. ITT is currently evaluating these materials but does not recommend a change at this time.

The 1985 and 1986 ITT IR&D bearing study is investigating processes, which when applied to the bearing, will alter the wear characteristics of the ball/raceway interface. Two treatments under investigation by ITT are Titanium Carbide and ion implantation of Titanium and Carbon.

These coatings alter the interface between the balls and raceways in an effort to alter the wear mechanics of a bearing and improve life. Titanium Carbide, TiC coating, is a coating which is deposited onto the balls and raceway surface. The coating is a 5 microinch tenaciously adherent coating of titanium carbide which is not allowed to crystallize, yielding a nearly amorphic substrate. The amorphic structure has no grain boundaries (origination of most surface cracks) and the usual brittle fragmentation associated with ultra-hard, ultra-thin materials is overcome. As the ball rolls along, the raceway drag forces at the contract interface are borne by the TiC coating while the impact loading is transmitted through the coating to the bulk material. Both ball and race are coated with the friction coefficient between the carbide/carbide interface in the range of 0.20 to 0.22. The coefficient of friction of dry steel on steel, is 0.8. Bearings used in the ITT-built INSAT-1 VHRR scanner use TiC coated bearings and have worked in orbit for over 3 years with no problem.

The second process alters the bearing surface on the atomic level. The process of ion implantation utilizes a chosen charged atomic species which is accelerated by an electric potential into the surface of the target material. This method of altering a material's surface atomic structure has its roots in the semiconductor industry. This technology dopes (alters) the substrate to improve the electrical characteristics of the material.

A material is defined by the unique arrangement of species atoms. The structure of these atoms is referred to as the atomic lattice. The characteristics of the material are directly related to this lattice. All lattice structures have various flaws which affect the material characteristics. These flaws are lattice tears or dislocations and atom vacancies.

The ion implantation process involves using a high energy (KeV) beam of energetic ions accelerated through an electric field which directs the desired ions into the surface (lattice of the target material). The incident ions impinge the surface to a shallow depth, typically .15 micrometers. These ions occupy the vacant lattice locations or interstitial locations. Interstitial locations are the voids between legitimate lattice locations, the voids between adjacent atomic spheres. The atomic packing density of the volume penetrated, increases approximately 50 percent and yields a totally amorphorus (non-crystalline) structure of glass/ceramic nature.

By occupying the interstitial and lattice vacancies, the lattice dislocations, voids and microstructural discontinuites are closed, thus altering the wear characteristics of the surface. These defects in the lattice are the source of crack propagation which leads to surface degradation/failure when the film thickness collapses and cannot sustain proper separation between the ball and race.

The raceways are treated and the balls are untreated. The intent is to change the metal to metal interface to a metal to ceramic contact. The coefficient of friction of this interface, dry is approximately .2.

C - 3

6.5   Recommendations for AVHRR/3 Scanner

ITT recommends the following changes be implemented to the scanner for the AVHRR/3. These recommendations are the result of discussions with the various manufacturers, technical organizations and testing completed at ITT. In general our philosophy is to not make any drastic changes to what is already proven to be quite successful.

6.5.1   Scan Motor

Appendix I specifies the requirements for changes to the AVHRR/3 scan motor. ITT recommends these changes to improve the overall scanner performance. Essentially the changes will provide a scan motor with increased synchronous output torque. The changes also reduce the variation in performance seen from motor to motor.

In addition to the above electrical changes ITT recommends some mechanical changes to the bearing mounting areas. As outlined in section 6.4.1 the tolerances on the bearing mounting bores and scan shaft lands will be tightened and specified to provide a better fit for the thin section bearings.

6.5.2   Bearings

The bearings should be re-specified to the new specification as outlined in section 6.4.3 and Appendix L. In addition the required lubrication processing will be reviewed in an effort to reduce bearing handling. The separatable bearing assembly will require some special handling fixtures but will reduce the possibility of handling damage now experienced.

6.5.3   Lubrication

Based on successful TIROS performance to date, ITT recommends we keep our present lubrication type KRYTOX 143AB and increase the amount of lube in the bearing. The increased sync torque of the motor will handle this increase in load and maintain a safe level of scanner torque margin. The amount of lube increase shall be a joint decision between NASA and ITT. As an alternate, the relaxation in the system jitter requirements by a factor two should be allowed by NASA/NOAA to accommodate the increase in lube.

7.0   Channel 1, 2 and 3A Gain Change

7.1   Requirements

A non-linear gain output for Channels 1, 2, and 3A in lieu of the present linear output is now required because of the proposed signal-to-noise requirements and the desire to resolve and report a change of 0.01 in aerosol optical thickness. A suggested dynamic range based on 1000 counts being equaled to 100 percent Albedo is:

Channel	Albedo Range (%)	Counts Range
1	0-25	0-500
	26-100	501-1000
2	0-25	0-500
	26-100	501-1000
3A	0-12.5	0-500
	12.6-100	501-1000

7.2   Dual Slope Amplifier for Albedo Channels

Figure 7.2-1 shows the amplifier design which will be used to implement the dual slope characteristic for the albedo channels.

It is desired that the signal-to-noise (S/N) is channels 1 and 2 for the AVHRR be increased to 9:1 at 0.5% Albedo and 20:1 at 0.5%A for the new Channel 3A. the data word must remain at 10 bit to be compatible with the NOAA satellite. Bit resolution required to resolve these increased S/N is 11 bits in Channel 1 and 2 and 12 bits in Channel 3A. Fortunately the higher resolution is required to obtain greater detail only at low Albedo levels. Hence a dual slope transfer response can be used which will provide the required high resolution at low levels and adequate resolution at the higher levels.

This division of the dynamic range yields 11 bit resolution in the range of 0-25%A and over 9 bit resolution for 25-100%A in channels 1 and 2. The resolution is 12 bits for 0-12.5%A and a little over 9 bits for 12.5-100%A in Channel 3A.

An amplifier which will achieve this dual slope transfer response is shown in Figure 7.2-1a. This amplifier converts the linear unipolar input shown in Figure 1b to a bipolar output as shown in figure 1c where the slope of the positive and negative voltage is different.

The circuit operates as follow. The value of V_{ref} into U1 sets the slope break point. Thus V_{ref}/V_m will be .25 for Channels 1 and 2 and .125 for Channel 3A. When e_{in} is zero the output of U_1 will be positive and it will be connected to R_2 through D_1 and must equal $+V_m$. Therefore the value of R_2 is given by:

e_OUT

R6

U2 OP27

R4

D1

R2

D2

R5

U1 OP27

R3

e_IN R1
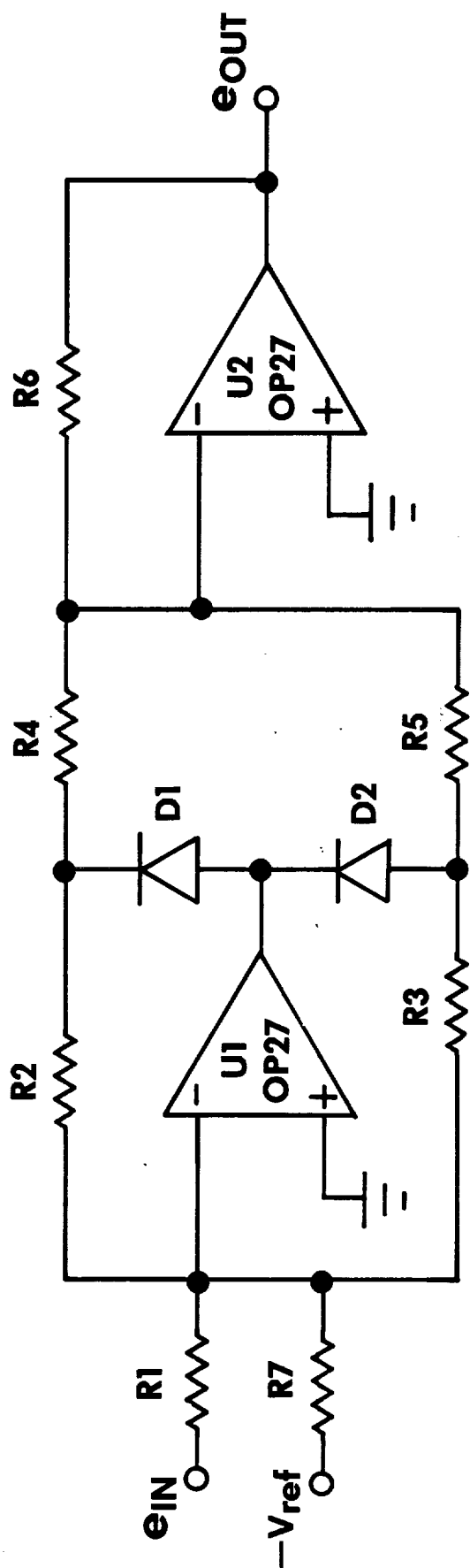
−V_ref R7

$R_2 = R_1 \, V_m/V_{ref}$

$R_3 = R_1/(1 - V_{ref}/V_m)$

$R_4 = R_5 = R_6$

$R_1 = R_7$

FIGURE 7.2-1c

V_m

100% A

$-V_m$
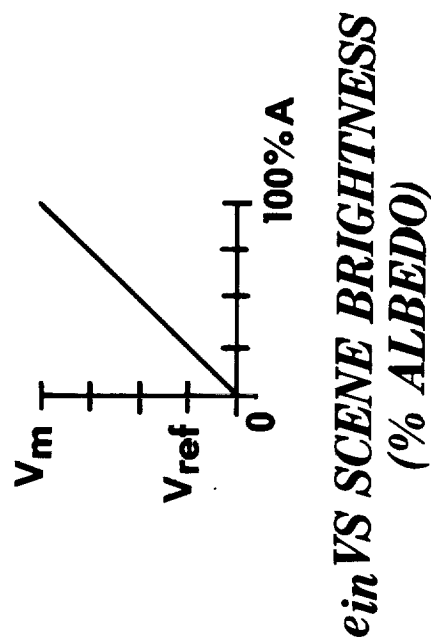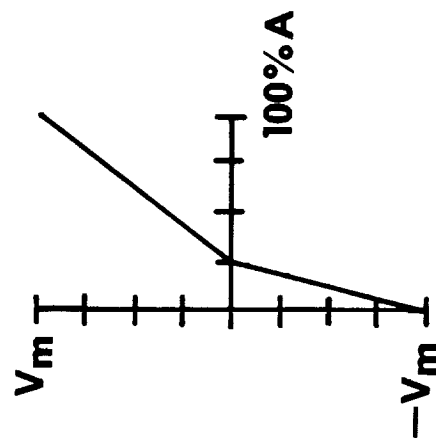
e_{out} VS SCENE BRIGHTNESS
(% ALBEDO)

AEROSPACE/OPTICAL DIVISION ITT

FIGURE 7.2-1b

V_m

V_{ref}

100% A

0

e_{in} VS SCENE BRIGHTNESS
(% ALBEDO)

$$R_2 = R_1 V_m / V_{ref}$$

This signal is inverted in the unity gain amplifier U_2 so that $e_{out} = -V_m$. When $e_{in} = V_m$ the output of U_1 is negative and is connected to R_3 through D_2 and must equal $-V_m$. Therefore the value of R_3 is given by:

$$R_3 = R_1 / (1 - V_{ref} / V_m).$$

This signal is inverted in U_2 so that $e_{out} = V_m$. Resistors R_4 and R_5 must be equal so that both polarity signals out of U_1 are properly summed at the input to U_2. If the peak outputs is $\pm V_m$ then R_6 must be adjusted accordingly.

The above design can be implemented into the existing AVHRR/2 channel 1 and channel 2 post amplifier circuits. Since channel 3A is an added feature to the AVHRR/3, A new circuit will be required.

8.0   Test Equipment Changes

8.1   Requirements:

        Changes in channels and the addition of Channel 3A will
require changes to the AVHRR/2 test equipment. Also, the Bench Check
Unit computer (HP 2100) will be obsolete in 1985 and Hewlett Packard
will not provide maintenance support for it.

        This part of the study will determine what changes are
required to the AVHRR/2 test equipment at subsystem and system test
levels as a result of changes made to the instrument. The study will
also determine what changes are recommended for the BCU computer system
(both hardware and software changes will be addressed.

        The output of this portion of the study will consist of a
list of AVHRR/2 and HIRS/2 test equipment which ITT A/OD recommends to
be replaced or reworked prior to the next series of flight models. Ths
list will include details of what must be done and what new equipment
is needed.

        The impact of each proposed change on the test equipment
will be addressed.

8.2   New AVHRR/3 and HIRS/3 Test Computers

        As part of the AVHRR and HIRS/2 Modification Study
Contract, ITT established new computer systems for the NOAA-K,L,M
Flight Model program expected next year. The AVHRR computing system is
considered obsolete by HP and is no longer considered maintainable by
them. Parts of the HIRS/2 computers are obsolete and the entire unit
is probably only a year away from total obsolescence.

        The goal for this study is to come up with identical (but
separate) computer hardware for HIRS and AVHRR. Differences would be
in software and peripherals (perhaps we will need different interface
boards for the two systems). It has been suggested that the AVHRR go
to a disk operating system so that programs can be written or changed
as needed (preferably in the FORTRAN format that HIRS/2 uses).

        An investigation into the test computer requirements for
the TIROS project was performed to determine if that replacement com-
puter hardware should be identical to that purchased for the GOES-I/M
program. Information resulting from that investigation is presented
here as an aid to selecting the final hardware configuration to be
implemented.

8.2.1   AVHRR Computer Use

        The present AVHRR test computer has the following
characteristics:

Present Tasks

Collect telemetry data
Collect line scan data
Measure scanner jitter
Store calibration information on Magnetic Tape
MIRP simulation
Monitor chamber target temperatures

Data Rate

- Data collected is 2400 words/line at 200 kw/sec rate.

- One minute of data is collected.
  (i.e. 2400 words/line x 6 lines/sec x 60 sec.= 864K
  words) or 1.728 Mbyte of data in 1 min.

- Avg. data rate $=\dfrac{864K \text{ words}}{60 \text{ sec}} = 14.4KW/sec$

Hardware

The present computer consists of a paper tape based system
with the following features:

- 24K word memory
- Floating point hardware
- Time base generator
- 800 BPI tape drive
- CRT terminal
- Matrix printer

- Interfaces for the following
    - Scanner/DVM
    - Two counter/timers ⎤ 5-16 bit parallel
    - D/A output
    - Laser recorder   ⎦
    - Temp monitor   16 bit ITT built
    - Instrument data   DMA 16 bit
    - MIRP   16 bit parallel

Software

The following programs are currently in use:
     21 operational
      6 special
    27 total programs

On the average, each program is approximately 1000 lines
long. Assuming a program development time of 15 minutes per line of
code, the total software development time was 6750 man hours.

New Tasks

New tasks and capabilities that must be incorporated in a new system are as follows:

- Duplicate magnetic tapes
- Control of chamber targets & baseplates
- Store a full 1 minute of data on disk & then process data
- Graphic plotter capability

8.2.2   HIRS Computer Use

The present HIRS test computer has the following characteristics:

Present Tasks

Normal data collection
Field of view testing
Calibration
Tape operation
Monitor chamber temperatures
Collect telemetry data

Data Rate

- Inst. Data = 2880 bits/sec
- BCU Data = 1280 bits/sec
  Total Data = 4160 bits/sec in 13 bit words
                   or 320 words/sec into the CPU

- one scan line repeats every 6.4 sec resulting in 2048 words/scan line

Hardware

The current computer consists of two disk based systems, each with the following features:

- 24k word memory
- 800 BPI Tape drive
- CRT terminal
- printer
- two 2 1/2 Mbyte disks

- Interfaces for the following
    - X axis Prog. Table   5-16 bit parallel
    - Y axis Prog. Table
    - Video subsystem
    - 16 channel 12 bit A/D
    - D/A
    - Instrument & BCU Data   DMA

Software

The following programs are currently in use:

15	FOV
9	Data Collection
15	Tape operation
10	Calibration
10	Special Trouble Shooting
5	Interface
10	Misc.
74	Total programs

Based on an average program length of 1000 lines and assuming program development time of 15 minutes per line of code, the total software development time was 18,500 man hours.

New tasks & Features

New tasks and capabilities that are required in a new system are listed below.

- Plot on hardcopy and CRT
  - Target temperatures
  - Field of view curves
- Noise pattern tests
- Control of chamber targets & baseplates
- Run two instruments at the same time from one computer
- Provide external RS 232 interface
- Have only one tape drive, preferably 1600 BPI
- Two disk drives (at least one removable)

8.2.3   Suggested Equipment

Based on the present system requirements and including new capabilities for incorporating the listed desirable features, the hardware requirements listed below were developed.

Memory size was set by allowing room for all of the AVHRR data to be resident in the CPU at once in addition to allowing 1 Mbyte for the resident portion of the operating system.

Paper tape systems have been out of date since before the one we use for AVHRR was purchased. Therefore, its use was not even considered. The new system will be disk based.

Disk size will be based on the requirement to duplicate magnetic tapes. 2400 ft of tape at 800 BPI is around 23 Mbyte. 1600 BPI requires twice that.

Current trends are toward more densely packed tapes. To maintain compatability with current specified requirements and still modernize our system somewhat, a dual capability 800/1600 BPI tape drive could be used.

Hardware Function for Replacement Computer

1	CPU
1	3 M Byte Memory
1	Floating point hardware
2	Disk drives, 50 Mbyte each (removable)
2	CRT terminal (color graphics)
2	Printer (Matrix)
1	Tape drive 800/1600 BPI
1	Graphic plotter (B size)
1	DMA interface (200 kw/sec rate)
9	General purpose interface (16 bit parallel)
1	RS 232 to outside world
8	IEEE Interface
1	Real time clock

Software Changes

In general, the software for the AVHRR test program will need to be completely rewritten, i.e., an effort of approximately 5000-7000 man hours.

If the present data handling philosophy used on the HIRS program is maintained, the existing programs can pretty well be used without much modification, i.e., less than 1500 man hours. If the philosophy is changed to merge the data sources in the computer instead of in the BCU, then more extensive software changes would be required, i.e., approximately 3000-5000 man hours.

Three different computer systems were considered as candidates for the new system. These are:

HP 1000
PDP 11/84
VAX 11/750

The last is the GOES-I/M computer and was considered to see if there were any "compatibility" savings possible.

Looking at TIROS alone, there is no justification for using a computing system as big as the GOES VAX. Both the HP-1000 and the DEC PDP-11/84 (which were established as the baseline candidates early in the study program) are more than adequate to service both HIRS/3 and AVHRR/3. The plan is to have two stand-alone but identical systems, one for AVHRR/3 and one for HIRS/3.

The previously established prices for the two baseline systems are as follows (1985 cost to ITT based on vender quotes):

    HP-1000 $222,000   plus service contract

    PDP-11/84 $249,800   plus service contract

This includes 2 computers plus 4 terminals, 4 printers and 2 tape recorders for each quote.

If we are being forced to a GOES/VAX-750 for "compatability," then the TIROS system should be identical to the GOES system. The GOES hardware quoted is $490,000. This would provide, essentially, two computers tied together in a cluster mode of operation. It would allow both AVHRR/3 and HIRS/3 testing to be done simultaneously. This is an 11 rack system that takes 600 ft^2 of floor space. One rack may be eliminated for TIROS if we eliminate 3 of the disks. But this reduces the "compatability" of TIROS to GOES.

The terminals and printers for the PDP-11/84 are identical to those used on the VAX-750. Thus a certain degree of "compatability" would exist if TIROS opted for the PDP-11/84. The HP-1000 is a physically smaller system than the PDP-11/84.

If all GOES and TIROS software is written in a common language (Fortran 77, for example), then the GOES programs can be used by TIROS to some extent no matter what hardware is selected for TIROS.

If the HIRS/3 data management philosophy and the way the data flows thru the BCU is kept the same, then "a large portion" of the existing HIRS/2 software will be usable. It was previously recommended that the philosophy be changed to reduce BCU problems and make HIRS/3 data processing look more like AVHRR/3.

A final selection is not necessary at this time. It is likely that whichever system of the two (HP1000 or PDP 11/85) offers the best deal at the time of purchase will be the one selected since they are essentially equivalent.

It is clear, however, that the TIROS program will not need a GOES - equivalent VAX system.

8.3   HIRS/3 Test Equipment Upgrade

The HIRS test equipment has basically the same problems as the AVHRR's. The computer is obsolete and not capable of being maintained by Hewlett Packard and the test collimator needs to be refurbished. The wideband channel 20 modification will require additional spectral and radiometric testing at system level. Those tests can be performed using the AVHRR/2 monochromator and integrating sphere.

8.3.1   HIRS/3 Bench Check Unit Redesign

The existing Bench Check Unit (BCU) for HIRS/2 has several severe limitations which limit the versatility of testing possible. It

is old and in constant need of repair. ITT proposes to rebuild the HIRS BCU for HIRS/3 to tie in more closely with the new computer and to interface between the HIRS and its test computer in a manner similar to the AVHRR.

8.3.1.1   AVHRR BCU Approach

In this system, shown in Figure 8.3-1 all individual pieces of test equipment supplying data to the computer are interfaced directly to the computer. Information from each device under computer control is then combined in the computer by software.

The present AVHRR system is a paper tape based system. Because of this, or primarily the lack of a disk, the test software was designed to run under an overall executive with the result that the system is rigid and lacks the capability to have changes easily made to test programs.

The memory size is very limited and as such, does not have the capacity necessary for storage of any significant amount of data. As a result, the instrument data is analyzed on the fly using moving averages, etc. rather than other methods which might be preferable.

Advantages

- Merging of data from various sources is
  under software control.

- With a disk based system, there is more flexibility
- ease of data manipulation.

Disadvantages

- More computer interfaces required.

8.3.1.2   HIRS BCU Approach

The philosophy for the present HIRS test set up is shown in Figure 8.3-2 and different than that of the AVHRR. It is more hardware oriented in that the data from the various sources are merged in the BCU before being sent to the computer. This makes the BCU hardware more complex and also results in a single point failure mechanism for all sources of data.

The HIRS computer is a disk based system and the various test programs are called up individually as required. This results in good flexibility in running various engineering tests, but with the merging of data sources in the BCU, there is no flexibility in the gathering of data.

With some minor exceptions, data is stored on magnetic tape as it is generated and then read back into the computer for analysis at a later time.

Figure 8.3-1 AVHRR Test Facility Block Diagram
(EXISTING)

AEROSPACE/OPTICAL DIVISION

ITT

193
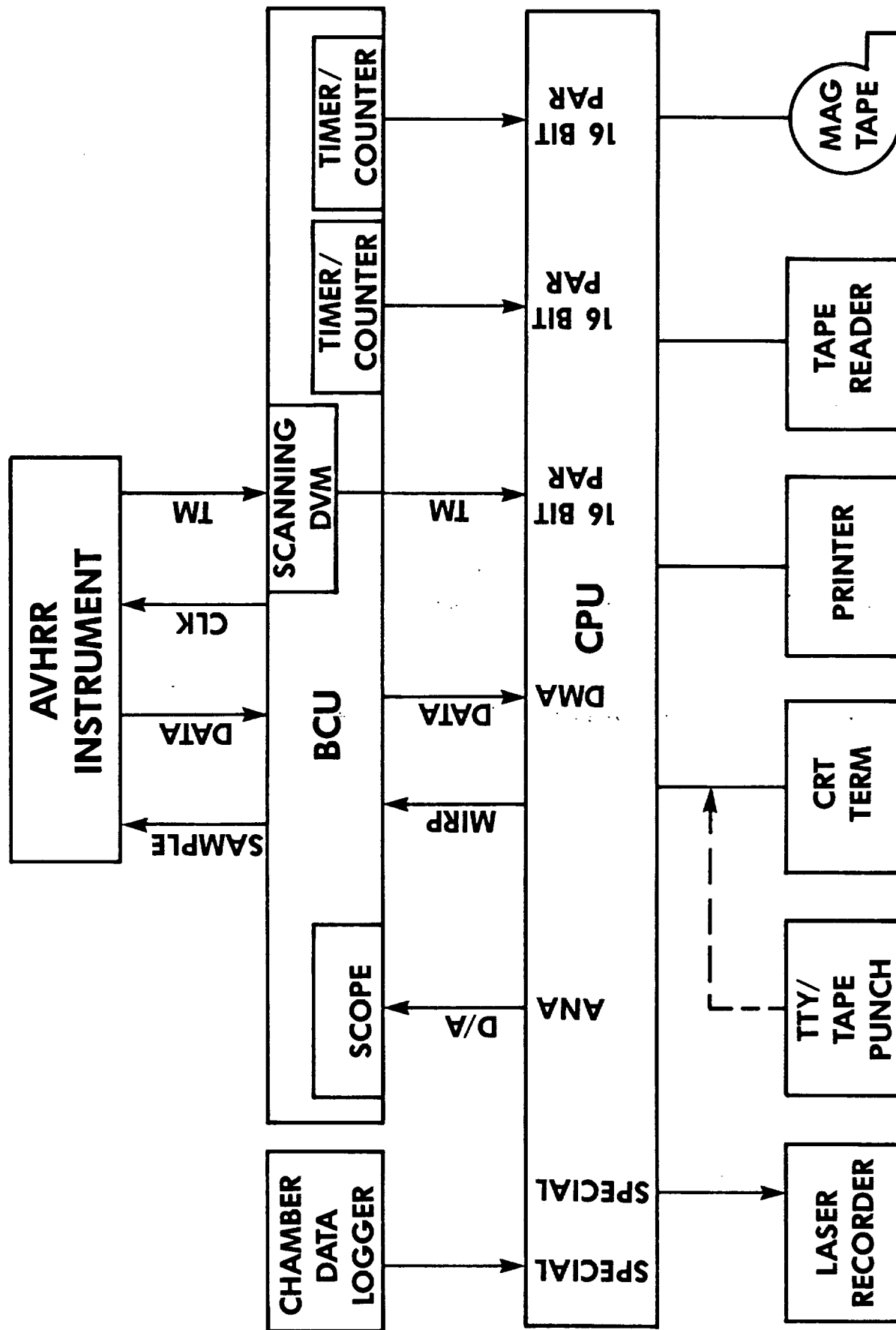
Figure 8.3-2 HIRS TEST FACILITY BLOCK DIAGRAM (EXISTING)

AEROSPACE/OPTICAL DIVISION   ITT

194
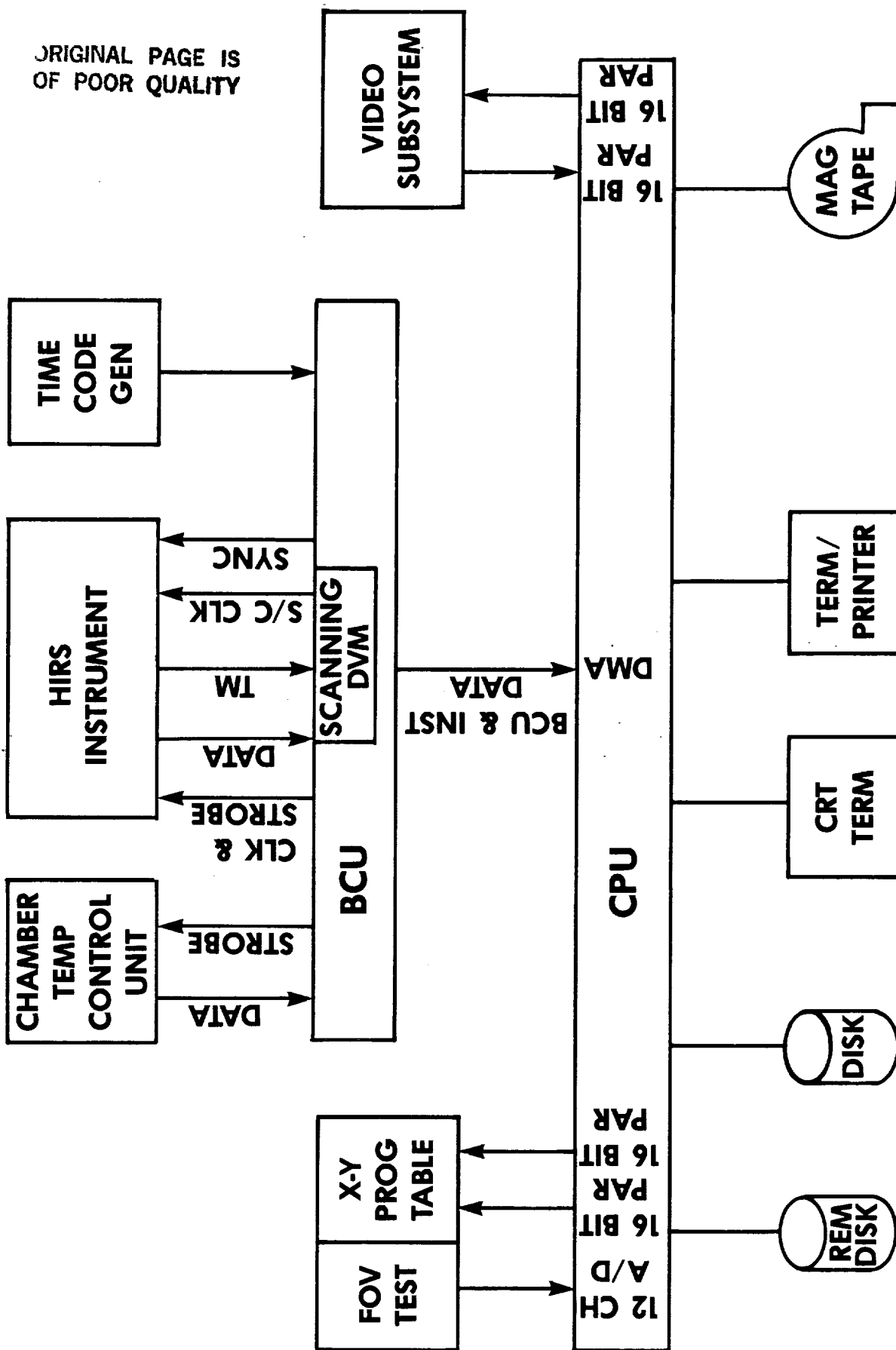
Advantages

- Fewer computer interfaces required.

Disadvantages

- Complex BCU.

- Lack of flexibility

- Single point failure for data collection.

- Instrument has to be operating to collect chamber
  baseplate & target temperature information.

8.3.1.3   Conclusion

The method used by AVHRR provides more flexibility as more
functions are under software control as opposed to being hardwired.
Merging data in the computer appears to be better suited for high data
rates. This method also allows for a less complex BCU at the expense
of more computer interfaces.

As an aside, the philosophy to be used by the GOES test
facility parallels that used on the AVHRR.

The software development time required to implement the
replacement computer on the HIRS program would increase somewhat if the
present philosophy were changed to that used on the AVHRR. However, in
the interest of flexibility and eliminating a troublesome BCU, ITT
recommends making the change.

8.3.2   HIRS/3 Test Computer

See Section 8.2 for a discussion of the new HIRS/3 com-
puter. The plan is for computer hardware identical to the AVHRR/3 com-
puter hardware (with different peripheral equipment as required) and
unique software for each.

8.4   AVHRR/2 Test Equipment

A review of the existing AVHRR/2 test equipment was con-
ducted to define what fixtures and equipment must be modified to accom-
modate the proposed changes or needed to be rebuilt due to age and
usage. Table 8.4-1 is a listing of bench level or subsystem level
equipment requiring changes. The list describes the equipment
requiring changes and the necessary work. Tables 8.4-2 & 8.4-3 are lists
of equipment changes for the vacuum chamber instrumentation, and a
listing of miscellaneous test equipment and fixturing.

Table 8.4-1 AVHRR/3 Test Equipment Modifications

A. Bench Test Setup

Assy Number   Description

8121604G2   Bench Test Cooler

1. Repaint and reinsulate the reservoir
2. Add alignment pins to Vacuum Housing.

8126026   Handing Fixture

1. Redesign attachment brackets to accommodate larger instrument.

8122048   Power Line Test Fixture

1. Redesign fixture to refine setup for noise susceptibility
    tests.

New   Circuit Board Test Fixture

1. Redesign tester to accommodate electronic circuit board
    changes.
2. Add test setup for A-D Converter testing.

New   Stability Monitor Calibration Assy.

1. Design a new Opto/Mechanical test setup to calibrate stability
    monitor.
2. A sunlit diffuser requires an extensive fixture for
    calibration.
3. A lamp monitor only requires correlation to the Visible Channel
    Calibration sphere.

8123484   Collimator Target Assy. Bench

1. Rework/replace parts in the slide assy.
2. Repaint/replace aperture targets.
3. Rework/replace worn gear drive system on the chopper assy.

8120160   Light Source Optics Test

1. Repaint Housing Assy.
2. Purchase spare lamps.

Table 8.4-2 Vacuum Chamber Instrumentation

Assy. Number | Description

Various Supports and Bracketry

1. Redesign targets/instrument supports and bracketry to accommodate changes in instrument outline. Approximately 25 pieces are affected.

8120079 | **Collimator Target Assy.**

1. Relube/rework the motor/gear assemblies.
2. Repaint the target housing.
3. Repaint/replace the aperture test targets.

8120157 | **Coherent Noise Target Assy.**

1. Rework/relube bearings and motor gear drive assys.
2. Clean and repaint target assy.

8120088G2 | **Temperature Controlled Baseplate**

1. Strip/repaint/reinsulate the instrument mounting plate.

8120104 | **Collimator Assy.**

1. Recoat primary and secondary mirrors
2. Recoat 45° mirror

8120065G2 | **Shroud and Radiant Cooler Assy.**

1. Redesign the shroud to accommodate the increased size of the instrument.
2. Remount Radiant Cooler target assy.

812096G2 | **Calibration Light Source**

1. Clean/repaint case.

8121008 | **Control Console**

1. Redesign the calibration target p.r.t. monitor system interface to be compatible with new computer system.

New | **Stability Monitor Target Assembly**

1. Design a new target assembly to test the added stability monitor.

2. Design to be based on type of monitor (light source or diffuser) may be complicated depending on final selection of monitor design. Design may also effect other targets depending on configuration.

Table 8.4-3 AVHRR/3 Test Equipment Modifications

Misc. Equipment

<u>Assy. Number</u>   <u>Description</u>

<u>8008725</u>   <u>Transit Case</u>

1. Redsign mounting plate and spares to better mount instrument in case.

<u>8120058</u>   <u>Portable Test Equipment</u>

1. Redesign P/C boards for new interface commands and TLM's.
2. Fab new cabling, worn connectors, etc.
3. Redesign front panel for added commands/TLM.

<u>Various Dust Covers, etc.</u>

1. Redesign dust covers to accommodate cooler/instrument con-figuration changes.
2. Various test parts change as instrument changes.

(New)   <u>Optics Test Fixture Ch. 1,2,3A</u>

1. Design new optics test fixturing to align and test new Aft Optics assembly.

9.0   AVHRR/2 ELECTRONIC REDESIGN

9.1   Requirements

        The AVHRR/2 uses Texas Instruments TTL components. It also
uses a discrete component A/D converter. Both vendors have indicated
that required parts will not be available for future procurements.

        The part of the study shall address, but not be limited to
the following topics:

   a.   Generate a preliminary design for an A/D converter using
        modern, available components/technology.

   b.   Establish a preliminary design approach to eliminate TTL logic
        in the AVHRR/2. Determine the types and numbers of components
        required to replace the TTL. Estimate impact on the unit in
        terms of power, volume, weight, inter-board wiring, etc. TTL
        parts need not be eliminated if appropriate substitutes can be
        obtained from other vendors.

   c.   Establish the requirements necessary to space-qualify the
        selected components (if they are not already so qualified).

   d.   Review the overall AVHRR/2 electronic design to determine if
        there are other improvements to be recommended.

   e.   Generate a conceptual design for a new CH.3 (3.7 um) pre-
        amplifier.

   f.   Define the instrument and instrument/spacecraft changes
        required if the spacecraft 5 volt bus is eliminated. Present
        plans are to eliminate this interface.

   g.   All redesigns will estimate the impact on the AVHRR/2 size,
        weight, power, etc.

   h.   RFI investigation

9.2   A/D Converter

        The A/D converter used in the AVHRR and manufactured by
Vector/Aydin Company is obsolete and cannot be produced. Therefore a
new A/D converter design is required. A new design must be transparent
to the AVHRR (i.e. electrically it must look just like the original A/D
converter) with the exception of two modifications. The first modifi-
cation is the addition of a third Albedo channel designated 3A which
will be alternated with the present Channel 3B. Selection of channel
3B or 3A will be by pulse command from the satellite. The second modi-
fication is to be able to convert unipolar data from the IR channels
(i.e. Ch 3, 4 and 5) and bipolar dual slope data in the Albedo channels
(see Section 7). In each case the output must be a 10 bit data word.

A diagram of the video multiplexer is shown in Figure 9.2-1. The switches used to select channel 3B or 3A and selection of channels 1 through 5 will be CMOS switches and are discussed in detail later in this section. The sample/hold amplifiers (SMP11) are high speed unity gain devices. they will acquire a 10V step in 5μs (0.01%) in the sample mode and settle to within 1mV in 1.5μs when switched to the hold mode.

The unity gain buffer consisting of the OP27 and the BUF03 provides a high input impedance so that resistance variations of the switches with signal level and temperature do not distort the signal. This combination provides the low frequency precision of the OP27 with the wide bandwidth, high slew rate and low output impedance of the BUF03.

The heart of the converter is the MN5246 manufactured by Micro Networks. It is a hybrid utilizing a multiplexed 7 bit flash converter to achieve 12 bit resolution with a total conversion time of 900 ns max. This device accepts bipolar video ($\pm 2.5V$). The output code is offset binary. Thus the use of the high speed sample and hold amplifier, CMOS switches, buffer amplifier and this A/D converter will allow acquisition of channel data and conversion at 3μs per channel. However care must be taken to heat sink the converter as it dissipates over 2w during operation.

The converter digital data is routed to holding registers after each conversion. The channel 3A/3B Select sends the proper code to the channel 3 register. This will be discussed later. The output of the 54LS374 is three state. During the normal 25μs readout time of these data each register will be sequentially switched to the output data bus for 5μs.

A timing diagram of the control signals for the multiplexing and conversion functions is shown in Figure 9.2-2. This timing diagram is compatible with but not identical to the present AVHRR timing. Differences are transparent to the AVHRR and the satellite and will require no change to the present design. The control logic which generates these control signals for the input/output mulitplexer and the converter is shown in Figure 9.2-3.

Analog multiplexing will be performed by CMOS switches (CD4053B). The CD4053 contains three SPDT switches, one of which is shown in Figure 9.2-4. However this CMOS is not compatible with TTL. Therefore a level shifter is required (CD40109B). One requirement of the CD40109B is that the high input must exceed 70% of the TTL V_{cc} (.7 x 5 - 3.5V). This can be assured by adding a pullup resistor to +5V on each input of the CD40109B.

The CD4053B require both plus and minus supply voltages to handle bipolar signals. Also the maximum difference between V_{dd} and V_{ee} cannot exceed 20V. Therefore the $\pm 15V$ will be divided to ± 7.5 in the circuits shown in Figure 9.2-4B. The current to operate the level

Figure 3.2-1 A/D CONVERTER DIAGRAM

ORIGINAL PAGE IS
OF POOR QUALITY

AEROSPACE/OPTICAL DIVISION

201
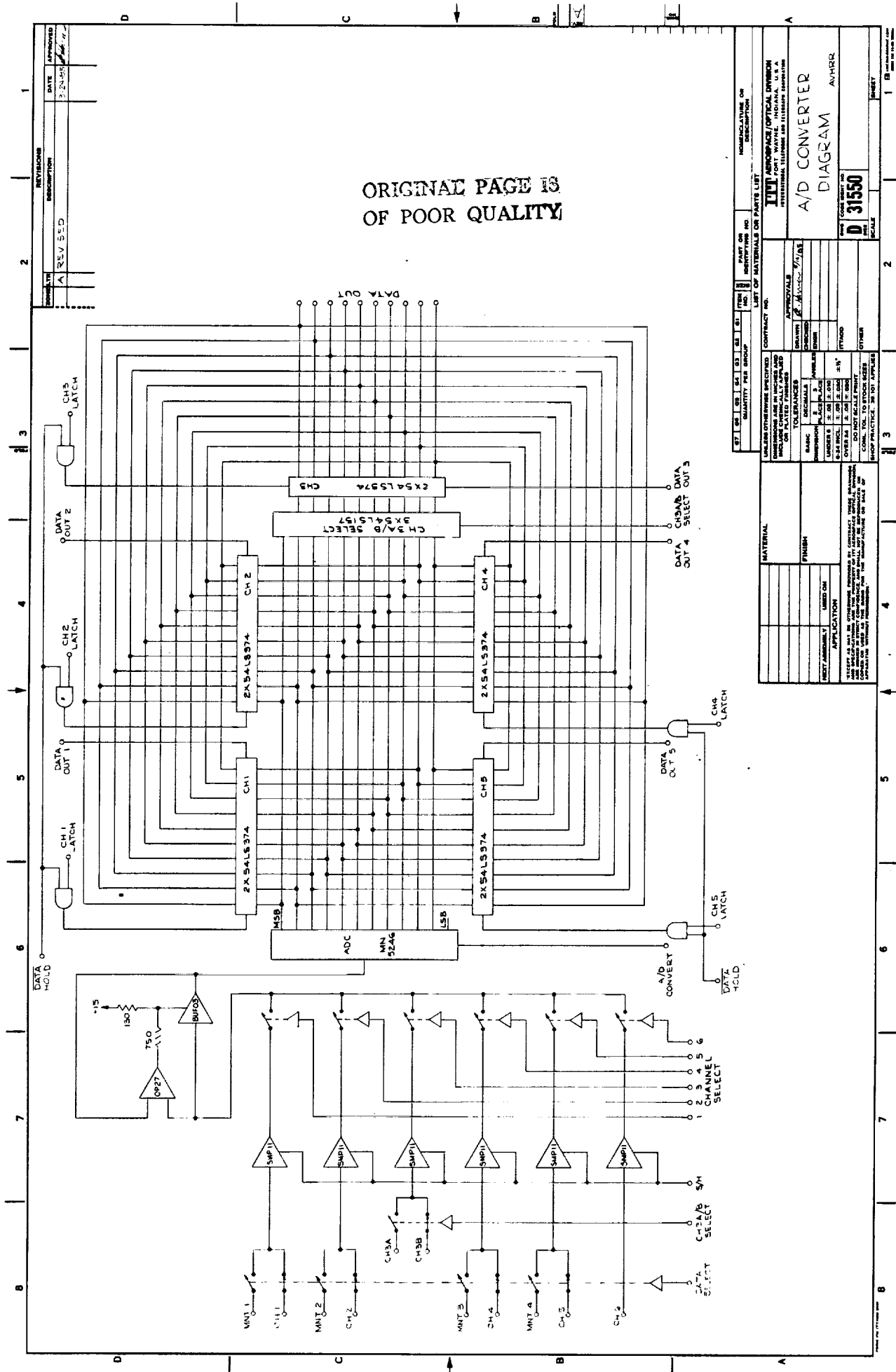
Figure 9.2-2 *A/D CONVERTER TIMING DIAGRAMS*

.9984 MHz
CLOCK

MIRP
SYNC

S/H

ADC
CONVERTER

CH1
SELECT

CH2
SELECT

CH3
SELECT

CH4
SELECT

CH5
SELECT

LATCH 1

LATCH 2

LATCH 3

LATCH 4

LATCH 5

DATA OUT 1

DATA OUT 2

DATA OUT 3

DATA OUT 4

DATA OUT 5

CH6
SELECT

AEROSPACE/OPTICAL DIVISION ITT

Figure 9.2-3   A/D CONVERTER LOGIC CONTROL DIAGRAM

ORIGINAL PAGE IS
OF POOR QUALITY

AEROSPACE/OPTICAL DIVISION

203
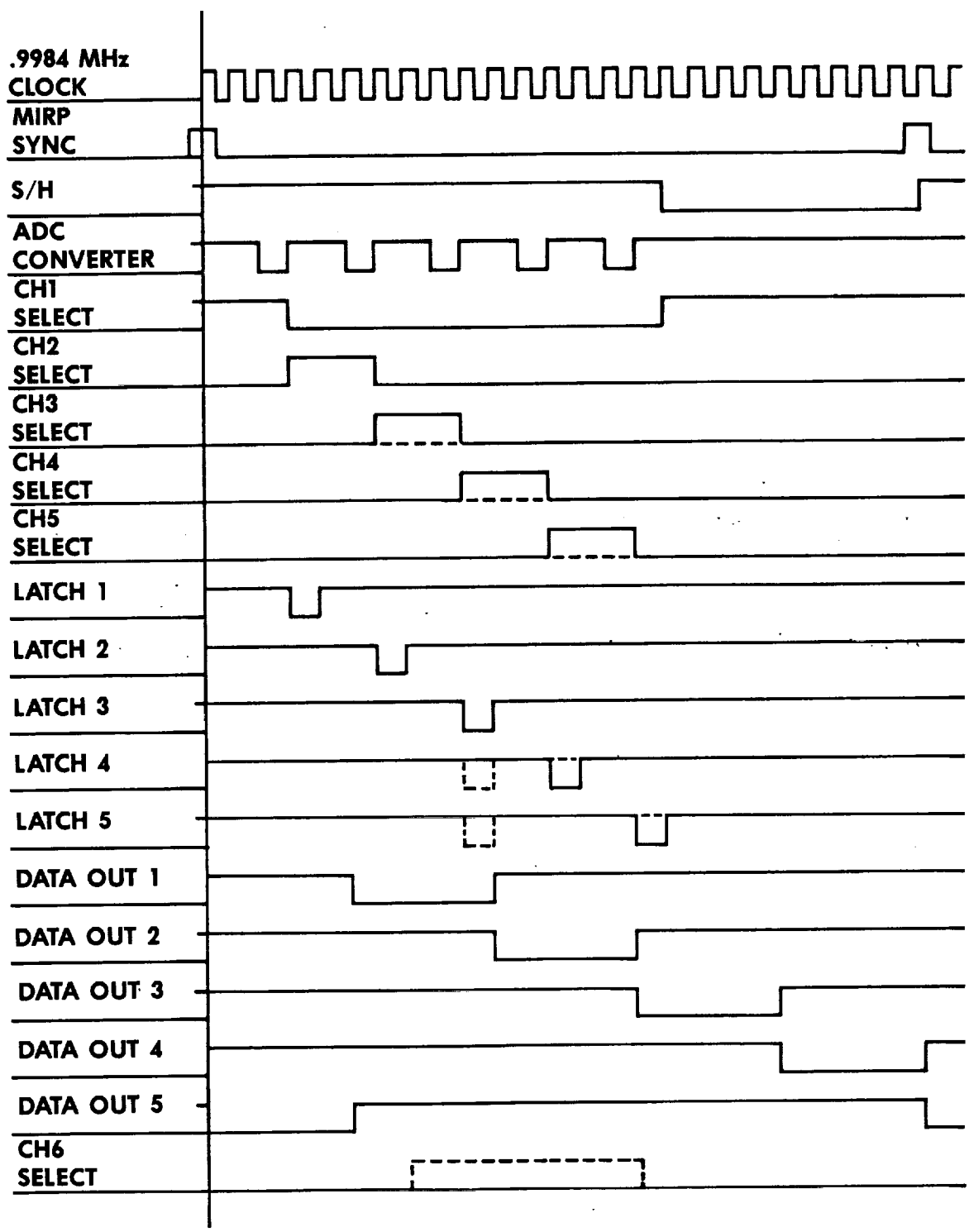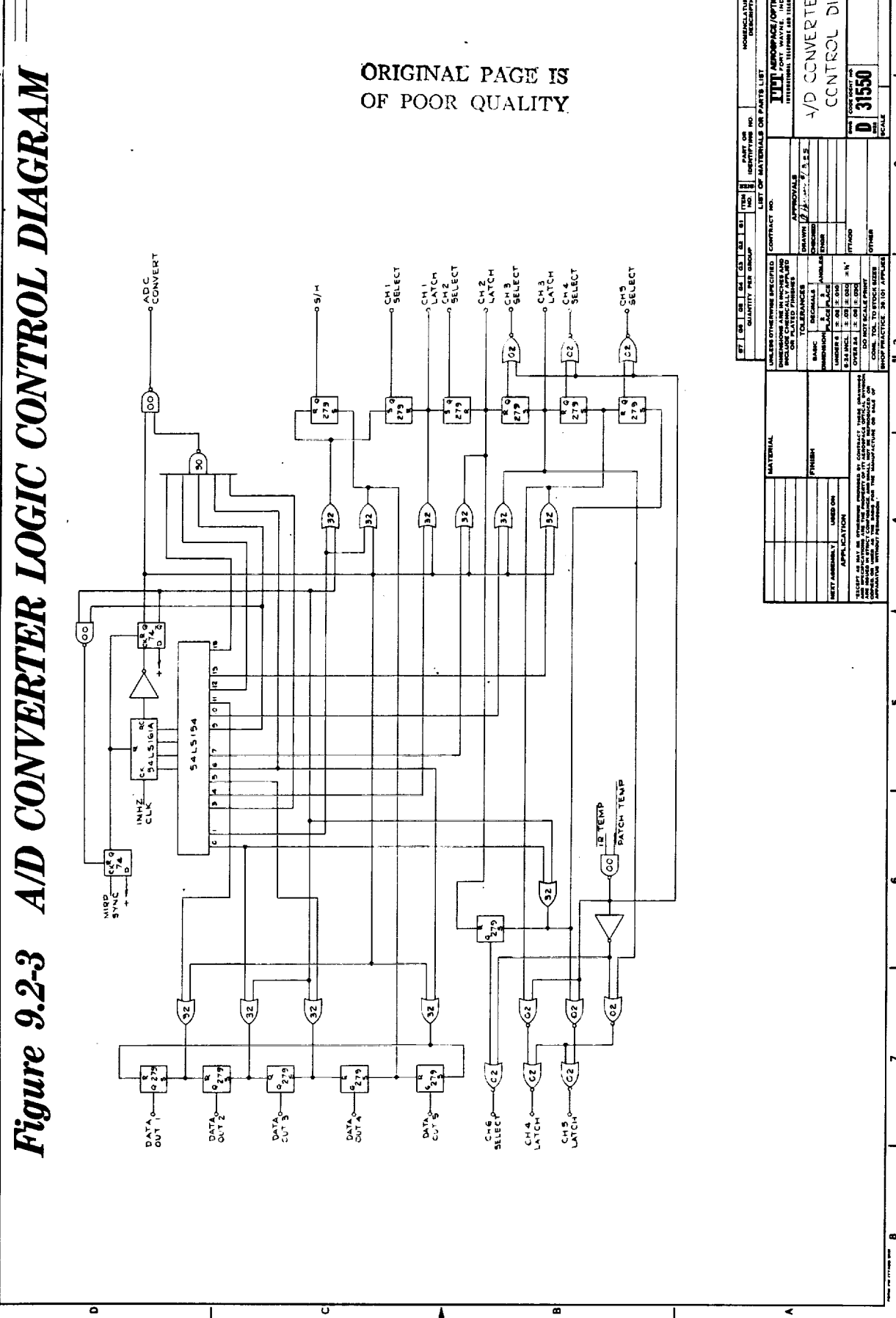
Figure 9.2-4A *LEVEL SHIFTER AND ANALOG CMOS SWITCH*
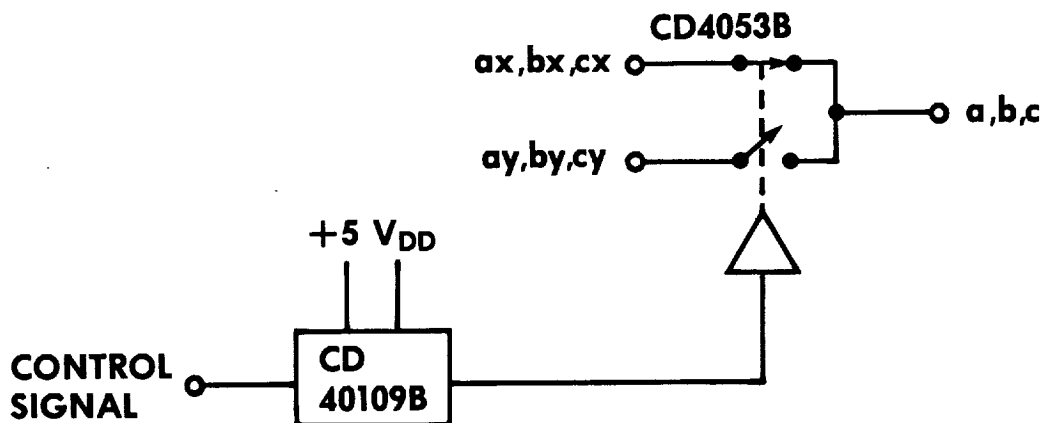
Figure 9.2-4B *CMOS SWITCH V_{DD}, V_{EE} GENERATOR*
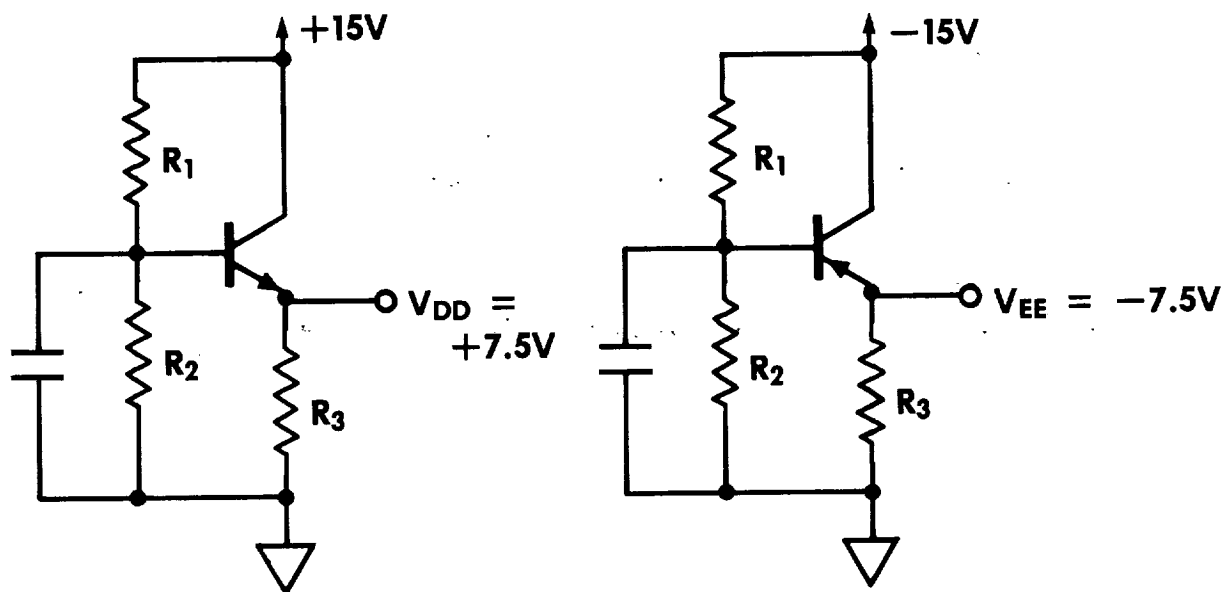
Figure 9.2-4C *DIGITAL MULTIPLEXER*
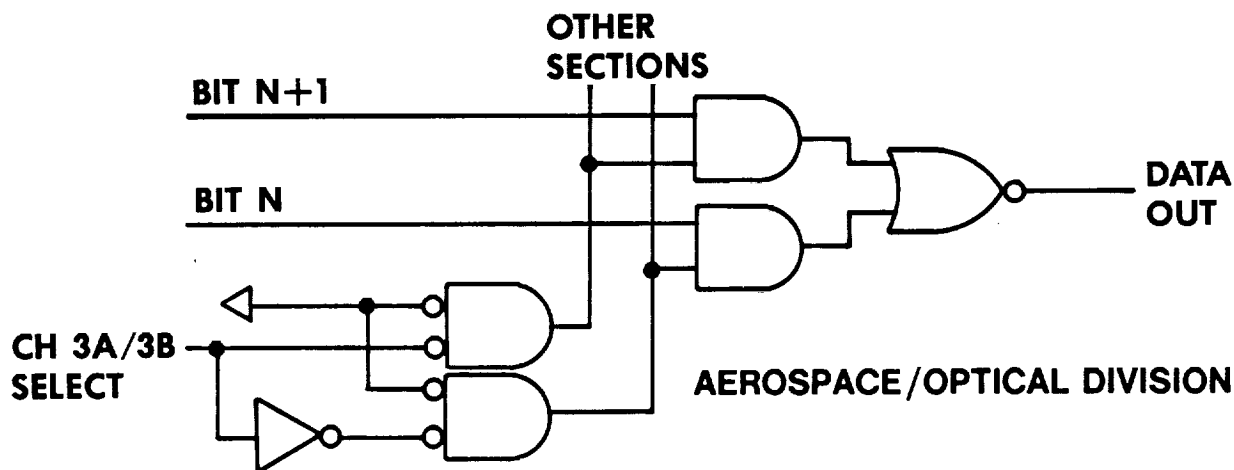
AEROSPACE/OPTICAL DIVISION **ITT**

shifters and switches will be less than 1ma exclusive of switching transients. Therefore, to maintain low source impedance (<20 ohms) for V_{dd} and V_{ee}, R_2 has been added and its resistance should be set to draw 1-2ma.

9.3   Component Changes

ITT has been informed by Texas Instruments that they are no longer using the "T" model flatpack (38510 model F3 package) for any of their integrated circuits. This is the package that is specified for AVHRR. What TI is using is the "W" flatpack (38510 model F2 package). This is the package that is specified for HIRS/2. According to TI documents, the 54LXX series will be available in the "W" flatpack.

We have compared the layout of AVHRR logic boards and HIRS/2 logic boards. The same spacing was used to layout both boards. Therefore the "W" flatpack will fit on the present AVHRR boards without any modifications to the boards. The same lead bending tool has been used for both the "T" and "W" flatpacks therefore no modification is required to the tooling.

The only modifications required will be to the parts lists. The new part numbers will be:

54L00	38510/02004 SDB
54L10	38510/02003 SDB
54L20	38510/02002 SDB
54L73	38510/02103 SDB
5440	38510/00301 SDB

These are non-radiation-hardened parts. The slash number indicates the specification for the specific part. The reliability level is Class S, the package is a "W" flatpack and the leads will be tin plated.

The approach of staying with the 54LXX devices is the simplest and least costly approach and has the least technical risk. However the 54LXX devices will undoubtedly be phased out in the future. They require at least 10 times the power of CMOS and about one half the power of 54LSXX. They are 10 times slower than the 54LSXX or the 54HCXX and approximately the same as 4000 series CMOS. Therefore there is no good reason to use the 54LXX devices in new designs. Hence use of the 54LXX will diminish overall and they will be phased out.

The next best approach is to substitute 54LSXX. These parts are direct replacements but are faster and would increase the power required from the 5V logic supply by about 1W. Radiation hardness of these parts should be similar to 54LXX. It is possible that the higher speed could cause problems such as increased RFI or timing anomalys. If these parts were used the part numbers would be:

```
54LS00          38510/30001 SDB
54LS10          38510/30005 SDB
54LS20          38510/30007 SDB
54LS73          38510/30101 SDB
```

The 5440 would be the same as before.

A third approach would be to substitute 54HCXX CMOS devices. TI representatives have been contacted and said that 54HCXX devices can be obtained in the W package and that by the time we need these parts they will be available in 38510 Class B. Additional screening would be required to make the part acceptable for space use. This approach would lower the power requirement to these logic elements by about 90% and would have the same potential speed problems as the 54LSXX. The radiation hardness of these CMOS devices is not known at this time.

The course of action recommended by ITT is to use 54LXX devices and have approach two or three as a fallback position in the event that TI discontinues these devices. A reevaluation of these alternate approaches can be made at that time.

9.4   Channel #3 (3.7 μm) Pre-Amplifier

9.4.1   3.8 Micron Preamp With Balanced Input

The possibility that the (3.7 micron) channel noise problem is due to the combination of lowered detector impedance due to contamination and magnetic pickup in the leads. A way of avoiding this problem is to use a balanced input preamp as shown in Figure 9.4-1. If the two leads from the detector to the preamp are bifilar they will pick up the same noise (emp) and no voltage will appear across R_1 hence no net noise will appear between the two inputs to the op-amp. If no pick-up noise voltage appears across R_1 no current can flow through R_1 hence the value of R_1 is immaterial (within reason).

Using this circuit it is not possible to bias the detector. There is a question whether any bias is required. The present AVHRR has a fixed bias of 18 mv on all detectors. This cannot be optimum because some detectors have minimum noise at zero bias and some may go up to 30-40 mv. Test data on AVHRR detectors from Cincinnati Electronics indicates that compared to a 5 megohm feedback resistor there is no minimum between 0 and 50 mv bias. The calculated value of the zero bias dynamic impedance is 335 megohms which is very large compared to the 16 megohm resistor used in AVHRR hence bias should not be required.

If bias is required the circuit shown in Figure 9.4-2 can be used. The circuit as shown will provide 18 mv of bias. This circuit provided the same noise cancellation as Figure 9.4-1 however if R_1 becomes smaller than R_2 the bias will be reduced a the ratio $R_1/(R_1 + R_2)$.

Figure 9.4-1   CHANNEL 4 PREAMP WITH BALANCED INPUT AND NO BIAS
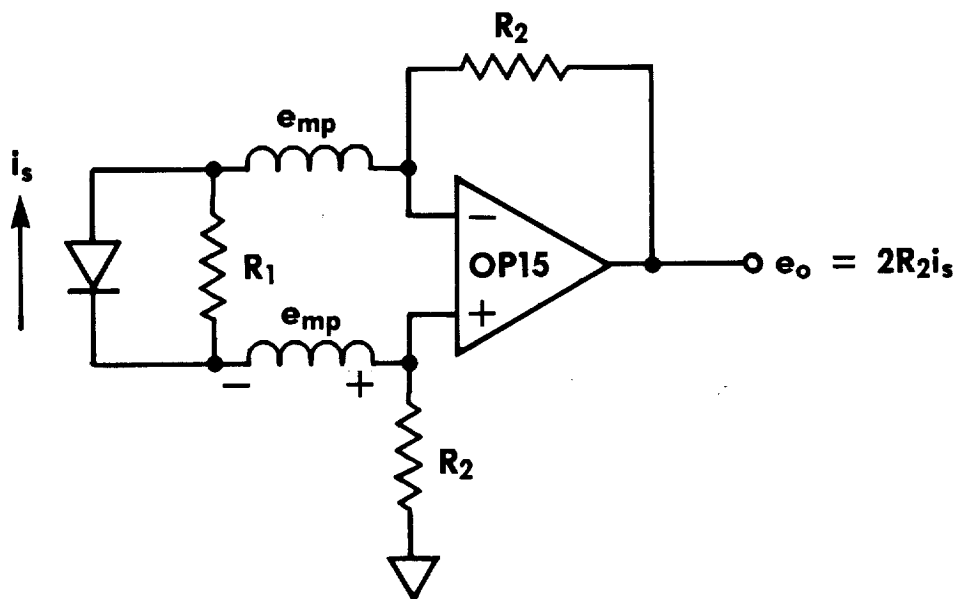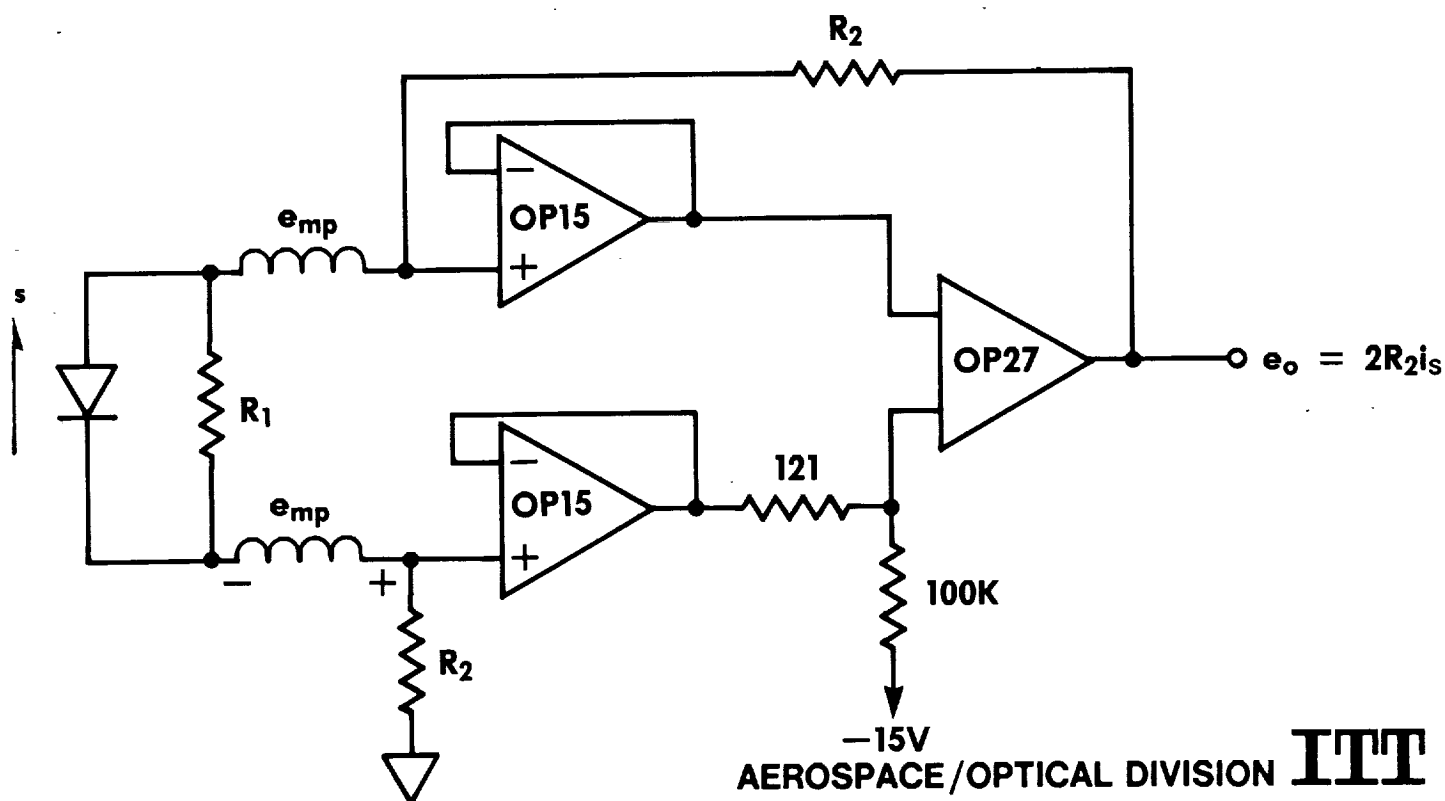

Figure 9.4-2   CHANNEL 4 PREAMP WITH BALANCED INPUT AND BIAS

AEROSPACE/OPTICAL DIVISION **ITT**

9.4.2   Evaluation of the Balanced Preamp Design

          It was decided to test a "balanced" input preamp modifica-
tion in S/N 206 in an attempt to evaluate this design as an improvement
in the noise characteristics of the 3.7 micron channel. The detector
was without bias which simplifies the preamp redesign considerably.
Using this assumption we can use the existing preamp which can be
reworked into a balanced input configuration. All rework was
accomplished outside of the radiant cooler which preserved the existing
optical performance of unit. The rework utilized existing parts and
the present P/C board.

          The redesigned preamp's performance was verified on the
AVHRR E.T.M. prior to any rework efforts on the flight model. The
following tasks were necessary to change the preamp:

          1. Remove R-9.

          2. Change R-10 from a tailor point to a 16.2 meg resistor.
             (Hard wire change due to different case size.) To keep
             the preamp gain the same change R-8 and R-10 to 8 meg
             resistors.

          3. Hard wire detector low side to Q-2 gate. (It was
             necessary to cut the copper run at terminal E-3).

          The AVHRR E.T.M. was first used to test the preamp modifi-
cation prior to its use in flight hardware. Final evaluation was per-
formed with the preamp installed in S/N 206 AVHRR/2, which is somewhat
different in design than the original E.T.M. The preamp was then
installed in S/N 206, AVHRR/2 for evaluation tests in a bench cooler
configuration. Note: Some differences exists in the preamp grounding
system between the two types of preamps. In the single ended design
one side of the detector is at signal ground; in the balanced input
preamp this same side of the detector is floating in a differential
configuration. This fact dictates some grounding differences in the
two designs.

9.4.2.1   Results

          There was no significant improvement in the noise perfor-
mance of the 3.7 micron channel with a "Balanced" input differential
preamp in place of the present design under the same set of conditions.
The level of the 62.4 kHz interference at the output of the preamp was
essentially the same. Under more ideal conditions (no cooler wiring
and resistor in place of detector) the balanced preamp noise perfor-
mance was slightly improved. System performance of the balanced input
preamp may have improved if system grounding were investigated. This,
however, would take a great deal of effort and could create problems in
other areas (conducted noise susceptibility). The balanced preamp
design also does not solve any detector lead pickup problem within the
cooler wiring.

9.5   Hybrid 3.7 Micron Detector

A separate investigation is being conducted utilizing a hybrid 3.7 micron detector designed by Cincinnati Electronics. This investigation is being completed under a separate contract (NAS5-29114 Task No. 5). It is mentioned here merely to indicate its importance to the performance of the 3.7 micron channel on the AVHRR/3 instruments. On completion of that investigation a separate report will be written describing that effort.

At present the hybrid detector is the preferred approach to redesign of the 3.7 micron channel since all high impedance leads and circuitry are internal to the detector package.

9.6   Elimination of 5V and 10V Telemetry Buses

NASA informed ITT that they want to eliminate the +5V TLM bus in the AVHRR. We proposed to connect an active +5V reference device on the +10V TLM bus to obtain a +5V bus which was active all the time. We were informed at the AVHRR CDR that no active devices can be connected to the +10V TLM bus. However they did say that we can use a +28V bus.

ITT proposes to use the circuit shown in Figure 9.6-1. Two devices are shown which will allow the AVHRR to eliminate both the +5V and +10V TLM buses. Both the REF 01 and the REF02 are characterized to a maximum input voltage of +40V, therefore +28V is well within their rating. If NASA is worried that a short in one of the devices will disable the +28V bus we can use a .25a fuse as shown for protection. The FM08 type fuse is on the QPL and they were used in INSAT and have been proposed for use in GOES. .
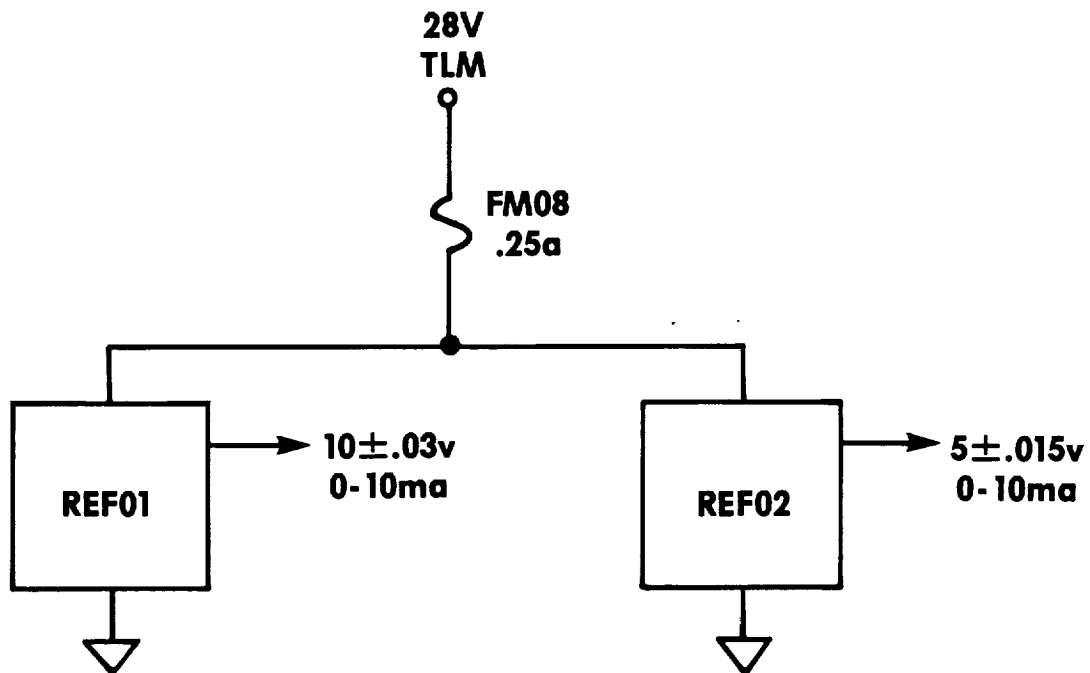

Figure 9.6-1. +5V and +10V TLM Buses

9.7   EMI Reduction Study

9.7.1   Requirements

Survey the AVHRR/2 and HIRS instruments for sources of
R.F.I. in the S.A.R.R. frequency bands and suggest redesigns that will
enable the instruments to meet the reduced levels of radiated emissions
for NOAA-H and subsequent spacecraft. All future flight hardware will
be required to meet this requirement. Appendix "G" to this report con-
sists of four memos written by G.S.F.C. personnal describing efforts
and results achieved by rework to present flight hardware. These
"fixes" have reduced E.M.I. to acceptable levels of performance;
however the AVHRR/2 units did not quite meet the specification require-
ments. Additional efforts of more permanent designs may be required
on the AVHRR/3.

ITT understands the need for reduced radiated EMI on the
new NOAA satellite with SARR. ITT has worked with NASA and Canada DOC
personnel to reduce levels in existing AVHRR/1 and AVHRR/2 flight units
to levels below the existing specification levels.

ITT is concerned that the new levels being considered by
NASA are not reproducible and are at the very limit of measurement
state of the art. Experience gained by the NASA personnel testing
existing flight models proves this is so. Improvements in performance
are discussed in terms of relative improvements not absolute.

For this reason, ITT strongly recommends that the new EMI
levels be stated as goals only. All improvements tested and proved to
date will be incorporated into AVHRR/3. ITT does not believe that the
test techniques available at this time allow a firm specification at
the desired levels to be acceptable.

9.7.2   RFI Suppression of HIRS/2 Instruments

Following the suggestion that a 1000 pf ceramic (style
CK06) capacitor be soldered in parallel with the "catch" diode of the
Scan Regulator (8122882G1) of the HIRS/2 engineering model board, RF
radiated by the assembly was virtually eliminated. A series of opera-
tional mode tests performed earlier on FM5 demonstrated conclusively
that other potential RFI generators in the HIRS/2 were causing negli-
gible RF radiation.

As CK06 or CK05 style ceramic capacitors (procured in
HI-REL versions to MIL-39014/01 or MIL-39014/02 from the Kemet Division
of Union Carbide Corp) have dissipation factors (D.F.) of up to 2.5% at
1 kHz (and up to a typical D.F. of 5% at 800 kHz) the circuit applica-
tion was questionable. This D.F. when expressed as the Quality Factor
(Q), or the reciprical of D.F., is the ratio of reactance (X_c) to
resistance (R). This results in a Q min of 40 to 1 kHz, decreasing
typically to 20 to 800 kHz. Since the X_c of a 1000 pf capacitor at the
switching regulator switching frequency of 19.5 kHz is approximately
8000 ohms, the resistance R could be as high as 8000 divided by 40 (Q)
or 200 ohms.

A HI-REL "glass" capacitor of 1000 pf value was in the qualified (bonded) HIRS/2 inventory and was used elsewhere in the instrument purchased to MIL-C-223269/9-4082. These glass (or porcelain according to the manufacturer) capacitors have a Q min of 1000 and a permissible DC working voltage of 200V @ 85°C compared to a Q min of 40 and an identical 200 DCWV of the M39014/01 ceramic capacitors. The high Q of the glass capacitor results in a power dissipation reduction by a factor of 25.

Examination of the capacitor "stress" in the circuit (see Figure 9.7.2-1) results in a calculated voltage stress ratio (actual applied voltage divided by the permissible voltage) of 0.14, well within the PPL recommendation of 0.5. At the switching frequency of 19.5 kHz, (with the X_c at the fundamental being about 8K) the equivalent resistance of 8 ohms. Inrush or charging current can be calculated by $I - C \, dv/dt$, yielding 280 mA peak for the 0.1 μsec measured rise time on the capacitor. Instantaneous power dissipation can therefore be 630 mW (for 0.1 μsec). However, the switching period is 51.3 μsec with dissipation of only at the rise and fall times (which at worst case are 0.1 μsec each). Therefore the duty cycle is only 0.39% resulting in an average power dissipation of 2.5 mW in the glass capacitor. As the measured waveform fall time is more nearly 1 μs, the actual power dissipation is closer to 1.3 mW. After talking to an Application Engineer at Vitramon, the capacitor manufacturer, even if the choice of that capacitor is not the "best" possible choice, it is an excellent choice (not to mention being in stock) that is being operated comfortably below any of its maximum ratings.

Shifting focus to the original regulator design, the only component seeing any increased stress by adding the capacitor is the 2N5153 switching transistor that furnishes the 280mA of inrush current to the capacitor plus the average value of output (load) current of approximately 400mA. As it is rated at 5 amperes, of maximum collector current, it therefore is being operated well within its rated saturated switch current rating.

In conclusion, the addition of the 1000 pf glass capacitor used to eliminate RFI generated by the circuit "catch" diode does not degrade switching performance nor does it compromise the reliability of the regulator design. Regarding the AVHRR switching regulator design, it is basically similar if not identical (i.e. the 2N5153 PNP becomes a 2N5154 NPN with the same ratings and the generic "catch" diode is a Micro-semiconductor MB202 diode rather than a MB204 diode), the preceeding analysis justifies the inclusion of the 1000 pf glass capacitor to the AVHRR if RFI is detectable and if the capacitor is found to eliminate the RFI.

9.7.3   R.F.I. Suppression of AVHRR/2 Instruments

Several R.F.I. modifications were made to existing AVHRR/2 instruments in an effort to reduce radiated emissions to existing levels. The initial modifications added improved shielding to the scan motor power supply input and output cabling. Additional suppression

Figure 9.7.2-1 BUCK REGULATOR WITH EMI SUPPRESSION
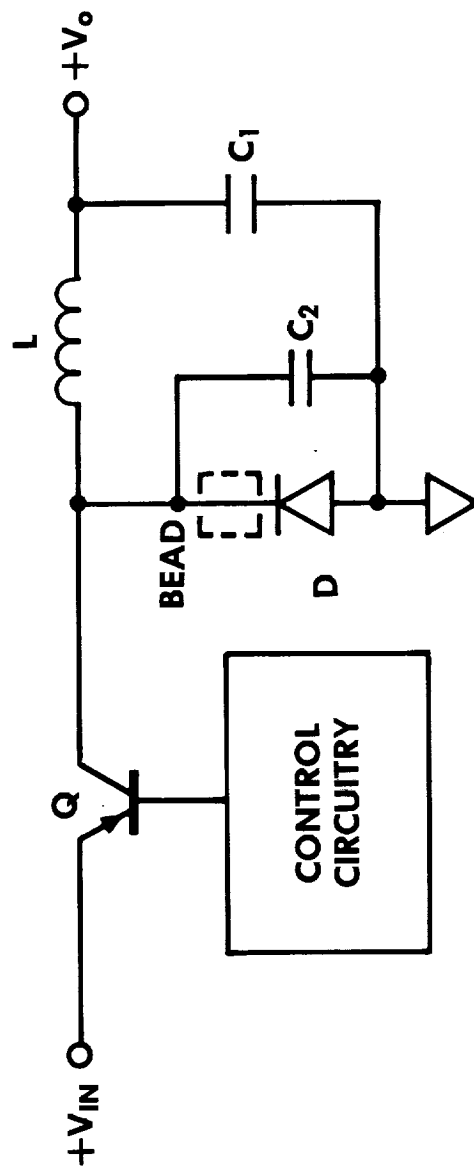
was accomplished with a decoupling filter added to the output drive of the motor power supply. Figure 9.7.3-1 represents these changes. The above changes made a significant reduction in the radiated emissions in the S.A.R.R. frequency bands.

However as indicated in the referenced memos in the Appendix, additional suppression was necessary as the result of spacecraft level systems tests with the S.A.R.R. instrument. This was accomplished by modifying the "catch" diode in the motor power supply switching regulator. The circuit is identical to that used in the HIRS/2I instruments so the description in Section 9.7.2 applies. With all three modifications installed E.M.I. radiations in the S.A.R.R. bands have been reduced to acceptable levels.

9.7.4   E.M.I. Suppression on New Instruments

As part of this study other areas of change were investigated. One major source of radiation appears to be the "catch" diodes, in the switching regulators. These diodes can be replaced by Schottky diodes which do not have characteristics that cause emissions during switching. A second approach would be to replace the discrete part regulator circuit with a hybrid device with controlled switching. Published data indicates that either approach would reduce radiated emissions.

Additional AVHRR/2 instrument suppression could be achieved by modifying the remaining "catch" diodes in other power supply circuits within the instrument. This was not done on existing instruments due to the extensive rework necessary and the fact that additional EMI reductions were not necessary to meet present spacecraft requirements.

The previously described sheilding modifications could be improved on future instruments by re-designing the cabling to eliminate all external wiring to and from the scan motor. This change would be much more effective than the existing "fix". Additional suppression can be achieved by replacing existing external interface connectors with newer style connectors containing built-in RFI suppression filters in each pin. These "filter pin connectors" are now available for use in this application and will fit into the present AVHRR designs without change. A review of the AVHRR/2-HIRS/2I packaging design indicates that significant E.M.I. containment could be achieved by incorporating R.F.I. gasketing material to all enclosures. This may require extensive mechanical redesign in some areas, but may be necessary if additional reduction is necessary.

The recommended changes for new instruments are:

● Permanent incorporation of the capacitor/R.F. bead on all regulator diodes.

● Permanent incorporation of the decoupling filter on the AVHRR scan motor supply output.

Figure 9.7.3-1 RF EMISSION SUPPRESSION IN AVHRR/3

AEROSPACE/OPTICAL DIVISION **ITT**
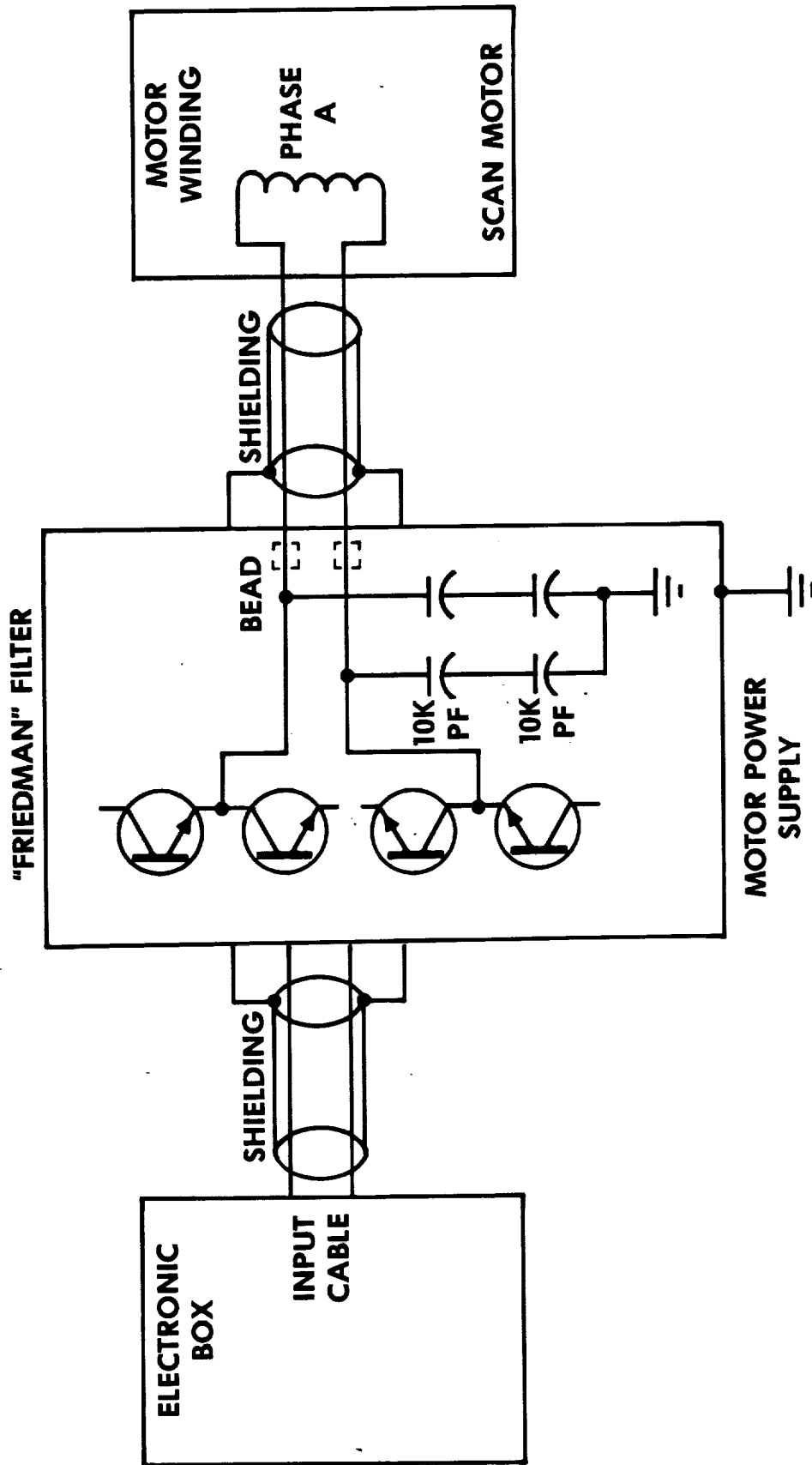
- Redesign the cable routing to and from the AVHRR scan motor power supply to eliminate external wiring.

- Replace all interface "D" style connectors with newer filter pin "D" style connectors.

- Redesign the packaging to include R.F.I. gasketing if necessary after testing the above changes on the E.T.M.

9.8   AVHRR/3 Electronic Redesign Impacts

Various electronic components and subsystems must be changed for the AVHRR/3. The extent of the changes will depend on the selected study options: however, significant changes are required due to obsolesence. The details of these design changes are discussed in different sections of the report. The impact of these changes on the electronics are outlined in this section.

Electronics redesign includes changes in the following areas:

- New TTL logic components
- New A/D converter
- Elimination of spacecraft 5V and 10V telemetry bus
- Stability monitor control
- Commands and status changes
- P/C board additions and modifications
- System power budget
- Mechanical re-packaging

9.8.1   New TTL Logic

The recommended approach to the I.C. logic package problem is to replace the "T" model flatpack with the "W" flatpack. This change will be electrically and mechanically transparent in the present design. The only change necessary is to change parts lists to the new numbers.

9.8.2   New A/D Converter

A new A/D converter is the most significant electronics change required for the AVHRR/3. The present design is obsolete and cannot be produced. An additional complication is added with the incorporation of a third visible channel and the necessity for the A-D converter to handle unipolar and bipolar data. In general the new A/D converter requirements are:

- Seven channel multiplexing
- Ten bit resolution
- Track/hold and conversion in 3 μsec
- Convert unipolar and bipolar data
- Added stability monitor multiplexing

A review of the design changes will reflect the following changes to the electronics.

- Eliminate the present A-D converter assy.
- Eliminate two logic control P/C boards
- Add a new A/D converter P/C board
- Add a new logic control P/C board
- Change wire lists and assembly procedures
- Generate new material lists and test procedures
- Change CH's 3B, 4 and 5 post amplifiers
- Change CH's 1 and 2 preamps
- Add channel 3B preamp
- Add R.F.I. gasketing to electronics packages (tentative)
- Change circuits to add R.F.I. fixes
- Change power supply and add 5V and 10V TLM
- Add commands for CH. 3B addition
- Add P/C circuitry for visible calibration target

Table 9.8-1 is a listing of the AVHRR/2 P/C boards noting changes required to update to the AVHRR/3. Figure 9.8-1 AVHRR/3 instrument laoyout shows the P/C nest with the added P/C cards.

Table 9.8-1. Printed Circuit Board

DESCRIPTION	MODIFICATION
- MOTOR POWER SUPPLY	- EMI FILTER-BOARD CHANGE
- SWITCHING REGULATOR	- EMI DIODE MOD-NO BOARD CHANGE
- RAMP CALIBRATION GENERATOR	- NEW LOGIC-NO BOARD CHANGE
- POWER CONVERTER AND SWITCHING REG.	- EMI DIODE MOD. - NO BOARD CHANGE
- MOTOR LOGIC	- NEW LOGIC-NO BOARD CHANGE
- AUXILIARY SCAN LOGICS	- NEW LOGIC-NO BOARD CHANGE
- IR POST AMPLIFIER	- NO CHANGES
- DAYLIGHT POST AMPLIFIER	- DUAL SLOPE MOD-NEW BOARD
- IR PREAMPLIFIER	- NO CHANGE
- TELEMETRY BD. NO. 2	- NO CHANGE
- DAYLIGHT PREAMP	- REPACKAGE-NEW BOARD
- BLACKBODY MUX LOGIC	- NEW LOGIC-NO BOARD CHANGE
- COMMAND RELAY NO. 2	- NO CHANGE-USE SPARE COMMAND
- COMMAND RELAY NO. 1	- NO CHANGE
- INTERFACE LOGIC NO. 1	- REDESIGN-NEW LOGIC CONTROL
- INTERFACE LOGIC NO. 2	- REDESIGN-NEW A-D CONVERTER
- CHANNEL 4 PREAMPLIFIER	- REDESIGN-NEW HYBRID PREAMP
- CH 5 POSTAMP	- NO CHANGE
- PATCH TEMP. CONTROL & TELEMETRY	- NO CHANGE
- CMD. RELAY NO. 4	- NO CHANGE-USE SPARE COMMAND
- LOGIC REGULATOR	- EMI DIODE MOD-NO BOARD CHANGE
- ±15V REGULATORS	- NO CHANGE
- MULTIPLEXER	- REDESIGN-ADD CH 3A MONITORS
- SCAN COUNT AND DECODE LOGIC	- NEW LOGIC-NO BOARD CHANGE

Figure 9.8-1 AVHRR/3 LAYOUT

ITT

AEROSPACE/OPTICAL DIVISION

Table 9.8-1. Printed Circuit Board (Continued)

DESCRIPTION	MODIFICATION
ADDITIONAL NEW P/C BOARDS	
- CH 3A PREAMP - CH 3A POST AMP - STABILITY MONITOR CONTROL - STABILITY MONITOR DRIVER - STABILITY MONITOR DIODE AMPS - STABILITY MONITOR COMMANDS	- ADD TO AFT OPTICS - ADD TO ELECTRONICS NEST - ADD TO ELECTRONICS NEST - ADD TO ELECTRONICS NEST - ADD TO ELECTRONICS NEST - ADD TO ELECTRONICS NEST

9.8.3   Telemetry Status Changes

The following table lists the various commands and status monitors that would be added to the system as the result of the proposed changes. The circuits for these functions will be implemented on the boards listed in Table 9.8-1.

Added Commands (CH. 3A Addition)

Channel 3 Select   3A/3B
Channel 3A   Enable/Disable

Added Commands (Stability Monitor)

Stability Monitor   On/Off
Stability Monitor Heat   On/Off
Stability Monitor Door   Open/Close

Added Digital "B" Command Status (CH. 3A Addition)

1   Channel 3 Select
2   Channel 3A Enable/Disable

Added Digital "B" Command Status (Stability Monitor)

3   Stability Monitor   On/Off
4   Stability Monitor Heat On/Off
5   Stability Monitor Door Open/Close

Added Analog Telemetry Status

There will be no added analog telemetry status as the result of the Channel 3A addition.

The following listing is suggested additions to the analog telemetry status as the result of the stability monitor addition to the AVHRR. Some changes can be expected depending on the design option chosen.

```
1   Monitor Lamp Current
2   Monitor Outgas Temp.
3   Monitor Door Position
4   Monitor Diode Temp.
5   Monitor Diode #1 Output
6   Monitor Diode #2 Output
7   Monitor Diode #3 Output
8   Monitor Diode #4 Output
```

In addition to the previously described telemetry monitors, the output of the monitor diodes will be added to the digital data stream going to the M.I.R.P. During the commanded calibration sequence, the outputs of the (4) monitor diodes will be switched into the normal Ch 1, 2, 4 and 5 sample and hold circuits ahead of the A-D converter. This will occur during the scan line when the diode monitors can view the calibration source. Synchronism must be tied to the scan mirror position. The (4) monitor outputs are then digitized to a resolution of 10 bits and shifted into the storage registers. The digitized data is held until back-scan dead time and shifted out to the M.I.R.P. in the normal sequential pattern. This sequence will repeat for any number of scan lines until the calibration sequence is commanded off.

9.8.4   Estimated Power Budget Changes

With the additions of the previously described circuits the following estimate of power changes will occur for the AVHRR/3:

Added Circuitry

● New A/D Converter	5.2W
● New A/D Logic Control	.3W
● CH 3A Preamp	.1W
● CH 3A Post Amp/Control	.9W
Total	6.5W

Deleted Circuitry

● A-D Converter	6.5W
● A/D Logic Control	.7W
Total	7.2W
Net Change	-.7W

The present AVHRR/2 instruments are drawing a nominal of 26W. The AVHRR/3 instrument power would be approximately .7W less. With the addition of a lamp source stability monitor this power would increase by approximately 20W during the calibration sequence.

9.9   Electronic Redesign Mechanical Impacts

          The extent of the mechanical changes due to electronics
redesign depend upon the design options chosen to be inlcuded in the
AVHRR/3. Baseline redesign however will dictate changes regardless of
the options chosen. See Figure 9.8-1 instrument layout.

9.9.1   Electronic Module Subassembly

          The majority of electrical related mechanical changes will
take place in the electronics module. The present A-D converter will
be removed and several P/C boards added. Table 9.8.1 lists the P/C
board changes and additions. The impact on the electronics module
structure is minimal. The instrument layout Figure 9.8-1 labels these
board changes. There are no basic dimensional changes in the size of
this subassembly. Several piece parts will change to accommodate the
added P/C cards.

          The new logic circuits change will also not have a signifi-
cant impact. The "W" style flatpack package will fit the "T" package
footprint without a change. All other proposed changes will take place
on the individual P/C assemblies. In some cases new boards will be
required and in others, modifications can be implemented.

          Some major package changes will be required if extensive
E.M.I. modifications are necessary. Electronic filtering can be
achieved on the P/C assemblies without affecting the package. Filter
pin connectors can also be added with a minimum of mechanical impact.
However if R.F.I. gasketing is required at the package panel junctions,
some major changes will be required. Special mechanical interfaces are
required to accommodate these gaskets.

          The re-routing of motor power input and output leads will
also require some mechanical changes. This re-routing is necessary to
keep all wiring internal to the module and the scan motor itself.

          The present packaging approach was not designed to contain
any level of R.F.I. radiation. Some or all of the above modifications
may be required on the AVHRR/3.

9.9.2   Optics Subassembly

          The added channel (3A) requires the addition of another
analog channel to the AVHRR. The preamp circuit will be a small P/C
assembly added to the side of the optic focus assembly. The post
amplifier and other necessary circuitry will be added as a P/C board in
the electronics module. The redesign of the aft optics also causes the
CH 1 and CH 2 preamps to change location. These will now be located to
the sides of their respective focus lens assemblies.

9.9.3   Scanner Subassembly

     The proposed increases in scan motor performance will be accomplished within the existing mechanical package. The re-routing of the scan motor leads will require a change to the housing and internal wiring connections. If R.F.I. gasketing becomes necessary some mechanical changes will be required to the housing and cover.

9.9.4   Radiant Cooler Subassembly

     The implementation of the hybrid 3.7 micron detector will cause some internal minor changes to the patch and radiator subassemblies. This is due to the increased number of leads between the detector and preamp (increase from 2 to 6). This increase requires some changes to the wiring terminal boards on the patch to accommodate the increased leads. A change from individual wires to ribbon cabling is also anticipated to improve wire routing and handling during construction. No external changes are required.

     The remaining circuitry of the 3.7 micron preamp will be re-packaged into the existing housing located on the back of the vacuum housing. All of the expected cooler modifications and hybrid detector performance details will have been proven out on a separate engineering study program and have not been a part of this study.

9.9.5   Calibration Monitor Subassembly

     The implementation of the calibration monitor for the AVHRR/3 depends upon the selected option. The following description is of the lamp source approach and is typical of what changes that are required. The calibration monitor subassembly will be added to the AVHRR as a separate removable unit. The monitor diodes will be added to the side panel opposite the monitor subassembly. Circuitry to operate the monitor will be included on P/C assemblies within the electronics module subassembly. The wiring interconnections between these separate functions will be accommodated in the electronics module and the baseplate. A separate connector will interface to the removable monitor subassembly. This subassembly will be added to the AVHRR so as not to interfere with the interface connectors that now exist.

     Note that the stability monitor is an add-on part to the AVHRR/3. The AVHRR/3 will work even if the stability monitor is removed. Thus, any potential delays or problems in stability monitor development will not delay delivery of AVHRR/3 flight models.

10.0   HIRS/2I STUDY

10.1   Requirements

The desired improvement for the HIRS/2I is to modify the Channel 20 spectral characteristics. Spectral symmetry and uniformity are desired such that an "ideal" total instrument spectral response function would be one that is flat within the 0.2 μm to 1.9 μm band or whatever band that can be achieved without modifying the relay optics such that it reduces the sensitivity of the short wavelength sounding channels (3.8 μm to 4.6 μm). Although it is never possible to achieve the "ideal" spectral response function, this study should examine the possibility and/or modifications which would be necessary to achieve as close as possible this function.

In addition, the following questions are to be examined.

1) How close could the modified HIRS/2I Channel 20 come to the "ideal" total instrument spectral response function?

2) Define the total instrument response characteristics for Channel 20, e.g., center frequency, 80%, 50%, 5% and 2% response points, tolerances, etc.

3) What would the total and/or out-of-band response for the channel be? Relate out-of-band to total integrated response within the bandpass region when viewing a solar source.

4) How stable would the spectral response be with time?

5) Could the stability of the spectral response be determined in the lab? How?

6) How accurately could the modified channel be calibrated in the lab?

7) How would it be calibrated in the lab?

8) What effect would the polarization of the reflected radiation have on the accuracy of the measured radiance?

9) To what extent might stray light affect the accuracy of the measured radiance?

10) What would the Noise-Equivalent-Radiance of a modified HIRS/2I Channel 20 be or its signal to noise ratio related to Albedo.

11) How would the field-of-view vary across the broadband spectrum of Channel 20?

This portion of the study is to be conceptual in nature. While not specifically included as a task in the SOW, a review of the HIRS/2 filter wheel life problem was suggested by the Technical Officer.

A review of the HIRS/2 test equipment was also part of this study. Recommended upgrades due to the channel 20 modification and age of the equipment were generated.

10.2   Channel 20 Modification Concepts

Two basic approaches were considered to allow implementation of the wide channel 20. First, a mechanical modification to the telescope and relay optics was considered. This approach would install a simple refractive telescope in the central obscuration of the present HIRS/2 reflective telescope. This approach requires considerable mechanical modification. It is described below in Section 10.2.1.

The second approach changes the coatings on a dichroic beamsplitter and perhaps the antireflection coating on a couple of relay lenses, removes the spectral filter from the filter wheel, and uses the unfiltered response of the detector (as modified by the optical transmissions and reflections) to define the bandpass. The detector can be either a silicon photodiode or an InGaAs photodiode similar to (but larger than) that used in the new AVHRR/3 Channel 3A.

This approach is discussed in Section 10.2.2. It is the approach recommended by ITT-A/OD.

The basic problem driving the implementation of a wideband channel 20 in HIRS/2 is the fact that the present narrow channel 20 (667 to 714 nm) has never been a driver in the instrument design. The primary design drivers were the shortwave and longwave IR channels.

There are several optical elements in HIRS/2 which were optimized for the IR channels and if allowed to remain in HIRS/3 would preclude any reasonably wide channel 20 bandpass. The primary problem is the longwave/shortwave beamsplitter. The response in the visible spectrum is shown in Figure 10.2-1. This dichroic reflects the longwave channels and transmits the shortwave and visible. The coating was optimized so that the passband of channel 20 occurred at a peak in the harmonic response pattern. It is a reasonable approach for a narrow visible band but essentially precludes any wide passband.

10.2.1   Refractive Telescope Approach

A quick geometric calculation of the present HIRS/2 optical system shows that there is a small unused spot in the center of the telescope secondary and the LW/SW beamsplitter. Calculations give adequate diameters for the optics and reasonable signal levels when compared to the present HIRS/2.

Figure 10.2-1   VISIBLE REFLECTION
HIRS/2I   LW/SW BEAMSPLITTER
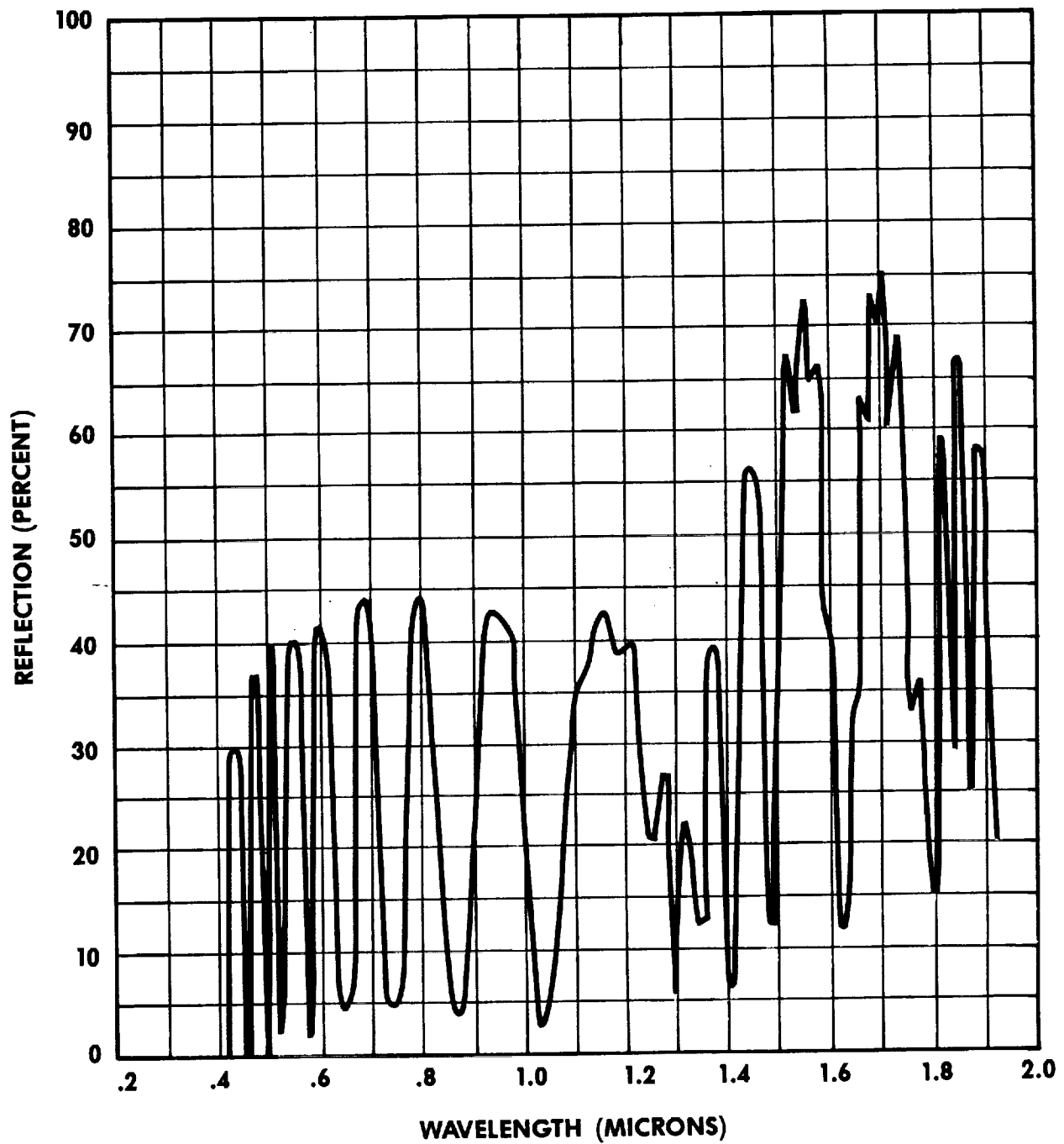
AEROSPACE/OPTICAL DIVISION **ITT**

Assuming that the present field stop (0.262 diameter) corresponded to a 1.5 degree field, the effective focal length of the telescope is 10 inches. For the present rough calculation the 10 inch value is close enough.

The beamsplitter is 1.5 inches from the field stop. Thus for a point image the beam diameter is 0.894 inches at the beamsplitter. If the point is at the extreme 1.5 degree field of view, the central ray will hit the beamsplitter 0.111 inches off center line. The central obscuration causes a central 0.450 diameter hole in the beam.

The secondary mirror is 2.470 from the beamsplitter and 3.970 from the field stop. At this position, a point image has a beam diameter of 2.342 inches and the central ray is .067 off the telescope center line. The unused central position is 1.191 inches in diameter.

When images from all portions of the field are considered, there is a central region .228 in diameter on the beamsplitter that is not used. This area can be aluminized and used for the new visible channel.

The central 1.056 inch diameter portion of the secondary mirror is not used. Thus a hole can be put in the secondary mirror and the new visible optics placed directly on the secondary. Figures 10.2-2 and 10.2-3 show the concept being discussed.

The new visible channel would have an aperture of approximately half an inch with a focal length of about 4 inches. This puts the image approximately at the regular field stop and allows SW lens #1 to act as a collimating lens for the rest of the system. A 1.5° FOV provides an image of .105 inch diameter which will pass through the SW field stop with lots of room. The new visible channel must then be re-imaged either at its own field stop or at the detector.

Even though the unused portion of the secondary is large enough to allow a one inch aperture for the new visible channel, the requirement to use the aluminized spot on the beamsplitter restricts the beam size. Working backwards from the image at the normal image plane, yields an aperture of approximately .6 inch. Light from a large objective would miss the aluminized spot. A smaller objective would not fully utilize the spot.

The small aperture gives a poor telescope that has large contributions from diffraction effects. However in this application the 11 arc second Rayleigh criterion is less than 1/2% of the FOV and far exceeds the system requirement.

The small aperture gathers very little energy. Compared to the present visible channel which uses the entire telescope aperture, only 1.4% as much light is collected. This is a 72 times reduction in the S/N ratio. The change in the beamsplitter from a multilayer to an aluminized coating provides a 2.4 time improvement for a resulting net

Figure 10.2-2 HIRS/2I WIDE-BAND VISIBLE

HOLE THRU CENTER
OF SECONDARY MIRROR

ALUMINIZED SPOT
ON BEAMSPLITTER

IMAGE AT APPROXIMATELY
NORMAL FIELD STOP

SW #1 LENS ACTS TO
COLLIMATE BEAM THROUGH
SW/VIS BEAMSPLITTER

NEW
VISIBLE
CHANNEL
OBJECTIVE

NEW
VISIBLE
OPTICS
AND
DETECTOR

AEROSPACE/OPTICAL DIVISION ITT

226
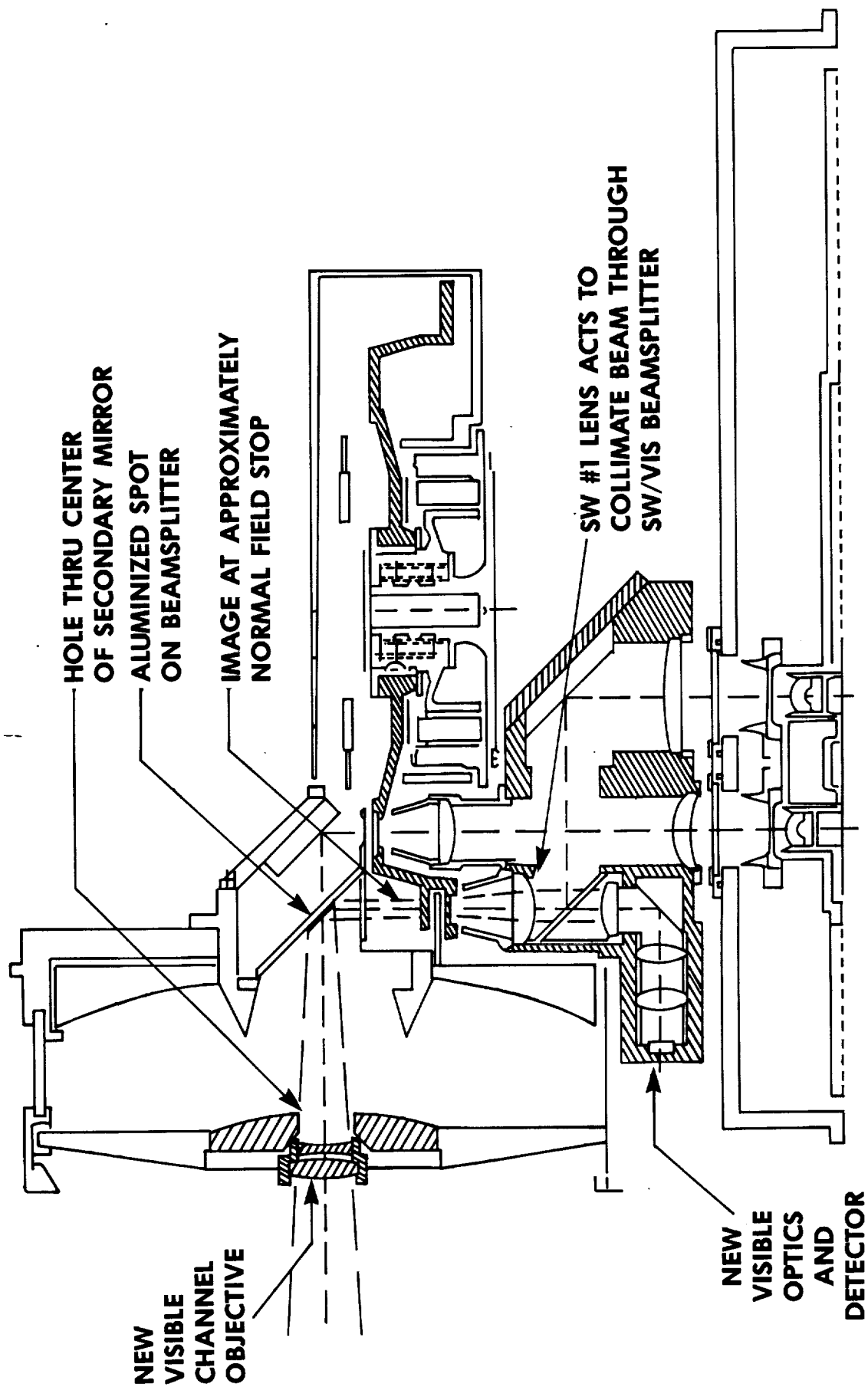
Figure 10.2-3 HIRS/2I WIDE-BAND VISIBLE CHANNEL

ITT
AEROSPACE/OPTICAL DIVISION

227
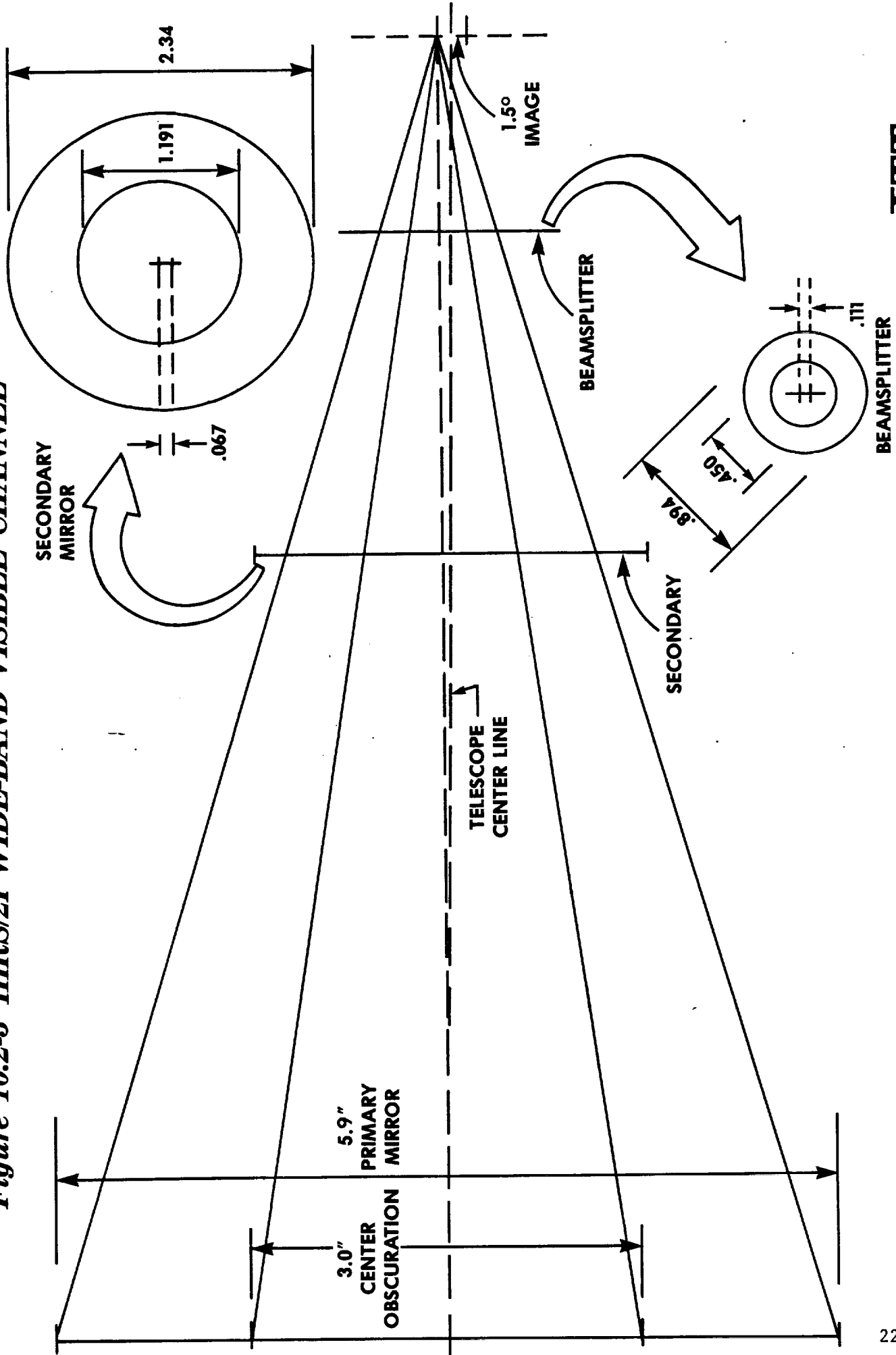
loss of 30. If the spectral filter is removed, the bandwidth can be widened from 0.045 microns to at least .8 microns for a further gain of about seventeen to yield a net loss of only 1.7. The solar energy curve and the detector response curve need to be factored in and a factor of 2 or 3 loss would not be unrealistic. This gives a new loss of only 4 or 5 from the present HIRS/2.

The addition of a compensating spectral filter and an even wider spectral bandwidths is possible. There is a trade off in the aluminized spot size between the visible and the other channels. The spot can be increased by 0.050 inch and increase the visible signal by 50% but only cut the rest of the channels by 2%.

In conclusion, it appears that a small (0.6 inch aperture) refracting system can be placed in the unused portion of the present HIRS/2 telescope. This channel would replace the present narrow band visible channel and cover the entire visible and near IR. It appears that a reasonable signal to noise could be expected as the light gathered is down a factor of 4 or 5 times. However the present system is digitizing limited, not S/N limited, so that it is expected that the full 13 bit accuracy of the present system can easily be maintained.

Several potential problems exist with this concept (aside from the obvious mechanical questions). Questions of scattered light in channel 20 and the effect of the added elements on the other short-wave channels were considered. Under some solar illumination conditions, light could be scattered from the scan cavity into the refractive objective. Levels will be low; however, detailed calculations were not performed.

The shortwave channels are very sensitive to changes in background radiation (which show up as noise in the signal). Addition of elements in the center of the telescope could created significant variations in background flux, resulting in potential degradation of the shortwave channels sensitivity.

Additionally both of the HIRS/2 test collimators would need to be rebuilt with off-axis mirrors. The present collimators have a large central obscuration. The present on-axis test collimator with its central obscuration must be replaced by an off-axis mirror with no obscuration. To minimize the overall modifications to the test equipment, i.e. changes to the translator, the pin hole, collecting mirror and light source) the focal length of the off-axis mirror should be maintained as closely as possible. (The present on-axis collimator has an EFL of 19.455 in.). Dave Dodgen builds an off-axis parabolic mirror that meets the need. The mirror has an EFL, 21.86"1 clear aperture, 8.15"; zonal radius*, 6.1"; and the on-axis blur angle is 0.035 mrad. The off-axis blur angles for the HIRS 1.5° FOV are calculated as follows.

*Final radius is the distance from the center of the mirror to the optical axis.

$$\text{Astigmatism} = 0.05\,\theta^2 f_n^{-1} \quad = 3.19 \times 10^{-5} \text{ rad}$$

$$\text{Coma} = 0.0625\ \theta f_n^{-2} \quad = 1.137 \times 10^{-4} \text{ rad}$$

where θ = angle (in radians) that the
   object and image are off-axis, 0.013 rad

$$f_n = \frac{\text{focal length}}{\text{effective diameter}} = 2.68$$

   With the off-axis system, the output from the test collimator can be directly input into the HIRS telescope (i.e. no reflecting mirror will be necessary). Therefore, the translator must not obscure the collimator output. If the translator is placed at the collimator's focal point, the translator will extend 3" above the optical axis of the collimator leading to a 1" obscuration of the collimator's output beam (Figure 10.2-4). Therefore, the light source must be reflected into the test collimator as shown in Figure 10.2-5.

   To compensate for the increased f-number, the focal length of the collecting mirror must be increased to 8" instead of the present 7". The FOV will be maintained by increasing the size of the pin hole form 0.060" to 0.067".

10.2-2 Coating Modification Approach

   OCLI indicated that the possibility exists that a modification of an existing "solar rejection" coating may be useful to replace the existing longwave/shortwave dichroic beamsplitter. It is this element in the present HIRS/2 optics which causes the "picket fence" spectral response in the visible and near IR spectrum and precludes a flat and expanded channel 20 spectral response.

   The existing solar rejection coating is used with a ZnSe substrate and has high average reflectance in the visible and near IR region from about 0.42 to 2.5 micron. It then begins to transmit and has good transmission to about 15 microns.

   The existing reflection from 0.35 to 2.5 microns is shown in Figure 10.2-6. A very high average reflectance in seen with a few holes.

   OCLI felt that this coating can be modified to reflect thru about 5.0 microns so that it can reflect the shortwave IR channels as well as the visible channel 20. this is the requirement for HIRS/2. OCLI believed that the "holes" in the visible portion of the reflectance curve cannot be fully eliminated; however, it was clear that if the modified coating is not worse than that shown in Figure 10.2-6, it is much better that the existing beamsplitter in this spectral band.

Figure 10.2-4

SINGLE MIRROR HIRS/2I COLLIMATOR

TO HIRS

OBSCURATION

PIN HOLE

SOURCE

OPTICAL AXIS

NOTE: PINHOLE IS AT THE FOCAL POINT OF THE COLLIMATOR

COLLECTING MIRROR

TRANSLATOR

AEROSPACE/OPTICAL DIVISION ITT

230
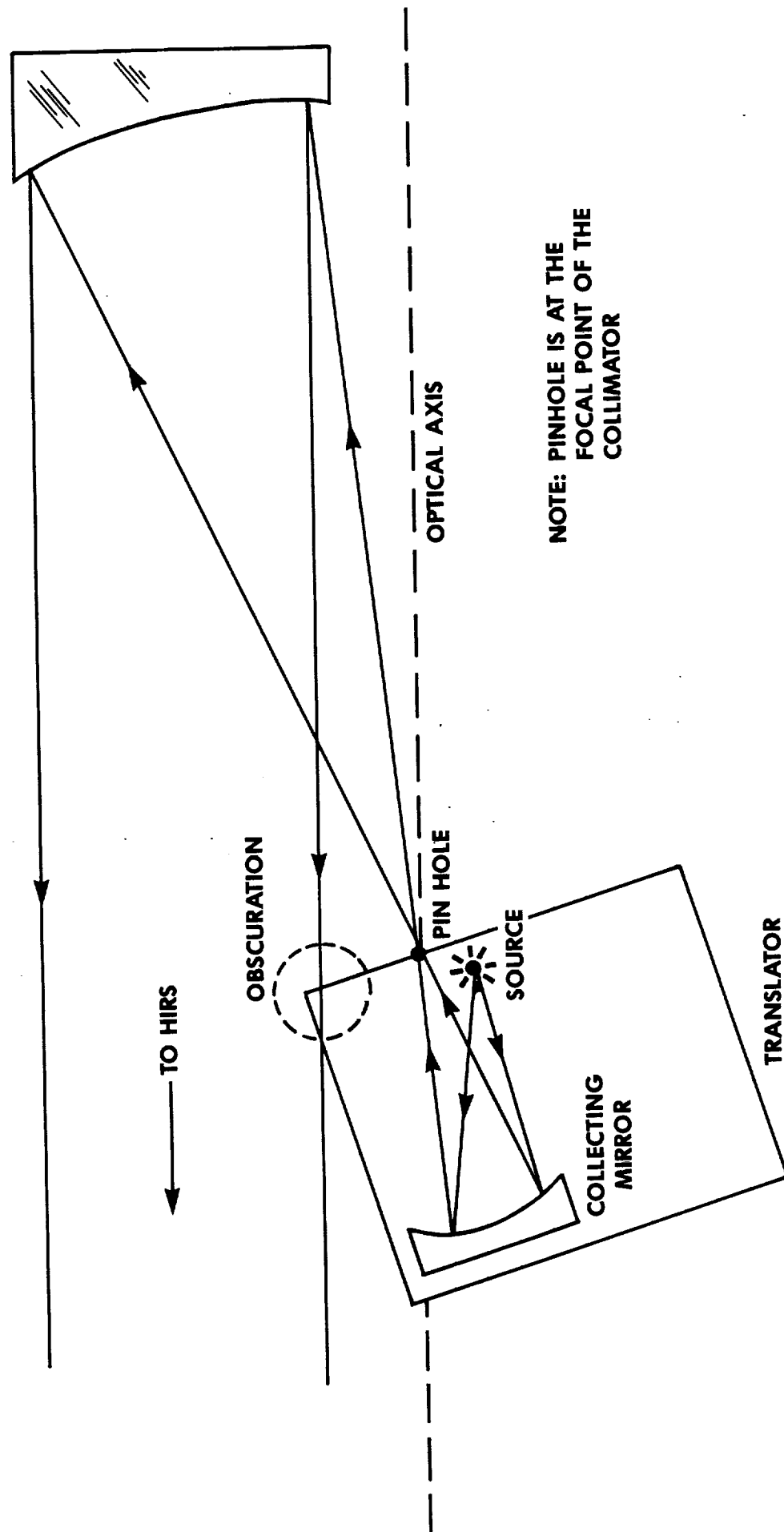
Figure 10.2-5

TWO MIRROR UNOBSCURED HIRS/21 COLLIMATOR

TO HIRS

DEFLECTING
MIRROR

FOCAL
POINT

PIN HOLE

SOURCE

OPTICAL
AXIS

AEROSPACE/OPTICAL DIVISION ITT

231
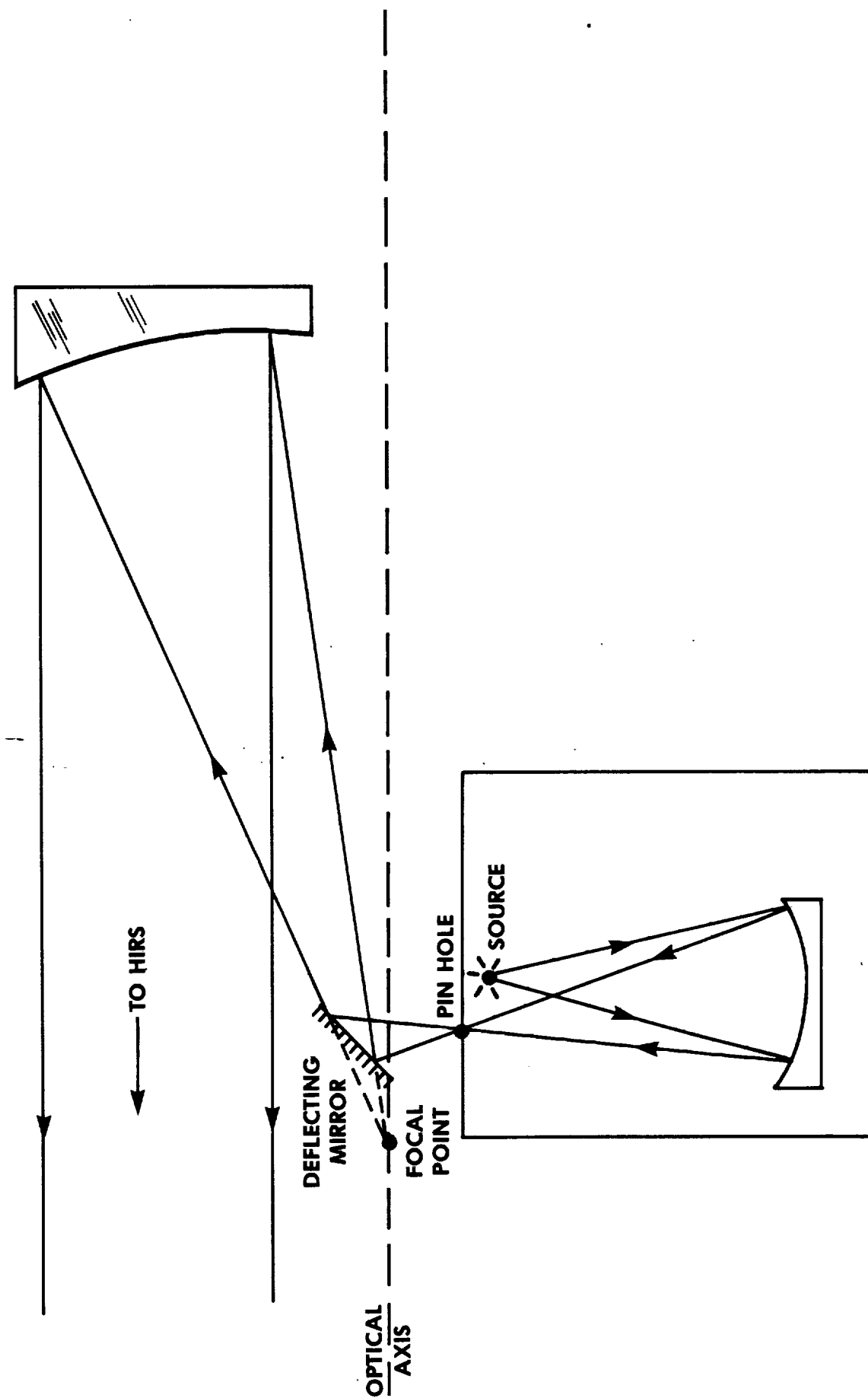
Figure 10.2-0 *REFLECTANCE OF SOLAR REJECTION*
COATING FROM OCLI

P/N: DESIGN B
WL RANGE: 0.350 - 2.500
AVG. %R: 90.5

DATE: 9 AUG 85   S/N: 10   R/N: 711-089/092

AEROSPACE/OPTICAL DIVISION **ITT**

WL in MI

%R

232
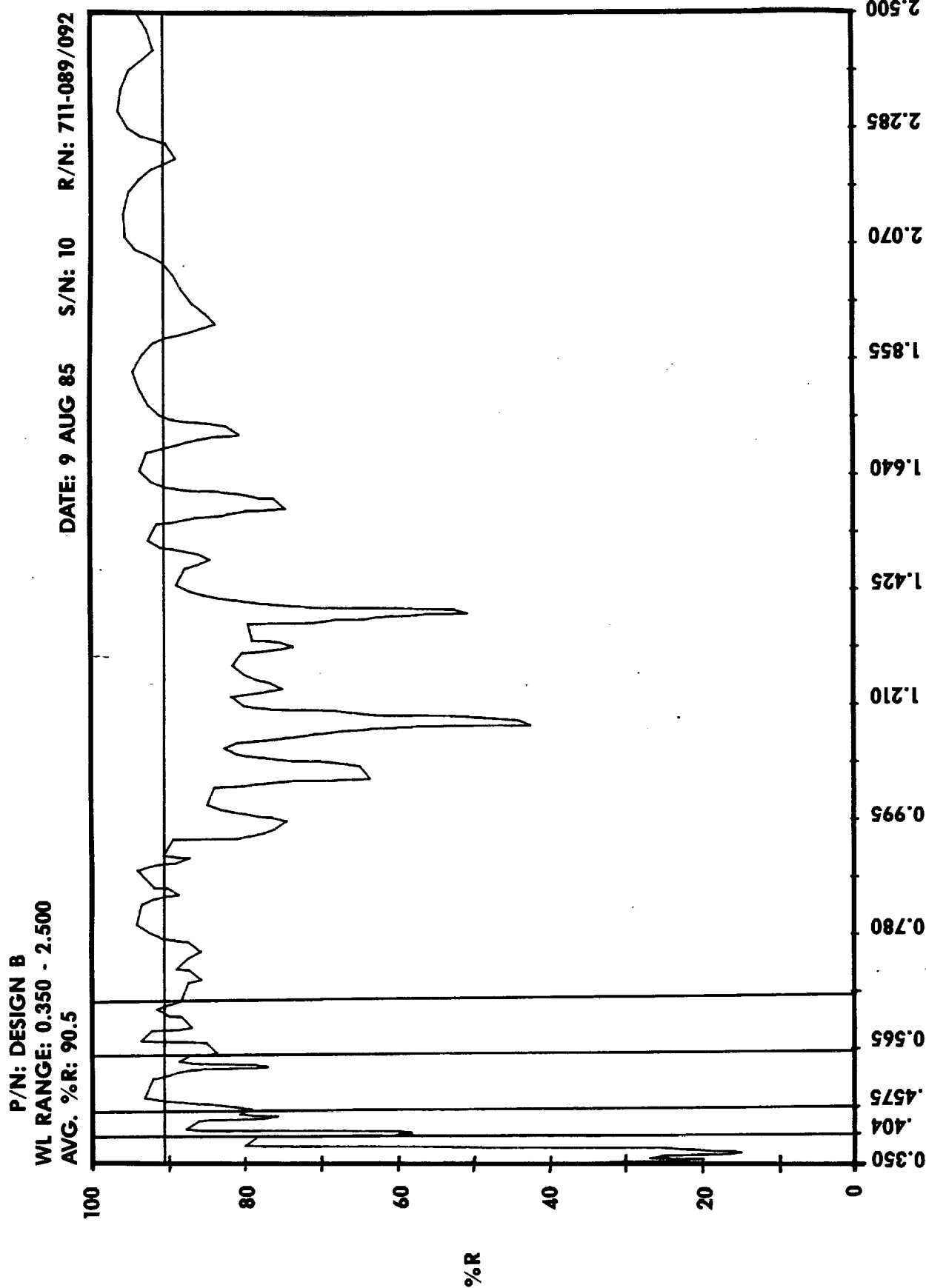
If this new beamsplitter were used in HIRS/3 and the visible spectral filter is removed, the channel 20 response would then be defined primarily by the detector response (either silion or InGaAs). If this were adequate for the users, this would result in a tremendous simplification compared to the proposed refractive telescope approach.

OCLI was given a subcontract to analyze the coating and generate expected performance. OCLI has completed their study to generate a new design for the longwave/shortwave dichroic beamsplitter. The study began with the standard OCLI solar rejection coating and modified it to allow the shortwave channels to be reflected as well as the visible.

Figure 10.2-7 is the measured performance of the present dichroic. Performance is acceptable in all channels; however, the severe ripple in the 0.4 to 2.0 micron region compromises the spectral bandwidth of any extended Channel 20 for HIRS/3.

Figures 10.2-8 thru 10.2-10 give the OCLI computer predicted reflection and transmission characteristics for the proposed coating for a germanium substrate. The coating gives excellent solar-region reflection as well as performance in the longwave and shortwave sounding channels.

Figures 10.2-11 thru 10.2-13 show OCLI computer predicted characteristics for a similar coating optimized for a lower index substrate (either Zinc Selenide or Cadmium Telluride). Use of these substrates will reduce the bulk absorption at the longwave end of the sounding channels. Thus, in addition to offering excellent solar channel reflection, these coatings should improve the NEΔN in the channels around 14 or 15 microns.

OCLI recommends (and ITT concurs) that the HIRS/3 use the coating on a Zinc Selenide substrate. OCLI has considerable experience coating this material and ITT uses ZnSe for AVHRR/2 and HIRS/2I cooler windows and lenses.

10.2-3   Expected Channel 20 Performance

10.2.3-1   Spectral Response

We have calculated an overall system spectral response for a HIRS/3 expanded channel 20 based on the following:

1. Eliminate the spectral bandpass filter.
2. Use the new LW/SW dichroic design.
3. Use either the SDC "blue enhanced" or the Epitaxx "Series V" detectors.
4. Incorporated no "band flattening" filters.

Figure 10.2-7   SHORTWAVE/LONGWAVE DICHROIC
BEAMSPLITTER REFLECTANCE
AND TRANSMISSION

AEROSPACE/OPTICAL DIVISION ITT

234
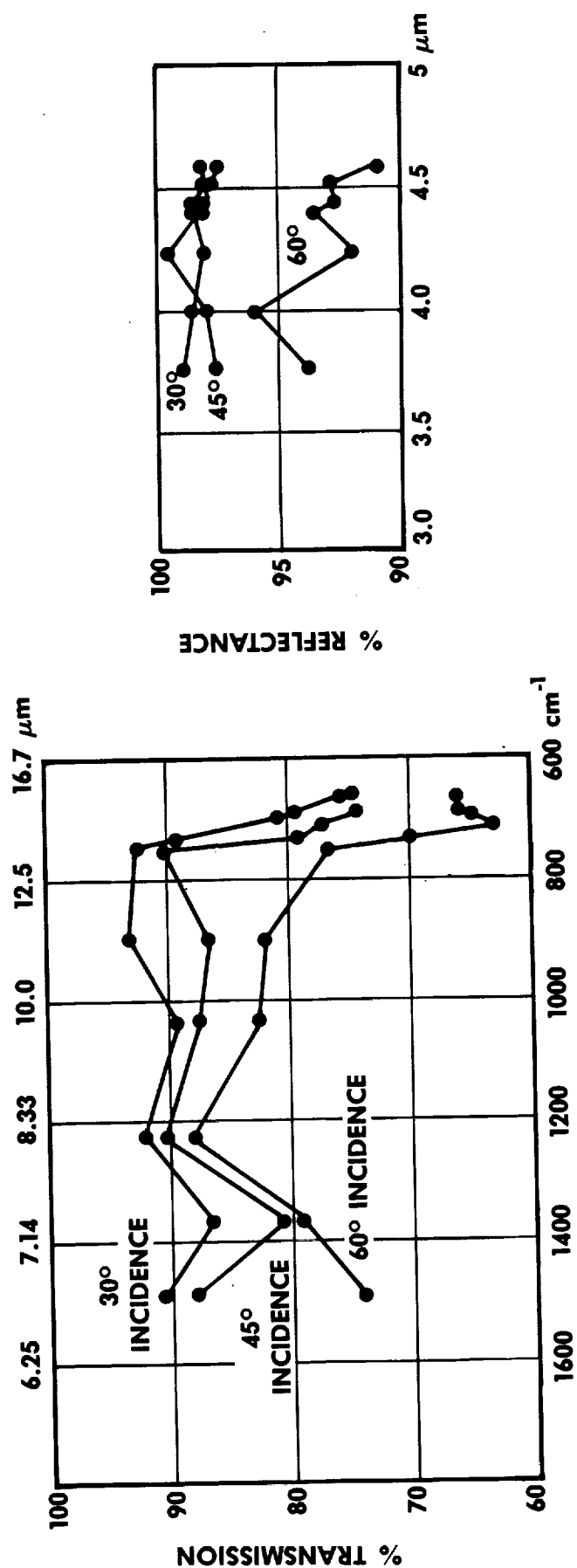
Figure 10.2-8 **VISIBLE REFLECTANCE OF NEW OCLI DICHROIC ON GERMANIUM SUBSTRATE**
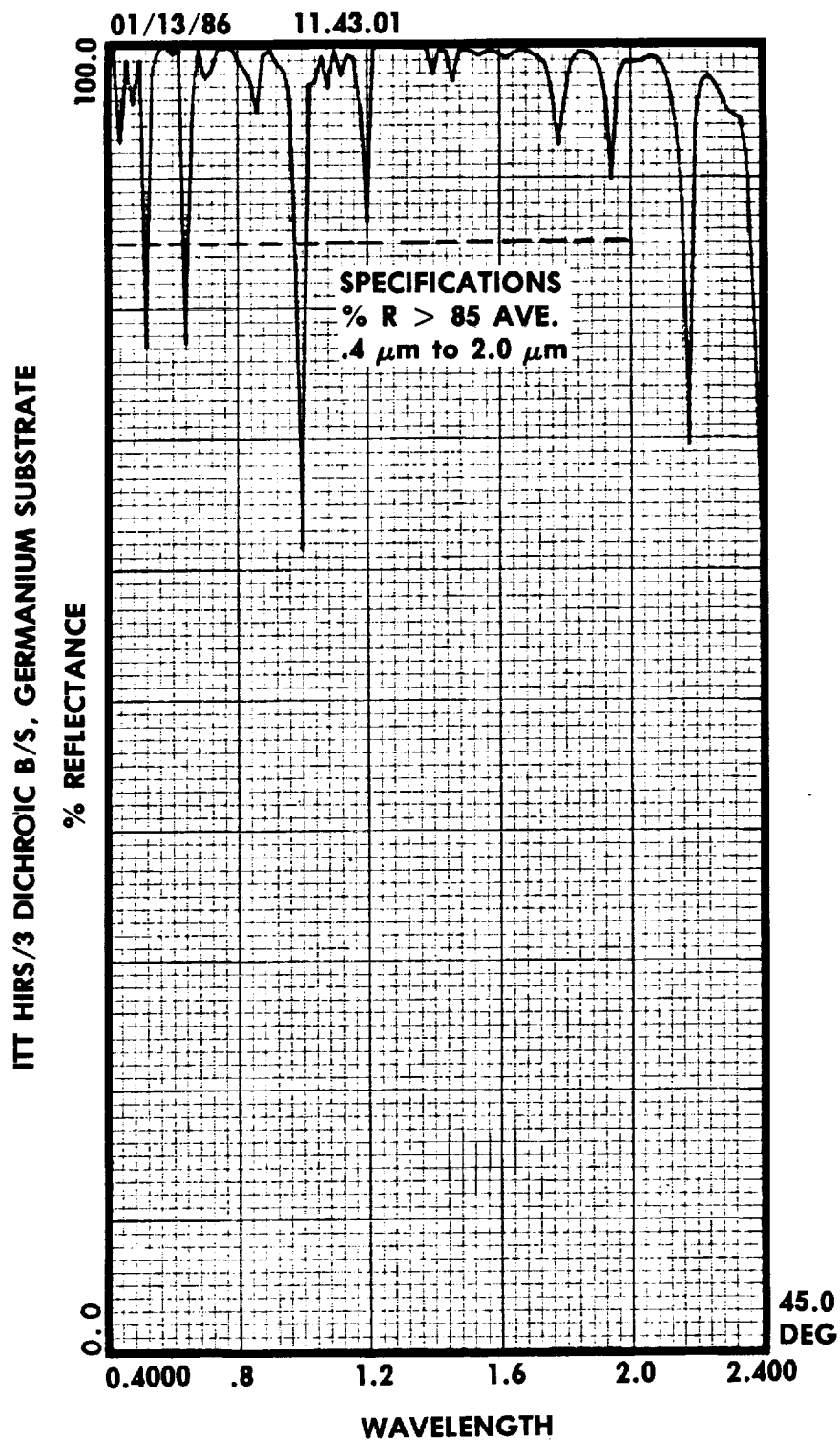
AEROSPACE/OPTICAL DIVISION **ITT**

Figure 10.2-9 SHORTWAVE IR REFLECTANCE OF NEW OCLI DICHROIC ON GERMANIUM SUBSTRATE

01/13/86   13.15.04

SPECIFICATIONS
% R > 85 ABS.
3.6 μm to 4.65 μm

ITT HIRS/3 DICHROIC B/S, GERMANIUM SUBSTRATE

% REFLECTANCE

100.0

0.0

3.000   WAVELENGTH   5.000

45.0
DEG
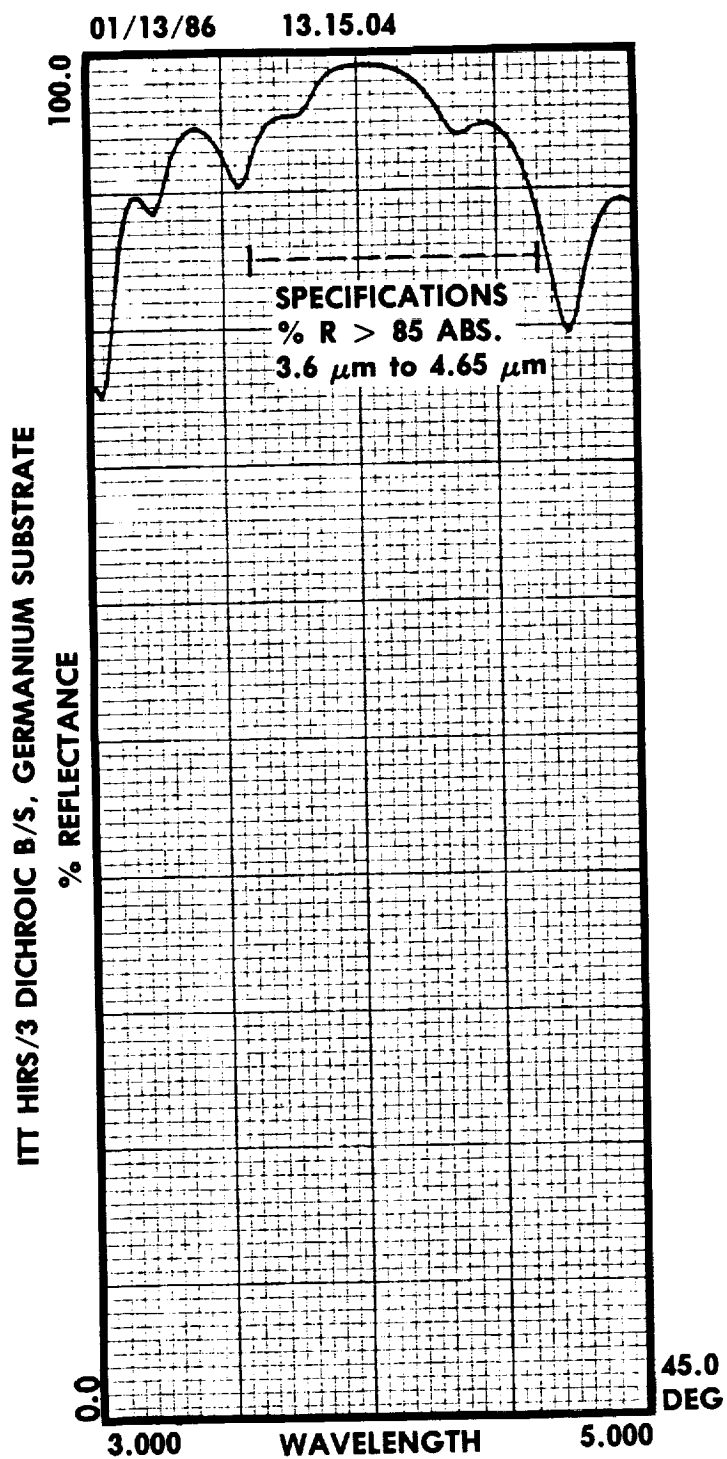
Figure 10.2-10 LONGWAVE IR TRANSMITTANCE OF NEW OCLI DICHROIC ON GERMANIUM SUBSTRATE

01/13/86   11.41.02

ITT HIRS/3 DICHROIC B/S, GERMANIUM SUBSTRATE
% TRANSMITTANCE

SPECIFICATIONS

NOTES:
— ALL DATA THEORETICAL
— BEST EFFORT AT THIS TIME
— CURVES ASSUMES SAME DESIGN
  1ST AND 2ND SIDES

100.0

0.0

45.0
DEG

3.000   5.0   7.0   9.0   11.0   13.0   15.00

AEROSPACE/OPTICAL DIVISION ITT

237
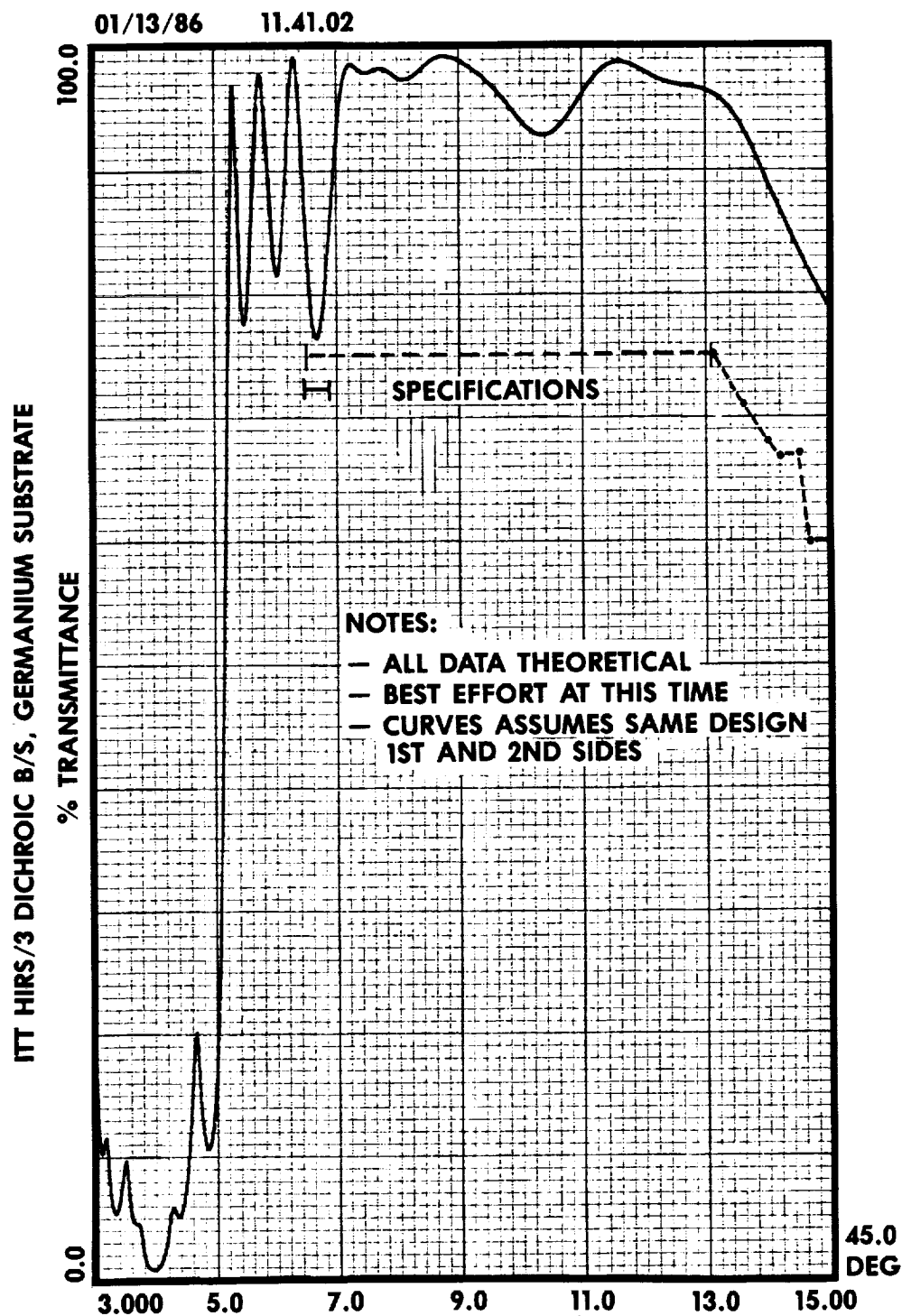
Figure 10.2-11   *VISIBLE REFLECTANCE OF NEW DICHROIC ON ZnSe SUBSTRATE*

Figure 10.2-12 SHORTWAVE IR REFLECTANCE OF NEW DICHROIC ON ZnSe SUBSTRATE

01/17/86   10.07.58

SPECIFICATIONS
% REFLECTANCE
≥ 85 ABSOLUTE

ITT HIRS/3 DICHROIC B/S, ZINC SELENIDE

% REFLECTANCE

100.0

0.0

45.0
DEG

3.000   WAVELENGTH   5.000

AEROSPACE/OPTICAL DIVISION ITT

239

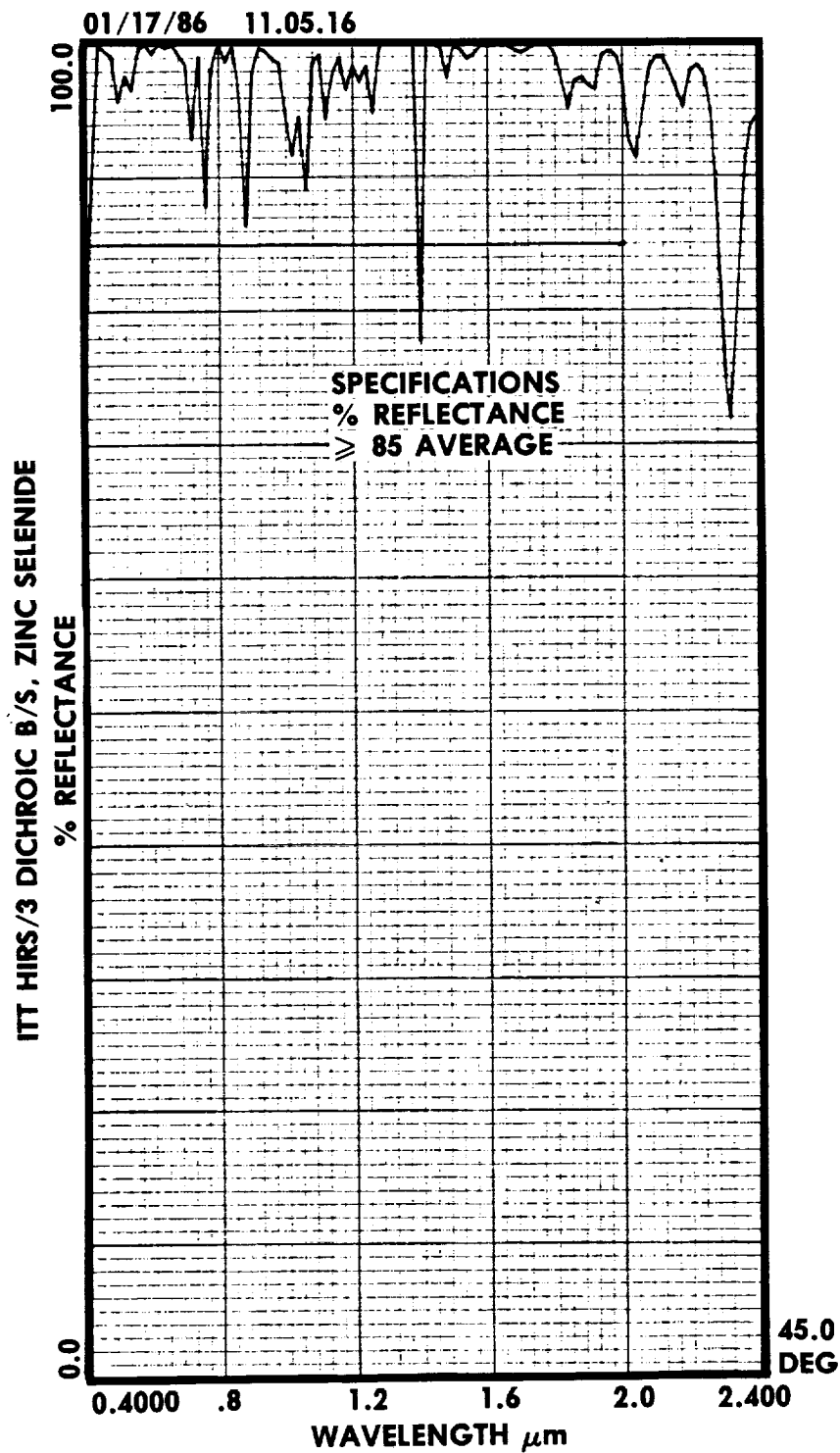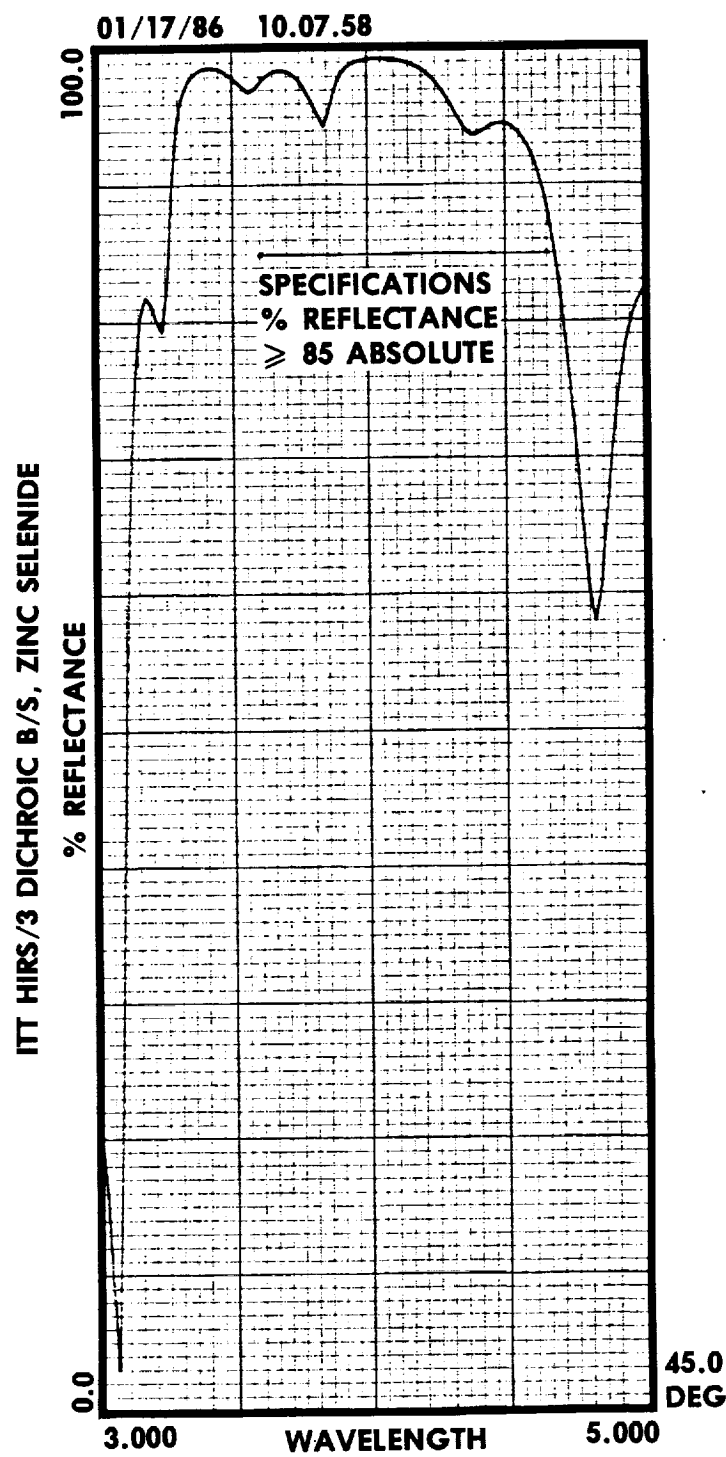*Figure 10.2-13 TRANSMITTANCE OF NEW DICHROIC ON ZnSe SUBSTRATE*

AEROSPACE/OPTICAL DIVISION

ITT

240
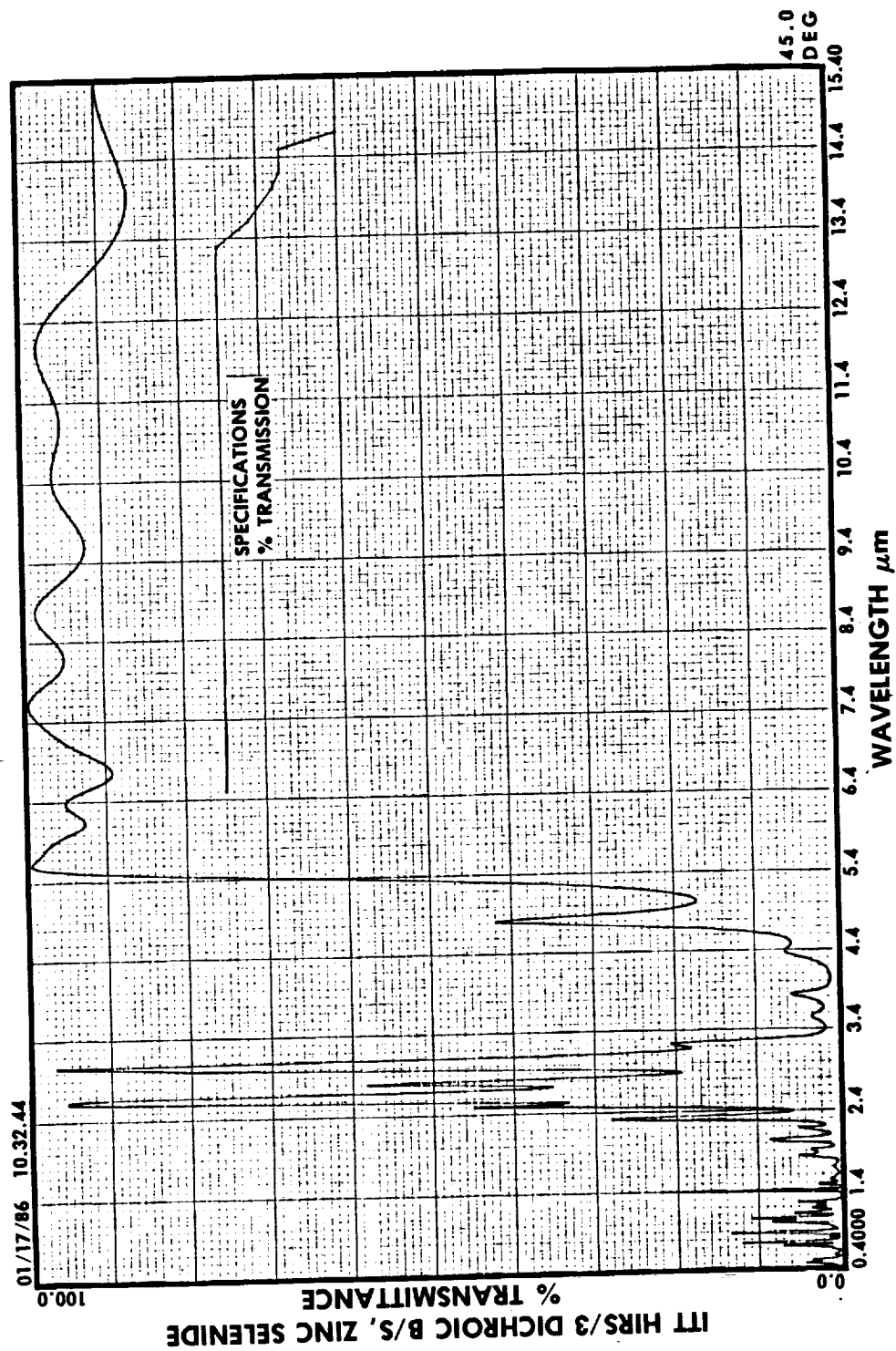
The proposed HIRS/3 channel 20 system uses the present SW/VIS beamsplitter and the present SW lens No. 1. Figure 10.2-14 shows the transmission of the beamsplitter. Figure 10.2-15 and 10.2-16 show the transmission of the SW lens in the visible and IR regions. The visible data covers only the present narrow spectral band. The IR data is presented as any coating change must not degrade the IR channels.

Figures 10.2-17 and 10.2-18 show the spectral response of the two detectors being considered for the new channel. Figure 10.2-17 if for silicon and covers .4 to 1.1µm while the InGaAs detector (Figure 10.2-18) covers .4 to 1.8µm.

Figures 10.2-19 and 10.2-20 show the response of a system that includes the detector and the SW/VIS beamsplitter. The two items peak at different wavelengths and tend to compensate each other giving a single peaked smooth curve.

Figure 10.2-21 is the solar spectral curve. the purpose of the new channel 20 is to measure the total energy in this curve. Thus the area under the curve can be used as a measure of the new channel. Unfortunately, a significant portion (8.7%) of the energy is located below .4µm. Reducing the cutoff wavelength to .36 cuts the energy lost to 5.3%. A cutoff at .34µm yields only 3.7% lost. Because of this strong lower wavelength effect it would be good to go as low as possible. Unfortunately this isn't realistic as shown in Figures 10.2-19 and 10.2-20. If we measure from .36 to 1.1µm (the 10% points of silicon) 69.1% of the solar energy is measured. If InGaAs is used (.4 to 1.8µm) then 82.9% is measured.

If the lower band edge is placed much lower than 0.50 micron, contamination control requirements will have to be addressed in considerably more depth than the present HIRS/2 or AVHRR/2 requires. This could represent a significant design and cost problem since careful handling would be required at all levels including spacecraft level testing. Handling similar to the SBUV would be required.

Using the above information, ITT has generated two representative expanded channel 20 spectral responses for HIRS/3. One is for a channel using a silicon detector (Figure 10.2-22) and the other is for a channel using an InGaAs detector (Figure 10.2-23). Either can be incorporated into HIRS/3. the use of the silicon detector is of considerably less impact since it is existing detector material. ITT recommends the use of the silicon detector.

10.2.3.2   Sensitivity

The sensitivity of the wideband channel 20 will be digitizer limited (roughly 1 part in 8000) with either the silicon or InGaAs detectors. This is a S/N of about 40:1 at 1/2% albedo. The channel would be calibrated to cover the full 0 to 100% albedo range.

Figure 10.2-14 VISIBLE TRANSMISSION HIRS/2I SW/VIS BEAMPSLITTER
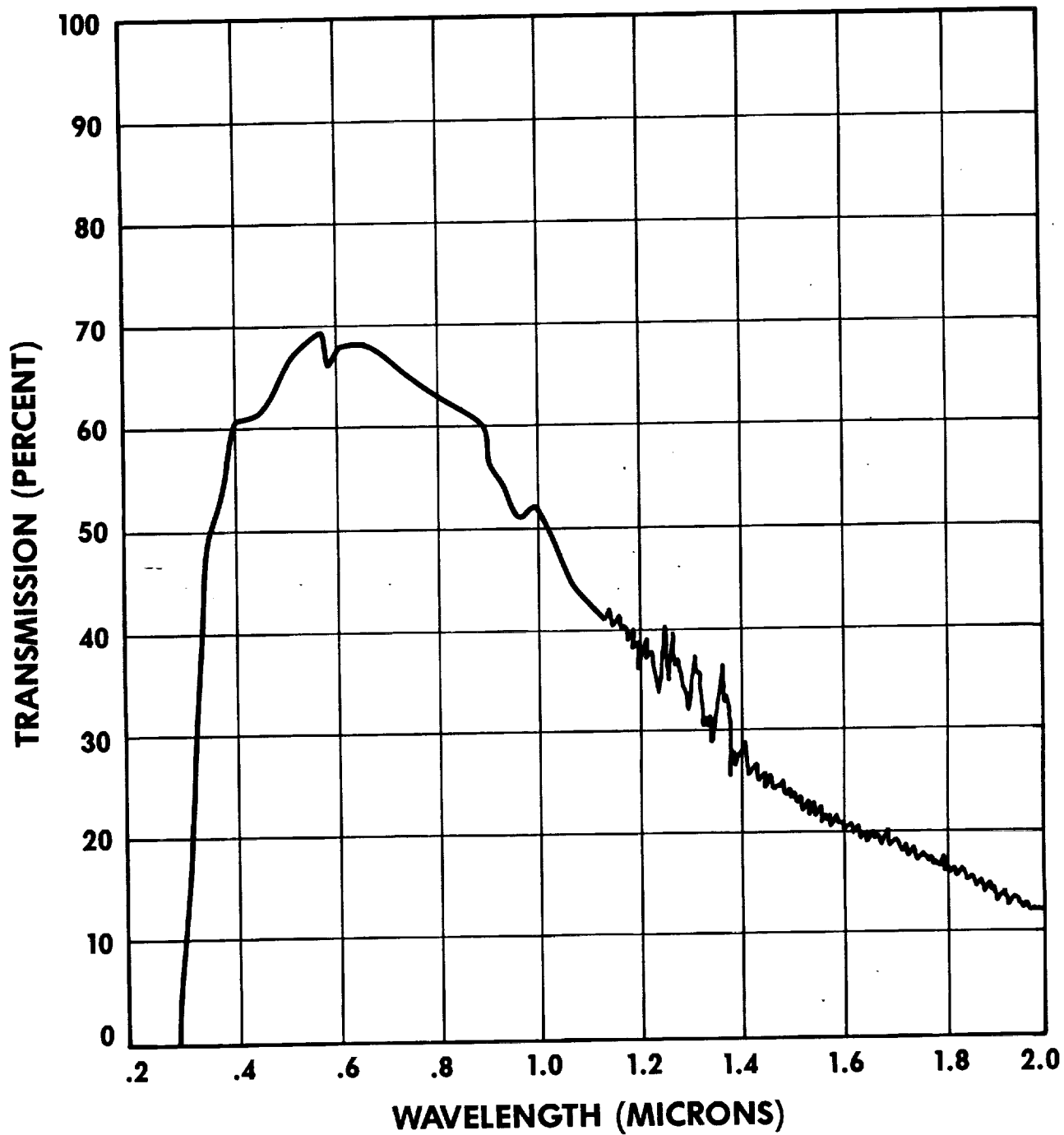
AEROSPACE/OPTICAL DIVISION ITT

Figure 10.2-15 PRESENT HIRS/2 S.W. LENS NO. 1
VISIBLE TRANSMISSION
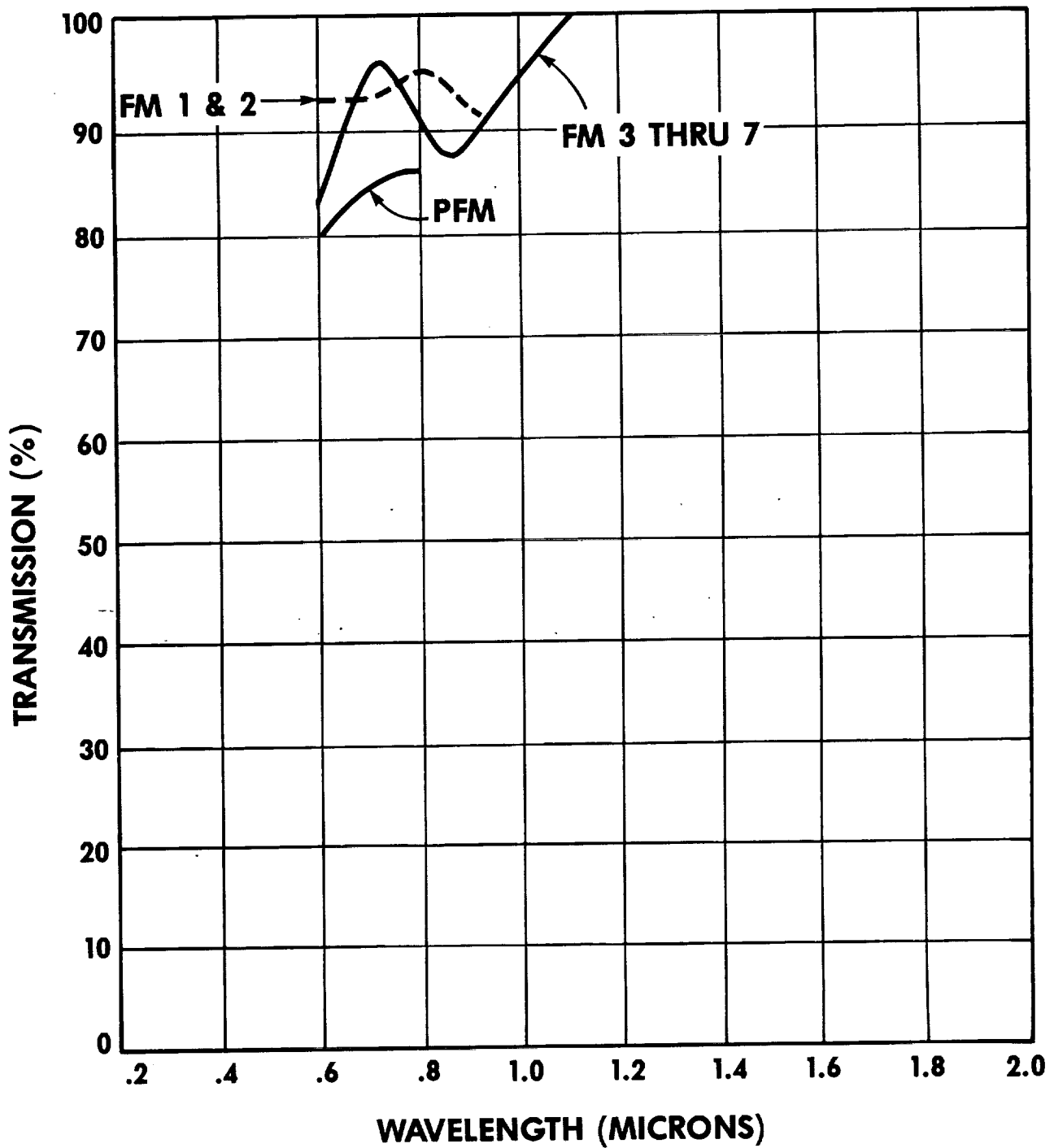
AEROSPACE/OPTICAL DIVISION ITT

Figure 10.2-16   PRESENT HIRS/2 S.W. LENS NO. 1
IR TRANSMISSION
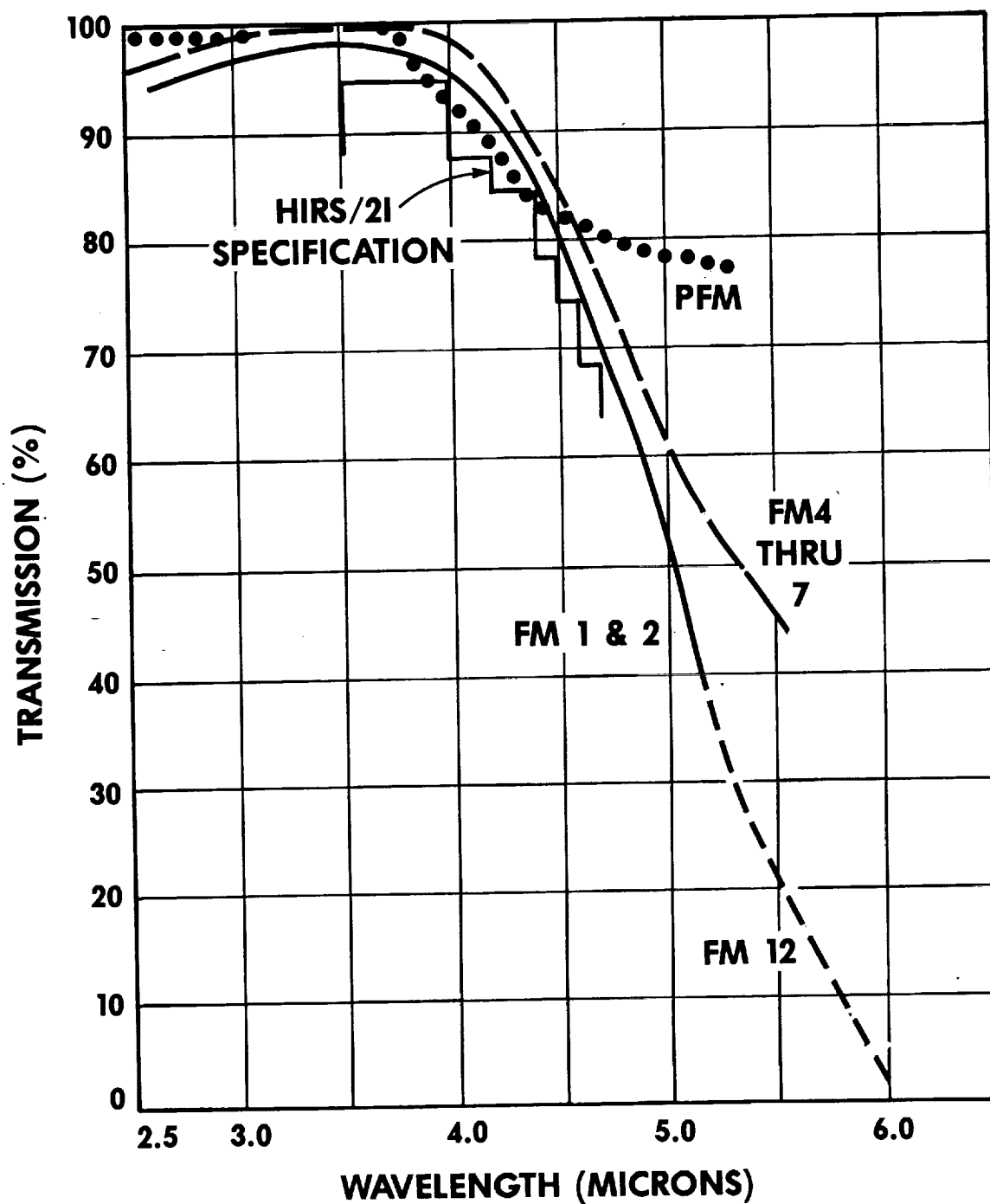
AEROSPACE/OPTICAL DIVISION ITT

Figure 10.2-17 SILICON DETECTOR RESPONSE
(SCD PHOTOVOLTAIC, UV + BLUE ENHANCED)
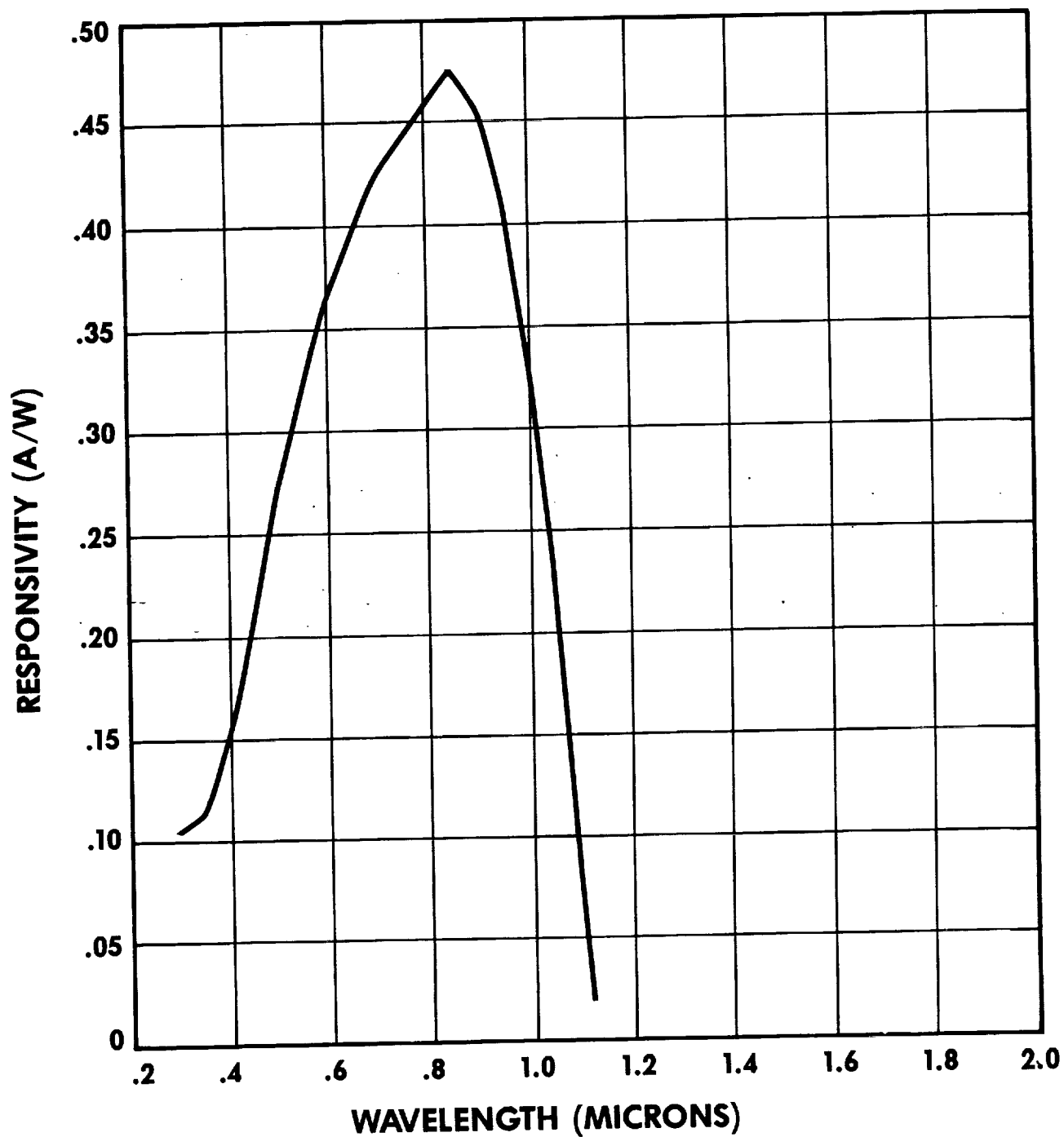
AEROSPACE/OPTICAL DIVISION ITT

Figure 10.2-18   InGaAs DETECTOR RESPONSE
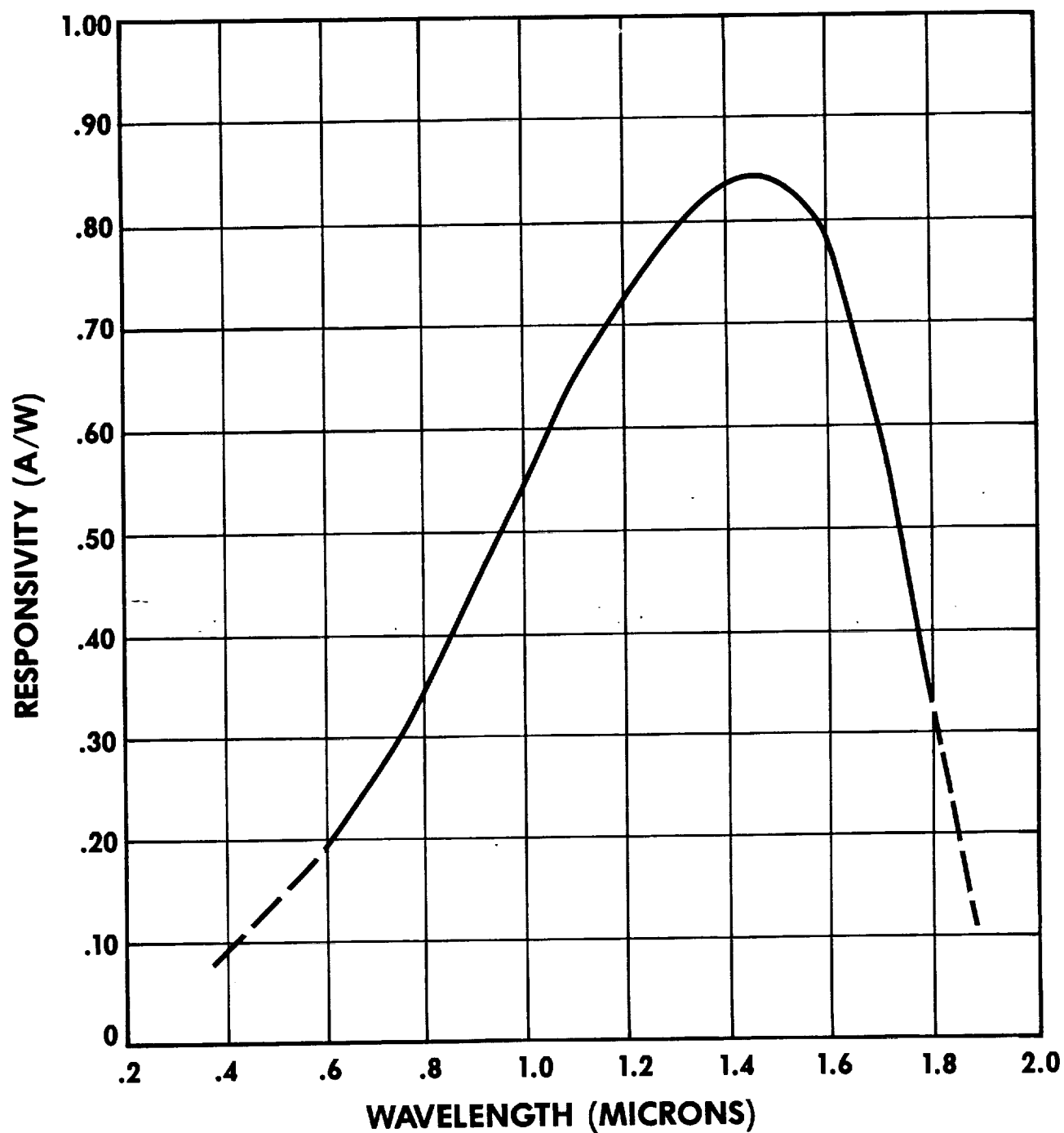
Figure 10.2-19 SILICON DETECTOR +
SW/VIS BEAMSPLITTER
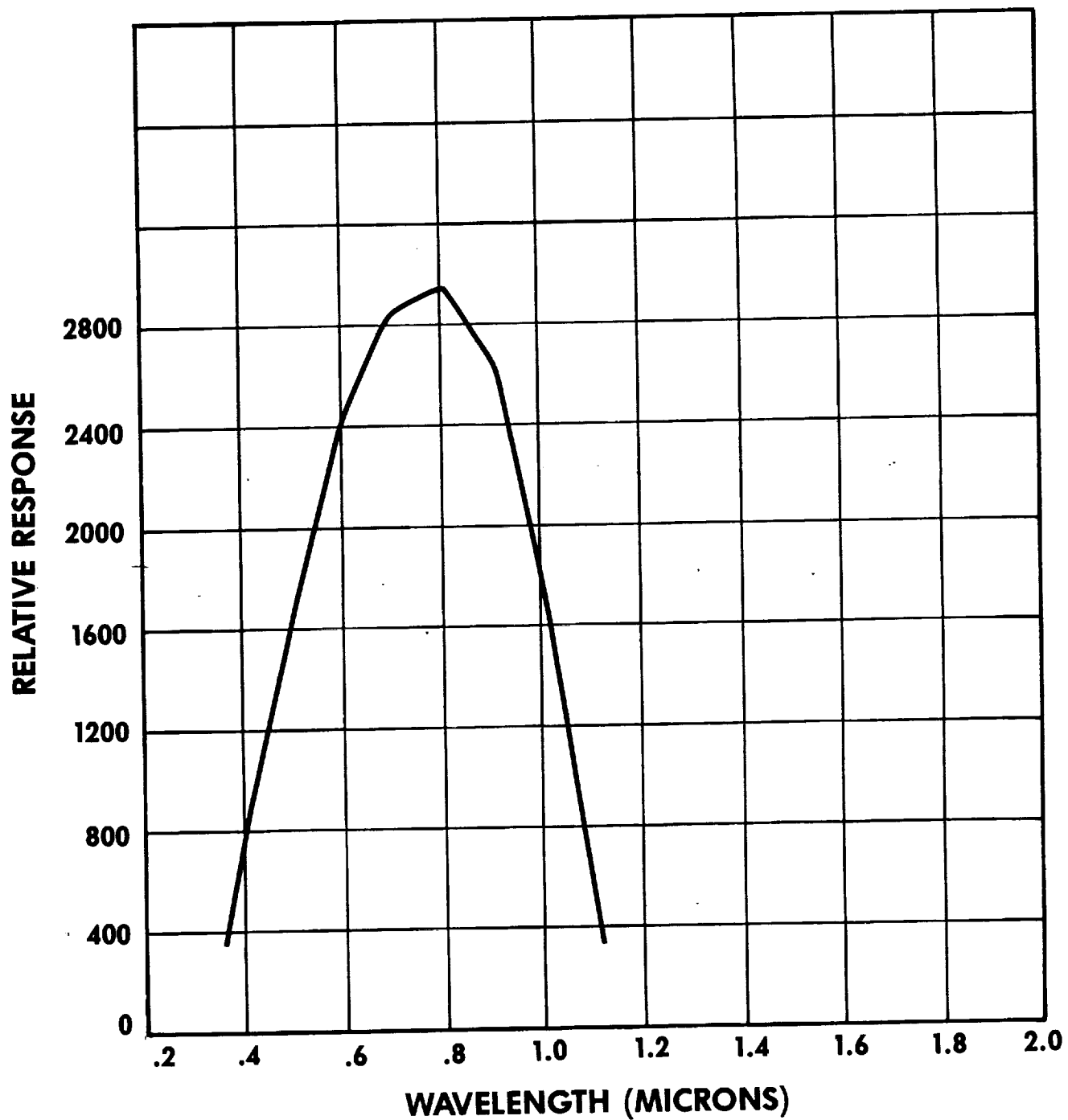
AEROSPACE/OPTICAL DIVISION ITT

Figure 10.2-20 InGaAs DETECTOR +
SW/VIS BEAMSPLITTER
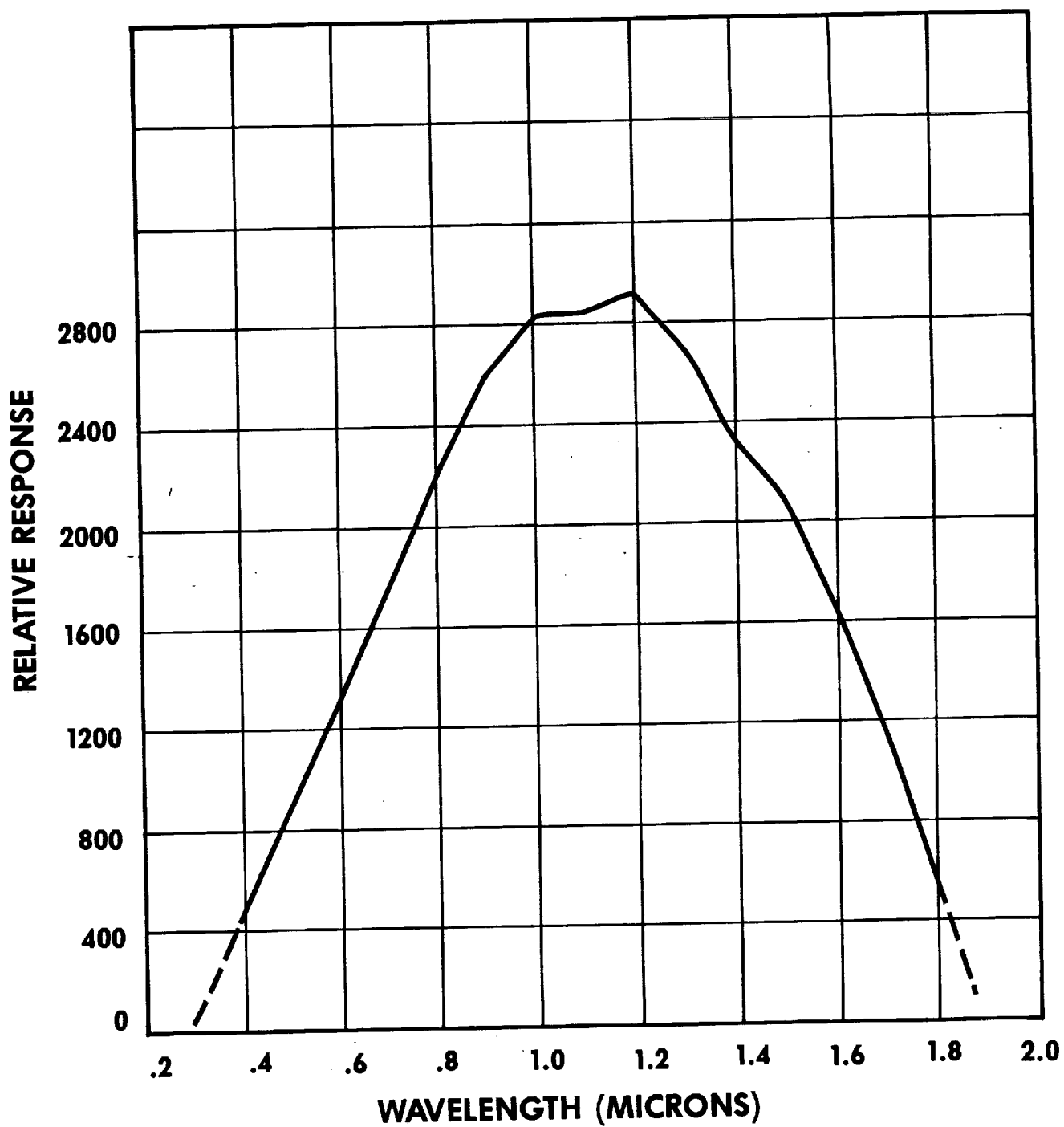
Figure 10.2-21 SOLAR SPECTRAL IRRADIANCE

WAVELENGTH (MICRONS)
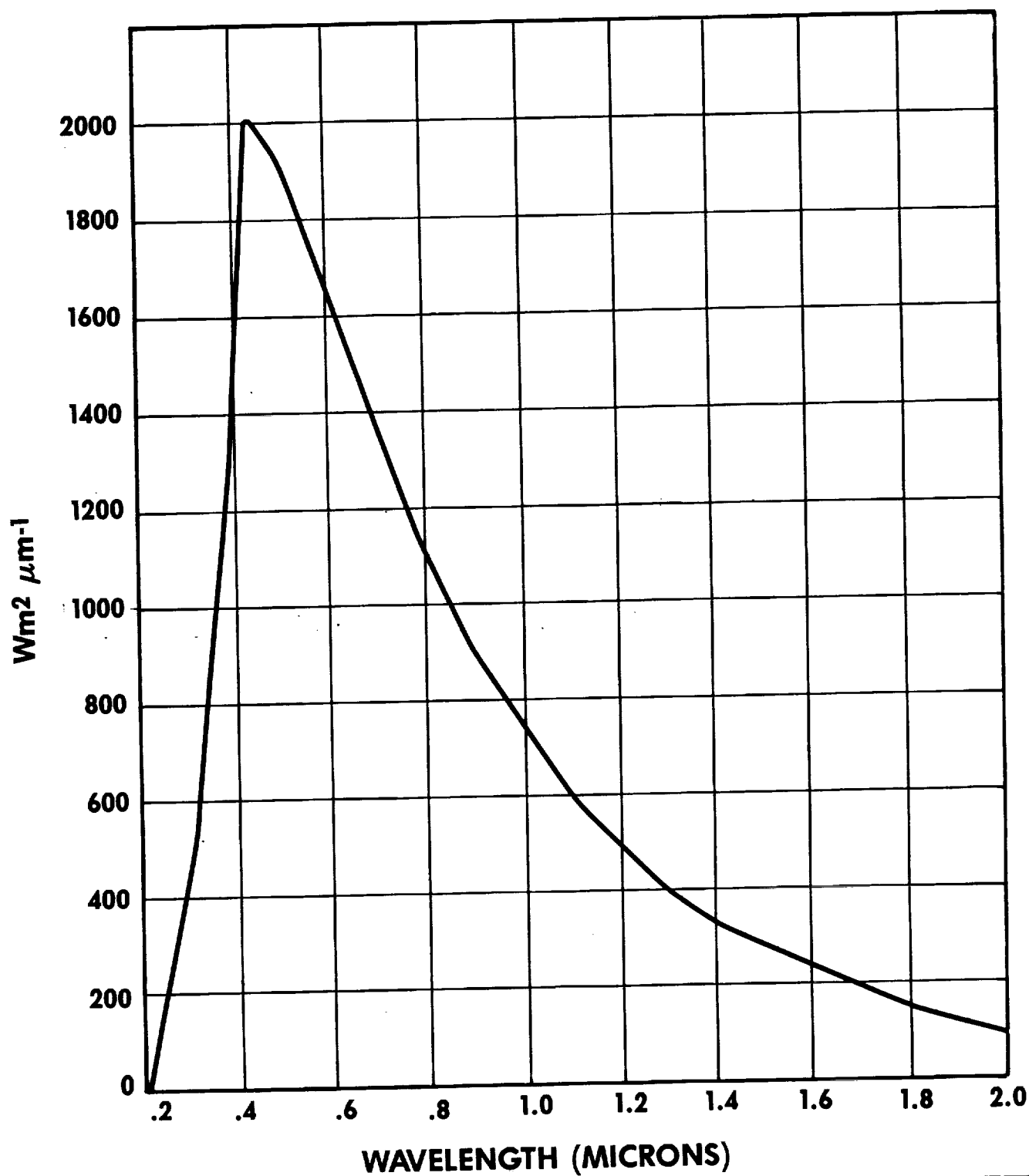
Figure 10.2-22   TOTAL SYSTEM SPECTRAL RESPONSE WITH SILICON DETECTOR

RELATIVE RESPONSE

WAVELENGTH (MICRONS)

ITT

AEROSPACE/OPTICAL DIVISION

250
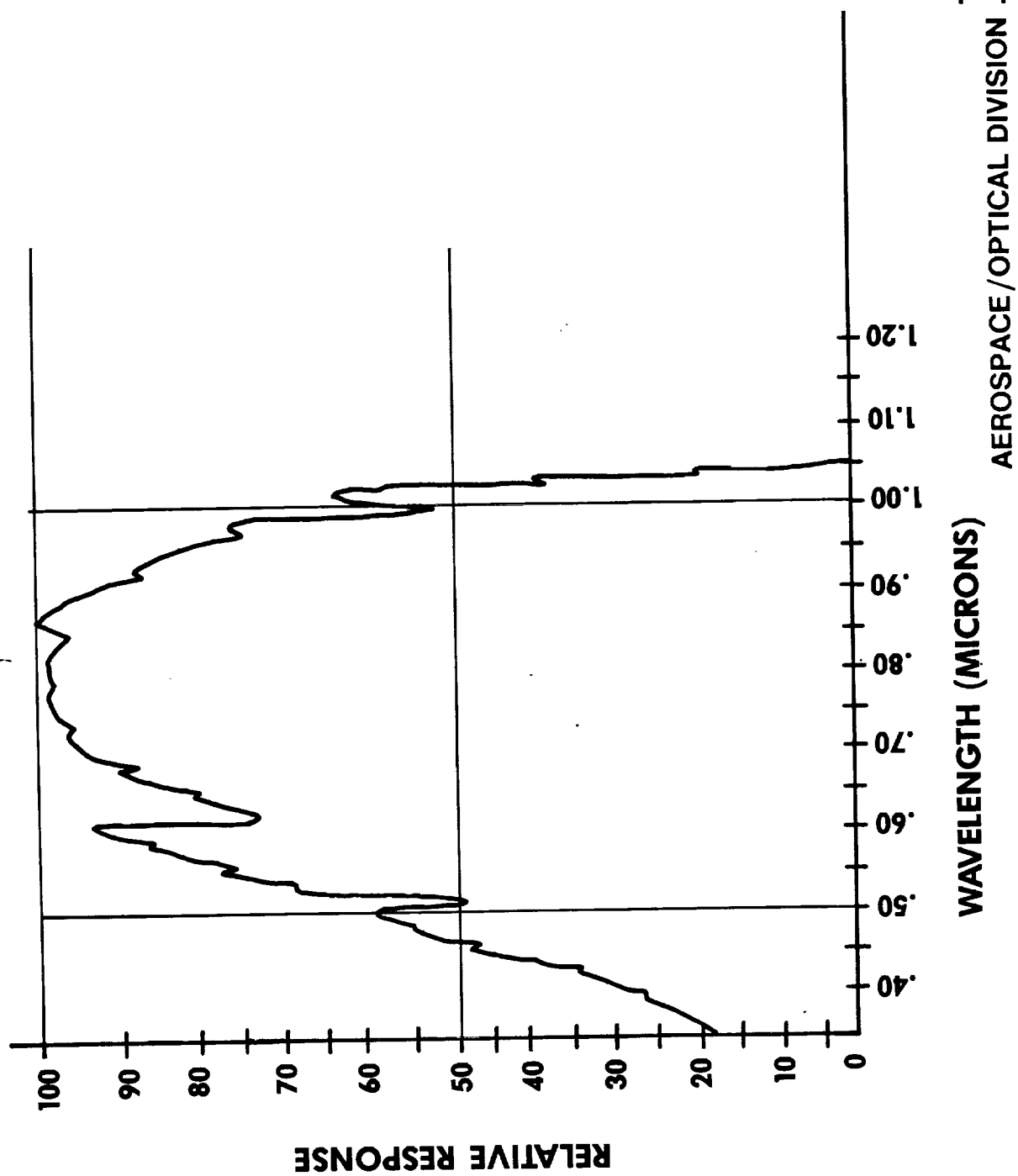
Figure 10.2-23 TOTAL SYSTEM SPECTRAL RESPONSE WITH InGaAs DETECTOR

ITT

AEROSPACE/OPTICAL DIVISION

251
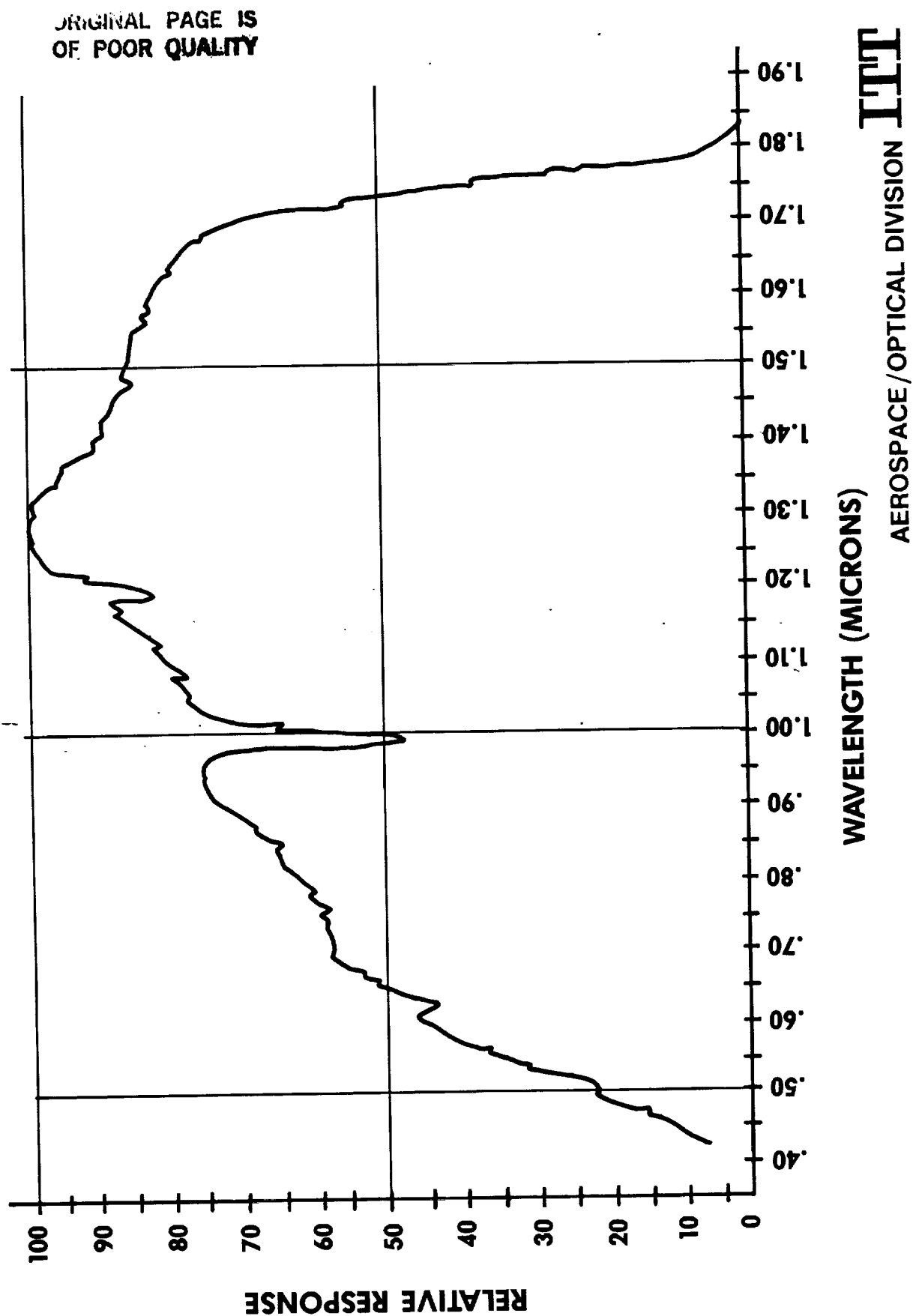
10.2.3.3 Polarization Sensitivity

The polarization sensitivity of the existing HIRS/2 and HIRS/2I optical elements (and total system) is not a measured parameter. Therefore no data exists. ITT plans to measure the polarization sensitivity in the existing channel 20 on FM-3I prior to its delivery. This data will only be marginally useful since the spectral band is so narrow. A detailed polarization analysis must be performed as part of an interim study or at the beginning of the HIRS/3 detailed design effort.

10.3 Electronic Modifications

The new wideband channel 20 will not require any new circuitry. Whether a silicon or indium gallium arsenide detector is used, the preamp circuit is the only circuit affected. The changes required to the preamp are merely gain changes to accommodate different signal levels.

10.4 Radiometric Calibration

The new channel 20 can be radiometrically calibrated using the AVHRR Integrating Sphere light source (which is used to calibrate the solar channels on AVHRR). The sphere has a 12 level output which can be used to verify the linearity of the channel 20 output (although in practice the HIRS/3 will be more linear than the bulb calibration for the sphere).

10.4.1 Calibration Sequence

The sphere is calibrated to NBS radiance standards by Optronic Laboratories, Inc. A typical calibration sequence is as follows:

a. The near normal spectral radiance of the 12-inch aperture was determined over the wavelength range of 350 to 2000 nm. Measurements were made at 50nm intervals over the 350 to 900nm wavelength region and at 100 nm intervals over the 900 to 2000nm region.

b. The relative intensity of the sphere source at all 12 levels was determined at two wavelengths.

10.4.2 Method of Calibration and Standards

An Optronic Laboratories Model 740A Optical Radiation Measurement System supplemented by a thermoelectrically cooled Ge detector, an infrared blazed grating and an IR blocking filter was used to compare the spectral output of the NASA sphere source to an Optronic Laboratories Model 420 Continuously Variable Integrating Sphere Calibration Source. The Model 420 was calibrated for spectral radiance over the 350 to 2000nm wavelength region relative to the NBS spectral

radiance and spectral irradiance scales. The estimated uncertainty in the calibration of the Model 420 relative to the NBS standards as a function of wavelength is given below.

Wavelength (nm)	Uncertainty (Model 420) (%)
350-400	±3
400-900	±2
900-1300	±3
1400-2000	±4

The uncertainty in the transfer calibration from the Model 420 to the NASA Sphere Source is estimated to ±1.5%.

10.4.3   HIRS/3 Calibration

The HIRS/3 channel 20 would be calibrated under ambient (non-vacuum) conditions with the unit at room temperature. This is the identical procedure used to calibrate AVHRR/2. A lamp source is used in the thermal vacuum chamber as a "liveness" check during vacuum testing.

10.5   Mechanical Implementation

Mechanical implementation of a wideband channel 20 is straight forward. The only mechanical impacts are the removal of the present spectral filter and a possible change in the detector package configuration.

Removal of the filter from the filter wheel will unbalance the wheel; therefore, it is likely that a clear substrate will be placed in the filter wheel to replace the filter and allow the wheel to be balanced. There are several possible substrate materials available including quartz or sapphire. A selection will be made when the detector choice is made by NOAA.

If the filter wheel can be dynamically balanced with no substrate installed, then an open hole may be left in the filter wheel.

The channel 20 detector mounts on the side of the relay optic housing. This approach will be maintained in the new HIRS/3. The mounting hardware and mounting hole size may change if the selected detector has a different physical package. This will not be a significant modification.

No other mechanical changes are needed to implement the wideband channel 20 for HIRS/3.

10.6   Test Equipment Changes

The changes to the HIRS/2 computer and other test equipment are discussed in section 8.0.

10.7   Filter Wheel Life

In the original statement of work, the life of the HIRS filter wheel was not addressed. Since the original design of the HIRS filter wheel, significant advancements in bearing and lubrication technology have transpired. These advancements warrant investigation and, if applicable, redesign the HIRS filter wheel bearing assembly to yield longer life. This section addresses the results of the various studies conducted to understand the failure mechanism of the HIRS instrument and compare its performance to the AVHRR scanner.

The HIRS and AVHRR instruments were originally designed to operate for a life of 2 years. The life of the HIRS and AVHRR instruments are listed in Table 10.7-1. From this listing, it is evident that both instruments have operated beyond their design life. The life limiting item for the HIRS system is the filter wheel; for AVHRR it is the scanner.

Table 10.7-1. Rotating Assemblies on TIROS Instruments Life History

|		
TIROS-N launched 10/78 spacecraft failed	HIRS/2, PFM 2.5 years	AVHRR/1, PFM 2.5 years
NOAA-6 launched 6/79	HIRS/2, FM-1 4 years filter wheel failed	AVHRR/1, SN103 5.5 years scanner still operating
NOAA-B launched 5/80 spacecraft failed to achieve orbit	HIRS/2, FM-2	AVHRR/1, SN104
NOAA-7 launched 6/81	HIRS/2, FM-4 3.5 years filter wheel failed	AVHRR/2, SN201 5 years scanner still operating
NOAA-8 launched 3/83 spacecraft failed 7/1/84	HIRS/2, FM-3 operating at failure	AVHRR/1, SN102 operating at failure
NOAA-9 launched 12/84 spacecraft still operational	HIRS/2, FM-6 Still operating	AVHRR/2, SN202 Still Operating
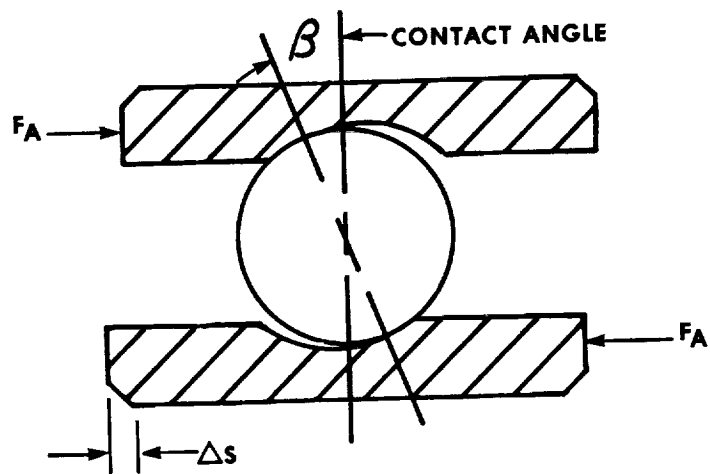
FIGURE 10.7.1-1
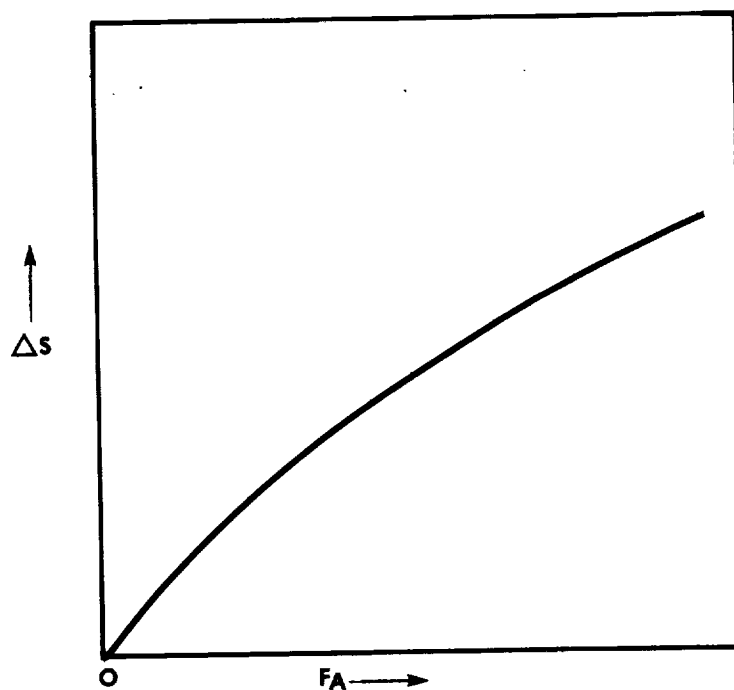
FIGURE 10.7.1-2   LOAD DEFLECTION CURVE

AEROSPACE/OPTICAL DIVISION ITT

The failure sequence of the HIRS differs from the AVHRR. The AVHRR scanner performance is monitored by its jitter performance. Jitter is termed as the variance of each successive rotational period of the scan mirror as compared to the absolute true rotational period. The design specification is that 98 percent or better of the rotations during a 20 minute interval are within ±16 microseconds of the absolute rotational period. During the instruments' operation in orbit, a degradation of the jitter indicates a degradation in the bearing performance. The time in which the scanner begins to indicate problems and adversely affects the instrument performance is a relatively long period, in the order of weeks. Once the jitter becomes extensive, the timing of the system becomes out of sync with the positioning of the scan mirror and requiring a re-syncing of the spacecraft data system.

The failure of the HIRS filter wheel is a "hard" failure. The filter wheel's function is to rotate a series of spectral filters through the optical path. The rotational period must be highly repeatable, yet the variance from one rotation to another is not as critical as with AVHRR scanner. A significant rise in the motor current indicates that the filter wheel is beginning to fail. This rise in motor current indicates that the bearing torque required to rotate the filter wheel is rising. The failure of the filter wheel occurs within a few hours.

10.7.1   Filter Wheel Preload

The current preload specified on the HIRS/2I filter wheel bearing is 12 pounds. It has been speculated that the premature life failure (as compared to the AVHRR) was due to the high, 30 pound preload placed on the earlier flight models.

Bearing design incorporates many factors; geometry, stiffness, operational speed, running torque, lubrication, operating temperature, and capacity. In any design, the governing parameters must be optimized. Although the AVHRR scanner and HIRS filter wheel are both rotating, each is very different from the other and cannot be directly compared.

Preload is geometry dependent. It is done to remove all bearing play, axial and radial, to stiffen the bearing. The rationale for preloading is:

...to decrease the subsequent deflection in a
bearing when an external load is applied to the bearing.

Figure 10.7.1-2 illustrates the "load deflection" curve for a given nonpreloaded bearing. The curve illustrates that for a given axial force, the bearing assembly is going to deflect from some original datum. Figure 10.7.1-1 illustrates a cross section of an angular contact bearing. The contact angle is the angle between the points of contact of the ball to the raceways and the radial center line. As an axial load Fa is exerted, the ball shifts its orientation with respect

to the raceway, shifting the contact angle. The relationship between the axial force Fa and the shift in the contact angle determines the bearing raceway deflection. The below equations govern the load deflection characteristics of a given single bearing.

$$\frac{F_\rho}{ZD^2K} = \sin \alpha_\rho \; (\frac{\cos \alpha^0}{\cos \alpha_\rho} - 1)^{1.5} \tag{1}$$

$$\delta\rho = \frac{BD \sin(\alpha_\rho - \alpha^0)}{\cos \alpha_\rho} \tag{2}$$

For a duplex set of bearings, the following equations govern axial force and deflection.

$$\frac{F_\rho}{ZD^2K} = \sin \alpha_1 \; (\frac{\cos \alpha^0}{\cos \alpha_1} - 1)^{1.5} - \sin \alpha_2 \; (\frac{\cos \alpha^0}{\cos \alpha_2} - 1)^{1.5}$$

$$\sin(\alpha_1 - \alpha^0) + \sin(\alpha_2 - \alpha^0) = \frac{2 \; \delta_\rho \cos \alpha^0}{BD}$$

Figure 10.7.1-3 graphically illustrates the deflection of a duplex set of bearings due to an axial load.
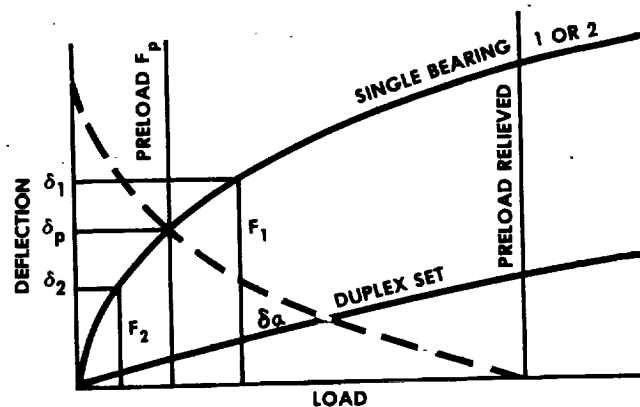
Figure 10.7.1-3. Deflection vs. Load for a Preloaded
Duplex Set of Ball Bearings

As an axial load is applied, the deflection of each individual bearing differs. As the axial load is increased, one bearing will support the load, while the other will support the load until the applied axial load equals the preload value of the bearing.

10.7.1.1   Preload Calculations

The following examples and calculations are for a single HIRS filter wheel bearing. A bearing is to have a preload of F (lbs). From equations (1) and (2), the deflection Δs is determined. The inner raceway is ground by Δs. When the bearing is assembled onto the shaft the Δs is incorporated into the assembly and the bearing is "pre" stress or preloaded. Figure 10.7.1-4 illustrates the load deflection
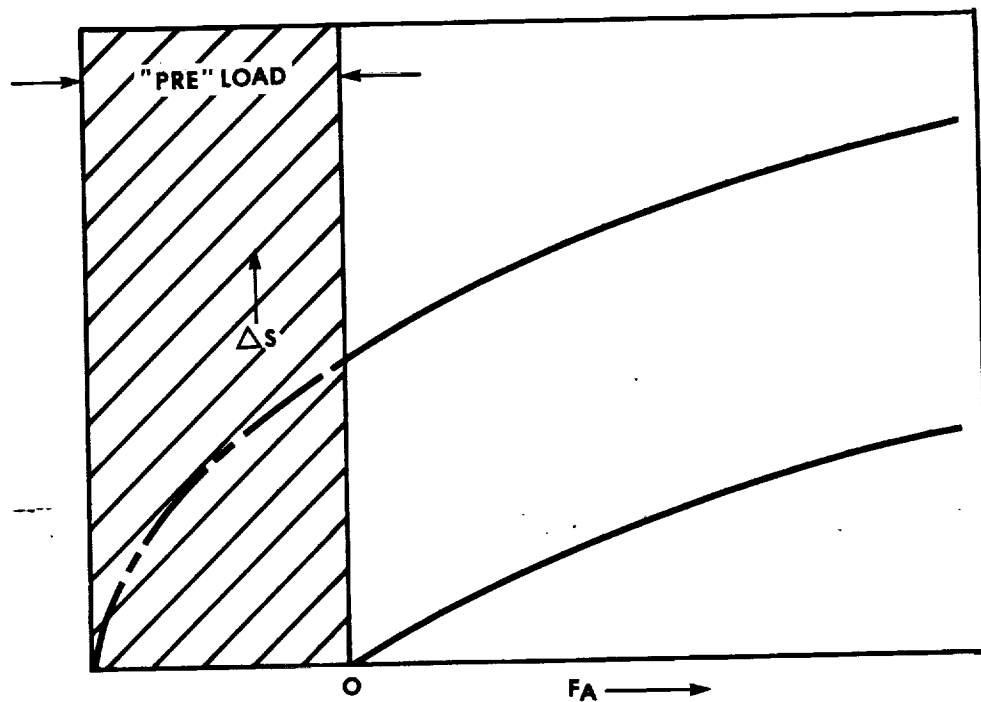
FIGURE 10.7.1-4   LOAD DEFLECTION CURVE FOR PRELOADED BEARING

curve for the preloaded bearing. Compare Figure 10.7.1-2 to Figure 10.7.1-4. As an axial force is applied to each bearing, each will deflect. Note that the slope, or rate of change of each curve is extremely different. As the load increases for the preloaded bearing, the rate of increase of bearing deflection decreases, which tends to reduce the bearing's overall deflection under additional load. The assembly with the preloaded bearing is much stiffer.

By preloading a bearing, the load deflection curve is shifted such that the curve is relatively linear. The stiffness, or spring constant of a bearing is defined as the first derivative of its corresponding load deflection curve. The overall intent of preloading the filter wheel is to keep the bearing stiffness linear throughout the range of loads exerted on the wheel during the intended load conditions.

As stated before, many parameters govern the performance of a bearing. The primary concern in bearing design is its ability to carry the various load conditions imposed on it. These loads for the filter wheel are divided into three conditions.

1. Ground Activity
2. Short Time Operation - launch simulation
                          - launch phase
3. Long Time Operation - space environment

For each condition, different forces are exerted both axial and radial on the bearing. The bearing design must withstand these loads. Table 10.7.1-1 lists the various axial and radial forces imposed on the filter wheel bearings for the various conditions. The various axial load forces are dependent upon the preload. Equation 3 calculates an equivalent radial load (Fe) for a zero clearance bearing as a function of the axial and radial loads.

$$F_e = XVF_R + YF_a \quad \text{where } F_a > 1.5 \, F_R \tan \alpha \qquad (3)$$

$$\text{where } F_a < 1.5 \tan \alpha$$

$V = 1.2$ for outer ring rotation $\alpha = 17.4°$

$X = 1 - 0.6/\eta$

$\eta = 1 - 0.33 \sin \alpha$

$Y = 0.4 \cos \alpha/\eta$

Table 10.7.1-1

- GROUND ACTIVITY

    Fr = (Weight of rotor + Filter Wheel) / 2 = 1.0 lbs   t = 4320 Hrs
    Fa = Preload

- SHORT TIME OPERATION

    -SIMULATED LAUNCH (Q = 5)

    <u>YAW & ROLL</u>

        Fr = W/2 + W/2(7.5)Qsin(wt)   t = 4.32 min
             W/2 + W/2(12.9)Q RMS   t = 2.0 min

        Fa = Preload

    <u>PITCH</u>

        Fr = W/2

                                             t = 4.32 min
        Fa = Preload + W(11.5)Qsin(wt)   t = 2.0 min
             Preload + W(12.9)Q RMS .

    -LAUNCH

    <u>YAW & ROLL</u>

                                             t = 2.16 min
        Fr = W/2 + W/2(5.0)Qsin(wt)   t = 1.0 min
             W/2 + w/2(8.6)Q RMS

        Fa = Preload

    <u>PITCH</u>

        Fr = W/2

                                             t = 2.16 min
        Fa = Preload + W(7.6)Qsin(wt)   t = 1.0 min
             Preload + W(8.6)Q RMS

- LONG TIME OPERATION - SPACE ENVIRONMENT

                                             t = 21,840 Hrs
    Fr = 0

    Fa = Preload

Table 10.7.1-2

YAW & ROLL

m$\ddot{X}$Q sin (wt)   Sinusoidal Vibration

m$\ddot{X}$Q RMS   Random Vibration

W

PITCH

m$\ddot{X}$Q sin (wt)   Sinusoidal Vibration

m$\ddot{X}$Q RMS   Random Vibration

W
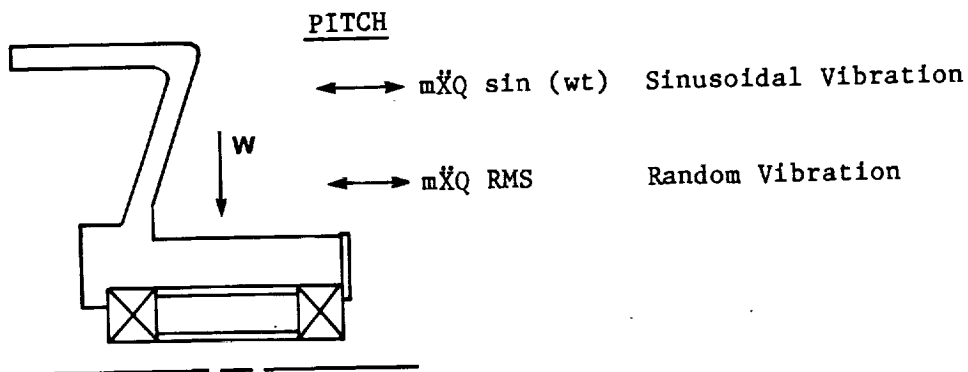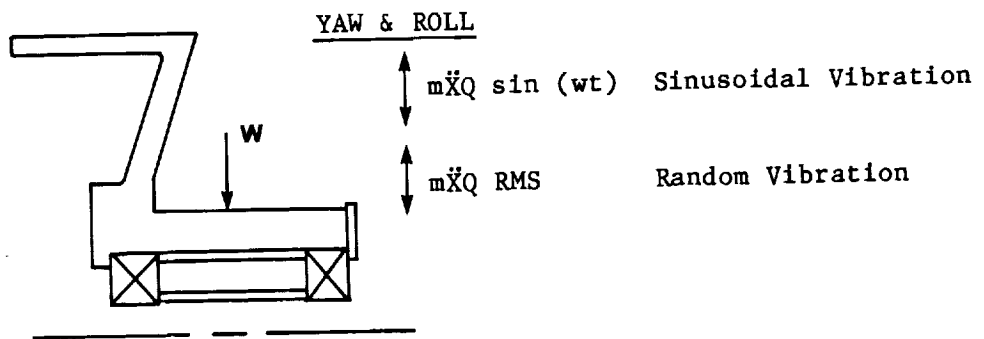
Q = Amplification Factor

(Typically for Design
Purpose Q = 5)

	YAW & ROLL		PITCH	
	SIMULATION	LAUNCH	SIMULATION	LAUNCH
$\ddot{X}$	7.5g	5.0g	11.5g	7.6g
$\ddot{X}$ RMS	12.9g	8.6g	12.9g	8.6g

Tables 10.7.1-3, 10.7.1-4, and 10.7.1-5 column 5 list the equivalent radial load for each load condition for the HIRS filter wheel bearing with a preload of 3, 12 and 30 lbs, respectively. Equation 4 calculates the accumulative damage over a loading time in terms of an equivalent force as a function of individual loading cycles and duration of loading. This method is weighted towards a space environment, therefore Fm is low.

$$F_m = \left[\frac{\Sigma F_K^{\rho} N_R}{N} \right]^{1/\rho} \qquad \text{where} \qquad (4)$$

F_m = mean effective load

N = total number of revolutions for F_K loads at N_K revolutions

ρ = 3.0 for point contact

Equation 5 calculates life assuming the bearing is continuously exposed to certain loading conditions. Thus, the total accumulated damage is a summation of each various loads for a fraction of time. This summation combines the effects of the various stresses imposed to obtain an overall estimate of the expected life of the bearing (Miner's Equation). Table 10.7.1-6 lists the various estimated life calculations for each preload value. T_i is the fraction time that the radial equivalent load F_{ei} is imposed. L_i is obtained from equation 6.

$$L = \left[\frac{1}{\left(\frac{T_1}{L_1}\right)^{1.4} + \left(\frac{T_2}{L_2}\right)^{1.4} + \left(\frac{T_3}{L_3}\right)^{1.4} + \left(\frac{T_n}{L_n}\right)^{1.4}} \right]^{0.71} \qquad \text{where} \qquad (5)$$

L_n = calculated life for a given condition

T_n = fraction of total life under condition

$(T_1 + T_2 + ...T_n = 1.0)$

The basic dynamic capacity of the HIRS filter wheel bearing as listed by Miniature Precision Bearing (MPB), the manufacturer is 550 lbs per bearing. Table 10.7.1-6 lists L as the expected life as calculated from equation 5. L_{Fm} is obtained by equation 6 for comparison check. The listed static capacities for radial and thrust loading are 332 and 730 lbs, respectively. Comparing these values to the maximum

Table 10.7.1-3

CONDITION	TIME (MIN.)/ REVOL.	Indv. Bearing Load (lbs)		F_e (lbs)	$F_3{}^3N_e$
		F_R	F_a		
1. GROUND ACTIVITY	$\dfrac{259,200 \text{ Min}}{155,520,000 \text{ Rev}}$	1.0	3.0	1.67	1,207,214
2. SPACE SIMUL. SINE-X-AXIS	$\dfrac{4.32 \text{ Min}}{2592}$	38.5	3.0	46.2	426,000
SINE Y-AXIS	$\dfrac{4.32 \text{ Min}}{2592}$	38.5	3.0	46.2	426,000
SINE Z-AXIS	$\dfrac{4.32 \text{ Min}}{2592}$	2.0	60.5	26.02	76,104
RAND X-AXIS	$\dfrac{2.0 \text{ Min}}{2300}$	65.5	3.0	78.6	971,175
RAND Y-AXIS	$\dfrac{2.0 \text{ Min}}{1200}$	65.5	3.0	78.6	971,175
RAND Z-AXIS	$\dfrac{2.0 \text{ Min}}{1200}$	1.0	67.5	28.99	48,728
LAUNCH SINE-X-AXIS	$\dfrac{2.16 \text{ Min}}{1296}$	26.0	3.0	31.2	65,602
SINE Y-AXIS	$\dfrac{2.16 \text{ Min}}{1296}$	26.0	3.0	31.2	65,602
SINE Z-AXIS	$\dfrac{2.16 \text{ Min}}{1296}$	1.0	41.0	17.8	12,182
RAND X-AXIS	$\dfrac{1.0 \text{ Min}}{600}$	44.0	3.0	52.8	147,198
RAND Y-AXIS	$\dfrac{1.0 \text{ Min}}{600}$	44.0	3.0	52.8	147,198
RAND Z-AXIS	$\dfrac{1.0 \text{ Min}}{600}$	1.0	46.0	19.9	7,881
3. SPACE ENVIRONMENT	$\dfrac{1,310,400 \text{ Min}}{786,240,000}$	---	3.0	1.27	2,685,201

PRELOAD 3

W = 2.0 lbs

Q = 5.0

TOTAL TIME = 1,569,628 Min F_m = 1.66 lbs $\Sigma F_e{}^3 N$ = 7,256,259

GOES/AVHRR.T1

Table 10.7.1-4

CONDITION	TIME (MIN.)/ REVOL.	Indv. Bearing Load (lbs) F_R	F_a	F_e (lbs)	$F_3{}^3N_e$
1. GROUND ACTIVITY	$\dfrac{259,200 \text{ Min}}{155,520,000 \text{ Rev}}$	1.0	12.0	5.5	43,124,400
2. SPACE SIMUL. SINE-X-AXIS	$\dfrac{4.32 \text{ Min}}{2592}$	38.5	12.0	46.2	426,000
SINE Y-AXIS	$\dfrac{4.32 \text{ Min}}{2592}$	38.5	12.0	46.2	426,000
SINE Z-AXIS	$\dfrac{4.32 \text{ Min}}{2592}$	1.0	69.5	29.8	114,323
RAND X-AXIS	$\dfrac{2.0 \text{ Min}}{1200}$	65.5	12.0	78.6	971,175
RAND Y-AXIS	$\dfrac{2.0 \text{ Min}}{1200}$	65.5	12.0	78.6	971,175
RAND Z-AXIS	$\dfrac{2.0 \text{ Min}}{1200}$	1.0	76.5	32.8	70,575
LAUNCH SINE-X-AXIS	$\dfrac{2.16 \text{ Min}}{1296}$	26.0	12.0	31.2	65,602
SINE Y-AXIS	$\dfrac{2.16 \text{ Min}}{1296}$	26.0	12.0	31.2	65,602
SINE Z-AXIS	$\dfrac{2.16 \text{ Min}}{1296}$	1.0	50.0	21,6	21,767
RAND X-AXIS	$\dfrac{1.0 \text{ Min}}{600}$	44.0	12.0	52.8	147,198
RAND Y-AXIS	$\dfrac{1.0 \text{ Min}}{600}$	44.0	12.0	52.8	147,198
RAND Z-AXIS	$\dfrac{1.0 \text{ Min}}{600}$	1.0	55.0	23.7	13,312
3. SPACE ENVIRONMENT	$\dfrac{1,310,400 \text{ Min}}{786,240,000}$	----	12.0	5.1	173,825,870

PRELOAD 12

W = 2.0 lbs

Q = 5.0

TOTAL TIME = 1,569,628 Min F_m = 5.2 lbs $\Sigma F_e{}^3 N$ = 220,390,197

GOES/AVHRR.T2

Table 10.7.1-5

CONDITION	TIME (MIN.)/ REVOL.	Indv. Bearing Load (lbs)		F_e (lbs)	$F_3{}^3N_e$
		F_R	F_a		
1. GROUND ACTIVITY	$\dfrac{259,200 \text{ Min}}{155,520,000 \text{ Rev}}$	1.0	30.0	13.10	582,705,187
2. SPACE SIMUL. SINE-X-AXIS	$\dfrac{4.32 \text{ Min}}{2592}$	38.5	30.0	27.6	90,826
SINE Y-AXIS	$\dfrac{4.32 \text{ Min}}{2592}$	38.5	30.0	27.6	90,826
SINE Z-AXIS	$\dfrac{4.32 \text{ Min}}{2592}$	1.0	87.5	37.46	227,084
RAND X-AXIS	$\dfrac{2.0 \text{ Min}}{1200}$	65.5	30.0	78.6	954,956
RAND Y-AXIS	$\dfrac{2.0 \text{ Min}}{1200}$	65.5	30.0	78.6	954,956
RAND Z-AXIS	$\dfrac{2.0 \text{ Min}}{1200}$	1.0	94.5	40.43	132,173
LAUNCH SINE-X-AXIS	$\dfrac{2.16 \text{ Min}}{1296}$	26.0	30.0	22.79	25,567
SINE Y-AXIS	$\dfrac{2.16 \text{ Min}}{1296}$	26.0	30.0	22.79	25,567
SINE Z-AXIS	$\dfrac{2.16 \text{ Min}}{1296}$	1.0	68.0	29.2	53,778
RAND X-AXIS	$\dfrac{1.0 \text{ Min}}{600}$	44.0	30.0	29.78	26,410
RAND Y-AXIS	$\dfrac{1.0 \text{ Min}}{600}$	44.0	30.0	29.78	26,410
RAND Z-AXIS	$\dfrac{1.0 \text{ Min}}{600}$	1.0	73.0	31.32	30,723
3. SPACE ENVIRONMENT	$\dfrac{1,310,400 \text{ Min}}{786,240,000}$	---	30.0	12.71	2,690,546,710

PRELOAD 30

W = 2.0 lbs

Q = 5.0

TOTAL TIME = 1,569,628 Min F_m = 12.78 lbs $\Sigma F_e{}^3N$ = 3,275,891,173

GOES/AVHRR.T3

GOES/AVHRR.T5

	PRELOAD 3 lbs			PRELOAD 12 lbs			PRELOAD 30 lbs		
T_1	Fe_1	L_1	$(L_1/T_1)^{1.4}$	Fe_1	L_1	$(L_1/T_1)^{1.4}$	Fe_1	L_1	$(L_1/T_1)^{1.4}$
.1651	1.67	1.00×10^8	5.07×10^{-13}	5.5	2.81×10^6	7.52×10^{-11}	13.1	2.08×10^5	2.89×10^{-9}
5.50×10^{-6}	46.2	4.74×10^3	3.09×10^{-13}	46.2	4.74×10^3	3.1×10^{-13}	27.6	2.23×10^4	3.54×10^{-14}
2.75×10^{-6}	26.0	2.66×10^4	1.05×10^{-14}	29.8	1.77×10^4	1.85×10^{-14}	37.5	8.87×10^3	4.87×10^{-14}
2.6×10^{-6}	78.6	9.64×10^2	1.01×10^{-12}	78.6	9.64×10^2	1.0×10^{-12}	78.6	9.64×10^2	1.01×10^{-12}
1.3×10^{-6}	29.0	1.92×10^4	5.8×10^{-15}	32.8	1.32×10^4	9.79×10^{-15}	40.4	7.1×10^3	2.33×10^{-14}
2.75×10^{-6}	31.2	1.53×10^4	2.3×10^{-14}	31.2	1.53×10^4	2.3×10^{-14}	22.8	3.95×10^4	6.02×10^{-15}
1.38×10^{-6}	17.8	8.29×10^4	8.13×10^{-16}	21.6	4.64×10^4	1.83×10^{-15}	29.2	1.88×10^4	6.49×10^{-15}
1.3×10^{-6}	52.8	3.18×10^3	7.2×10^{-14}	52.8	3.18×10^3	7.2×10^{-14}	29.8	1.77×10^4	6.49×10^{-15}
6.4×10^{-7}	19.9	5.9×10^4	4.46×10^{-16}	23.7	3.51×10^4	9.23×10^{-16}	31.3	1.53×10^4	2.95×10^{-15}
.8348	1.27	2.28×10^8	1.55×10^{-12}	5.1	3.52×10^6	5.31×10^{-10}	12.7	2.28×10^5	2.45×10^{-8}

T_1 = 26,160 Hrs

$\Sigma(T_1/L_1)^{1.4} = 3.49 \times 10^{-12}$

L = 136,330,000 Hrs

L_{Fm} = 102,205,000 Hrs

$\Sigma(T_k/L_1)^{1.4} = 6.07 \times 10^{-10}$

L = 3,499,000 Hrs

L_{Fm} = 3,325,000 Hrs

$\Sigma(T_1/L_1)^{1.4} = 2.74 \times 10^{-8}$

L = 234,000 Hrs

L_{Fm} = 233,000 Hrs

Table 10.7.1-6

loading conditions for each preload condition, it is evident that the bearing has a considerable factor of safety for each preload.

$$L = 2.81 \ (C/F_e)^3 \qquad \text{where} \qquad (6)$$

L = Expected bearing life (Hours)

C = Basic dynamic load rating (Pounds)

F_e = Equivalent radial load (Pounds)

The conditions that restrict the use of the above equation are:

1) Material hardness of race >58 R_C

2) Speed = 600 RPM

3) 99% Survival Rate

4) EHD lubrication where $\Lambda = 1.5$

5) ABEC-7 mounting procedures

6) Duplex-Pair

The above calculations are based on fatigue life, which is a stress calculation that calculates life as a function of the number of stress cycles the bearing material experiences. These calculations assume that the mechanics of rolling a ball over the raceway does not involve friction and wear. From the analysis presented, we can say that the bearing design will support the load for the desired operating life without failing. The analysis indicates that the effect of reducing the preload from 30 to 12 pounds is insignificant. This assumes that sufficient lubrication is available to maintain separation between the balls and races to prevent spalling.

10.7.2   Conductance Loss

The loss of lubrication in both AVHRR and HIRS rotating systems is believed to be the cause of the failure. If the bearings were to be supplied with a constant supply of oil, they would theoretically operate indefinitely. The oil maintains the separation between the surface of the balls and races to prevent the surfaces from contactings and spalling. The loss of lubricant in spaceborne bearing systems is through outgassing. Outgassing of lubrication is a function of vapor pressure governed by temperature and pressure. The temperature of the lubrication is that of the bearing (the temperature of the motor housing). Vapor pressure simply relates the random motion of liquid molecules to the energy required to overcome the attractive forces needed to escape the liquid. Spaceborne bearing assemblies that have a path to space will outgas. The low surrounding pressure and the

267

"warm" operating temperature of the bearings will drive the liquid molecules to the vapor state allowing them to travel to a source of lower energy (colder surface). With a direct unobstructed path to cold space, the lubrication will outgas. One method to prevent lubrication loss is to totally enclose the bearing assembly and operate in a oil atmosphere, which supplies a constant, never depleting oil supply. The other method is to use labyrinth seal to decrease the conductance (increase the resistance) of the flow path.

10.7.2.1 Conductance Loss Modeling

In an effort to compare the HIRS filter wheel to the AVHRR scanner, the following analytical calculations based on molecular flow conductances were utilized. Conductance is a measure of the number of molecules to pass through a geometric cross section, expressed in units of volume per time. Conductance is dependent on the geometric parameters of the cross section, length of the flow path, and the molecular characteristics of the vapor flowing through the cross section.

The following models are based on molecular flow between the bearings and cold space. The geometry of the flow path from the bearings through the various labyrinth seals, spaces and vents along with the molecular characteristics of the lubrication and the temperature of operation, determines the conductance. Molecular flow is based on the random motion and differs from viscous flow in that it is not the bulk transfer of mass from one potential to another (i.e., garden hose), but rather a random probability that a molecule going to a source is equal to the random probability that another molecule travels in the opposite direction.

Two basic equations used in the conductance model calculations are:

Conductance through a short tube:

$$C = 3.81 \left(\frac{T}{m}\right)^{1/2} \left(\frac{D^3}{L+1.33D}\right)$$

Conductance through an annular tube:

$$C = \frac{\pi}{3} \left[\frac{Tk}{2\pi m}\right]^{1/2} \left[(D_o^2 - D_i^2)^2/(D_o+D_i)\right]\left(\frac{K_o}{L}\right)$$

where $K_o = f\left(\frac{D_i}{D_o}\right)$

Figure 10.7.2-1 HIRS/2I FILTER WHEEL CONDUCTANCE MODEL

AEROSPACE/OPTICAL DIVISION **ITT**

269
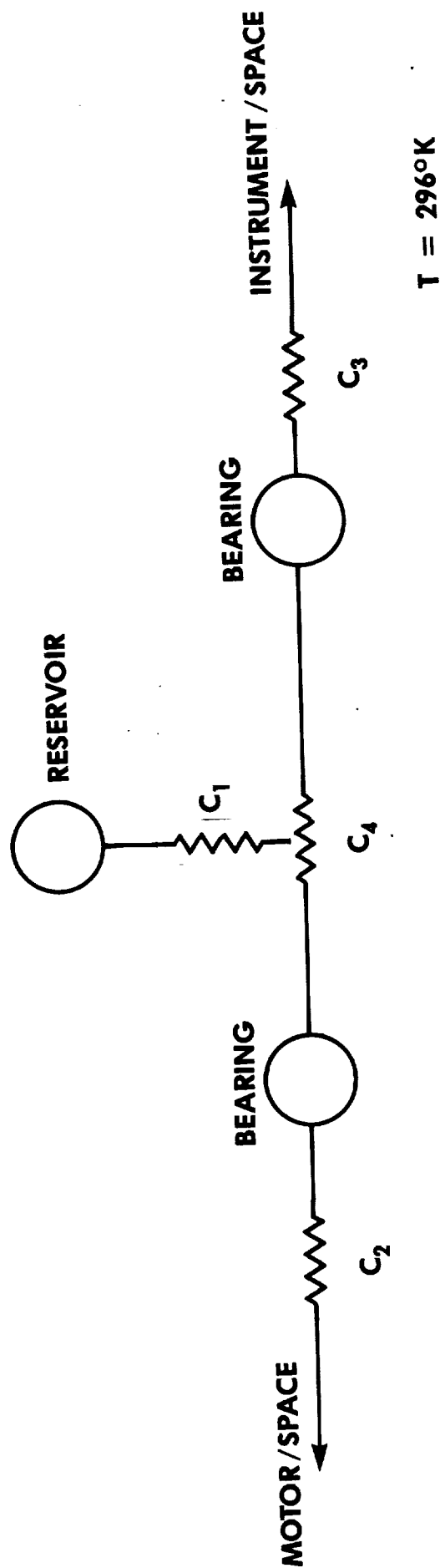
Figure 10.7.2-2 AVHRR/2 SCANNER CONDUCTANCE MODEL

MOTOR/SPACE ———/\/\/\/——— C_1

BEARING

C_2

BEARING

C_3 ——— SCAN MIRROR/SPACE

T = 288°K

AEROSPACE/OPTICAL DIVISION **ITT**
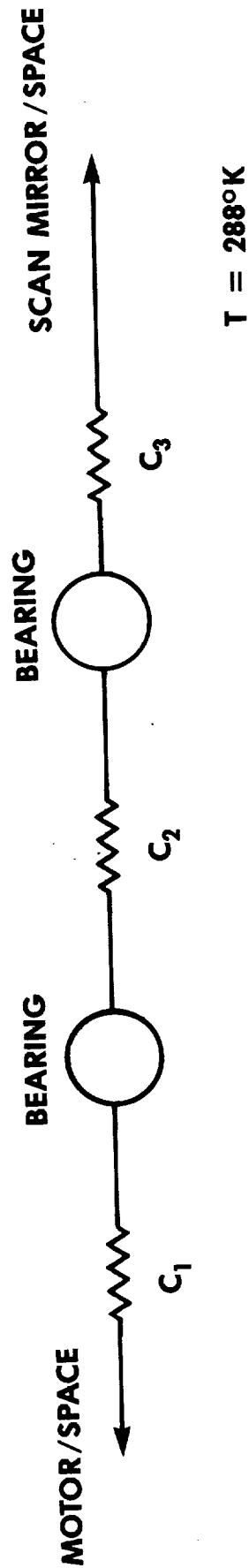
C = conductance	cm^3/S	
k = Boltzmann's Constant	1.3805x10^{-16} g cm^2/S^2	
M = Molecular Weight	g/mole	
m = mass (of molecule)	g	
D = diameter	cm	
L = length	cm	
T = temperature	Kelvin	

The HIRS filter wheel uses Apeizon C and the AVHRR scanner uses Krytox 143AB lubricant. The operating steady state temperature of the HIRS filter wheel is 23 degrees centigrade and 15 degrees centigrade for the AVHRR scanner. The molecular weight of the Apeizon C is 479 grams/mole and 3700 grams/mole for Krytox 143AB.

The conductances of the flow paths between the bearings to cold space are worst case estimates. Figures 10.7.2-1 and 10.7.2-2 are the graphic representation of the HIRS and AVHRR flow conductance.

10.7.2.1   Conductance Model Calculations

To solve the conductance equations, the geometry of the passage must be known, as well as the temperature of the surfaces and fluid, and the molecular weight of the fluid. Table 10.7.2.1-1 lists the molecular weight of the two lubricants used, Apiezon C and Krytox 143AB.

Table 10.7.2.1-1

	HIRS/2I Filter Wheel	AVHRR Scanner
	Apiezon C	Krytox 143AB
M-molecular weight	479 g/mole	3700 g/mole
m-mass (molecule)	7.957 x10^{-22}g	6.15 x 10^{-21}g

The HIRS filter wheel operates at 23°C and the AVHRR scanner operates at 15°C. For the HIRS filter wheel system, conductances are calculated from the reservoir to the bearings, between bearings and from each bearing to space. To compare the conductance performance of each lubricant in a system, the conductances were reduced to terms of temperature, T; molecular weight, M; and mass of individual molecule, m. Table 10.7.2.1-2 are the conductances as calculated for the HIRS filter wheel assembly using Apiezon C and Krytox 143AB.

Table 10.7.2.1-2. HIRS Filter Wheel Conductance

	Apeizon C	Krytox 143AB
C_1	19.0 cm^3/g	6.8 cm^3/g
C_2	905.6 cm^3/g	325.8 cm^3/g
C_3	13.9 cm^3/g	5.0 cm^3/g
C_4	5099.1 cm^3/g	2193.8 cm^3/g

The same approach was taken with the AVHRR scanner assembly. Table 10.7.2.1-3 lists the conductances using Apiezon C and Krytox 143AB.

Table 10.7.2.1-3. AVHRR Scanner

|	Apeizon C	Krytox 143AB
C_1	8.0 cm^3/g	2.9 cm^3/g
C_2	1606.3 cm^3/g	577.8 cm^3/g
C_3	225.9 cm^3/g	81.3 cm^3/g

From these calculations, three observations can be made. First, the use of Krytox (a much heavier molecular weight oil) lessens the outgassing conductance. The oil is less probable to migrate through a passage. Second, the reservoir in the HIRS system does not allow lubrication to flow to the bearings. To improve flow, a large hole (or holes) need to be employed. Third, the AVHRR front end bearing's (bearing on scan mirror side) labyrinth seal, C_3 is a much better seal than the HIRS front end seal, C_3. Seal performance is evident by comparing C_3 to the corresponding filter wheel bearing C_3.

The models do not calculate oil loss or flow rates. Electrical analog circuits can be derived to explain the flow rates and trends using the calculated resistance values. The inverse of the conductances values yield resistances. The oil in the reservoir and bearing retainers act as sources, modeled as capacitors which discharge by a currently unknown decay function. This decay is a function of vapor pressure, oil loss and molecular characteristics of the oil. These parameters are currently under investigation by ITT.

The electrical circuit describing the two systems are:
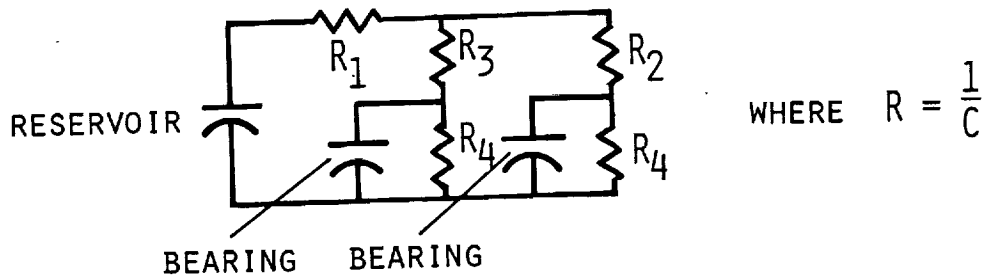
(A) HIRS/2I FILTER WHEEL

$$\text{WHERE} \quad R = \frac{1}{C}$$
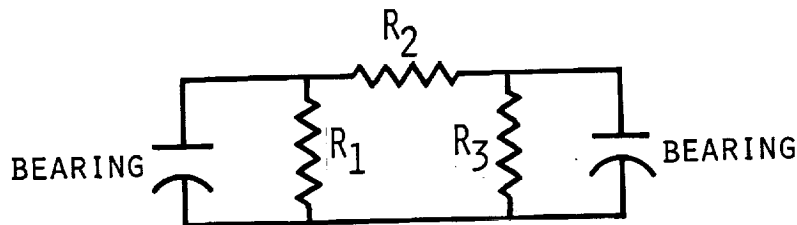
(B) AVHRR SCANNER

FIG. 10.7.2-3

      Once the mechanics of the oil vaporization is understood and modeled by a mathematical function, the two electrical circuits can be solved, and the flow rates may be determined.

10.7.3   Recommendations

      ITT is currently investigating improvements to the HIRS filter wheel. This investigation is using information gained through IR&D programs, the AVHRR/2 program and the GOES design effort. At this time, ITT is not ready to make a formal recommendation. However, from the information presented in this section, the following are strong candidates for filter wheel changes. The development of a new bearing specification similar to the AVHRR/3 bearing spec (Appendix L). The incorporation of labrynth seals in the filter wheel to improve the conductance flow resistance. Possibly, the change in lubrication from Apeizon C to Krytox 143AB. However, ITT is not ready to change the lubricant from Apeizon C to Krytox 143AB until further tests, both experiment/life test and analytical test are conducted.
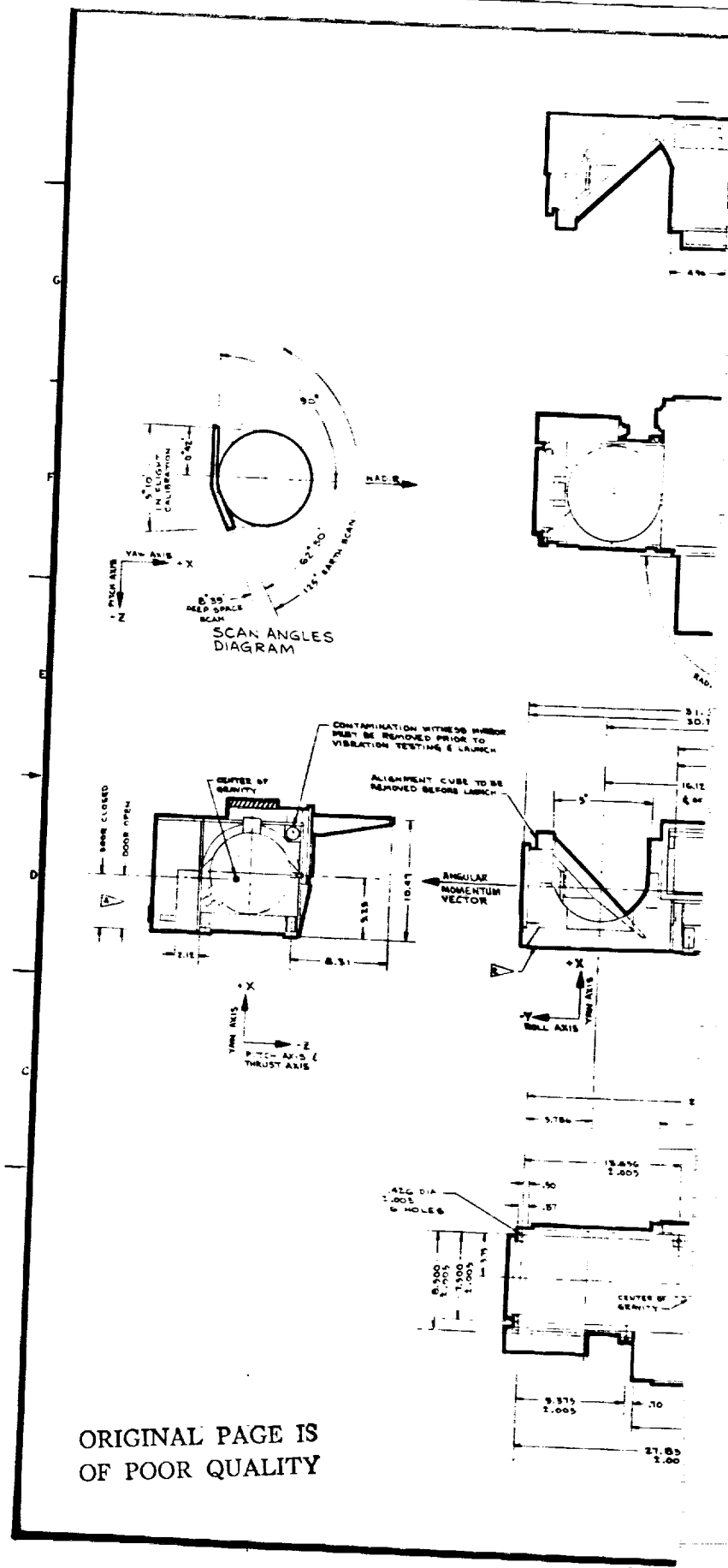
273

SCAN ANGLES
DIAGRAM

CONTAMINATION WITNESS MIRROR
MUST BE REMOVED PRIOR TO
VIBRATION TESTING & LAUNCH

ALIGNMENT CUBE TO BE
REMOVED BEFORE LAUNCH

CENTER OF
GRAVITY

ANGULAR
MOMENTUM
VECTOR

Figure 1.4-2

CONNECTOR PANEL
SCALE: ½

REF DESIG	GSFC PART NO
J1	311PA05-4P-C-12
J2	-3P-
J3	-3P-
J4	-4S-
J5	-1P-
J6	-2P-
J7	-3S-
J33	311P405-18-C-12

NOTE:

1. RADIANT COOLER DOOR TO BE IN POSITION "A" DURING LAUNCH, AND IN POSITION "B" FOR COOLER OPERATION IN ORBIT.

2. THE SIX MTG PADS ON THE INSTRUMENT ARE FLAT WITHIN .005. THE SURFACE ON WHICH THE INSTRUMENT IS TO BE MOUNTED SHOULD BE SHIMMED TO WITHIN .001 OF EACH MOUNTING PAD.

3. OVERALL DIMENSIONS DO NOT INCLUDE THE THERMAL BLANKET. THE THERMAL BLANKET EXTENDS APPROX .25 INCHES OVER THE OUTSIDE SURFACES. FASTENERS FOR BLANKET MAY EXTEND APPROX .12 IN BEYOND BLANKET SURFACE AT RANDOM PLACES.

4. CENTER OF GRAVITY LOCATION TO BE SUPPLIED AT A LATER DATE

ITT AEROSPACE/OPTICAL DIVISION
FORT WAYNE, INDIANA, U.S.A.

OUTLINE DRAWING - AVHRR/3 INSTRUMENT

E 31550 B150176

OUTLINE DRAWING AVHRR/3 INSTRUMENT

4

FOLDOUT FRAME